Parameter estimation in single molecule microscopy

Thorsen, R.O.

DOI
10.4233/uuid:db85753a-8d32-4a0b-b220-780fed198672

Publication date
2021

Document Version
Final published version

Citation (APA)
Thorsen, R. O. (2021). *Parameter estimation in single molecule microscopy*. [Dissertation (TU Delft), Delft University of Technology]. https://doi.org/10.4233/uuid:db85753a-8d32-4a0b-b220-780fed198672

Important note
To cite this publication, please use the final published version (if applicable).
Please check the document version above.

Parameter estimation in single molecule microscopy

Parameter estimation in single molecule microscopy

Dissertation

for the purpose of obtaining the degree of doctor
at Delft University of Technology
by the authority of the Rector Magnificus Prof.dr.ir. T.H.J.J. van der Hagen,
chair of the Board for Doctorates,
to be defended publicly on
Tuesday, 7 September 2021 at 10.00 hours.

by

Rasmus Østergaard THORSEN

Master of Science in Electrical Engineering,
Technical University of Denmark, Denmark
Born on Bornholm, Denmark

This dissertation has been approved by the promotors.

Composition of the doctoral committee:

Rector Magnificus,	chairperson
Prof.dr. B. Rieger,	Delft University of Technology, promotor
Prof.dr. S. Stallinga,	Delft University of Technology, promotor

Independent members:

Prof.dr. M.D. Lew	Washington University in St. Louis, USA
Dr. K.S. Grußmayer	Delft University of Technology
Prof.Dr. S. Lévêque-fort	CNRS/ University of Paris-Saclay, France
Dr. K. Mortensen	Technical University of Denmark, Denmark
Prof.dr. Y.M. Blanter	Delft University of Technology

Reserve member:

Prof.dr.ir. N. de Jong	Delft University of Technology

The work in this dissertation was conducted at the Computational Imaging Group, Faculty of Applied Sciences, Delft University of Technology.

Keywords: photometry, aberrations, structured illumination, dipole emitters, point-spread-function engineering, polarization

Printed by: Gildeprint, Enschede, The Netherlands

An electronic version of this dissertation is available at `http://repository.tudelft.nl/`.

1 Summary

Single molecule localization microscopy (SMLM) is a technique that increases the effective resolution by an order of magnitude compared to widefield microscopy. This leap in resolution enables the study of molecular structures on the order of tens of nanometers. The structure of interest is labeled with fluorophores that stochastically switch between an off and on-state. The resulting blinking behavior is recorded over typically thousands of camera frames in which different sparse subsets of the molecules are visible, enabling these to be localized with nanometer precision. This means that the resolution is not limited by diffraction. Instead, the resolution is limited by how well these label positions are determined and the density of molecules that label the imaged structure.

This thesis considers several aspects of parameter estimation in SMLM. To begin with, we discuss accuracy in photon count estimation. We demonstrate that photon counts are often wrongly estimated in standard localization microscopy. This aspect can often be ignored in the localization of symmetric spots, but when photon counts are used as parametric indicators, this can lead to severe quantitative errors. We show this in the context of a debated photometric approach, namely TRABI, where the detected photons for a molecule event are used as a parametric indicator of the axial position. The impact of optical aberrations is analyzed, and we reveal that to convert the photometric approach to an accurate axial position, aberrations must be calibrated to within 10 mλ.

Next, we investigate ways to enhance localization precision. Unlike other super-resolution techniques, SMLM employs a standard widefield microscope setup. A recent breakthrough named MINFLUX, a concept for retrieving molecule positions with (minimal) emission fluxes, showed that tuning the illumination pattern might be the future of SMLM. This implementation, however, was based on a scanning approach and is therefore slow for larger field-of-views. We present SIMFLUX that combines centroid estimation and illumination pattern induced photon count variations over a typical micron-sized field-of-view. SIMFLUX achieves on average a twofold improvement in localization precision over standard SMLM with the same photon count, which enables faster imaging or higher resolution or imaging with dimmer fluorophores.

The last part of this thesis considers localization microscopy extended with the modality of imaging the molecular orientation. When the label is fixed in space, the label orientation becomes a central part of quantifying the local order within biological complexes. We address the problem of orientation imaging with an engineered PSF named the Vortex PSF. This approach also enables an estimate of the transition between free and fixed dipole emitter limits. The analysis incorporates field-dependent aberrations in the PSF model using Nodal Aberration Theory, enabling an accurate calibration of aberrations over the entire imaging field.

To conclude this thesis, we expand upon the concept of MINFLUX to estimate molecular orientation in low light conditions. Here the excitation polarization offers a natural way to induce photon count variations and, in combination with the orientation-dependent PSF, can be used to enhance the orientation precision. We propose and analyze two modes: i) polarized epi-illumination to extract the in-plane angle only and ii) obliquely incident polarized light to retrieve the full solid-angle.

2 Samenvatting

Enkel molecule lokalisatie microscopie (SMLM) is een krachtige techniek die de effectieve resolutie een orde van grootte verhoogt in vergelijking met standaard fluorescentiemicroscopie. Deze toename in resolutie maakt het mogelijk om moleculaire structuren van de orde grootte van tientallen nanometers te bestuderen. De bestudeerde biologische structuren worden gelabeld met fluoroforen die stochastisch schakelen tussen een aan en uit-stand. Het resulterende knipperende patroon wordt vastgelegd in doorgaans duizenden camerabelden waarin de verschillende schaarse subsets van de moleculen zichtbaar zijn. Hiermee kan de locatie van de moleculen met nanometer precisie bepaald worden. De resolutie wordt niet langer beperkt door diffractie, , maar door in hoeverre de positie van de fluorofoor-labels nauwkeurig kan worden vastgesteld en door de dichtheid van moleculen die de bestudeerde structuur labelen.

Dit proefschrift behandelt diverse aspecten van parameterschatting in SMLM. Ten eerste, bediscussiëren wij de nauwkeurigheid van het inschatten van foton tellingen. Wij laten zien dat foton tellingen systematisch verkeerd worden gemaakt in standaard lokalisatiemicroscopie. Hoewel dit aspect grotendeels genegeerd kan worden in de lokalisatie van symmetrische spots, kan het gebruik van foton tellingen als parametrische indicator leiden tot ernstige kwantitatieve fouten. Wij laten dit fenomeen zien in het kader van een veelbesproken foto metrische benadering genaamd TRABI, waarbij de gedetecteerde fotonen van een actief molecuul worden gebruikt als parametrische indicator van de axiale positie. De impact van optische aberraties is geanalyseerd, en wij laten zien dat wanneer we de foto metrische benadering converteren tot een nauwkeurige axiale positie, de aberraties tot binnen 10 mλ moeten worden gekalibreerd.

Vervolgens onderzoeken wij manieren om de lokalisatieprecisie te verbeteren. In tegenstelling tot andere superresolutietechnieken maakt SMLM gebruik van een standaard fluorescentiemicroscopie opstelling. Een recente doorbraak genaamd MINFLUX, een concept voor het vaststellen van molecuulposities met (minimale) emissiefluxen, toonde aan dat het omvormen van het belichtingspatroon een stap vooruit kan bieden voor SMLM. Deze implementatie was echter gebaseerd op een scanbenadering en is vanwege die reden beperkend voor het gebruik van grotere beeldvelden. Wij presenteren SIMFLUX, welke middelpuntsschatting en belichtingspatroon geïnduceerde verandering in foton telling combineert voor een standaard micron-formaat beeldveld. SIMFLUX bereikt gemiddeld een tweevoudige verbetering van de lokalisatieprecisie ten opzichte van standaard SMLM met gelijk aantal getelde fotonen, wat snellere beeldvorming of beeldvorming met minder sterke fluoroforen mogelijk maakt.

In het laatste deel van dit proefschrift wordt lokalisatiemicroscopie verder uitgebreid met de modaliteiten van het in beeld brengen van de moleculaire oriëntatie. Wanneer een label een rigide positie en orientatie heeft, dan wordt de oriëntatie van het label een cruciaal onderdeel van het kwantificeren van de lokale orde binnen biologische complexen. De problemen rondom oriëntatiebeeldvorming pakken wij aan met een speciaal ontworpen PSF genaamd Vortex PSF. Dit ontwerp maakt het mogelijk om het tussengebied van de vrije en vaste dipool emitter limieten in te schatten. Daarnaast houden we rekening in de analyse met veldafhankelijke aberraties in het PSF-model met behulp

van nodale aberratietheorie, wat leidt tot een nauwkeurige kalibratie van aberraties over het gehele beeldveld.

Ter afsluiting van dit proefschrift bespreken we hoe belichtingsmodulatie de moleculaire oriëntatie bij lage lichtomstandigheden beter kan helpen inschatten. In het bijzonder biedt de excitatiepolarisatie een vanzelfsprekende mogelijkheid om variaties in het aantal foton tellingen te induceren en kan, in combinatie met de oriëntatie-afhankelijke PSF, worden gebruikt om de oriëntatieprecisie te verbeteren. Wij stellen de volgende twee modi voor: i) gepolariseerde epi-belichting om specifiek de hoek van de moleculen in het beeldveld vast te stellen en ii) schuin invallend gepolariseerd licht om de volledige ruimtehoek te schatten.

Contents

1 Introduction

1.1 From microscopy to nanoscopy

Most microscopy investigations in the life sciences are carried out with visible light and lenses. The success of light microscopy has even slowed the development of imaging modalities such as electron and scanning probe microscopy. This success mainly relies on two key points. High contrast is enabled by the use of fluorescence as a contrasting modality. Moreover, it allows for the detection of specific cellular components through fluorescence tagging. These key points have enabled scientists to image whole cells and some of their components (see Fig. 1.1). Beyond still images, fluorescence can be made compatible with live-cell imaging via, e.g., the use of genetically engineered fluorescent proteins, and can be quantitative in a calibrated system. Fluorescence microscopy seems almost perfect to image the sub-cellular scale if only it could resolve the smallest parts of the cell. Since the work of Ernst Abbe 150 years ago [1], however, a resolution to discern something as tiny as a normal-sized virus or protein complexes seemed unlikely, at least until the early 2000s.

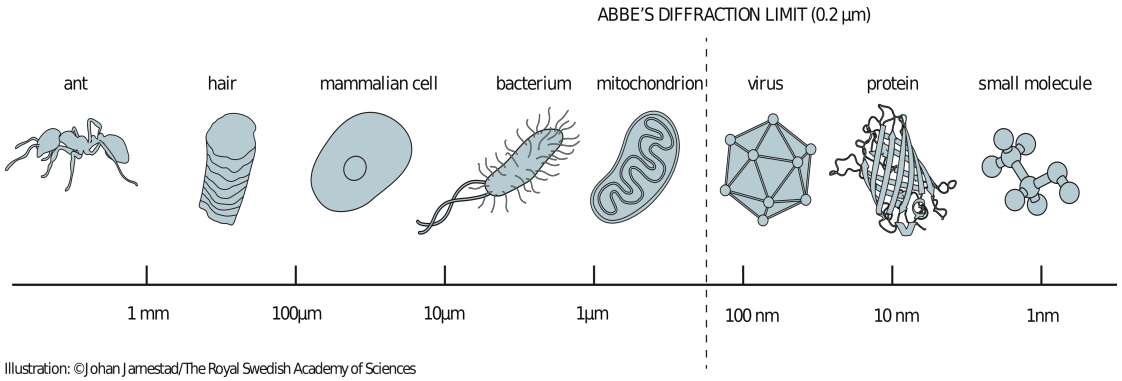

Fig. 1.1: Length scale of relevant biological structures in comparison to the diffraction limit. Figure from [2].

1.1.1 Diffraction limit of light

A fluorescent molecule emits light that is imaged by a microscope as a blurry spot. The limited sharpness of this spot emerges from the diffraction of light at the aperture of the objective lens. The shape of this blurry spot is commonly known as the Point Spread Function (PSF), and its footprint is determined by the emission wavelength λ and by the numerical aperture (NA) of the objective lens. When imaging with a perfect lens

of sufficiently low NA, the PSF is well-described by an Airy function. The modulation of a spatially periodic object is visible in the image provided the spatial period is larger than [1]:

$$d = \frac{\lambda}{2n \sin \alpha} = \frac{\lambda}{2\mathrm{NA}} \tag{1.1}$$

where n is the refractive index of the imaging medium, and α is half the maximum angle of the cone of light collected by the microscope. This equation was first conceptually described by Abbe in 1873 [1], and in the following years, mathematically derived by Helmholtz [3] and experimentally proven by Stephenson [4]; and in short, is referred to as Abbe's diffraction limit. In the axial direction, the usually worse resolution is often approximated by the expression $\approx \lambda/2n \sin^2 \alpha$ [5]. The attainable resolutions are 200-300 nm laterally and 500-700 nm axially. Hence the axial resolution is roughly twice as weak as the lateral resolution, which shows that it is more challenging to see axial than transverse details of a structure. The diffraction limit is truly limiting the capabilities of

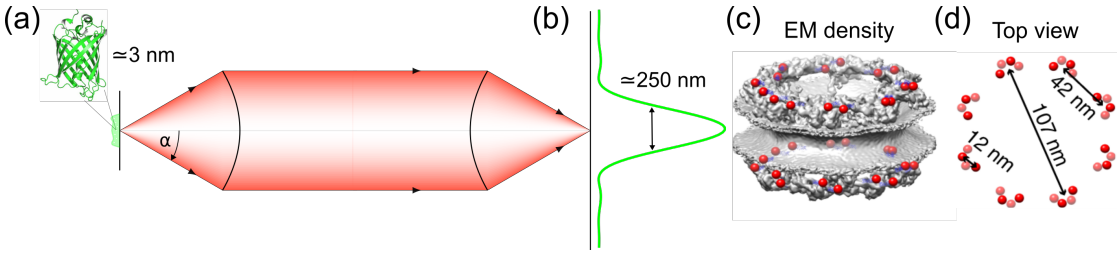

Fig. 1.2: Resolution in light microscopy. (a) The optical imaging system detects the light emitted by a single-molecule as a spot known as the PSF. The PSF width depends on the wavelength of emission and the light collection capacity of the objective lens. (b) The diffraction of light limits the resolution of the system such that emitters typically closer than the width of the PSF cannot be resolved, leading to a loss of structural detail. (c) Electron microscopy (EM) density of the nuclear pore complex (NPC) with reference protein (Nup96) indicated in red. (d) Top view of a single NPC. (c-d) Figure from [6].

scientists who investigate the inner working of cells. For example, protein complexes are molecular machines where biological functions are executed. In such complexes, the distance between sub-components is typically in the range of a few nanometers, far smaller than the diffraction limit. When such protein complexes are imaged with a microscope, the PSFs from the sub-components overlap, and a conventional fluorescent microscope can not resolve these. One such example is the nuclear pore complex (NPC), a large protein complex located in the nuclear membrane of eukaryotic cells, schematically shown in Fig. 1.2. Its composition has been mapped in great detail through electron microscopy (EM) [7]. NPCs are composed of around 30 proteins that regularize the transport across the nuclear membrane and are spatially arranged in an eight-fold symmetric structure. The overall size is approximately half of Abbe's diffraction limit (see the top view: Fig. 1.2). Even if only one protein in each sub-unit of the NPC is labeled and imaged, diffraction leads to a single blurry spot as an image of the entire complex. Hence it is impossible

to, e.g., distinguish the number of sub-components from its overall composition or to discover the precise position of all the protein sub-components. The latter challenge, could in principle, be better addressed with fluorescence microscopy than with electron microscopy.

1.1.2 Beyond diffraction

Over the past decades, many innovative efforts have been made to overcome the diffraction limit to resolution. With the advent of super-resolution microscopy, also called optical nanoscopy [8], light diffraction is no longer the limiting factor to resolution. There are, roughly speaking, three different families of techniques to improve resolution beyond the classical Abbe limit.

The historically first of these is stimulated emission depletion (STED) microscopy. STED was already introduced in the 1990s [9] and experimentally demonstrated in 2000 [10], and has since been improved and refined immensely. In STED, a doughnut-shaped depletion beam is combined with the focused excitation light spot. The depletion beam effectively decreases the size of the PSF to a size smaller than the diffraction limit. In biological samples, STED has achieved a lateral resolution down to 20 nm [11] and axial resolution to 6 times smaller than the diffraction limit [10]. Multi-color imaging has also been performed with STED microscopy [12]. Rather than using stimulated emission to turn off fluorescence, super-resolution has also been achieved with reversible saturable optical fluorescence transitions (RESOLFT) [13]. RESOLFT takes advantage of reversibly photo-switchable proteins, extending STED to low light intensities, approaching the regime of live-cell imaging.

The second family of techniques is centered on structured illumination microscopy (SIM). SIM is a widefield technique capable of doubling the diffraction-limited resolution [14]. In 2D SIM, the sample is excited with a pattern of sinusoidal intensities with spatial frequency at the diffraction limit. This makes it possible that the microscope transmits higher spatial frequencies than usually allowed. Moreover, modulating the illumination patterns to vary in all three spatial dimensions has enabled SIM extension to 3D imaging [15]. This allows optical sectioning with an axial resolution of around 300 nm and successfully imaging cellular structures with high contrast [16]. It has been shown that SIM can reach a theoretically unlimited resolution if the fluorescence response is made non-linear by saturating fluorophores in the excited state [17]. So far, saturated SIM (SSIM) has been reported to reach an experimental resolution of around 50 nm [18, 19].

Single Molecule Localization Microscopy (SMLM) is the third flavor in nanoscopy techniques. Unlike STED and SIM, which tune the illumination pattern to improve resolution, SMLM employs a standard wide-field microscope setup. As we shall see in Sec. 1.4, however, tuning the illumination might be the future of SMLM! In the rest of this thesis, the SMLM family of techniques will be the focal plane of interest.

1.1.3 Single-Molecule Localization Microscopy (SMLM)

The key idea of SMLM is to manipulate the photophysical properties of the fluorophores that label the biological specimen of interest so that they can switch stochastically between an off and on-state. In this way, a set of many recordings can be made in which different sparse subsets of fluorophores are visible. The sparsity enables an accurate and precise determination of the visible fluorophores' positions, collecting all the position information from the entire image, which constitutes the super-resolution reconstruction.

In 2006, closely related variants of this idea were proposed and demonstrated [2]: beginning with Betzig, Hess, and co-workers [20], who named the technique PALM (Photoactivated Localization Microscopy) and joined later by Zhuang and co-workers [21], who called it STORM (Stochastic Optical Reconstruction Microscopy), and by Hess and co-workers [22], who called it fPALM (fluorescence-PALM), and the accumulated binding modality developed by Sharonov and Hochstrasser [23]. Since 2006, several ways to manipulate fluorescence for localization have followed [24]. We shall refer to all these approaches collectively as SMLM. Nowadays, SMLM is routinely used for biological imaging in 2D and 3D and multiple colors [25].

SMLM has given us a better understanding of the structural composition of cells on the molecular scale as it allows unprecedented resolution while keeping the advantages of fluorescence. Among other applications, counting the number of protein molecules of a particular species in a single cell, studying the spatial structure of protein complexes, and probing the spatial interactions between different proteins, have been studied. Of such studies, several fascinating images are presented in Fig. 1: Fig. 1a shows lysosome membranes and is one of the first taken by Betzig et al. using PALM [20]. To the left, the image was made using a conventional fluorescence microscope, whereas the middle image shows its SMLM equivalent. To the right, the image of the membrane has been enlarged to the same scale equivalent to Abbe's diffraction limit (Eq. 1.1). Fig. 1b compares conventional fluorescent (upper) and 3D STORM (lower) images of actin in the axons of neurons [26]. This SMLM image unveiled a periodic, actin-spectrin-based membrane skeleton in axons. Fig 1c shows individual NPCs resolved using widefield microscopy and dual-color SMLM displaying distinct rings of the NPC where the eight corners are very well resolved (see Fig. 1.2) [6].

1.1.4 Processing pipeline of SMLM

This sub-section outlines the image processing steps from raw camera frames to the final super-resolved visualization and its quantitative analysis. In a typical experiment, the imaging conditions are tuned such that a vast amount of fluorophores are in their off-state, and in each frame, a small subset is stochastically activated. To ensure that all fluorophores are captured at least once, tens of thousands of frames are acquired. In contrast to conventional microscopy images, these raw frames are not immediately meaningful, and several processing steps are required. The processing pipeline needed to reconstruct a super-resolved image is outlined in Fig. 1.4 and explained step-by-step in the following.

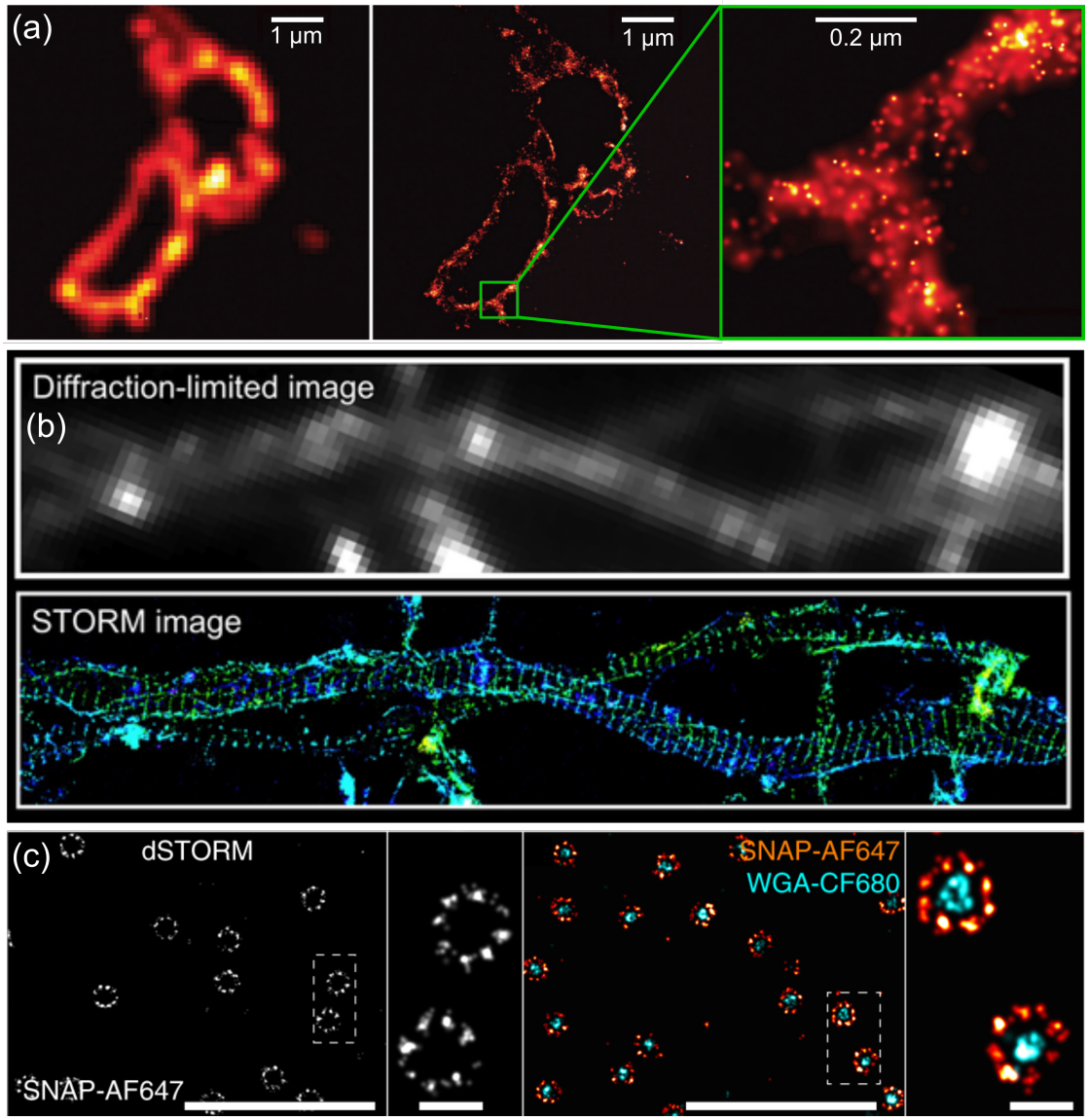

Fig. 1.3: Applications of SMLM. (a) The centre image shows lysosome membranes and is one of the first ones taken by Betzig et al. using SMLM imaging [27]. To the left, the same image taken using conventional microscopy. To the right, the image of the membranes has been enlarged. (b) A comparison of conventional fluorescent (upper) and 3D STORM (lower) images of actin in the axons of neurons [26]. The axial position in the STORM image are color-coded. (c) Nuclear pore complexes (NPCs) imaged with widefield microscopy (scalebar 1 μm) with zoomed insert showing clear NPC rings (scalebar 100 nm) [6].

Segmentation

After the image acquisition, the first step is to distinguish pixels that contain the often weak single-molecule PSFs from the noisy background. The raw images are segmented into a smaller region of interests (ROIs), usually expanding over 9-by-9 pixels, each ROI containing the image signal of a single molecule. A widely used method is peak detection using local maxima with a user-defined intensity threshold [21]. A peak detector on symmetric-like PSFs usually achieves pixel-wise resolution. If sub-pixel segmentation is needed or the PSFs are non-symmetric, weighted centroids provide a more safe option. More complicated segmentation algorithms range from wavelet theory [28] to probabilistic frameworks based on likelihood ratio tests [29]. These segmentation routines usually result in millions of segmented single-molecule images from tens of thousands of raw frames to be localized next.

Localization

Once the molecules are segmented, the next step is to localize with sub-pixel resolution. Methods range from simple center of mass (CM) determination [30] to iterative algorithms that incorporate an image formation model. Most often, a Gaussian model is fitted to the segmented PSF using a least-square (LS) or maximum likelihood estimator (MLE) [24]. The segmented images also contain valuable information about the number of emitted photons and fluorescence background, and possibly the axial location of the molecule or the molecular orientation.

The focus of this thesis, which falls in this stage of the SMLM pipeline, is to investigate new estimators to enhance the precision in which molecular properties can be accurately estimated. Therefore this step and its intricacies are discussed in much more detail, starting in Sec. 1.2.

Filtering and correction

Accurate quantification from localizations requires corrections for multiple inherent sources of error. Typical estimation errors include overlapping molecules, optical and sample induced aberrations, causing uncertain localizations. On the contrary, overcounting and undercounting due to multiple localizations of a fluorophore or incomplete photoconversion gives inaccurate quantification. These cumulative issues lead to the next step, filtering inaccurate estimates and temporal linking of localization events. The filtering can be done based on estimated outliers in the localization step (e.g., low photon count and high background) and the goodness of fit measures. The goodness of fit can be quantified in terms of statistics with a chi-squared test [31] or with a heterogeneity measure based on Wasserstein metrics [32]. Lastly, estimates of the same fluorophore are linked across sequences of frames when the on-time typically is longer than the camera frame time. The filtering returns a reduced number of proper localization events, yet it allows for a higher resolution in the reconstruction.

The long acquisition times, typically lasting tens of minutes and even up to a few hours for some cases, result in a non-negligible sample drift. The lateral plane drift

can be corrected using fiducial markers added to the sample or using spatio-temporal cross-correlation of localizations imaged at different times [33]. If needed, the axial drift can be corrected during acquisition with an auto-focus feedback system.

Reconstruction and visualization

In this final step, a super-resolved image is constructed from the localizations. The reconstruction is not an image in itself but rather a list of estimated positions. Therefore, by plotting the localizations, a pointillistic image is generated with a resolution an order of magnitude smaller than the diffraction limit. The reconstructed resolution mainly depends on the density of labels and the precision with which the fluorophores were localized. According to the Nyquist sampling theorem [34], the average distance between neighboring fluorophores must be twice smaller than the desired resolution. The image resolution can be quantified with the Fourier ring correlation (FRC) [35], which takes all factors into account, and with the advantage that no detailed knowledge of the sample is needed.

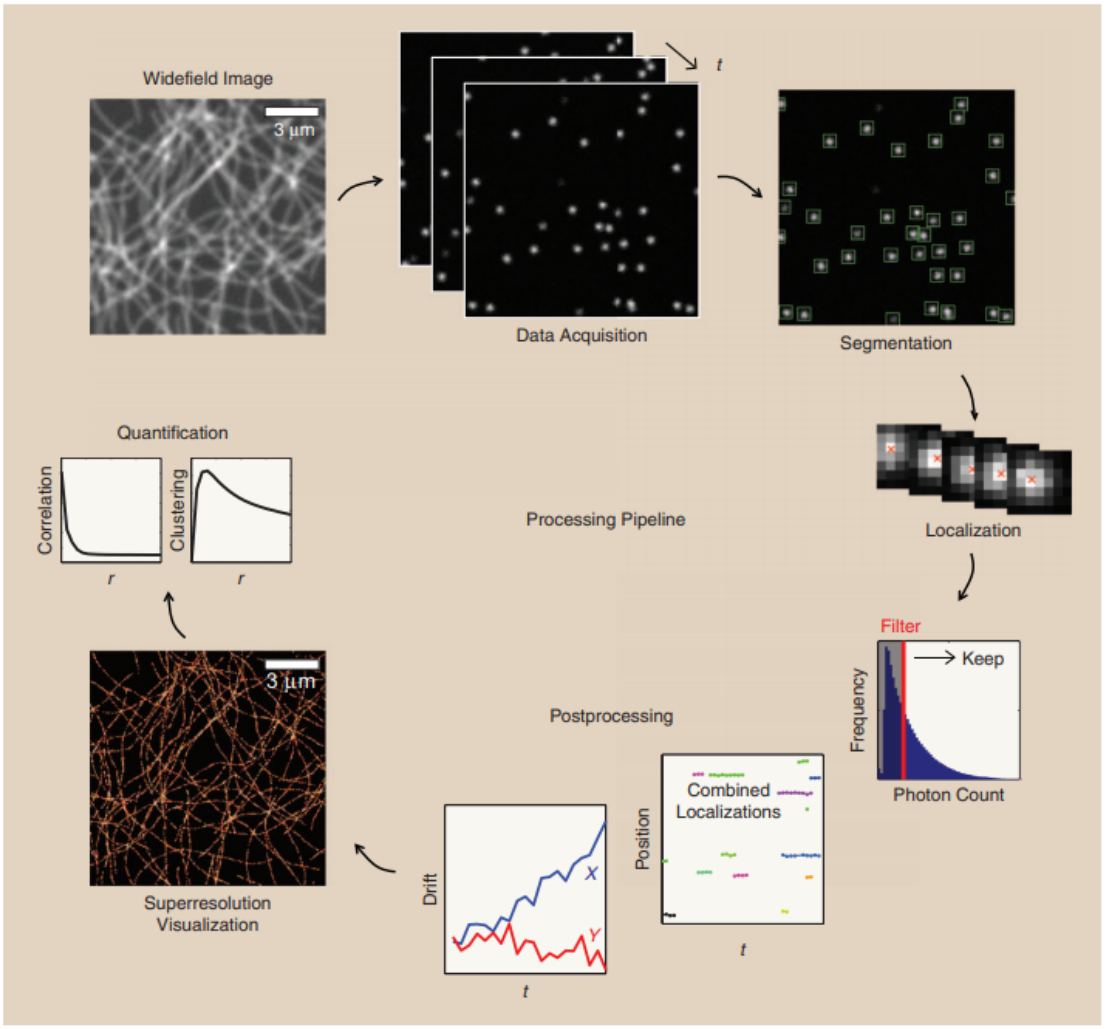

Fig. 1.4: SMLM image processing pipeline. The consecutive steps in this pipeline are acquisition of raw data, segmentation of ROIs, localization of potential fluorophores in the ROIs, post-processing of the localizations (e.g., filtering, frame connection, drift correction), and visualization of the localizations. Image from [36].

1.2 Parameter estimation in SMLM

This section relates SMLM to the field of statistical parameter estimation [37]. Firstly the most common single-molecule estimators are addressed. After reviewing standard deviation and bias as a measure of precision and accuracy, we review the concept of Fisher information and the key notion of the Cramér-Rao Lower Bound (CRLB) as a precision limit.

1.2.1 Estimators for SMLM

Single molecule estimators can be very simple but are not necessarily very accurate nor very precise. The most straightforward estimators do not require an imaging model, making them non-iterative and very fast to execute. The perhaps most simple of these is the centroid estimate [30]. Suppose the photons emitted by a molecule and collected at the pixels of the camera are taken to arrive at the centers of the pixels. In that case, the centroid, the average photon position, is easily computed, giving an estimate of the molecule position.

Numerous other model-independent estimators mainly look and regroup pixels in the neighborhood of a candidate pixel. Such estimators use or combine, for example, interpolation or template matching [38]. Another estimator employs radial symmetry, valid when the PSF is circularly symmetric so that contours of the detected number of photons are radially constant, either by computing radial symmetry centers [39] or based on maximum radial symmetry [40]. An alternative to intensity-based methods is based on the properties of the Fourier transform. Such estimators use the insight that the Fourier transform of a single-molecule image is the phase-moduated Fourier transform of the PSF, referred to as Fourier-domain localization algorithms (FDLA) [41] and phasor based in 3D [42]. In this case, localization becomes a problem of phase estimation, which can be done in a single iteration after a fast Fourier transform (FFT).

The use of direct estimators can be preferred when computational simplicity is required. However, they have limited use in practice. For instance, background most often biases the centroid toward the center of the image, giving systematic errors. To remove bias requires more advanced estimators as the background-corrected centroid estimator virtual windows center of mass (VWCM) [30]. Therefore caution is needed when using single-iteration estimators independently, but they provide excellent starting values for iterative estimators suited for SMLM. The two primary flavors of iterative estimators are the Least-Squares estimator (LS) and the Maximum Likelihood Estimation (MLE), which require an imaging model. Both methods have the additional advantage that they allow for the estimation of more parameters than the molecule position.

Least-squares (LS) estimator

The LS estimator tries to fit the parameters of an expected PSF model (μ; detailed in Sec. 1.2.2) to the segmented single-molecule images (n). The underlying statistical assumption is that each image value of a pixel n_k where $k = 1, \ldots, K$ is an observation

with normally, independently, and identically distributed noise, around the mean, given by the PSF model values μ_k of the pixels. This assumption, however, is generally only approximately true [43]. The mathematical problem statement of LS is the minimization of the sum of the square errors between the image n and model μ over the parameter set $\Theta = (x_0, y_0, \dots)$, where x_0 and y_0 are the x and y coordinates of the molecule's position and where the dots indicate possible other fit parameters. That is,

$$\Theta_{\mathrm{LS}} = \arg\min \sum_{k=1}^{K} (n_k - \mu_k(\Theta))^2, \tag{1.2}$$

where the parameters are varied to find values that minimize the argument for all pixels.

Maximum likelihood estimation (MLE)

Central in MLE is the likelihood function concept, which quantifies the likelihood for observing the images (n), given the underlying imaging model (μ). This likelihood function then necessarily relies on knowing the correct statistical distribution of possible observations around the mean expected values, i.e., MLE relies on knowing the correct noise model. A test for this latter assumption is the so-called likelihood ratio test [37]. In single molecule imaging, the statistical distribution of the images derives from the number of photons arriving at a pixel in the time interval defined by the camera shutter. For modern sCMOS or EMCCD-cameras, this follows a Poisson distribution, the standard deviation of which is known as shot noise. Gaussian read noise (for sCMOS-cameras) can mostly be neglected, and electron multiplication noise (for EMCCD-cameras) can usually be taken into account by appropriately redefining the camera gain [44]. In statistical parameter estimation, the log-likelihood is a natural measure of *goodness of fit*, and in the case of shot noise only, the log-likelihood can be written as:

$$\ell(n|\Theta) = \sum_{k=1}^{K} \left[n_k \log \mu_k - \mu_k - \log(n_k!) \right], \tag{1.3}$$

where $\mu_k = \mu_k(\Theta)$ and the summation is over all pixels k. Using this definition, MLE finds the parameters $\Theta = (x_0, y_0, \dots)$ which maximize the log-likelihood between the image n and model prediction μ. Formally,

$$\Theta_{\mathrm{MLE}} = \arg\max \ell(n|\Theta). \tag{1.4}$$

The advantage of LS compared to MLE is that it is relatively agnostic to the noise distribution and can produce reliable and robust outcomes when knowledge on noise statistics is absent. On the other hand, MLE is always superior when a physically correct noise model is applied [45]. MLE has the attractive property that it attains the information limit (lowest possible variance) if the number of instances is large enough; see 1.2.3. The performance of LS approaches that of correctly applied MLE in case the signal-to-background ratio of the single-molecule image is relatively low [45]. The noise level is more uniform across the image, and the Gaussian noise assumption that is

appropriate for LS becomes a better approximation to the true noise statistics.

Maximizing likelihood functions (or minimizing least squares) with respect to parameters usually results in a nonlinear optimization problem that cannot be solved in closed form. For that reason, it has to be addressed by iterative numerical optimization. This is done in practice using iterative routines such as the Levenberg-Marquardt [46], or Newton-Raphson optimization approaches [37].

A problem of LS and MLE-based estimators is that overlapping spots from nearby emitters will inevitably degrade the achievable localization. Other false positive localizations, arising from, e.g., structured background, may arise as well. Overlapping spots from multiple emitters can, in principle, be incorporated into the MLE likelihood function. To correctly compute the joint likelihood for several emitters, a clustering step can be necessary, which significantly adds to the complexity and computational burden [47]. Another natural extension to MLE is the so-called Maximum A Posteriori estimation (MAP), which considers prior probabilities on the fit parameters [48]. An overview of the diverse set of localization algorithms, with a comparison of performance, can be found in [49].

1.2.2 Image formation and Point Spread Function (PSF) model

The image formation model describes the expected photon count across the image as a function of the molecule position $\vec{r}_0 = (x_0, y_0)$ and signal strength, and, if needed, other molecular parameters. The expected photon count μ_k at pixel k is given by integrating the PSF (h) over the pixel area A_k:

$$\mu_k = \int_{A_k} h(\vec{r} - \vec{r}_0)\, \mathrm{d}\tilde{\mathrm{r}} \tag{1.5}$$

where in 2D SMLM the model PSF is conventionally approximated by a symmetric Gaussian:

$$h(\vec{r}) = \frac{N}{2\pi s^2} \exp\left(\frac{\vec{r}}{2s^2}\right) + b. \tag{1.6}$$

The parameters to be estimated are the molecular coordinates (x_0, y_0) together with the signal photon count N and background photons per pixel b and the Gaussian spot width s. Therefore, a Gaussian model is simple and widely used in localization microscopy, despite its lack of physical foundation. A benefit of a simple method is that one can derive analytical approximations that describes the limiting estimation error [45] (Sec. 1.2.3). Moreover, it is numerically efficient with MLE implementation on graphical processing units (GPUs) for high-speed computations [50]. Hence, a Gaussian model may be superior in ease of use, but it comes with severe shortcomings in less than ideal imaging conditions.

One weakness of the Gaussian PSF model is its inability to estimate photon count numbers accurately [51]. The exact microscope PSF has a long tail (i.e., the full diffraction pattern), which may not be fully apparent, yet its contribution is notable as it

scales with the area. The Gaussian cannot represent these diffraction patterns at all, given photon count inaccuracies up to 30 percentage points, as will be discussed in chapter 2 of this thesis. This, however, does not bias the localization estimate for circularly symmetric spots [52].

Single-molecule spots that are asymmetric will bias the localization when using the circularly symmetric Gaussian PSF model (Fig. 1.5). The observed spots can be easily deformed due to optical and sample induced aberrations [53]. An example is formed by field-dependent coma induced by light propagation through the sample, embedding medium, and coverslip. All practically used microscopes suffer from some level of aberrations, which distorts the PSF in different ways (Fig. 1.5). Another physical effect that impacts the symmetry of the single-molecule spot is the imprint of the molecule's dipole moment. This gives rise to anisotropic emission patterns as well (Fig. 1.5). In practice, rotational diffusion during image acquisition will average out some of these effects, depending on the relevant time scales in the experiment: rotational relaxation time, fluorescence lifetime, excitation-emission cycle time, and camera frame time [54]. In the absence of full rotational mobility, the molecular orientation is accessible for single-molecule imaging, as treated in Sec. 1.3.3.

In the paraxial limit (NA $\ll 1$), the imaging PSF can be approximated like the Airy pattern $4J_1(\nu r)^2/(\nu r)^2$, where J_1 is the Bessel function of the first kind with the argument νr, with $\nu = 2\pi\mathrm{NA}/\lambda$ [5]. The Airy pattern was used as the imaging model of the first paper to implement MLE for localization of a single-molecule [55]. Most often in SMLM, however, objective lenses exceed the paraxial limit substantially to improve resolution according to Abbe's diffraction limit and collect as many emitted photons as possible. The photon collection efficiency for such lenses scales typically as $\propto 1 - \cos\alpha$, where α is the half-angle of the collection cone of the objective, related to the numerical aperture by $\mathrm{NA} = n \sin\alpha$. For high-NA imaging, an accurate model requires rigorous treatment of numerous factors, such as the interfaces between the sample and lens (between medium, coverslip, and immersion oil) and vectorial effects such as polarization and apodization in the objective lens [52]. An example image generated with a vectorial model is shown in Fig. 1.5. This model is computationally expensive compared to the Gaussian model, as it requires multiple 2D Fourier transforms. Localization with such a PSF model, therefore, would benefit hugely from acceleration by GPU implementation.

Experimental PSFs retrieved by imaging point-like emitters within a specimen provides an accurate, model-free representation of the microscope's response for specific imaging conditions. It is not easy to recover these PSFs as they tend to have a low signal-to-noise ratio and are sampled sparsely with the pixel grid of the camera. Methods using experimentally acquired PSF have been developed that, in theory, achieve more accurate estimates. For example, these include interpolated PSFs [56], correlation [57], or phase retrieval [58]. A relatively recent and practical approach to accurately retrieve the PSF is to use cubic splines (cspline) [59], which can be used in localization. This approach has been significantly optimized for 3D imaging and computational speed ($> 10^5$ localizations per second) [60]. Any theoretical PSF is limited by model assumptions based on our limited knowledge of the optical system and sample. These experimentally

retrieved PSFs ease some of these limitations; however, they are microscope dependent, and accuracy could degrade over time.

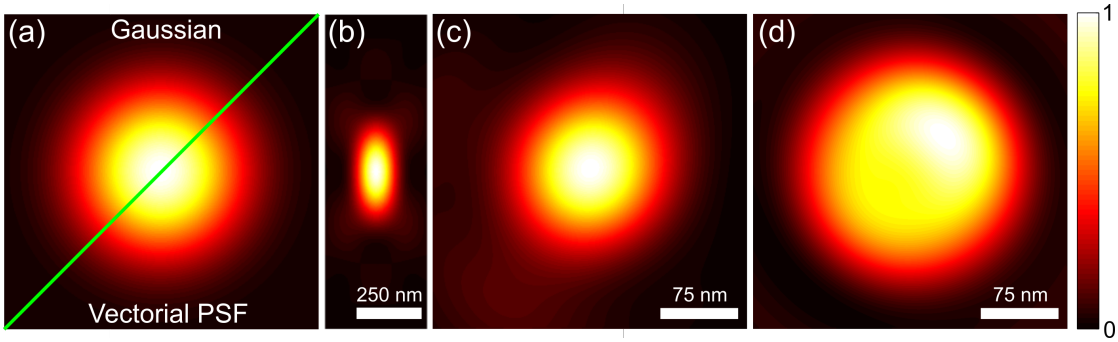

Fig. 1.5: Point-spread-functions (PSFs) models. (a) Gaussian model compared to a focused image of a single-molecule calculated from the vectorial PSF model, (b) and extended in the axial direction. (c) The vectorial image in a) corrupted with aberrations at the Maréchal diffraction-limit, (d) and with a fixed dipole moment.

1.2.3 Precision and accuracy

Both precision and accuracy are fundamental to the performance of SMLM [61]. Both aspects limit the certainty by which the molecule can be localized. This uncertainty originates from the stochastic nature of the photons that make up the image; say, it is not expected that the exact position can be retrieved exactly. It is, nonetheless, expected that, on average, the estimator retrieves the correct position.

In Fig. 1.6 a molecule is localized multiple times, and the localization precision σ_{xy} describes the spread (one standard deviation) of these estimates around its mean value $(\overline{x}, \overline{y})$. On the other hand, the localization accuracy is quantified by the localization bias Δ_{xy}, which describes the deviation of the mean of the measured position from the true position coordinate (x_0, y_0). An estimator is said to more accurate if its bias is smaller, which may have different sources. Single-molecule images all contain some amount of imperfection caused by optical instruments and by the sample. These imperfections, when not taken into account, return an undesired bias with deteriorated localization uncertainty. The most important metric is the precision with which single molecules can be localized. In Sec. 1.2.1, it was discussed that different estimators of the same parameters from the same images generally achieve different precision. The question may, therefore, be posed as to what precision can ultimately be achieved. For the general class of unbiased estimators, the answer is given in the form of a lower bound on their variance, the so-called Cramér-Rao lower bound (CRLB). This theoretical limit provides the best possible performance that any unbiased estimator can achieve. However, it does not provide information about the bias, nor does it indicate how to find these optimal estimators.

The advantage of knowing the CRLB is twofold. For example, when designing an experiment, the best-case scenario for a given measurement scheme can be estimated

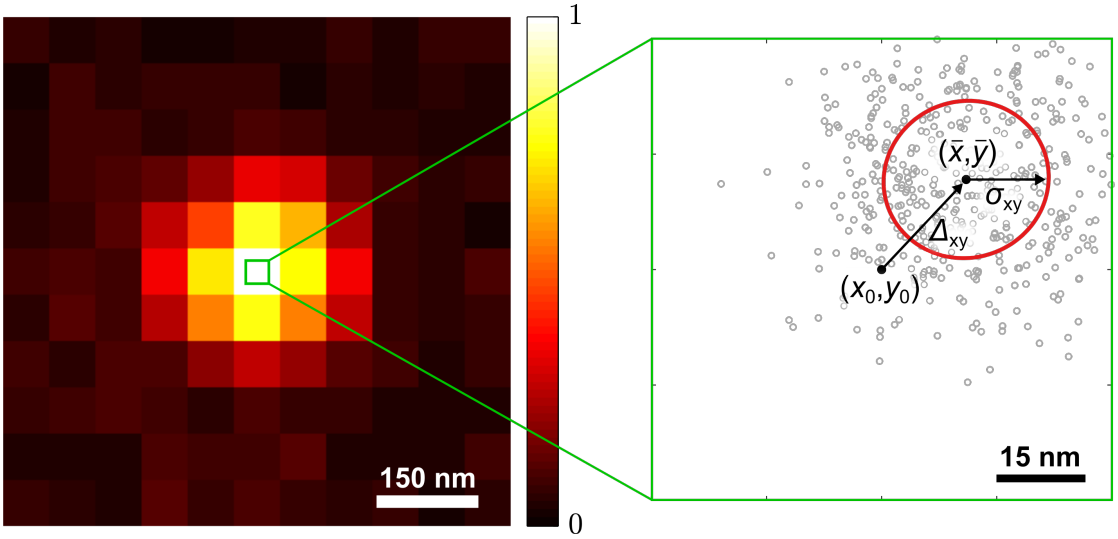

Fig. 1.6: Localization precision and accuracy. To the left, intensity image of a simulated aberrated single-molecule PSF. The exact molecule position (x_0, y_0) can be estimated from such an image with a localization precision σ_{xy} and a localization accuracy Δ_{xy} as shown in the insert to the right. The gray circles are estimated positions from different images of the same molecule, and $(\overline{x}, \overline{y})$ is the mean of these estimates.

beforehand. Additionally, one can benchmark an estimator's performance by fitting a representative ensemble of images, obtaining the estimates, and comparing the estimated variance with the CRLB. The efficiency of an estimator is the ratio of the CRLB and the mean squared error of the estimator. If an estimator has efficiency less than one, it either has a variance exceeding the CRLB or is biased, or both.

The key to determining the CRLB lies with the calculation of the so-called Fisher information. According to estimation theory [37], the CRLB is given by the diagonal elements of the inverse of a square matrix measure known as the Fisher information matrix $\boldsymbol{I}(\Theta)$. The Fisher information is closely related to the likelihood function (Eq. 1.3) and is a measure of the amount of information that an image holds about the parameters. For images where each pixel $k = 1, \ldots, K$ is corrupted by shot and readout noise, the Fisher information matrix elements are computed as:

$$[\boldsymbol{I}(\Theta)]_{ij} = \sum_{k=1}^{K} \frac{1}{\mu_k + \sigma_r^2} \frac{\partial \mu_k}{\partial \Theta_i} \frac{\partial \mu_k}{\partial \Theta_j} \tag{1.7}$$

where $\mu_k = \mu_k(\Theta)$ (Eq. 1.5) is the expected photon count on the k'th pixel given parameters $\Theta = (x_0, y_0, \ldots)$, and σ_r is the root-mean-square of the Gaussian-distributed readout noise [44]. The Fisher information is based on assessing how the likelihood function is affected by changes in the parameters. If the likelihood function does not vary significantly with the parameters, then the data contains relatively little information about the parameter and vice versa. This expectation is taken over all possible values,

so that the Fisher information is an indicator of how, on average, the likelihood function changes with the parameters.

Given the Fisher information matrix, the CRLB follows straightforwardly. The Cramér-Rao inequality states that any unbiased estimator's co-variance matrix is not smaller than the inverse of the Fisher information matrix [37]. In other words, the best attainable precision of parameter Θ_i is given by:

$$\mathrm{CRLB}_{\Theta_i} = [\boldsymbol{I}(\Theta)]^{-1}_{ii} \tag{1.8}$$

where the matrix inversion implies that a larger Fisher information results in a smaller bound on the variance. To compute the CRLB for a particular imaging model involves the determination of the model pixel values with respect to the parameters. In some simple cases, an analytical calculation of the Fisher information is possible. Otherwise, numerical approximations must be taken.

In the case of a Gaussian model (Eq. 1.6), a concise approximation of the CRLB exists. The lower bound on the localization precision, in the absence of camera readout noise ($\sigma_r \approx 0$), is given to a good approximation by [45]:

$$\sigma^2(x_0, y_0) = 2\frac{s_a^2}{N}\left(1 + 4\tau + \sqrt{\frac{2\tau}{1+4\tau}}\right) \tag{1.9}$$

where N is the number of signal photons, $s_a^2 = s^2 + a^2/12$ with a is the pixel size, and τ is a normalized dimensionless background parameter given by $\tau = 2\pi s_a^2 b/(Na^2)$ with b the number of background photons per pixel. The pre-factor of 2 accounts for the excess noise of the electron multiplication process of an EMCCD [51], and is absent for sCMOS cameras.

In the limit of low background ($N \gg b$), the localization precision scales as $\sigma^2 \propto s/N$, which shows that a more narrow PSF (high resolution according to Abbe) and more photons add to the improvement of the localization precision. Unfortunately, the PSF width is limited by diffraction, and there is a limited budget of photons, determined by photo-bleaching rates. For example, to resolve a myosin walk on actin with 1.5 nm resolution [62], it requires a total of 1.4 million collected photons, divided into 10,000 photons per frame. These photon numbers are unreasonably high for typical single-molecule experiments where photon counts usually range from a few hundred to a few thousand, achieving a 10-30 nm resolution.

1.3 Extensions of 2D SMLM

So far, the discussion focused in detail on two-dimensional (2D). Here we review several extensions of this primary modality: localization in three-dimensions (3D), multicolor imaging, and imaging molecular orientation.

1.3.1 Imaging in 3D

A lot more information can be obtained about the sample by extending the localization to 3D [26]. Without this extension, the visualization of structures stretched out in the axial direction can easily be misinterpreted.

The standard PSF is limited in 3D imaging, as the molecule's axial position must be retrieved from a single 2D depth slice. One limitation follows from the 3D PSF shape, which changes relatively slowly with changing axial position relative to its focal plane (Fig. 1.5). This slow change can be interpreted as a small amount of Fisher information (Eq. 1.7), resulting in poor axial precision (Eq. 1.8). Additionally, in the absence of aberrations, the 3D PSF is symmetric around its focal plane, making the axial position ambiguous. In fact, at the focal plane, the Fisher information is zero, and the anticipated axial localization precision diverges. These limitations may be partly overcome using extremely bright nanoparticles [63]. There is, however, a low budget of photons when imaging single-molecules, especially over an extended axial range. One of the most used 3D methods to overcome these limitations is PSF engineering.

PSF engineering attains precise axial localization by optically encoding the axial position in the PSF shape. By far, the most widely used method is astigmatic imaging [64]. Placing a relatively weak cylindrical lens into the imaging path from sample to camera forms an elliptical PSF with an ellipticity that varies with axial position. Its simplicity has resulted in analytical models enabling more advanced estimators to optimize the precision [65]. Another popular version of PSF engineering is to use a PSF that twists like a double helix (DH) along the optical axis [66]. Comparable is the reported SPINDLE (DH-PSF-S) study to obtain an analytical expression for the pupil function in vortex singularities [67]. A related PSF is the corkscrew-PSF, which generates only a single lobe compressing the photons more than the DH-PSF [68]. This comes with the drawback that two-measurements are then needed for a single depth estimation as the determination of the rotation angle is ambiguous from a single image.

Another step in sophistication in PSF engineering is incorporating Fisher information in the optimization of the PSF design. It was noted that the standard PSF has low Fisher information; hence it makes sense to look for the opposite, PSFs with a large amount of Fisher information. The family of information-optimized PSFs is the so-called tetrapod PSF family [69]. The tetrapod PSF is optimized to generate the most Fisher information (i.e., the best axial precision) over a specific depth. A distinction between these information-optimized PSFs and, for example, astigmatic PSFs, is that a spatially extended PSF is generated where the axial position is encoded in a non-trivial way. So, the encoding of the axial position is not in straightforward geometric parameters (e.g., ellipticity, rotation) but the intricate shape of the PSF. Another branch of 3D localization methods uses two or more recordings of the molecules acquired at different axial planes simultaneously, so-called biplane or multi-plane methods [70, 71].

Apart from the PSF shape, photon count estimation can also construct an axially dependent parameter. This was the gist of the so-called temporal radial-aperture-based intensity estimation (TRABI) method [72]. TRABI is based on the fact that Gaussian PSF fitting underestimates single-molecule intensities systematically [51]. Nonetheless,

using such inaccuracies may not be the best parameter as these may be very susceptible to model errors. The ability of TRABI to resolve 3D structures has been compared to more advanced spot fitting methods [60] and shown to perform less well which is a subject of discussion in Chapter 2.

1.3.2 Imaging molecular species

Another useful extension of standard 2D SMLM is imaging differently labeled molecules in the same sample to study, e.g., protein interaction. This is commonly accomplished by labeling the molecules of interest with fluorophores that have distinctive emission spectra [73]. This makes the technical challenge one of multi-color fluorescence imaging. A straightforward method is to use dichroic beamsplitters and image single-molecules in parallel for the two, or sometimes more, color channels [71]. Alternatively, the emission color can be encoded in the PSF shape by PSF engineering methods [74, 75, 76], possibly in combination with deep-learning methods [77].

1.3.3 Imaging molecular orientation

Another parameter that has been the focus of several studies over the years is molecular orientation [78]. The introduction of orientation estimation can provide unparalleled insight into the acrobatics of motor proteins [79] and measure molecular order and disorder in single cells. Recently it has been introduced in material sciences for measuring the deformation of polymers [80].

A light-emitting molecule is well described as a classic radiating electric dipole [5]. Its orientation will inherently affect how it interacts in absorption and emission with the surrounding electromagnetic field. Molecular orientation is mostly ignored in standard SMLM as the molecules are assumed to rotate freely. That is, the PSF is an average of the PSFs for all different orientations of the emission electric dipole [52]. Unless such a degree of rotational mobility can be guaranteed, molecular orientation can no longer be ignored. These localization biases are found to reach several nanometres for typical optical system parameters [19, 17, 81, 82, 52]. In the opposite case, in which the molecule's dipole moment is fixed, the orientation becomes an accessible parameter in single-molecule imaging. The interplay between different time scales describes the cross-over between the free and fixed dipole limits [54]. These include the fluorescence lifetime and the rotational relaxation time, as known from anisotropy imaging, and their relative magnitude determines the impact of rotational diffusion on the image formation. The amount of diffusion can be quantified by a single additional parameter related to a model for the underlying model rotational confinement, e.g., a Wobble-in-cone model [83] or a harmonic orientational potential model [54].

Fixed dipoles generate PSFs that vary in shape with their orientation relative to the coordinate frame of the objective lens [84]. An early method to estimate orientation based on this effect is [85], where the molecules are imaged slightly off focus to increase the PSF shape variance with respect to molecular orientation. The need to defocus increases the PSF size, which inherently spreads the limited number of photons across

more pixels, degrading localization precision. Thus, long exposures are necessary to overcome this photon dilution, making this method less ideal for single-molecule imaging. The means to simultaneously estimate position and orientation was demonstrated on bright in-focus immobile molecules [51], using MLE with a theoretically correct fixed dipole PSF. A reported low computational speed (0.4 molecules/s [86]) is a significant drawback and is yet to be shown to be compatible with imaging biological samples. Alternative methods apply a Gaussian imaging model weighted by Hermite polynomials combined with polarized detection [87], and dipole image formation in terms of a weighted sum of six basis templates [81].

Exercising the same reasoning as applied to 3D SMLM (Sec. 1.3.1), PSF engineering can be used to improve orientation estimation [88]. The DH-PSF was initially intended for 3D localization, but its shape variations turn out to be exploitable for orientation estimation as well [89]. It was found that the molecular orientation is reflected most prominently in the asymmetry of the two lobes. Another proposed PSF engineering method for orientation estimation is quadrated pupil imaging [90]. Here, the collected emission is first split into orthogonally polarized channels where the PSF appears as a pair of four-point stars with lobes of unequal intensity. The integrated intensity around each of the eight lobes indicates the molecular orientation. These four-pointed images, however, are not easily compatible with precise localization.

A particularly relevant method of orientation estimation involves modulating the polarization of the excitation [86, 90] over three different polarization states (i.e., three camera frames) and analyzing the corresponding emitted intensities for retrieving the orientation of the molecules in the focal plane. The determination of in-plane molecular orientation and rotational immobility was compatible with position estimation in a super-resolution imaging experiment. The approach was demonstrated on samples of stretched linear lambda phase DNA (λ-DNA), stained with an intercalating and groove binding dye (e.g., SYTOX orange [91]), as shown in Fig 1.7. Intercalating dyes generally align perpendicular to the DNA strand, as the DNA axis bends, and the mean molecular orientation rotates accordingly. This demonstrates the intricate importance of the need to relate the orientation of the fluorescent probe to the structure to which it is bound, be it other macromolecules or cellular organelles.

1.4 Modulation enhanced parameter estimation

As described so far, SMLM employs a wide-field illumination. This is unlike other super-resolution techniques such as STED and SIM (Sec. 1.1), which tune the illumination pattern to enhance the resolution. In this section, a new advancement in SMLM is treated. Here, the signal of single molecules is modulated with targeted illumination to enhance the precision in which molecular properties can be estimated. We refer to these methods as modulation enhanced SMLM.

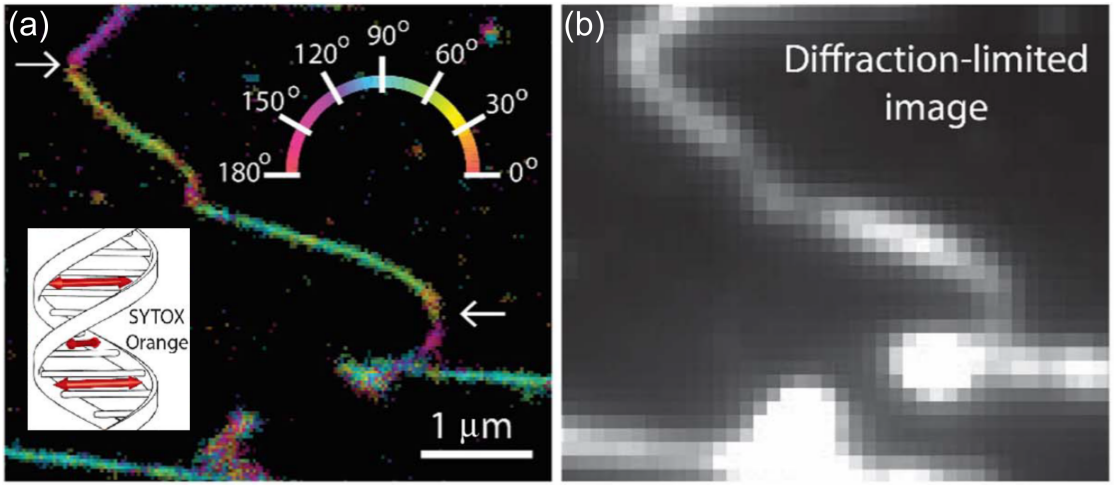

Fig. 1.7: Applications of orientation SMLM. (a) A super-resolution image of a λ-DNA strand exhibiting multiple local trajectories. The strand is color-coded with the mean orientation of the estimated molecules. The insert shows that due to the intercalative binding mode of SYTOX ORANGE, its absorption dipole moments align perpendicular to the DNA axis. (b) For comparison, a diffraction-limited image. Figure from [90].

1.4.1 MINFLUX

In 2017 a breakthrough in super-resolution microscopy was published, namely MINFLUX [92], which unites single molecule imaging with coordinate-targeted illumination. Here molecules are illuminated so that enhanced localization precision is reached with minimal emission fluxes (MINFLUX) [92]. In this way, MINFLUX extracts more information on the localization per fluorescence emission photon than standard wide-field illumination.

The concept of MINFLUX is sketched in Fig. 1.8. A doughnut illumination spot if shifted over an area of size L, and the position of a single-molecule in this scanning range is determined by a triangulation method, which uses the total detected photon count for the different doughnut positions as input. The localization precision of this procedure scales as [92]:

$$\sigma_x = L/\sqrt{N} \tag{1.10}$$

which is advantageous compared to conventional SMLM ($\propto s/\sqrt{N}$), as the beam separation L can in principle be chosen arbitrarily small, whereas s is diffraction-limited to a width on the order of λ/NA. Therefore MINFLUX can obtain a localization precision of a few nanometres with an order of magnitude fewer emitted photons than SMLM. In Fig. 1.8, MINFLUX resolves a square array of fluorophores nanometres apart, which cannot be done with conventional SMLM at the same level of detected photons. Recently, MINFLUX has been extended with multi-color and 3D imaging [93].

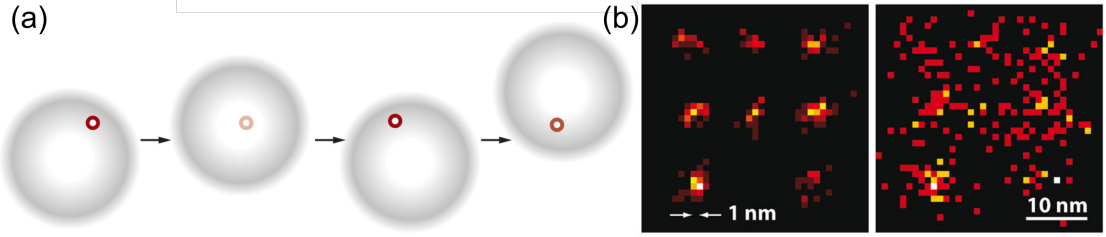

Fig. 1.8: MINFLUX. (a) Graphical representation of MINFUX. (b) Microscope images of a square array of fluorophores reconstructed using MINFLUX (left) and conventional super-resolution microscope (right). (a) Figure from [94] (b) and [92].

1.4.2 Modulation enhanced SMLM

The use of illumination modulation to enhance localization precision can be generalized to increase the precision in estimating any molecular parameter. This can be understood by considering the general case of parameter estimation from L recorded images, where the illumination is modulated proportional to the modulation function $P_l(\Theta)$, where $\sum P_l = 1$ over $l = 1, \dots, L$. The modulation function depends on the parameters for which the precision is to be enhanced $\Theta = (x_0, y_0, \dots)$, e.g., molecular position employing the modulation function as four displaced illumination beams (MINFLUX) [92] or in-plane molecular orientation employing the modulation function as three polarization states [90]. As discussed in the case of MINFLUX (Sec. 1.4.1), the photon efficiency of the modulated parameters can be greatly improved, which leads to enhanced precision compared to conventional SMLM.

The Fisher information can be used to quantify how a modulation scheme increases the photon efficiency following the procedure in Sec. 1.2.3. The imaging model in Eq. (1.5) is adjusted to include the modulation function, say the expected photon count on pixel k for the illumination state l is given by:

$$\mu_k^l = \int_{A_k} P_l(\Theta) h(\vec{r} - \vec{r}_0, \Theta)\, \mathrm{d}\tilde{\mathbf{r}}, \tag{1.11}$$

where $H(\vec{r}, \Theta)$ is the PSF model. In the case of low background ($N \gg b$) and shot noise only, the relevant Fisher matrix elements in Eq. (1.7) can be approximated as:

$$[I(\Theta)]_{ii} \approx \underbrace{\sum_{k=1}^{K} \frac{1}{h(r,\Theta)} \left(\frac{\partial h(r,\Theta)}{\partial \Theta_i} \right)^2}_{\text{Conventional SMLM}} + \underbrace{N \sum_{l=l}^{L} \frac{1}{P_l(\Theta)} \left(\frac{\partial P_l(\Theta)}{\partial \Theta_i} \right)^2}_{\text{Modulation enhanced SMLM}}, \tag{1.12}$$

where the first term is the same as for conventional SMLM, i.e., in the case of molecule position $\approx N/s^2$ (Eq. 1.8), and the second term is the additional amount of Fisher information generated by the modulation scheme. From the definition of the CRLB in Eq. (1.8), the additional Fisher information implies a smaller bound on the achievable precision. This, of course, leads to the question of how to design such a modulation

function $P(\Theta)$, how big the improvement in precision can be, and how to realize this in practice for a given set of parameters.

1.5 Motivation and outline of this thesis

The focus of this thesis is on new estimation schemes for molecular parameters in SMLM, where the aspects of accuracy and precision are analyzed in detail. The key challenges and research questions that are addresses are:

- The use of photon counts as parametric indicators, especially in the context of 3D localization, has been proposed in the literature. However, the accuracy of different ways to estimate the number of detected photons originating from a single molecule emission event lacks so far. Important in addressing this challenge is to focus on the imaging model used in the estimation and the role of aberrations in this.

- How can modulation of the intensity be used to improve localization precision that is compatible with standard wide-field imaging on a camera? How can simulation help test if the optimal precision can be reached for different signal and background levels and the various parameters describing the illumination modulation? Another topic of interest is detecting molecular on-events, as the on-off switching can get mixed up by blinking due to the illumination modulation. Full field-of-view simulations will be explored to investigate these questions.

- In what way can the PSF be engineered to avoid molecule orientation degeneracy near focus, and is it possible then to measure the rotational diffusion from the PSF? Quantification of the degree of fixed versus freely rotation emission dipole will be explored. It is well-known that PSF engineering suffers from optical aberrations, so how can these be incorporated into the model to generate a spatial variant PSF model?

- How can modulation of the polarization of the illumination be used to improve the estimation of molecular orientation, analogous to how the modulation of the illumination intensity is used to improve the estimation of molecular position? Is it possible to optimize the modulation to estimate the molecular orientation in the entire 3D space angle, i.e., both the azimuthal and polar angles?

This thesis describes several methods that have been developed specifically to address these challenges. In chapter 2, we show that photon count as an indicator for the axial position is susceptible even to typical optical aberrations. In chapter 3, we propose to extract the molecule's position in a combined estimation from shifting sinusoidal illumination patterns to enhance the localization precision. In chapter 4, we suggest a new imaging model for orientation estimation and rotational diffusion using PSF engineering. In chapter 5, we use polarization modulation to enhance orientation precision. The final chapter of this thesis, Chapter 6, provides concluding remarks about the work presented and an outlook and recommendation for future research opportunities.

1.6 References

[1] E. Abbe. “Beitrage zur Theorie des Mikroskops und der mikroskopischen Wahrnehmung”. In: *Archiv für Mikroskopische Anatomie* 9 (1873), 413—468.

[2] P. release. NobelPrize.org. *Nobel Media AB 2020.* `https://www.nobelprize.org/prizes/chemistry/2014/press-release/`. [Online; accessed 01-April-2020]. 2020.

[3] H. von Helmholtz. “Die theoretische Grenze fur die Leistungsfahigkeit der Mikroskope”. In: *Ann. Phys. Chem.* (1874), 557—584.

[4] J. Stephenson. “Observations on Professor Abbe’s Experiments illustrating his Theory of Microscopic Vision”. In: *The Monthly Microscopical Journal* 17 (1877), 82–88.

[5] M. Born and E. Wolf. *Principles of Optics: Electromagnetic Theory of Propagation, Interference and Diffraction of Light.* Elsevier Ltd., 1980. ISBN: 978-0-08-026482-0.

[6] J. Thevathasan et al. “Nuclear pores as versatile reference standards for quantitative superresolution microscopy”. In: *Nat Methods* 16 (2019), pp. 1045–1053.

[7] A. von Appen et al. “In situ structural analysis of the human nuclear pore complex”. In: *Phys. Rev. Lett.* 526 (2015), pp. 140–143.

[8] S. Hell. “Toward fluorescence nanoscopy”. In: *Nat. Biotechnol.* 21 (2003), pp. 1347–1355.

[9] S. Hell and J. Wichmann. “Breaking the diffraction resolution limit by stimulated emission: stimulated-emission-depletion fluorescence microscopy”. In: *Optics Letters* 19.11 (1994), pp. 780–782.

[10] T. Klar et al. “Fluorescence microscopy with diffraction resolution barrier broken by stimulated emission”. In: *PNAS* 97.15 (2000), pp. 8206–8210.

[11] F. Gottfert et al. “Coaligned Dual-Channel STED Nanoscopy and Molecular Diffusion Analysis at 20 nm Resolution”. In: *Biophysical Journal* 105.1 (2013), PL01–L03.

[12] G. Donnert et al. “Two-color far-field fluorescence nanoscopy”. In: *Biophys J.* 92.8 (2007), PL67–L69.

[13] M. Hofmann et al. “Breaking the diffraction barrier in fluorescence microscopy at low light intensities by using reversibly photoswitchable proteins”. In: *PNAS* 102.49 (2005), pp. 17565–17569.

[14] M. Gustafsson. “Surpassing the lateral resolution limit by a factor of two using structured illumination microscopy”. In: *Biophysical Journal* 198.2 (2001), pp. 82–87.

[15] M. Gustafsson et al. “Three-Dimensional Resolution Doubling in Wide-Field Fluorescence Microscopy by Structured Illumination”. In: *Biophysical Journal* 94.12 (2008), pp. 4957–4970.

[16] L. Schermelleh et al. “Subdiffraction Multicolor Imaging of the Nuclear Periphery with 3D Structured Illumination Microscopy”. In: *Science* 320.5881 (2008), pp. 1332–1336.

[17] R. Heintzmann, T. Jovin, and C. Cremer. “Saturated patterned excitation microscopy—a concept for optical resolution improvement”. In: *J. Opt. Soc. Am. A* 19.8 (2002), pp. 1599–1609.

[18] M. Gustafsson. “Nonlinear structured-illumination microscopy: Wide-field fluorescence imaging with theoretically unlimited resolution”. In: *PNAS* 102.37 (2005), pp. 13081–13086.

[19] D. Li et al. “Extended-resolution structured illumination imaging of endocytic and cytoskeletal dynamics”. In: *Science* 349.6251 (2015). ISSN: 0036-8075. eprint: `https://science.sciencemag.org/content/349/6251/aab3500.full.pdf`.

[20] E. Betzig et al. “Imaging Intracellular Fluorescent Proteins at Nanometer Resolution”. In: *Science* 313.5793 (2006), pp. 1642–1645.

[21] M. Rust, M. Bates, and X. Zhuang. “Sub-diffraction-limit imaging by stochastic optical reconstruction microscopy (STORM)”. In: *Nature Methods* 3 (2006), pp. 793–796.

[22] S. .Hess, T. Girirajan, and M. Mason. “Ultra-High Resolution Imaging by Fluorescence Photoactivation Localization Microscopy”. In: *Biophysical Journal* 91 (2006), pp. 4258–4272.

[23] A. Sharonov and R. M. Hochstrasser. “Wide-field subdiffraction imaging by accumulated binding of diffusing probes”. In: *Proceedings of the National Academy of Sciences* 103.50 (2006), pp. 18911–18916. ISSN: 0027-8424. eprint: `https://www.pnas.org/content/103/50/18911.full.pdf`.

[24] M. Thompson, M. Lew, and W. Moerner. “Extending Microscopic Resolution with Single-Molecule Imaging and Active Control”. In: *Annual Review of Biophysics* 41 (2012), pp. 321–342.

[25] T. Klein, S. Proppert, and M. Sauer. “Eight years of single-molecule localization microscopy”. In: *Histochemistry and Cell Biology* 141 (2014), pp. 561–575.

[26] R. Dickson, D. Norris, and W. Moerner. “Actin, Spectrin, and Associated Proteins Form a Periodic Cytoskeletal Structure in Axons”. In: *Science* 339.6118 (2013), pp. 452–456.

[27] E. Betzig et al. “Imaging Intracellular Fluorescent Proteins at Nanometer Resolution”. In: *Science* 313.5793 (2006), pp. 1642–1645.

[28] I. Izeddin et al. “Wavelet analysis for single molecule localization microscopy”. In: *Optics Express* 20,9 (2012), pp. 2081–2095.

[29] C. Smith et al. “Probability-based particle detection that enables threshold-free and robust in vivo single-molecule tracking”. In: *MoleCular Biology of the Cell* 26.22 (2015), pp. 4057–4062.

[30] A. Berglund et al. "Fast, bias-free algorithm for tracking single particles with variable size and shape". In: *Optics Express* 16.18 (2008), pp. 14064–14075.

[31] M. Siemons et al. "High precision wavefront control in point spread function engineering for single emitter localization". In: *Optics Express* 16.7 (2018), pp. 8397–8416.

[32] H. Mazidi et al. "Quantifying accuracy and heterogeneity in single-molecule super-resolution microscopy". In: *bioRxiv* (2020).

[33] Y. Wang et al. "Localization events-based sample drift correction for localization microscopy with redundant cross-correlation algorithm". In: *Optics Express* 22.13 (2014), pp. 15982–15991.

[34] H. Shroff et al. "Live-cell photoactivated localization microscopy of nanoscale adhesion dynamics". In: *Nat. Methods* 5, (2008), pp. 417–423.

[35] R. Nieuwenhuizen et al. "Measuring image resolution in optical nanoscopy". In: *Nat Methods* 10 (2013), pp. 557–562.

[36] B. Rieger, R. Nieuwenhuizen, and S. Stallinga. "Image Processing and Analysis for Single-Molecule Localization Microscopy: Computation for nanoscale imaging". In: *IEEE Signal Processing Magazine* 32.1 (2014), pp. 49–57.

[37] A. van den Bos. *Parameter Estimation for Scientists and Engineers*. John Wiley & Sons, Inc., 2007. ISBN: 978-0-470-14781-8.

[38] T. Takeshima et al. "A multi-emitter fitting algorithm for potential live cell super-resolution imaging over a wide range of molecular densities". In: *Journal of Microscopy* 271.3 (2018).

[39] R. Parthasarathy. "Rapid, accurate particle tracking by calculation of radial symmetry centers". In: *Nat Methods* 9 (2012), pp. 724–726.

[40] H. Ma et al. "Fast and precise algorithm based on maximum radial symmetry for single molecule localization". In: *Optics Letters* 37.13 (2012), pp. 2481–2483.

[41] B. Yu et al. "Fast Fourier domain localization algorithm of a single molecule with nanometer precision". In: *Optics Express* 36.22 (2011), pp. 4317–4319.

[42] K. Martens et al. "Phasor based single-molecule localization microscopy in 3D (pSMLM-3D): An algorithm for MHz localization rates using standard CPUs". In: *J. Chem. Phys.* 148.12 (2018), p. 123311.

[43] A. Abraham et al. "Quantitative study of single molecule location estimation techniques". In: *Optics Express* 17.26 (2009), pp. 23352–23373.

[44] S. Stallinga. "Single emitter localization analysis in the presence of background". In: *Proc. SPIE 9630, Optical Systems Design 2015: Computational Optics* 96300V (2015).

[45] B. Rieger and S. Stallinga. "The Lateral and Axial Localization Uncertainty in Super-Resolution Light Microscopy". In: *ChemPhysChem* 15,4 (2014), pp. 664–670.

[46] J. More. *The Levenberg-Marquardt algorithm: Implementation and theory*. Springer, Berlin, Heidelberg, 1978. ISBN: 978-3-540-35972-2.

[47] F. Huang et al. "Simultaneous multiple-emitter fitting for single molecule super-resolution imaging". In: *Biomed Opt Express* 2.5 (2011), pp. 1377–1393.

[48] M. Lindén et al. "Pointwise error estimates in localization microscopy". In: *Nat. Commun.* 8.15115 (2017).

[49] D. Sage et al. "Super-resolution fight club: assessment of 2D and 3D single-molecule localization microscopy software". In: *Nat. Methods* 16 (2019), pp. 387–395.

[50] C. Smith et al. "Fast, single-molecule localization that achieves theoretically minimum uncertainty". In: *Nature Methods* 7 (2010), pp. 373–375.

[51] K. Mortensen et al. "Optimized localization analysis for single-molecule tracking and super-resolution microscopy". In: *Nat. Methods* 7 (2010), pp. 377–381.

[52] S. Stallinga and B. Rieger. "Accuracy of the Gaussian Point Spread Function model in 2D localization microscopy". In: *Optics Express* 18.24 (2010), pp. 24461–24476.

[53] D. Burke et al. "Adaptive optics correction of specimen-induced aberrations in single-molecule switching microscopy". In: *Optica* 2.2 (2015), pp. 177–185.

[54] S. Stallinga. "Effect of rotational diffusion in an orientational potential well on the point spread function of electric dipole emitters". In: *J. Opt. Soc. Am. A* 32.2 (2015), pp. 213–223.

[55] F. Aguet, D. V. D. Ville, and M. Unser. "A maximum-likelihood formalism for sub-resolution axial localization of fluorescent nanoparticles". In: *Optics Express* 13.26 (2005), pp. 10503–10522.

[56] A. Tahmasbi, E. Ward, and R. Ober. "Determination of localization accuracy based on experimentally acquired image sets: applications to single molecule microscopy". In: *Opt Express* 23.6 (2015), pp. 7630–7652.

[57] A. York et al. "Confined Activation and Subdiffractive Localization Enables Whole-Cell PALM with Genetically Expressed Probes". In: *Nat Methods* 8.4 (2011), pp. 327–333.

[58] S. Quirin, S. Pavani, and R. Piestun. "Optimal 3D single-molecule localization for superresolution microscopy with aberrations and engineered point spread functions". In: *PNAS* 109.3 (2011), pp. 675–679.

[59] H. Babcock and X. Zhuang. "Analyzing Single Molecule Localization Microscopy Data Using Cubic Splines". In: *Scientific Reports* 7.552 (2017).

[60] Y. Li et al. "Real-time 3D single-molecule localization using experimental point spread functions". In: *Nature Methods* 15 (2018), pp. 367–369.

[61] R.E.Thompson, D. Larson, and W.W.Webb. "Precise Nanometer Localization Analysis for Individual Fluorescent Probes". In: *Biophysical Journal* 82, (2002), pp. 2775–2783.

[62] A. Yildiz et al. “Myosin V Walks Hand-Over-Hand: Single Fluorophore Imaging with 1.5-nm Localization”. In: *Science* 300.5628 (2003), pp. 2061–2065.

[63] M. Speidel, A. Jonas, and E. Florin. “Three-dimensional tracking of fluorescent nanoparticles with subnanometer precision by use of off-focus imaging”. In: *Optics Letters* 28.2 (2003), pp. 69–71.

[64] H. Kao and A. Verkman. “Tracking of single fluorescent particles in three dimensions: use of cylindrical optics to encode particle position.” In: *Biophys J.* 67.3 (1994), pp. 1291–1300.

[65] B. Huang et al. “Three-Dimensional Super-Resolution Imaging by Stochastic Optical Reconstruction Microscopy”. In: *Science* 319.5864 (2008), pp. 810–813.

[66] S. Pavani et al. “Three-dimensional, single-molecule fluorescence imaging beyond the diffraction limit by using a double-helix point spread function”. In: *PNAS* 106.9 (2009), pp. 2995–2999.

[67] G. Grover et al. “Super-resolution photon-efficient imaging by nanometric double-helix point spread function localization of emitters (SPINDLE)”. In: *Biophys J.* 20.24 (2012), pp. 26681–26695.

[68] M. Lew et al. “Corkscrew point spread function for far-field three-dimensional nanoscale localization of pointlike objects”. In: *Biophys J.* 36.2 (2011), pp. 202–204.

[69] Y. Shechtman et al. “Optimal Point Spread Function Design for 3D Imaging”. In: *Phys. Rev. Lett.* 113 (2014), p. 133902.

[70] P. Prabhat et al. “Simultaneous imaging of different focal planes in fluorescence microscopy for the study of cellular dynamics in three dimensions”. In: *IEEE Trans Nanobioscience* 3.4 (2004), pp. 237–242.

[71] C. Winterflood et al. “Dual-Color 3D Superresolution Microscopy by Combined Spectral-Demixing and Biplane Imaging”. In: *Biophys J.* 109.1 (2015), pp. 3–6.

[72] C. Franke, M. Sauer, and S. van de Linde. “Photometry unlocks 3D information from 2D localization microscopy data”. In: *Nature Methods* 14 (2017), pp. 41–44.

[73] M. Bates, G. D. B. Huang and, and X. Zhuang. “Multicolor Super-Resolution Imaging with Photo-Switchable Fluorescent Probes”. In: *Science* 317.5845 (2007), pp. 1749–1753.

[74] J. Broeken, B. Rieger, and S. Stallinga. “Simultaneous measurement of position and color of single fluorescent emitters using diffractive optics”. In: *Optics Letters* 39.11 (2014), pp. 3352–3355.

[75] C. Smith et al. “Simultaneous measurement of emission color and 3D position of single molecules”. In: *Optics Express* 24.5 (2016), pp. 4996–5013.

[76] Y. Shechtman et al. “Multicolour localization microscopy by point-spread-function engineering”. In: *Nature Photon* 10 (2016), pp. 590–594.

[77] E. Hershko et al. “Multicolor localization microscopy and point-spread-function engineering by deep learning”. In: *Optics Express* 27.5 (2019), pp. 6158–6183.

[78] E. Betzig and R. Chichester. “Single Molecules Observed by Near-Field Scanning Optical Microscopy”. In: *Science* 26.5138 (1993), pp. 1422–1425.

[79] S. Rosenberg et al. “Rotational Motions of Macro- molecules by Single-Molecule Fluorescence Microscopy”. In: *Acc. Chem. Res.* 38.7 (2005), pp. 583–593.

[80] M. Wang et al. “Nanoscale deformation in polymers revealed by single–molecule super-resolution localization–orientation microscopy”. In: *Materials Horizons* 6 (2019), pp. 817–825.

[81] F. Aguet et al. “Super-resolution orientation estimation and localization of fluorescent dipoles using 3-D steerable filters”. In: *Optics Express* 17.8 (2009), pp. 6829–6848.

[82] J. Engelhardt et al. “Molecular Orientation Affects Localization Accuracy in Superresolution Far-Field Fluorescence Microscopy”. In: *Nano Lett.* 11.1 (2010), pp. 209–213.

[83] D. E. O’Reilly. “Solution of the rotational diffusion equation for a polar molecule in an electric field”. In: *J. Phys. Chem.* 74.17 (1970), pp. 3277–3279.

[84] R. Dickson, D. Norris, and W. Moerner. “Simultaneous Imaging of Individual Molecules Aligned Both Parallel and Perpendicular to the Optic Axis”. In: *Phys. Rev. Lett.* 81.5322 (1998), pp. 5322–5325.

[85] E. Toprak et al. “Defocused orientation and position imaging (DOPI) of myosin V”. In: *PNAS* 103.17 (2006), pp. 6495–6499.

[86] M. Backlund et al. “The role of molecular dipole orientation in single-molecule fluorescence microscopy and implications for super-resolution imaging”. In: *Chemphyschem.* 15.4 (2014), pp. 587–599.

[87] S. Stallinga and B. Rieger. “Position and orientation estimation of fixed dipole emitters using an effective Hermite point spread function model”. In: *Optics Express* 20.6 (2012), pp. 5896–5921.

[88] L. von Diezmann, Y. Shechtman, and W. E. Moerner. “Three-Dimensional Localization of Single Molecules for Super-Resolution Imaging and Single-Particle Tracking”. In: *Chemical Reviews* 117.11 (2017). PMID: 28151646, pp. 7244–7275. eprint: `https://doi.org/10.1021/acs.chemrev.6b00629`.

[89] M. Backlund et al. “Simultaneous, accurate measurement of the 3D position and orientation of single molecules”. In: *PNAS* 109.47 (2012), pp. 190870–19092.

[90] A. Backer, M. Lee, and W. E. Moerner. “Enhanced DNA imaging using super-resolution microscopy and simultaneous single-molecule orientation measurements”. In: *Optica* 3.6 (2016), pp. 8397–8416.

[91] S. Bakshi et al. “Nonperturbative Imaging of Nucleoid Morphology in Live Bacterial Cells during an Antimicrobial Peptide Attack”. In: *Appl. Environ. Microbiol.* 80 (2014), pp. 4977–4986.

[92] F. Balzarotti et al. “Nanometer resolution imaging and tracking of fluorescent molecules with minimal photon fluxes”. In: *Science* 355.6325 (2017), pp. 606–612.

[93] K. Gwosch et al. “MINFLUX nanoscopy delivers 3D multicolor nanometer resolution in cells”. In: *Nature Methods* 17 (2020), pp. 217–224.

[94] J. Xiao and T. Ha. “Flipping nanoscopy on its head”. In: *Science* 355.6325 (2017), pp. 582–584.

2 Impact of optical aberrations on axial position determination by photometry

2.1 Main text

Recently, Franke, Sauer and van de Linde [1] introduced a way to estimate the axial position of single-molecules (TRABI). To this end, they compared the detected photon count from a temporal radial-aperture-based intensity estimation to the estimated count from Gaussian point-spread function (PSF) fitting to the data. Empirically they found this photometric ratio to be around $0.7 - 0.8$ close to focus and decreasing away from it. Here, we explain this reported but unexplained discrepancy and furthermore show that the photometric ratio as indicator for axial position is susceptible even to typical optical aberrations.

In Fig. 2.1A we show the photon count from a 45 nm bead imaged with an aberration-corrected microscope [2] (see Supplementary Methods for details) estimated by three different methods (Gaussian PSF fit, TRABI, Vectorial PSF fit [3]) as a function of aperture radius or fit box size, respectively (for reproducibility see Supplementary Fig. 2.2). It is evident that the estimated count increases with increasing area for all three methods, i.e. no method finds the true count for a realistic area as the true microscope PSF has a very long tail. Simulations of full-vectorial PSFs support this conclusion (Supplementary Fig. 2.3), showing that the tail deviates substantially from the Airy PSF model [3]. It is also evident that with any aperture based method the true count can only be approximated up to 90% with aperture radii less than one micron (Supplementary Fig. 2.4) and that Gaussian PSF fitting performs worse as a Gaussian cannot fit the long tail at all. This, however, does not bias the localization estimate of Gaussian fitting for round spots [3]. The suitability of sub-diffraction sized beads for these experiments was investigated in simulation and found to increase the FWHM by only a few nanometers compared to the single-molecule PSF (Supplementary Fig. 2.5) while giving access to more light over a longer period during the experiment.

Next, we varied the axial position of the sample while imaging aberration corrected beads and evaluated the photometric ratio between photon count estimates from Gaussian fitting and TRABI as a function of defocus, as shown in Fig. 2.1B (see Supplementary Fig. 2.3 for sensitivity to fit area). The residual wavefront aberration was 24 mλ

Published as *Impact of optical aberrations on axial position determination by photometry*, R.Ø. Thorsen, C.N. Hulleman, M. Hammer, David Grünwald, S. Stallinga, B. Rieger, Nature Methods, **15**, 989-990 (2018)

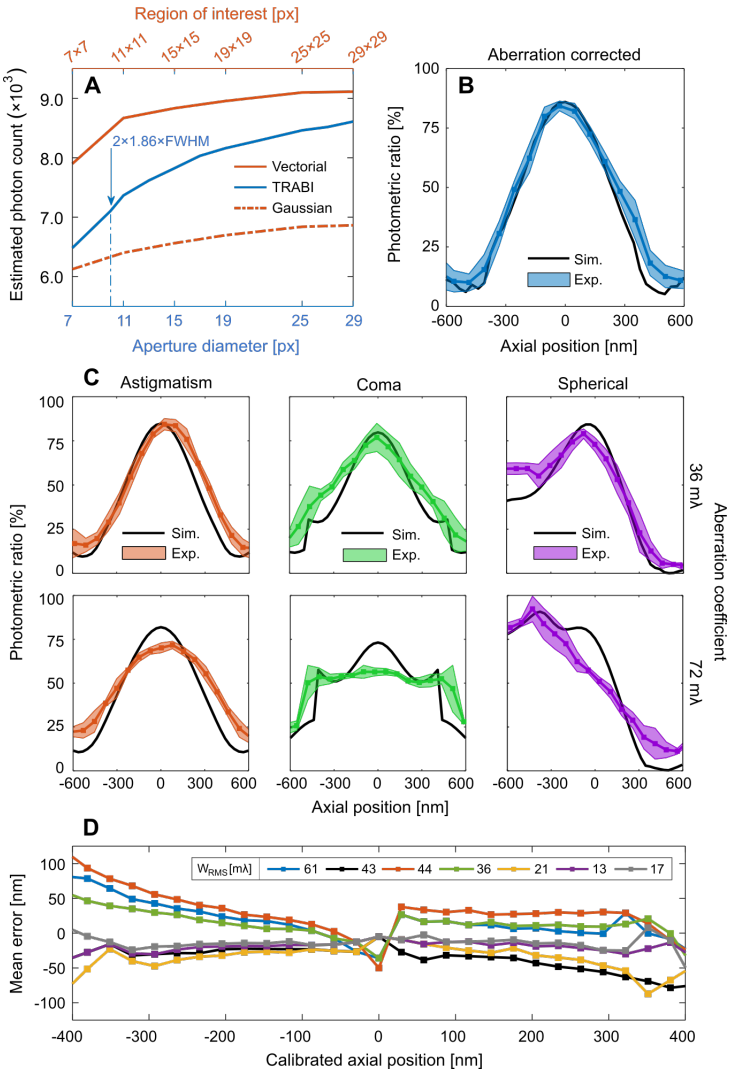

Fig. 2.1: Photon count estimation and the effects of aberrations on the photometric ratio. (A) Estimated photon count for a 45 nm diameter bead imaged with an aberration corrected microscope as a function of analysis area on the camera. Three lines show the count for fitting with a fully-fledged vectorial or simplified Gaussian PSF model compared to TRABI, FWHM = 214.5 nm; pixel size= 80 nm. Aperture diameter of $2 \times 1.86 \times \text{FWHM}$ as suggested by Franke et al. [1]. (B) The photometric ratio (Gaussian fit over TRABI value) over six bead measurements as a function of the axial position. The colored error band indicates one standard deviation. Area of fit 7×7 pixels and aperture radius 1.86×FWHM. (C) Effect on the photometric ratio for beads single-mode aberrated with root-mean-square aberration coefficients set at half (36 mλ; first row) and full diffraction limit (72 mλ; second row). (D) Axial estimation error for seven typical aberration-uncorrected microscopes, assessed by comparing the estimated axial position for simulated single-molecule PSFs with aberrations equalling the experimentally found microscope aberrations to the calibrated axial position using the aberration-corrected photometric ratio (see Supplementary Material and Fig. 2.8 for details for individual aberration measurements). W_{RMS} is the mean measured wavefront error.

RMS (see Supplementary Fig. 2.6 for experimentally retrieved aberration coefficients). Simulations using the fitted residual aberrations result in photometric ratios that agree well with experiment. We find a photometric ratio of 85% in contrast to the values around 75% in focus reported by Franke et al. [1], which we attribute to aberrations present in their experiment. To assess the influence of aberrations, we experimentally engineered PSFs with small amounts of astigmatism, coma or spherical aberration. Photometric ratios obtained from these experiments match those obtained from simulations with added aberrations (see Fig. 2.2C). The maximum value of the photometric ratio in focus, overall shape and values strongly depend on the aberrations, resulting in curves that are either broadened, flattened or made asymmetrical. The amounts of added aberrations still represent a lens that sells as diffraction limited (Maréchal diffraction limit is at 72 mλ), indicating that these aberration levels and combinations thereof are seen in typical setups. We estimated the impact of these small aberrations on the expected axial position error by comparing against an aberration corrected calibration and find errors between $\pm$100 to $\pm$200 nm over 800 nm dynamic range (see Supplementary Fig. 2.7). Sample induced refractive index mismatch, e.g. by using oil immersion into a watery enviroment, leads to spherical aberration but also non-spherical components [4] on the same order as we simulated here. In Fig. 2.1D we show the axial estimation error for seven non-corrected systems from different vendors and labs (see Supplementary Methods for details) and find them to be on the order of $\pm$50 to $\pm$100 nm. We measured the aberrations on these systems using through-focus bead acquisitions (see Supplementary Fig. 2.8 for details on the individual wavefront errors). We then calculated the axial estimation error as the difference between the calibrated aberration-free photometric ratio based position estimate compared to the simulated estimate with aberrations equalling the experimentally found microscope aberrations. We conclude that in order to convert the photometric ratio to a viable, accurate depth map the optical aberrations must be known to a very high degree (wave front uncertainty < 10 mλ results in axial uncertainty < 20 nm).

Data availability

The data is available for download at `https://doi.org/10.4121/uuid:557b6445-5d40-402a-b214-93d7c6415195`. The software is available as Matlab scripts in open-source from `ftp://qiftp.tudelft.nl/rieger/outgoing/Rasmus_photoncount.zip`.

Acknowledgments

B.R., C.N.H. acknowledge European Research Council grant no. 648580 and B.R., R.Ø.T., D.G. acknowledge National Institute of Health grant no. U01EB021238. We thank Job Dekker for providing access to serval microscopes and Keith Lidke for providing PSF data.

Author contribution

RØT performed simulations and analyzed data, CNH performed experiments, MH and DG provided 3D PSF data from several microscopes, SS and BR designed and coordinated the research. BR, SS, RØT wrote the manuscript, and all authors commented on it.

Author information

Rasmus Ø. Thorsen[1], Christiaan N. Hulleman[1], Mathias Hammer[2], David Grünwald[2], Sjoerd Stallinga*[1] and Bernd Rieger*[1]
1 Department of Imaging Physics, Delft University of Technology, Delft, The Netherlands
2 RNA Therapeutics Institute, University of Massachusetts Medical School, Worcester, Massachusetts, USA
* These authors contributed equally.
Correspondence to s.stallinga@tudelft.nl or b.rieger@tudelft.nl

Competing interests

The authors declare no competing financial interests.

2.2 References

[1] C. Franke, M. Sauer, and S. V. De Linde. "Photometry unlocks 3D information from 2D localization microscopy data". In: *Nature Methods* 14.1 (2016), pp. 41–44. ISSN: 15487105.

[2] M. Siemons et al. "High precision wavefront control in point spread function engineering for single emitter localization". In: *arXiv* 26 (2018). ISSN: 23318422. arXiv: 1802.06584.

[3] S. Stallinga and B. Rieger. "Accuracy of the Gaussian Point Spread Function model in 2D localization microscopy". In: *Optics Express* 18.24 (2010), p. 24461. ISSN: 1094-4087.

[4] D. Burke et al. "Adaptive optics correction of specimen-induced aberrations in single-molecule switching microscopy". In: *Optica* 2.2 (2015), p. 177. ISSN: 2334-2536.

2.A Appendix

2.A.1 Optical microscope setup

The experimental data is acquired with a setup that consists of a Nikon Ti-E microscope with a spatial light modulator (SLM) for aberration correction and PSF engineering, as described by us earlier [1]. In short, beads are excited by a 488 nm laser (Sapphire 488-100 CW CDRH, Coherent) through a dichroic filter set (Ex: Semrock FF01-460/60-25, Di: Semrock Di02-R532-25X36, Em: Semrock FF01-545/55-25) and an objective lens (APO TIRF 100x/1.49, Nikon). The emission fluorescence passes (peak $\lambda = 552$ nm) through a relay system (f1 = 100 mm, Thorlabs AC254-100-A and f2 = 200 mm, Thorlabs AC508-200-A) resulting in a final magnification of 200×. The SLM (XY-series, 512×512, 15 μm pixel size, Meadowlark) is placed in the Fourier plane of the relay system. The fluorescence image signal is captured on an EMCCD camera (iXon Ultra - X987, 512×512, 16 μm pixel size, Andor) which has in effect a back-projected pixel size of 80 nm in the object plane.

2.A.2 Sample preparation

Fluorescent beads of 45±8 nm diameter (FluoSpheres 0.04 μm 505/515, ThermoFisher) with peak emission at 552 nm through our filter set are used in the imaging experiments. The beads are immersed in a mounting medium of immersion oil (n=1.518 Type F, Nikon) to match the refractive index to the coverslip and immersion oil used for the objective lens. The beads are diluted to 1011 particles/mL in water, and 2.5 μL of the solution is drop-cast on a coverslip. After evaporation of the water, a drop of immersion oil is applied, and the coverslip is glued around the edges with nail varnish to a microscope slide. This step ensured the rigidity of the sample and is necessary for precise z-positioning.

2.A.3 Data acquisition

Fluorescent beads are imaged with 3.5 mW of excitation power (measured at the back aperture of the objective) and an exposure time of 1 second. For each set of aberration (type and magnitude), the experiment is repeated three times in the same field of view (FOV) to test for reproducibility. For each FOV, we select two beads located in regions with a low bead density to avoid crosstalk of beads. This is done to ensure a large region of interest with the no/minimal overlap of their respective PSF shoulders. This results in a total of six configurations, i.e. two beads measured three times. These six configurations are used to compute the mean and standard deviation of the data as shown as error bars in Figure 2.1B,C and Supplementary Figure 2.6. The data in Figure 2.1A and Supplementary Figure 2.2 and 2.3 B,C are for individual beads.

2.A.4 Aberration retrieval and correction

Our setup contains an additional light path for pixel-wise calibration of the LCoS SLM to ≤ 20 mλ RMS wavefront aberration as described earlier [1]. After calibration of the SLM, we acquire a z-stack of the fluorescent bead by moving the piezo stage in steps of 80 nm from -800 nm to $+800$ nm around focus. The z-stack is fitted with a 3D full vectorial PSF model in order to estimate the aberrations of the optical system [1]. The retrieved aberration coefficients are fed to the SLM with opposite sign in order to correct for the aberrations. Subsequently, another z-stack is acquired and fitted to verify the compensation of the aberrations. We then add aberrations of a desired type and magnitude deliberately in order to investigate the impact of aberrations in a well-controlled fashion.

2.A.5 Simulation of a realistic PSF model

We use the vectorial PSF model also for simulating the effect of arbitrary aberrations on photon counting [2]. In addition we take into account the non-zero size of a bead by convolving the PSF with the bead size. This fully-fledged PSF model takes the following effects into account: interfaces between media, polarization, dipole orientation (here freely rotating dipoles are assumed) and type and magnitude of aberrations. The simulation parameters are based on our optical setup: i.e., medium refractive index $n = 1.518$, numerical aperture NA $= 1.49$, wavelength $\lambda = 552$ nm, backprojected pixel size $= 80$ nm. We assume that the refractive indices between the imaging medium, coverslip, and immersion medium are matched (based on the immersion of the beads in oil). In Supplementary Figure 2.4 and 2.5 we use a smaller sampling distance of 1 nm to exclude quantization effects. The bead diameter is 45 nm except in Supplementary Figure 4 where the bead diameter is varied from 0 to 180 nm. Results for the Airy PSF model shown in Supplementary Figure 2.4 follow directly from the derivation as detailed in Born & Wolf [3] (Chapter 8). The simulated PSFs are normalized such that the sum over the detection plane is unity, then multiplied by the desired number of signal photons and a constant number of background photons per pixel is added before applying shot noise.

2.A.6 Photon count estimation

To determine the gain and offset, the EMCCD camera is calibrated using the procedure described by van Vliet et al. [4]. For these experiments, we used an EM gain setting of 50 to reduce the read-noise to $< 1e^-$ RMS while retaining a good dynamic range and linear response (maximum intensity is kept under 5000 ADU - the linear regime for our camera settings). Excess noise in EMCCD cameras leads to an overestimation of the gain by a factor of two [5], but this does not pose any problems in the further analysis of the data as only ratios of photon count estimates are of interest here. The fitting procedure with a vectorial or Gaussian PSF model is implemented with a Levenberg-Marquardt iterative scheme for Maximum-Likelihood estimation (MLE) as described in Smith et al. [6]. The number of iterations is terminated by the tolerance in the residual. The

tolerance limit is set to 10-6 and 10-4 for the vectorial and Gaussian fitter, respectively (maximum number of iterations is 75). Typically the number of iterations is less than 20.

TRABI [7] is designed to take advantage of fluorescent on-off blinking of photoswitchable or photoactivatable fluorophores. TRABI can estimate both signal and background with a "single aperture" by incorporating time information, i.e. estimating the background in the off-state and the foreground signal in the on state. Here we image non-blinking fluorescent beads, which does not allow us to apply the method directly. Instead, we estimate the number of background photons by an aperture located far away from the bead. For background averaging we use 7 successive frames in the through-focus stack as suggested by Franke et al. [7].

2.A.7 Estimation of error axial position estimation

The error in the axial position estimate from the photometric ratio is done in the following way. The experiments on different beads give the photometric ratio $PR(z)$ as a function of axial position z with uncertainty $\Delta PR(z)$ (Fig. 2.1B,C). The experimental aberration-corrected calibration curves $PR(z)$ and $PR(z) \pm \Delta PR(z)$ (Supplementary Fig. 2.7A) are up-sampled to 1 nm axial steps and stored in a look-up-table (LUT). Given a measured value PR_{exp}, the LUT will give the estimated axial position z_{exp} with uncertainty Δz_{exp}. This uncertainty represents statistical variations in the photometric ratio curves due to e.g. variations across the field-of-view of the microscope, and is on the order 25 nm away from focus to 65 nm close to focus (Supplementary Fig. 2.7B). The estimated axial position change in case aberrations are present as the photometric ratio curves change (Supplementary Fig. 2.7C). If calibration is done on an aberration-corrected setup, the application of the aberration-free LUT on photometric ratio measurements on aberrated spots will also lead to a bias in the axial position estimate (Supplementary Fig. 2.8D). These inaccuracies can amount up to 100 nm for aberration levels at 50% of the diffraction limit.

2.A.8 Microscope specifications for PSF retrieval of Supplement Figure 2.8

Dataset 1 is obtained with our setup described in Supplementary Methods prior to aberration correction.

Dataset 2 is acquired on a Leica DMi8 microscope. The sample (TetraSpeck Fluorescent Microspheres, 200 nm, well 4, RI: mounting medium 1.472) is excited by a Leica PL 6000, diode laser through a filter set (Chroma ZT/594rpc, Chroma 89100bs), and an objective lens (Leica Plan-Apochromat 63x/1.40 Oil DIC, RI: embedding medium 1.518). The fluorescence image signal (emission peak at $\lambda = 580$ nm) is captured on a sCMOS camera (Hamamatsu C11440 ORCA-flash 4.0, detector 13.312×1312mm^2, pixel size 6.5x6.5 μm^2, chip size 2048×2048).

Datasets 3,4,5,6 are acquired on a Nikon Eclipse Ti-E microscope. The sample (TetraSpeck Fluorescent Microspheres, 200 nm, well 4, RI: mounting medium 1.472) is excited by a Lumencor SPECTRA X, diode laser through a filter set (dataset 3,5: Ex.: SPECTRA X Chroma 470/24, Em.: SPECTRA X, ET515/30m Single Bandpass, and dataset 4,6: Ex.: SPECTRA X Chroma Excitation Filter 550/15, Em.: SPECTRA X, ET595/40m Single Bandpass) and an objective lens (dataset 3,4: CF160 TIRF Apo 60x/oil DIC 1.49 NA, dataset 5,6: CF160 SR/TIRF Apo 100x/oil 1.49 NA, RI: embedding medium 1.518). The fluorescence image signal (emission peak dataset 3,5: λ = 515 nm, dataset 4: λ = 570 nm, dataset 6: λ = 580 nm) is captured on a sCMOS camera (Andor Zyla 5.5 sCMOS, detector 16.6×14 mm, pixel size 6.5×6.5 μm^2, chip size 2560×2160).

Dataset 7 is acquired on an Olympus IX71 microscope. The sample (FluoSpheres F-8789, dark red, Invitrogen, 40 nm) is excited by a HL63133DG, Thorlabs, 637 nm diode laser through a filter (FF01-692/40-25, Semrock), dichroic mirror (650 nm, Semrock) and an objective lens (UAPON 150XOTIRF, Olympus America Inc., NA 1.45, RI: immersion medium 1.52). The fluorescence image signal (emission peak λ = 690 nm) is captured via a 2× magnification relay optics on an EMCCD camera (iXon 897, Andor, Andor Technologies PLC., CCD size 515×515, pixel size 12 μm). Setup details and sample preparation is described further by Liu et al. [8].

2.A.9 Supplementary figures

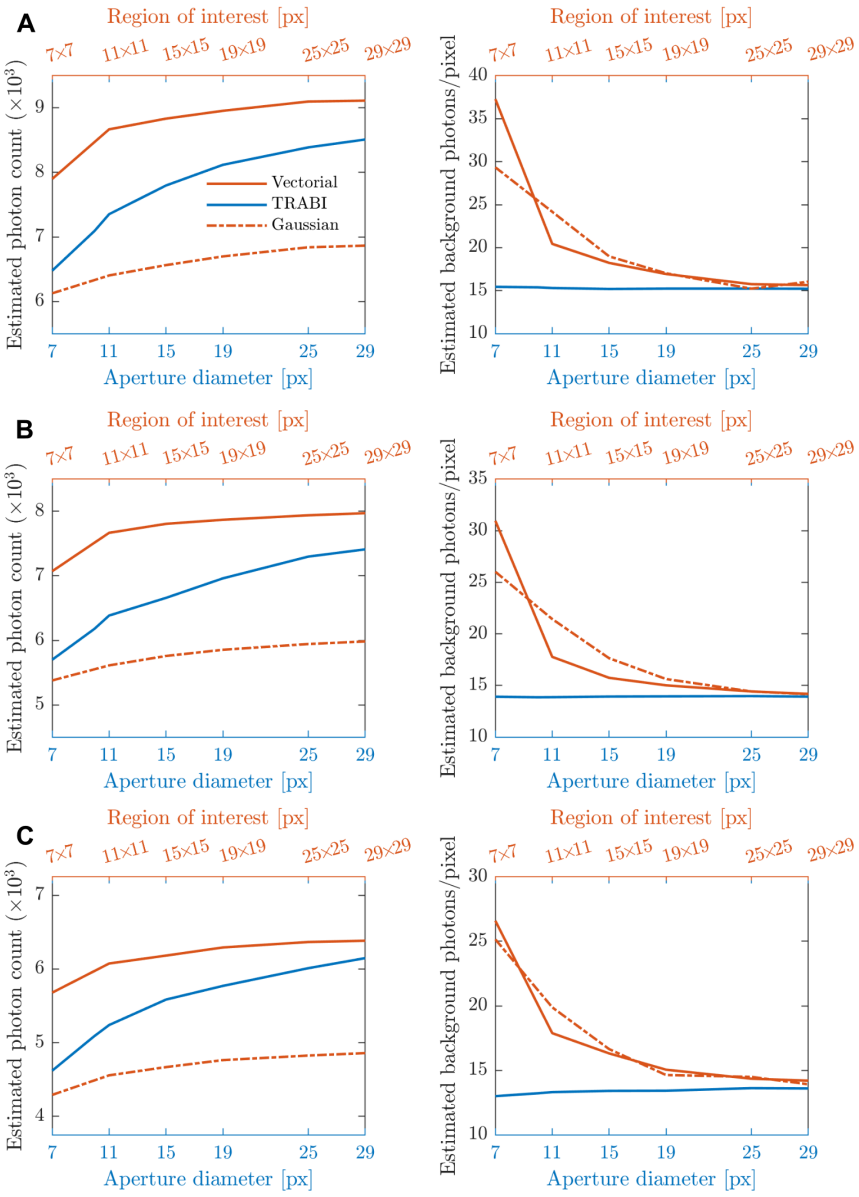

Fig. 2.2: Reproducibility of photon count estimation. (A-C) Estimated photon counts and background photons per pixel for three measurements of three separated 45 nm diameter beads imaged with an aberration corrected microscope as a function of analysis area on the camera, pixel size= 80 nm. The three lines show the count for fitting with a fully-fledged vectorial, TRABI or a simple Gaussian PSF.

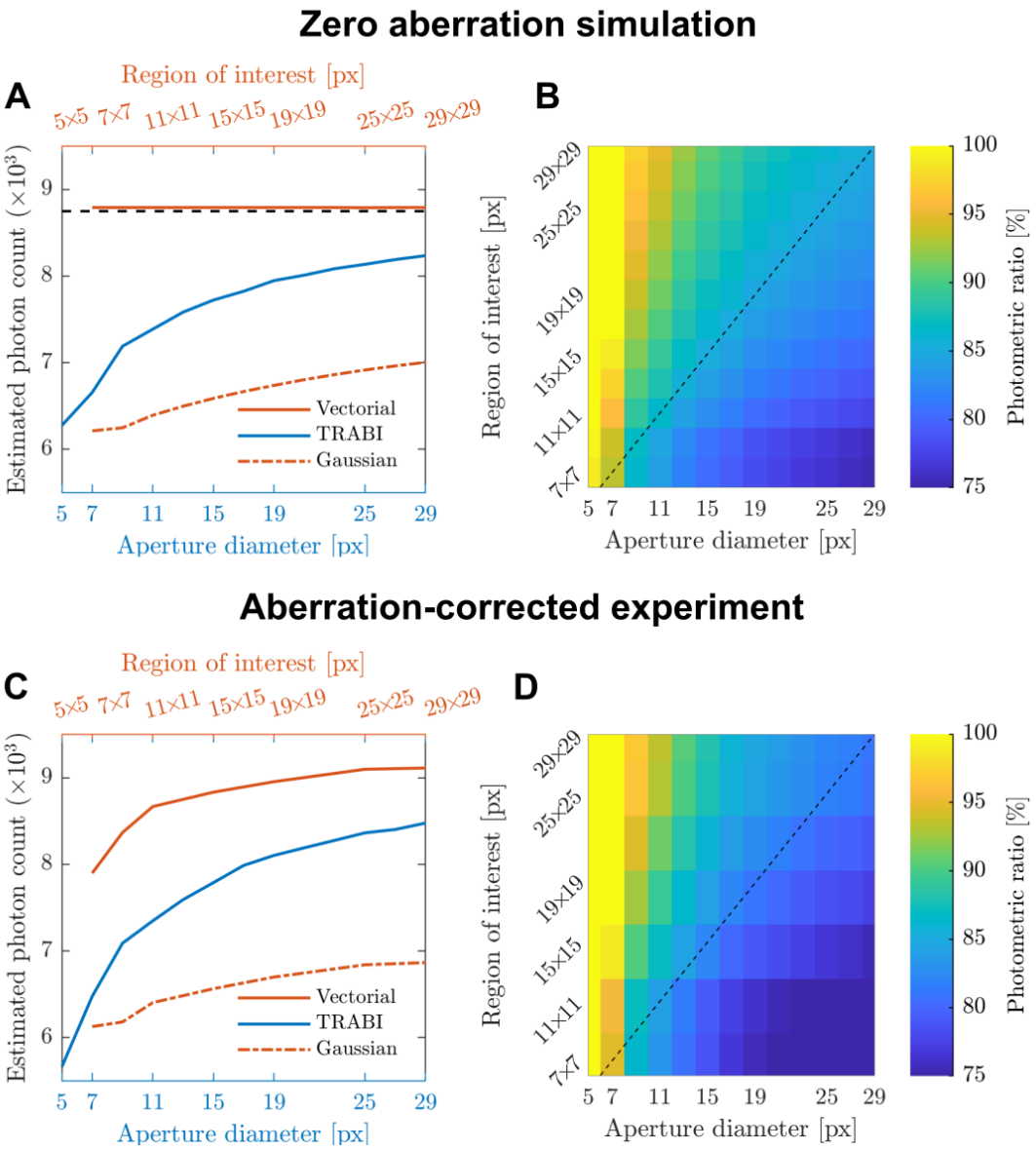

Fig. 2.3: Comparison of photon count estimations in simulation and experiment. (A) Photon count estimation for a single simulated 45 nm bead PSF as a function of PSF image area on the camera for three different estimation algorithms: vectorial fit, TRABI, and Gaussian fit (8750 signal photons, 15 background photons, same pixel size, NA and refractive index values as experiment). (B) The photometric ratio between Gaussian fit and TRABI photon count estimation as a function of PSF fit size. The dashed line indicates when the circular aperture size fits precisely within the square region of interest. (C-D) Same as panels (A,B) but for an experimentally recorded aberration-corrected 45 nm bead, indicating good quantitative agreement between experiment and simulation.

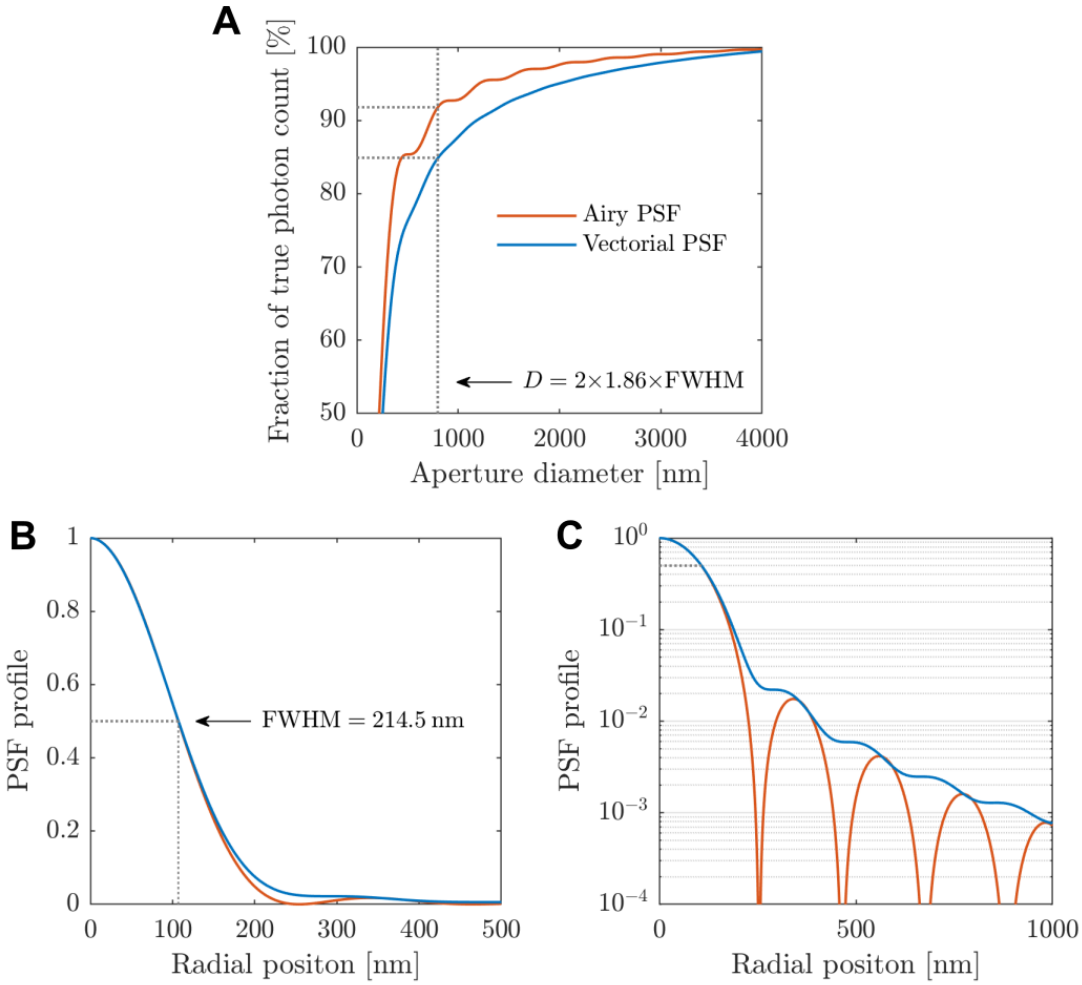

Fig. 2.4: TRABI photon count estimate as a function of aperture size and PSF model. (A) Ratio of the estimated photon count by TRABI and simulated number of signal photons captured at the camera as a function of aperture diameter for two PSF models. TRABI aperture diameter (d) of $2 \times 1.86 \times$FWHM (FWHM = 214.5 nm) as suggested in Franke et al. [7] is indicated. For this aperture size, we find TRABI to estimate 92% and 85% of the total number of photons according to the low NA scalar Airy PSF model and the high NA vectorial PSF model, respectively. The fraction of the total energy contained within an aperture of the prescribed radii in the Airy PSF model ($\mathrm{PSF}_{\mathrm{Airy}}(\rho) = [2J_1(D)/D]^2$ where $D = 2\pi\rho(\mathrm{NA}/\lambda)$; $\mathrm{FWHM} = 0.514(\lambda/\mathrm{NA})$) follows the analytically derived formula by Born & Wolf [3] (Chapter 8; Fig. 8.13), in contrast to the 100% reported by Franke et al. [7] in their supplement. The PSF simulations were performed with 2500 signal photons and no background photons and a pixel size of 1 nm (to exclude quantization effects). Otherwise, the simulation parameters were the same as the experimental parameters. (B-C) Characterisation of the Airy and vectorial PSFs as a function of the radial position in a linear and log scale, respectively, showing the long tail of the PSF.

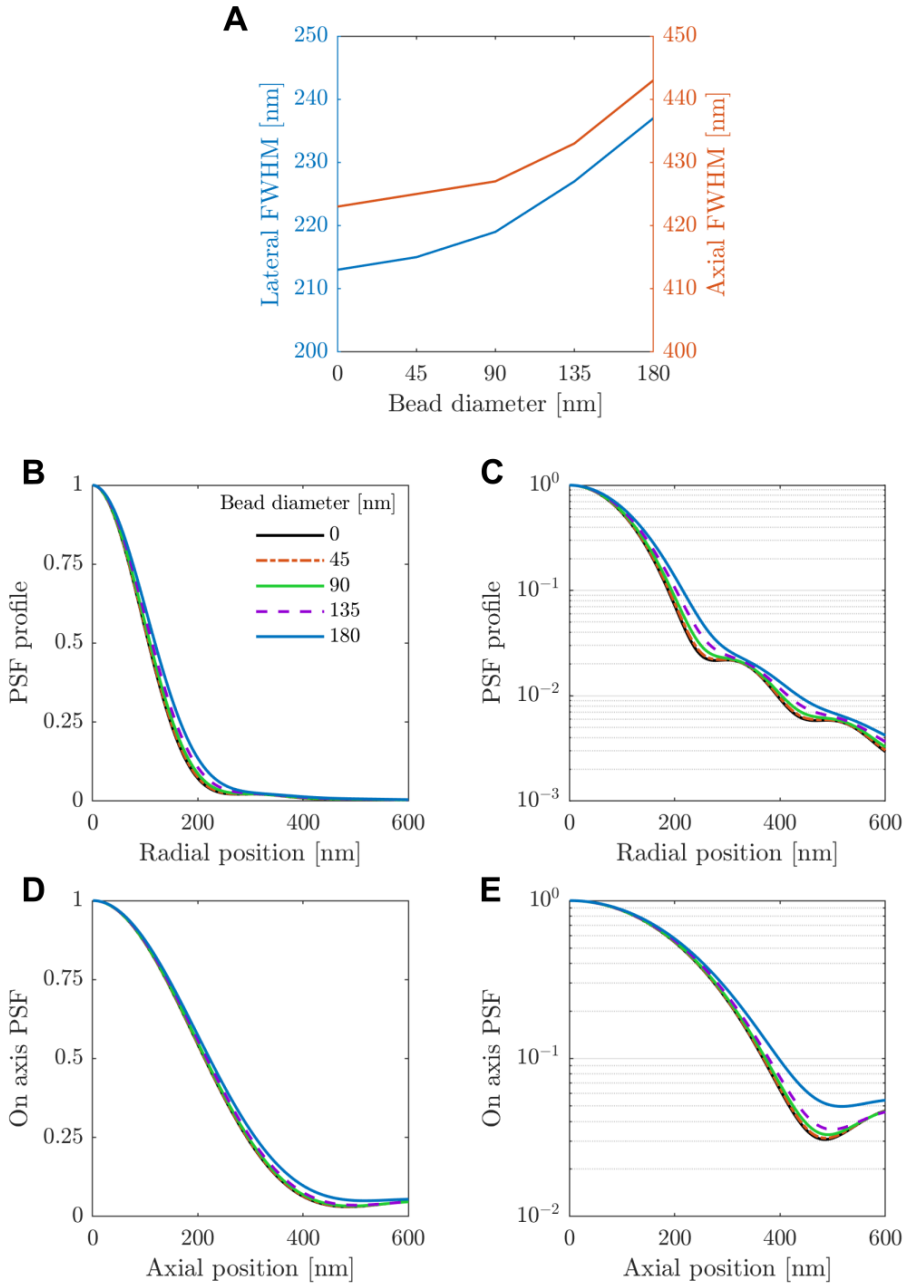

Fig. 2.5: The effect of bead size on the PSF shape. (A) The lateral and axial FWHM as a function of bead size. (B-C) Lateral average PSF in linear and log scale, respectively, as a function of the radial positon. The PSFs are displayed for different bead sizes. (D-E) On axis PSF in linear and log scale, respectively, as a function of the axial position. The 45 nm bead captures the full tail-behaviour in both the lateral and axial direction of an actual single-molecule emitter, and has a FWHM within a few nanometers of a single-molecule emitter, whereas PSF details clearly get lost with larger (> 90 nm) beads.

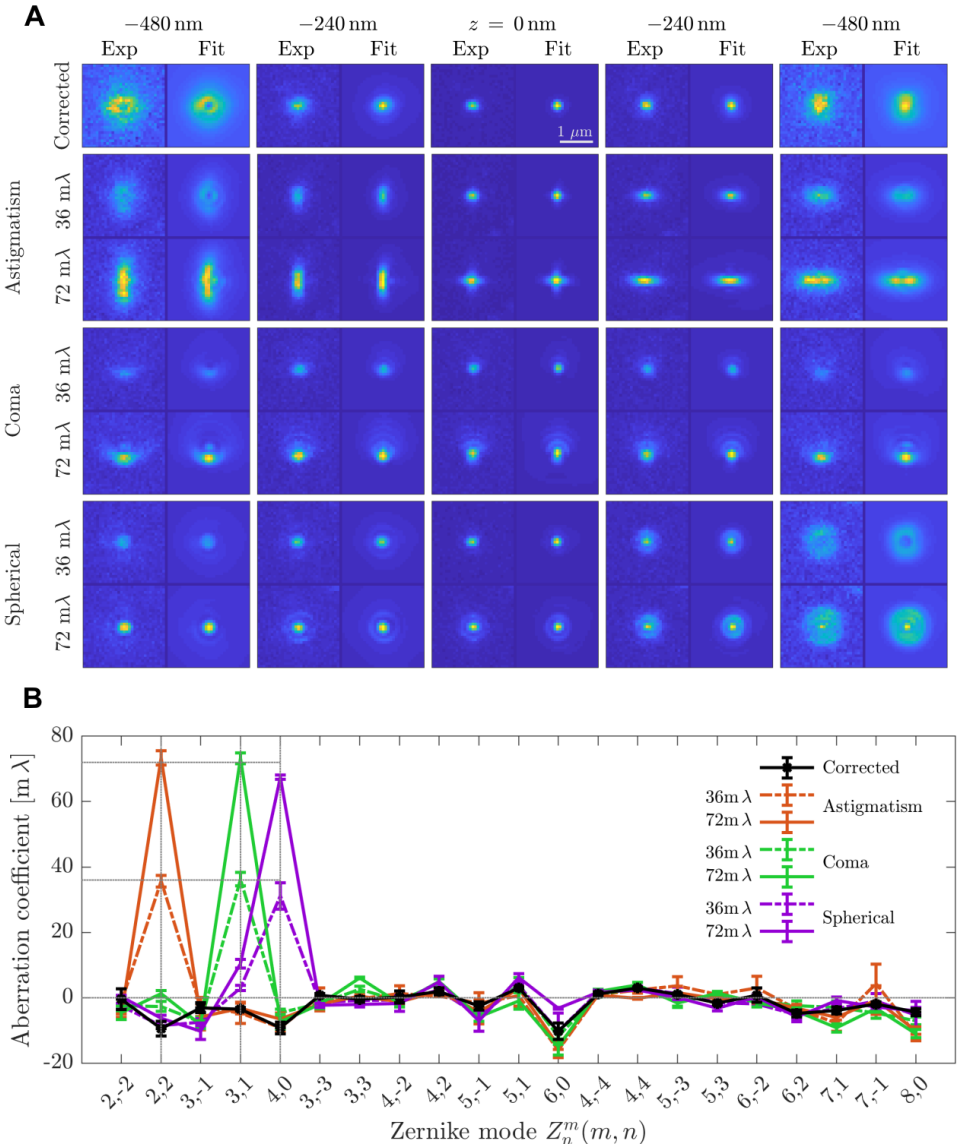

Fig. 2.6: Quantification of aberration retrieval and correction. (A) Through-focus PSF image stacks of experimental and fitted PSFs after aberration correction and, subsequently, aberrated with a single primary Zernike mode: astigmatism (Z_2^2), coma (Z_3^1), and spherical aberration (Z_4^0), with aberration coefficients 36 mλ and 72 mλ (root-mean-square values). The region of interest for each PSF image is 31×31 pixels with a pixel size of 80 nm. All 4×4 sub-image pairs are contrast stretched with the same factor for better visibility of spot shape. The estimated photon counts were within $9,500 - 21,000$ signal photons and $15 - 18$ background photons per pixel. Reproducibility as shown in B). (B) Fitted Zernike modes and retrieved aberration coefficients. The coefficients are averaged over six measurements with error bars indicating one standard deviation. The aberration fit routine includes all tertiary Zernike modes (all Z_n^m with $2 < n + |m| \leq 8$) and assumes optical parameters as described in Supplementary Methods. (Horizontal dashed lines are used to guide the eye).

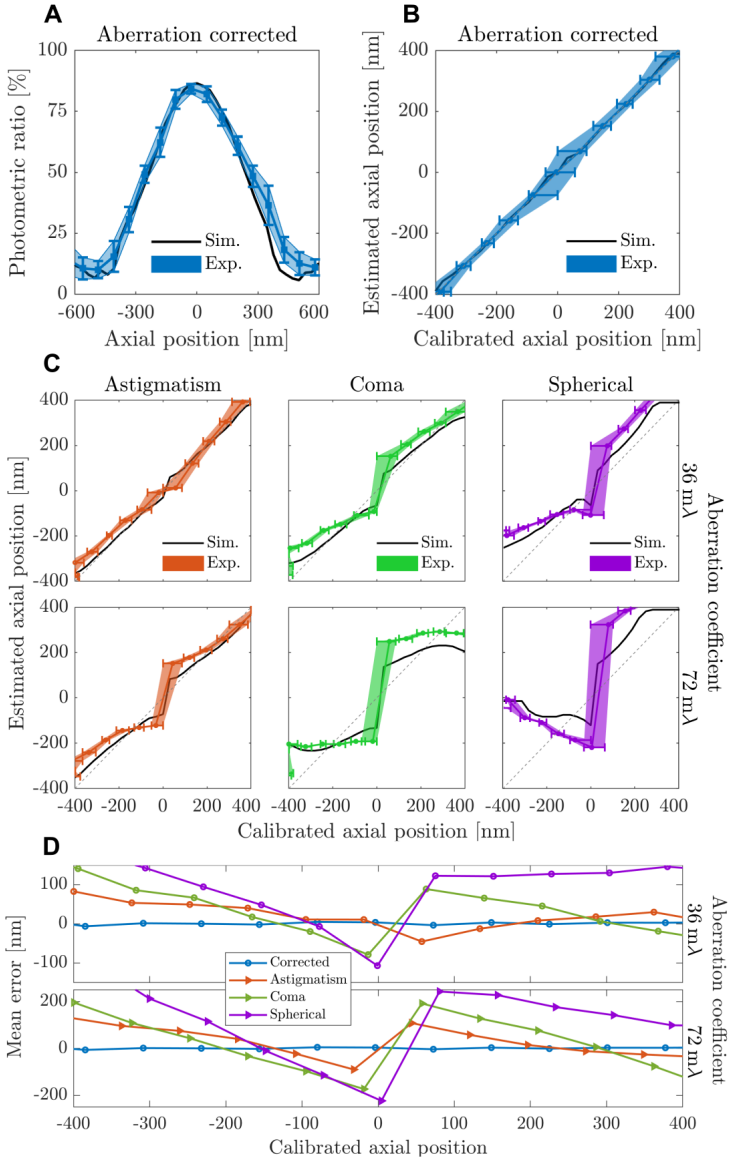

Fig. 2.7: Axial calibration of the photometric ratio and axial estimation error caused by small single-mode aberrations. (A) The photometric ratio over six 45 nm bead measurements after aberration-correction (Exp.) and simulated vectorial PSFs (Sim.) as a function of axial position (see Supplementary Methods). (B) The estimated axial position of aberration-corrected beads as a function of the calibrated axial position shown in A). Around focus the error is a bit larger as expected due to near parabolic shape of the photometric ratio curve (see Supplementary Methods for a description of the error analysis). (C) Estimated axial position for single-mode aberrations on 45 nm beads using the calibrated axial position from the aberration corrected data in A). The grey dashed line is used to guide the eye for the correct estimation. Experimental data (Exp.) in A,B,C are shown as mean ± s.d. over six bead measurements. (D) Error of the estimated axial position as the distance between the mean estimated position and the true (calibrated) position.

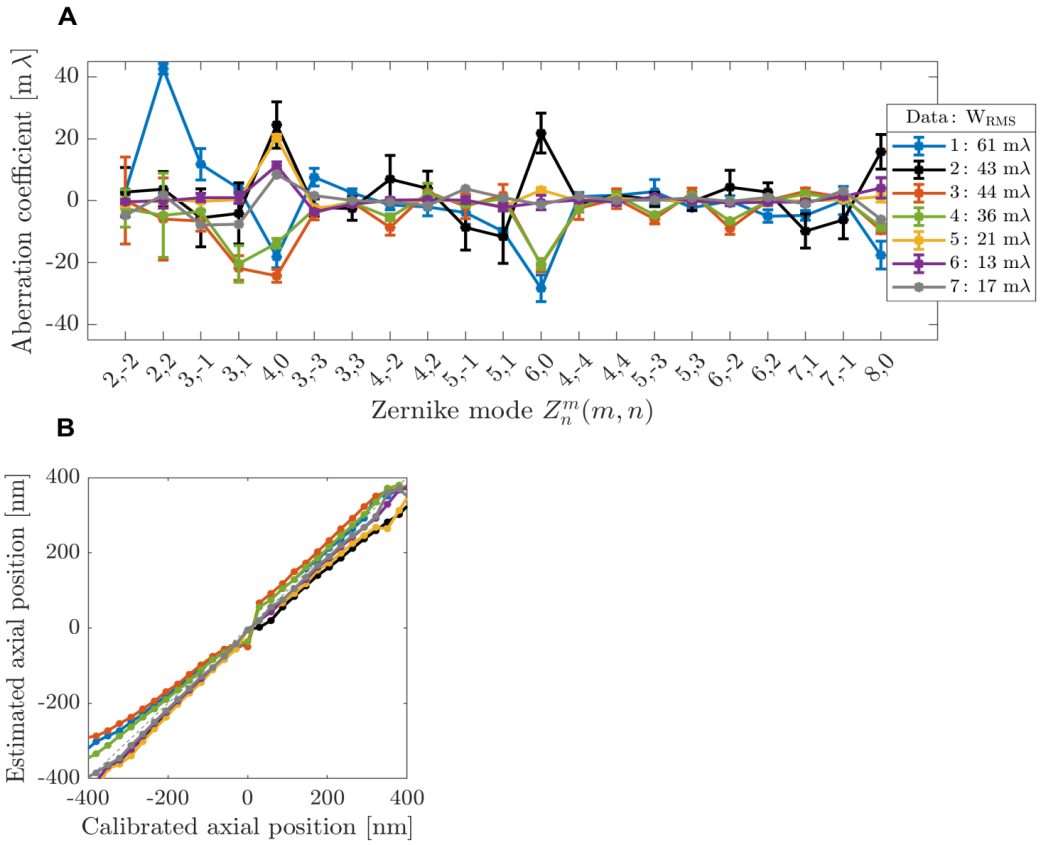

Fig. 2.8: Typical microscope aberrations and their influence on the estimated axial position. (A) Fitted Zernike modes and retrieved aberration coefficients for several microscopes, Data 1-7 (specifications are given in Supplementary Methods). The coefficients are averaged over six and one bead measurement(s) for datasets 1-6 and 7, respectively, with error bars indicating one standard deviation and WRMS is the mean of the wavefront error. The aberration fit routine includes all tertiary Zernike modes and assumes optical parameters for each microscope as described in Supplementary Methods. (B) Estimated axial position for simulated single-molecule PSFs with aberrations equalling the mean experimentally found microscope aberrations in (A) compared to the calibrated axial position using the aberration-corrected photometric ratio (see Supplementary Fig. 6a). Area of fit 7×7 pixels and aperture radius $1.86 \times$ FWHM.

References

[1] M. Siemons et al. *High precision wavefront control in point spread function engineering for single emitter localization*. 2018. arXiv: 1802.06584.

[2] S. Stallinga and B. Rieger. "Accuracy of the Gaussian Point Spread Function model in 2D localization microscopy". In: *Optics Express* 18.24 (2010), p. 24461. ISSN: 1094-4087.

[3] M. Born et al. *Principles of Optics*. Cambridge University Press, 1999.

[4] L. V. Vliet, D. Sudar, and I. Young. *Digital fluorescence imaging using cooled charge-coupled device array cameras*. Tech. rep. Castleman 1996. 1998, pp. 109–120.

[5] B. Rieger and S. Stallinga. "The lateral and axial localization uncertainty in super-resolution light microscopy". In: *ChemPhysChem* 15.4 (2014), pp. 664–670. ISSN: 14397641.

[6] C. S. Smith et al. "Fast, single-molecule localization that achieves theoretically minimum uncertainty". In: *Nature Methods* 7.5 (2010), pp. 373–375. ISSN: 15487091.

[7] C. Franke, M. Sauer, and S. V. De Linde. "Photometry unlocks 3D information from 2D localization microscopy data". In: *Nature Methods* 14.1 (2016), pp. 41–44. ISSN: 15487105.

[8] S. Liu et al. "Three dimensional single molecule localization using a phase retrieved pupil function". In: *Optics Express* 21.24 (2013), p. 29462. ISSN: 1094-4087.

3 Localization microscopy at doubled precision with patterned illumination

3.1 Abstract

MINFLUX offers a breakthrough in single molecule localization precision, but is limited in field of view. Here we combine centroid estimation and illumination pattern induced photon count variations in a conventional widefield imaging setup to extract position information over a typical micrometer-sized field of view. We show a near two-fold improvement in precision over standard localization with the same photon count on DNA-origami nanostructures and tubulin in cells, using DNA-PAINT and STORM imaging.

3.2 Main text

Single-molecule localization microscopy [1, 2, 3] circumvents the diffraction limit using centroid estimation of sparsely activated, stochastically switching, single-molecule fluorescence images. Improvement over state-of-the-art image resolutions of around 20 nm toward values below 5 nm is desired for truly imaging at the molecular scale. Achieving 5 nm resolution requires improvements in labeling strategy to reduce linker sizes [4, 5, 6, 7] and methods to overcome low labeling density such as data fusion [8], but also a step forward in localization precision. Efforts so far have targeted an increase in the number of detected photons, N, by chemical engineering of brighter fluorophores [9], or by avoiding photo-bleaching via cryogenic techniques [10, 11, 12]. These improvements scale localization precision according to $\lambda/(\mathrm{NA}\sqrt{N})$, where λ is the fluorescence emission wavelength and NA is the microscope objective numerical aperture [13].

Recently, a new concept called MINFLUX was proposed [14], in which a doughnut illumination spot is shifted over an area of size L, of $\tilde{5}$ nm, and the position of a single molecule in the scan range is determined by triangulation based on the detected photon count for the different doughnut positions. The localization precision of this procedure scales as $L/\sqrt{N}$, which is advantageous compared to $\lambda/(\mathrm{NA}\sqrt{N})$, as the scan range L can in principle be chosen to be arbitrarily small. Drawbacks of MINFLUX are

Published as *Localization microscopy at doubled precision with patterned illumination*, J. Cnossen, T. Hinsdale, **R.Ø. Thorsen**, M. Siemons, F. Schueder, R. Jungmann, C.S. Smith, B. Rieger, S. Stallinga, Nature Methods, **17**, 59-63 (2020)

the limited field of view (FOV), and the low throughput, as the molecules are imaged one molecule at a time in the tiny region of interest (ROI) of size L. Balzarotti et al. suggested the use of sinusoidal illumination patterns [14], similar to those used in structured illumination microscopy (SIM) [15] and used earlier for single-molecule tracking [16]. The extension of the triangulation procedure to spatially extended illumination patterns, however, remains a challenge.

Here, we propose to extract the molecule's position in a combined estimation from both the relative position with respect to the shifting sinusoidal illumination pattern during all camera frames within the molecule's 'on-event' and from the estimated centers of the detected spots on the camera. This solves the challenge of photon count-based localization with spatially extended illumination patterns. Our method, which we call SIMFLUX, overcomes the limited FOV and throughput of MINFLUX, and is compatible with standard widefield imaging on a camera. SIMFLUX is realized by an optical architecture for fast millisecond time scale switching of orthogonally oriented sinusoidal illumination patterns, and by a bespoke data processing strategy for spatiotemporal localization in relation to the shifting illumination patterns.

Figure 3.1a shows our optical architecture. A fast operable Pockels-cell switches between the two arms of a polarizing beam splitter in which piezo mounted gratings are placed that deliver the diffraction orders for interference based sinusoidal illumination patterns along two orthogonal directions (see Methods for details). This enables cycling through six patterns (two orientations, three phase steps) on the millisecond time scale with sufficient power throughput. Only two orientations are needed, because this suffices for a Fisher matrix that gives rise to an isotropic region of confidence for localization in the xy plane (see Supplementary Note). This differs from SIM, where three or five orientations are needed for a near isotropic filling up of the support in image Fourier space [15].

The processing pipeline (see Methods) requires the detection of single-molecule emission events in space as well as in time, in combination with a retrieval of the illumination pattern parameters (pitch, orientation, modulation depth and three phases per orientation, and relative intensity of the two beam splitter arms). First, the entire set of acquired images is processed using a standard single-molecule localization microscopy (SMLM) pipeline for selecting ROIs per frame and for an initial localization fitting. This is done on the moving sum of six frames to enhance signal-to-noise ratio for robust initial on-event detection. Next, the photon count is estimated for all individual frames within the six frame blocks. Then, the pitch and orientations of the patterns are estimated using Fourier domain peak finding [17] on the localization reconstruction. The pattern phases are subsequently retrieved by fitting the sinusoidal illumination pattern to the estimated single-frame photon counts. Blocks where a molecule is not in the on-state in all six frames are filtered out by comparing the estimated single-frame photon counts to the expected values from the retrieved illumination patterns. Next, the ROIs in the frames belonging to molecular on-events are fitted with a maximum likelihood estimation (MLE) routine, taking into account the centroid positions in each frame and the fluorescence signal strengths in relation to the shifting illumination pattern. The difference in the average position of these SIMFLUX localizations and the corresponding

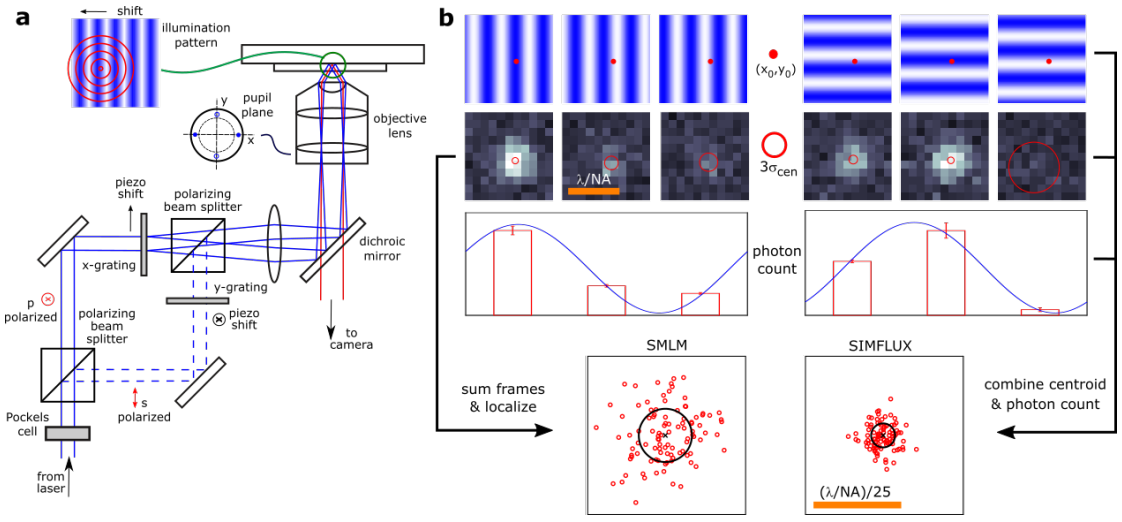

Fig. 3.1: Principle of SIMFLUX. a, A sinusoidal illumination pattern is created in a total internal reflection–SIM setup by two counter propagating evanescent waves. Fast switching between two orthogonal line patterns is achieved by placing two piezo mounted gratings in the two arms of a polarizing beam splitter, selecting the operational arm by a polarization switching Pockels cell. b, A total of six images are recorded with three shifted patterns per orthogonal orientation of the line pattern. Combining the centroid estimates of the six frames with precision σ_{centroid} (σ_{cen}) with the photon count in relation to the pattern shift improves the localization precision with a factor of around two compared to the standard centroid estimate on the sum of the six frames.

SMLM localizations is indicative for an error in the estimation of the pattern pitch and orientations, and can therefore be used to adjust the estimates. After updating them, a next round of pattern phase estimation and SIMFLUX fitting can start. This iterative procedure converges in three to four rounds.

The Cramér-Rao Lower Bound (CRLB) for the localization precision (see Supplementary Note) is given by:

$$\Delta x_0 = \frac{\sigma}{\sqrt{N}\sqrt{1 + 2\pi^2\sigma^2/p^2}} \tag{3.1}$$

with $\sigma \approx \lambda/4\,\mathrm{NA}$ being the width of the point spread function (PSF) and N the total number of collected photons during the on-event of the molecule. The smallest pitch (p) of the standing wave illumination pattern is $p \approx \lambda/2\mathrm{NA}$, indicating that the improvement factor over the SMLM precision $\sigma/\sqrt{N}$ can reach values up to around $\sqrt{1 + \pi^2/2} \approx 2.4$. An imperfect modulation depth m (between 0.90 and 0.95) indicates a lower improvement factor of close to 2 (see Supplementary Note). Simulations with Gaussian and vector PSFs show that our method achieves the CRLB for a wide range of realistic photon counts and background photon levels (Supplementary Figs. 3.4 and 3.5). It appears further that background has the same relative impact as in conventional SMLM, indicating that SIMFLUX can be used under the same experimental conditions as conventional SMLM [13] (Supplementary Fig. 3.6). Simulations further show that to reach a two-fold improvement in localization precision the modulation must be at least 0.9, and must be known with a precision of around 0.04; for the pattern phases, a precision of 2° is required (Supplementary Figs. 3.7 and 3.8). We meet these conditions in our experiments. Supplementary Fig. 3.9 shows that there are small variations in localization precision depending on the position of the molecules with respect to the minima of the illumination patterns, leading to improvement factors compared to conventional SMLM that range between 1.6 and 2.3, with an average of 2.1 (for $p/\sigma \approx 2$ and $m \approx 0.95$). These variations can be reduced by increasing the number of phase steps (Supplementary Fig. 3.10 and Supplementary Note).

We have tested our method on DNA-origami nanostructures imaged with DNA-PAINT [18] (see Methods). Figure 3.2a shows the SIMFLUX reconstruction over the full $26 \times 26\,\mu\mathrm{m}^2$ FOV of nano-rulers with binding site spacing of 80 nm and Fig. 3.2b–d show five selected SIMFLUX nano-ruler images across the FOV, with improved precision compared to the SMLM images. The latter uses the fits from the sum of six frames used for SIMFLUX, which effectively provides a spatially uniform illumination. The projections of the localizations in Fig. 3.2d,e on the x axis provides localization histograms (Fig. 3.2f,g), indicating an improvement in localization precision with a factor of around 2. The localization error, measured from the accumulated data of 420 segmented binding sites across the whole FOV, improves from 17.3 to 9.6 nm (Fig. 3.2h–k), an improvement factor of 1.8. The achieved precision, determined from repeated localizations of long-lasting on-events (Fig. 3.2l,m), is 2.3 times better for SIMFLUX, close to the expected improvement factor of 2.1 (for $p/\sigma = 1.85$, $m = 0.92$). The localization precision values determined in this way are slightly greater than the CRLB, as opposed to the precision

values from the cluster analysis, that exceed the CRLB more (Supplementary Fig. 3.12). We attribute this difference to a residual drift after correction of around 4 nm, a level that is reasonable in view of the difficulty for precise estimation on the sparse sample. Drift may also be the root cause for the washing out of the dependence of the precision on global phase, anticipated by theory and for an improvement factor that is less than the theoretical value 2.1. The histogram of nearest neighbor localizations (Fig. 3.2n,o) shows the expected peaks at the single and double binding site distance for the origami, indicating that SIMFLUX does not compromise accuracy. The Fourier ring correlation (FRC) resolution [19] improves from 16.4 to 8.6 nm (Fig. 3.2p), an improvement factor of 1.9, comparable to the improvement factor 1.8 found from cluster analysis. A precision improvement of 2.0 can also be achieved for the case of four phase steps (Supplementary Fig. 3.13), which can provide more robustness against errors in detecting the on-off transitions. Figure 3.2q–t and Supplementary Fig. 3.14 show further results on DNA-origami grids with binding site spacing of 40 and 20 nm, revealing similar resolution improvements.

Next, we imaged tubulin filaments in cells with DNA-PAINT (Fig. 3.3a–c), resulting in better visibility of the filaments and the hollow structure of tubulin [20] (Fig. 3.3d,e). The improvement in localization precision determined from long-lasting on-events is a factor 2.5 (Fig. 3.3f), and an FRC-resolution improvement factor of 2.1 is obtained (Fig. 3.3g). We also experimented with (d)STORM imaging of tubulin in cells (Fig. 3h–l), giving a relative improvement of precision with a factor 2.3 (Fig. 3.3m) and an improvement of FRC resolution with a factor 1.4 (Fig. 3.3n). The improvement in (d)STORM imaging is less than the improvement in PAINT imaging, possibly due to larger fluctuations in the intensity during the molecule's on-time (Supplementary Fig. 3.15).

In conclusion, we have demonstrated a practical way to extend the MINFLUX concept to sinusoidal illumination patterns, improving FOV and throughput to standard SMLM experimental settings. We envision that our technique can also be used to achieve the same precision as SMLM but with four-fold less light, enabling either faster imaging or imaging with dimmer fluorophores. Our optical setup can potentially achieve the same resolution gain as MINFLUX over a small FOV in a neighborhood of size L of crossing illumination pattern minima, if we shift dark fringes of the pattern over a small total translation range L instead of the full pattern pitch p (see Supplementary Note and Supplementary Fig.. 3.16). Another next step for SIMFLUX would be the extension to three-dimensional interference patterns for an improvement in both lateral and axial localization precision (see Supplementary Note). Similar results as reported here have been demonstrated recently [21], using a more complex setup for very fast pattern switching and for multiplexing the phase images on two separate cameras for readout within a single camera frame, and a localization algorithm based on the modulation by the shifting illumination pattern alone.

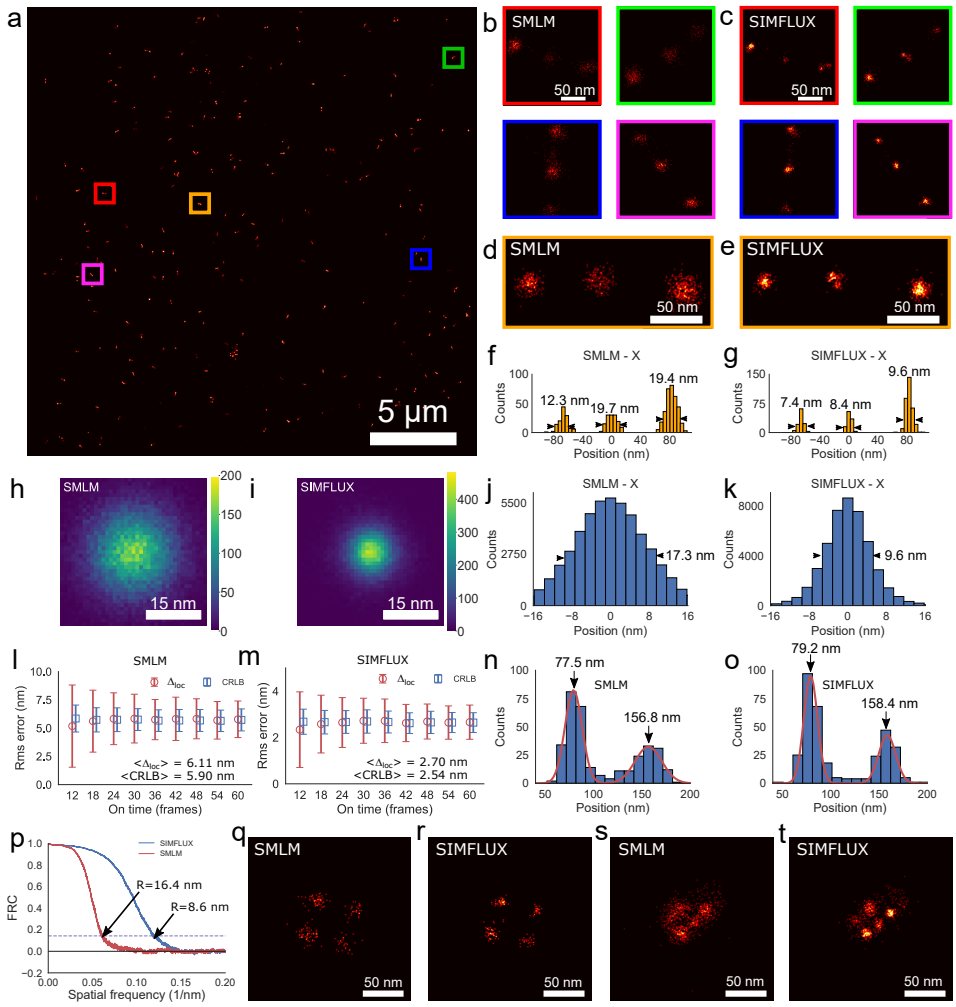

Fig. 3.2: Demonstration of SIMFLUX on DNA-origami nano-stuctures. a, Full 26 μm wide FOV SIMFLUX image of sparsely distributed nano-rulers with 80 nm spacing. Four independent imaging experiments were done with similar outcome. b,c, Zoom-in on four conventional SMLM and SIMFLUX nano-ruler instances color indicated as boxes in a, both reconstructions are based on the same underlying data. d,e, SMLM and SIMFLUX image of nanoruler instance of box in a. f,g, Histograms of localizations in d,e projected on the x-axis. h,I, 2D histograms of SMLM and SIMFLUX localizations in the image plane, assembled from 420 segmented binding sites, and j,k, histograms of localizations projected onto the x-direction. l,m, Localization error Δ_{loc} and CRLB (mean and s.d.) determined from repeated localizations of long molecular on events. Number of localizations per data point are given in the Supplementary Table. n,o, Histogram of nearest neighbour localizations for SMLM and SIMFLUX and bimodal Gaussian fits. p, FRC curves for dataset of a with resolution values R. q,r, SMLM and SIMFLUX images of DNA-origami grids with 40 nm spacing between binding sites. Two independent imaging experiments were done with similar outcome. s,t, SMLM and SIMFLUX images of DNA-origami grids with 20 nm spacing between binding sites. Two independent imaging experiments were done with similar outcome.

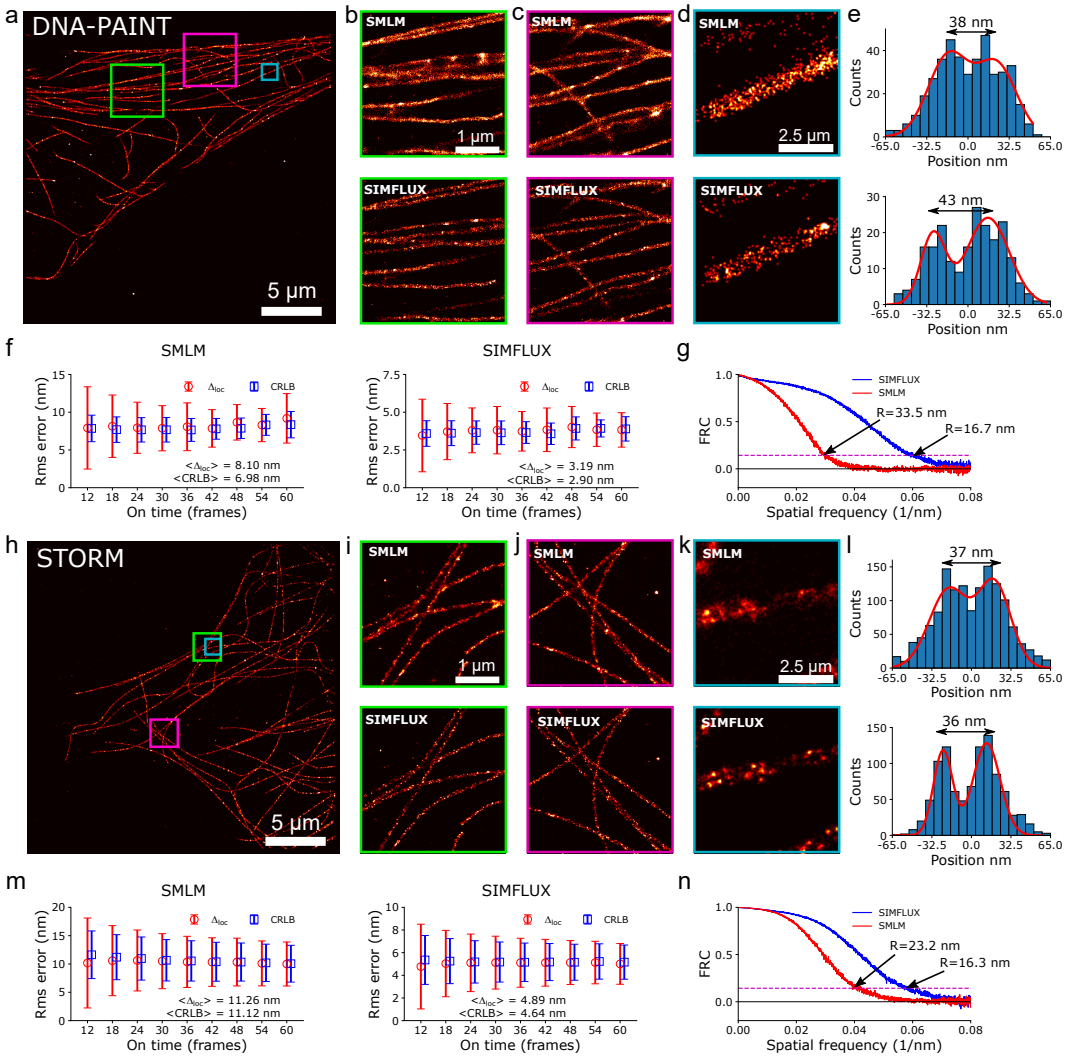

Fig. 3.3: Demonstration of SIMFLUX on cellular tubulin with DNA-PAINT and (d)STORM. a, Full 26 μm wide FOV SIMFLUX image of tubulin sample imaged with DNA-PAINT. Three independent imaging experiments were done with similar outcome. b-d, Zoom-in on SMLM and SIMFLUX images of boxes in a, both reconstructions are based on the same underlying data. e, Cross-section histogram of the tubulin segment in d with bimodal Gaussian fit. f, Localization error Δ_{loc} and CRLB (mean and s.d.) determined from repeated localizations of long molecular on events in the dataset of a. g, FRC curves for dataset of a with resolution values R. h, Full 26 μm wide FOV SIMFLUX image of tubulin sample imaged with (d)STORM. Four independent imaging experiments were done with similar outcome. i-k, Zoom-in on SMLM and SIMFLUX images of boxes in h, both reconstructions are based on the same underlying data. l, Cross-section histogram of the tubulin segment in k with bimodal Gaussian fit. m, Localization error Δ_{loc} and CRLB (mean and s.d.) determined from repeated localizations of long molecular on events in the dataset of h. n, FRC curves for dataset of h with resolution values R. Number of localizations per data point in f and m are given in the Supplementary Table.

3.2.1 Methods

Experimental setup

A custom total internal reflection (TIRF) structured illumination microscopy (SIM) microscope was built to implement the SIMFLUX method (Supplementary Figure 14). The setup uses a 200 mW, 640 nm, diode laser (Toptica, CLUP-640) that is spectrally filtered with a 640/20 nm (Chroma, ET640/20m) bandpass filter and spatially filtered by coupling into a polarization maintaining single mode fiber (ThorLabs, PM630-HP) via an NA matched aspheric lens, L1 (f = 3.3 mm, ThorLabs, C340TMD-A). The output of the fiber is collimated by an objective, L2 (0.45/20X A-PLAN, Zeiss). SIMFLUX utilizes two orthogonal sinusoidal modulation patterns in the focal plane of the objective lens. The optical architecture overcomes drawbacks of typical SIM architectures. Rotating gratings are too slow to generate multiple illumination patterns for a typical molecular on-event (10s of ms), Spatial Light Modulators (SLMs) are sufficiently fast, but too power-inefficient to generate a sufficiently high illumination intensity (kW/cm^2) over an extended field of view (10s of μm). A simple way to generate these is to build an interferometer and self-interfere a laser at the sample plane. The approach is a modification of an earlier architecture, where two pairs of diffraction orders are generated with two orthogonally oriented gratings and combined with a polarizing beam splitter [22]. In our setup, custom etched binary phase gratings (HOLOOR, DS-281-1-Y-A) with pitches of 8.496 μm are used to generate $\pm$1st diffraction orders with near theoretical diffraction efficiency limits of around 79%. Distinct and orthogonal interference patterns at the focal plane with controllable phase are generated using a fluid filled KD*P Pockels cell (Leysop, EM508-2T-F-AR640) to alternate the laser between two beam paths and piezoelectric stages (PI, P-753.1CD) to phase shift the binary phase gratings. Before being sent through the Pockels cell and diffraction gratings, the laser intensity is controlled via a half wave plate (ThorLabs, DS-281-1-Y-A) and a Glan-Taylor polarizer (GL10-A) to attenuate when needed while maintaining at least a 1000:1 intensity extinction ratio between each path. The beam then passes through the Pockels cell that is aligned such that applying a half wave voltage switches the beam between s and p polarizations. Two mirrors (ThorLabs, PF10-03-G01) then align the laser to the main optical axis of the system. A quarter wave plate and half wave plate (ThorLabs, WPQ05M-633 & WPH05M-633) are placed after the second mirror to reduce any elliptical polarization induced by reflection. A cube polarizing beam splitter (ThorLabs, CCM1-PBS252/M) selects the beam path based on s or p polarization entry. A high extinction ratio Glan-Taylor polarizer (ThorLabs, GL10-A) is then placed in each beam path after the polarizing beam splitter to ensure at least 104 polarization purity in each beam path. A binary phase grating is then placed in both beam paths. Each grating is mounted on a nanometer resolution piezoelectric translation stage to induce phase shifting. The stages have a step and settle time of 3-4 ms, giving an upper limit to the framerate of 250 Hz. The gratings are aligned on the piezoelectric stages so that their main diffraction axes are orthogonal to one another. The azimuthal alignment of the gratings is chosen such that the polarization of the interfering diffraction orders is parallel in the objective focal plane for each

beam path. After light is diffracted from each binary phase grating, a second polarizing beam splitter recombines the two paths into the main system illumination path. Two more beam steering mirrors are needed to recombine the beam path that is reflected off the first beam splitter. After recombining into a single optical axis, the diffracted orders are collimated by L3 (ThorLabs, ACA254-075-A) and sent through a spatial filter mask to filter all but the ±1st diffraction orders. From there a 4f system L4,5 (Edmund Optics/ThorLabs, 49-395-INK/AC508-180-A-ML) relays the spatial filter to the rear focal plane of the objective (Nikon, CFI Apo 1.49 TIRF 100XC Oil) after reflecting off a long pass dichroic mirror (Semrock, Di03-R660-t1-25.2x35.6). If the light from the ±1st orders is well focused in the rear focal plane, collimated light will emerge from the objective and be incident on the sample plane. Careful alignment is needed here, as a defocus at the rear focal plane will result in a distortion of the sinusoidal illumination pattern. The ±1st orders enter at opposite edges of the back focal plane at a radius ±2.91 mm from the optical axis, corresponding to a Numerical Aperture NA_i=2.91/2.0=1.455 (the focal length of the Nikon 100x objective lens is 2.0 mm). The illumination NA_i exceeds the sample refractive index of n_{med}=1.33 and therefore provides TIRF illumination. A TIRF illumination system is chosen in order to reduce background fluorescence by providing an interface bound optical sectioning of 100-200 nm, and to be compatible with DNA-PAINT based localization. The sample plane is illuminated with a power density of 600 W/cm^2 over an 80 μm illumination diameter. Control of the sample plane and system focus is achieved with a XYZ 100x100x100 μm travel range piezoelectric slide stage (Mad City Labs, 1D100). Emitted fluorescence is collected by the same Nikon objective in an epi-illumination configuration and passes through the long pass dichroic mirror and a bandpass 690/50 nm emission filter (Chroma, ET690/50m) before being imaged by an infinity corrected tube lens (ThorLabs, TTL200-A) onto an sCMOS camera (Hamamatsu, ORCA Flash 4.0 V2). The pixel size of our camera in the sensor plane is 6.5 μm giving a back-projected pixel size in the sample plane equal to 65 nm. Image acquisition was controlled using a standard desktop workstation equipped with a camera link frame grabber (Hamamatsu, AS-FBD-1XCLD-2PE8). Micro-manager serves as the main image acquisition software, but is integrated with a custom Python script to control an Arduino which triggers the PI piezoelectric stage controllers and the Pockels cell to iterate through imaging states. Micro-manager also controls the piezoelectric sample stage from Mad City Labs. The PI piezo electric stages were initialized to receive triggers from the Arduino via the program MikroMove.

A second set of hardware was incorporated into the system to facilitate (d)STORM imaging. These alterations included replacing the original sCMOS (Hamamatsu, ORCA Flash 4.0 V2) with another sCMOS (Andor, Zyla 4.2) for better pixel blanking between subsequent frames. The laser was replaced with a 200 mW, 638 nm, laser diode (Omicron, PhoxX+ 638-200) in a fiber-less free space configuration to achieve an appropriate power density at the sample plane of 1.5 kW/cm2 for (d)STORM imaging. Micro-manager was also replaced with the Andor Solis frame capture software to facilitate high speed spooling to hard disk without data loss.

The modulation contrast of the system was characterized by imaging a pre-prepared slide of 20 nm GATTA-beads (GattaQuant, Bead R) and finely phase shifting the illumi-

nation pattern over the sample. By imaging after each phase shift, a direct measurement of the sinusoidal wave can be traced over the image series duration (Supplementary Figure 3.18). Median values of the modulation contrast of 0.91 and 0.92 in the two pattern directions were measured. The observed values for the modulation contrast may be related to polarization impurity at the back focal plane. An analysis of the electromagnetic evanescent wave at the sample results in a modulation contrast $m \approx 1 - 2(\mathrm{NA}_i^2/n_{\mathrm{med}}^2)R$, with R the intensity ratio of undesired (p) to desired (s) polarization at the back focal plane. Excluding other causes, a value of R around 3 to 4% is consistent with the observed modulation contrast. A contributing factor to polarization impurity could be the reflection of the beams converging to the back focal plane of the objective after reflection at the dichroic. The polarization purity may also be affected by the quality of the dichroic. According to the specification of the manufacturer, the reflection for s-polarized light is at near 100%, and the reflection for p-polarized light is about 98%, at the laser wavelength of 640 nm.

The pitch of the interference pattern in the sample plane was calibrated by imaging high density, blinking, fluorophores that are evenly distributed in the sample plane, and localizing the fluorophores under static standing wave illumination conditions. The illumination pattern arises from the interference of evanescent waves and is therefore not directly visible, however, super-resolved localization images show it quite clearly (Supplementary Figure 3.19), giving a pitch equal to 219.94 nm. This estimate of the pitch agrees well with the expected value $\lambda_{\mathrm{ex}}/(2\mathrm{NA}_i) = 640/(2*1.455) = 219.9$ nm. The direct calibration of stage translation to phase for the piezo mounted diffraction gratings can be calculated from this data as well, giving a sample plane pattern shift to grating translation ratio of 51.6 nm/μm.

Samples

Gattaquant nanorulers based on DNA-PAINT, GATTA-PAINT (PAINT 80R ATTO 655), were used as the main samples for our imaging experiments. They consist of three equally-spaced binding sites separated by 80 nm between each with an approximate surface density of $1/\mu\mathrm{m}^2$. Other DNA-PAINT based nanostructures were imaged with uniformly decreasing structure sizes: 2×2 grids with 40 nm binding site distance and 4×3 grids with 20 nm binding site distance (see Supplementary Fig. 3.20 for designs) were synthesized and prepared according to the protocols provided by Schnitzbauer et al. [18] employing 5'-TTATACATCTA-3' as DNA-PAINT docking strand (positions marked in red in Supplementary Fig. 3.20) and 5'-CTAGATGTAT-3'-Cy3B as DNA-PAINT imager sequence. Both nanostructures were imaged using 5 nM imager strand concentration.

For the tubulin imaging with DNA-PAINT in Figure 3, COS-7 cells were passaged every other day and used between passage number 5 and 20. The cells were maintained in DMEM supplemented with 1% Sodium-Pyruvate and 10% Fetal Bovine Serum. Passaging was performed using 1× PBS and Trypsin-EDTA 0.05%. 24 h before immunostaining, cells were seeded on ibidi 8-well glass coverslips at 30,000 cells/well. For fixation, the samples were pre-fixed and pre-permeabilized with 0.4% glutaraldehyde and 0.25% Triton X-100 for 90 s. Next, the cells were quickly rinsed with 1× PBS once followed by

fixation with 3% glutaraldehyde for 15 min. Afterwards, samples were rinsed twice (5 min) with 1× PBS and then quenched with 0.1% NaBH4 for 7 min. After rinsing four times with 1× PBS for 30 s, 60 s, and twice for 5 min, samples were blocked and permeabilized with 3% BSA and 0.25% Triton X-100 for 2 h. Then, samples were incubated with 10 μg/ml of primary antibodies (1:100 dilution) in a solution with 3% BSA and 0.1% Triton X- 100 at 4 degrees overnight. Cells were rinsed three times (5 min each) with 1× PBS. Next, they were incubated with 10 μg/ml of labeled secondary antibodies (1:100 dilution) in a solution with 3% BSA and 0.1% Triton X-100 at room temperature for 1 h. For fiducial based drift correction, the samples were incubated with gold nanoparticles with a 1:1 dilution in 1× PBS for 5 min. Finally, samples were rinsed three times with 1× PBS before adding imager solution. Imaging was carried out using an imager strand (P1-8nt: 5-AGATGTAT-Atto655-3', P1-7nt: 5-GATGTAT-Atto655-3') concentration of 2 nM in imaging buffer (1×PBS supplemented with 500mM NaCl).

For the tubulin imaging with (d)STORM in Figure 3, COS-7 cells were seeded onto 18 mm coverslips. After 24 hours of incubation, the cells underwent extraction with 0.1% glutaraldehyde and 0.2% Triton X-100 in PEM80 for one minute and were fixed with 4% PFA in PEM80 for 10 minutes. The cells were then rinsed three times in 1× PBS for 5 minutes and permeabilized with 0.2% Triton X-100 in PEM80 for 15 minutes. Cells were again rinsed three times in 1× PBS for 5 minutes, after which blocking was performed in 3% BSA for 45 minutes on RT. Next, the cells were incubated in primary antibody mouse anti alpha-Tub (Sigma, 1/1000) overnight at 4 degrees. The following day the cells were rinsed three times in 1× PBS for 5 minutes and incubated with anti-mouse Alexa647 (Life Technologies, 1/500) for 1 hour at RT. After three rinses the cells were mounted on 80 uL cavity slides with AbbeLight Storm buffer.

Data acquisition

A simple data acquisition sequence was defined to acquire six (or any other arbitrary number) phase shifted images during the on-time of a single blinking event of a fluorophore (Supplementary Figure 18). For the DNA-origami samples in this experiment, the average on-time of blinking events is 100-200 ms for the GattaQuant nano-rulers, 1 s for the 40 nm 2×2 grids, and 100 ms for the 20 nm 4×3 grids. For the DNA-PAINT tubulin and STORM tubulin samples the average on-time is 400-500 ms and 100 ms, respectively. All DNA-PAINT origami samples were imaged at 70 frames per second with 10 ms exposure time per frame, the DNA-PAINT tubulin samples at 14 frames per second with 40 ms exposure time per frame, and the (d)STORM samples at 200 frames per second with 4 ms exposures. These settings ensured that typically a full phase cycle of each pattern orientation was captured. The nano-ruler dataset consists of 30,000 frames, the origami grid samples of 100,000 frames, the DNA-PAINT tubulin dataset of 13,000 frames, and the (d)STORM tubulin dataset of 150,000 frames.

Simulation setup

Simulated point spread functions (PSFs) are generated according to a vectorial PSF model [23]. The NA is taken to be 1.49, the wavelength 680 nm, the refractive index 1.515 (medium, cover slip and immersion fluid assumed to be matched), with a pixel size of 65 nm in object space, and the region of interest (ROI) is 11×11 pixels large. The PSF coordinates within the ROI are drawn from a uniform distribution with a width of half the illumination pattern pitch. Unless stated otherwise, we take 6000 detected signal photons and 30 background photons per pixel, and we add noise according to Poisson statistics. The simulations are run for 5000 randomized instances. The pitch of the excitation pattern is taken to be 243.75 nm, which is set equal to about 2× the spot width for the sake of simplicity. The number of signal photons reported corresponds to the number of photons captured over the entire FOV, i.e. taking into account the spatially extended tail of the PSF that falls outside the ROI [24].

We have also used simulations of blinking emitters over a full FOV (Supplementary Figure 3.22). A filamentous structure, similar in appearance to microtubule, is generated using the worm-like chain model. The simulated filaments fill a FOV of several μm. Binding sites along the filaments are randomly generated at an average separation distance of 5 nm. At each binding site flexible linkers are simulated using a normal distribution with a standard deviation of 3 nm. Randomly switching fluorophores are simulated at the end of the linkers, using an average on-time of 9 frames and an average off-time of 54000 frames. Random transitions between both states were simulated at a rate of 1× the frame-rate. The illumination pattern is shifted in 3 steps over the pitch of 220 nm with a modulation depth of 0.95 in both the x and y-direction to match the expected experimental values. The locations of the resulting set of emitters that are are in the on-state in a frame are blurred with the vectorial PSFs as described above. Shot noise is subsequently added, using 2000 detected signal photons per spot and 10 background photons per pixel. The entire simulation consists of 120,000 camera frames. Localizations with fitted background more than two times the average background and/or signal photon count more than two times the average (mainly occurring due to nearby fluorophores that are on simultaneously) are designated as outliers.

Processing pipeline

Supplementary Figure 3.23 gives a schematic overview of the entire processing pipeline. First, the set of acquired images where first offset and gain corrected to convert ADUs into photons [25, 26]. The total set of acquired images is I_p^{lk} with $l = 1, \ldots, L$ the pattern orientations, $k = 1, \ldots, K$ the pattern phases, and $p = 1, \ldots, P$ the label for the groups of $L \times K$ frames, giving a total of $L \times K \times P$ acquired frames. The detection of isolated emitting molecules is aided by first applying a sum over the $L \times K$ blocks of frames, i.e. the set of I_p^{lk} is summed to $J_p = \sum_{lk} I_p^{lk}$. This averages out the effect of the shifting and rotating illumination pattern, and increases the Signal-to-Noise Ratio (SNR) for spot detection. ROIs of size 9×9 pixels are identified by a two-stage filtering process to reduce photon noise and local background followed by an intensity threshold

[27, 28]. In short, we apply uniform filters to the raw images with filter size 4 and 8 pixels and take the difference. We then computed the local maximum in a 5×5 pixels neighbourhood for all pixels and accept the central pixel as candidate for a single-molecule spot if its value is the local maximum and is higher than a threshold of 10 (for the nanoruler dataset of Fig. 3.2 and Supplementary Fig. 3.14) or 3.23 (for the grid DNA-origami datasets of Fig. 3.2 and Supplementary Fig. 3.14). Now a 9×9 pixel ROI is segmented out for all candidates and each ROI, labelled with index s, is extracted and fitted for emitter position $\vec{r}_s = (x_s, y_s)$, signal photon count N_s and background b_s using established Maximum Likelihood Estimation (MLE) fitting [29, 30] using a Gaussian PSF model. The fits are done with a fixed Gaussian spot width of 119 nm, determined from a separate fit on the first few frames of the entire dataset.

In a next step the signal photon count and background in the ROI with label s in the $L \times K$ original individual frames I_p^{lk} are analysed for estimating the signal photon count N_s^{lk} and background b_s^{lk} given the estimate of the emitter position (x_s, y_s) obtained from fitting the moving sum images J_p. The underestimation of the signal photon count [24] by 30% due to the use of the Gaussian PSF model has a limited impact on the subsequent analysis, as only the relative signal photon count for different phases and orientations of the illumination pattern is used. The single-frame localizations within the sequences of $L \times K$ frames are kept and merged into a single localization estimate, according to standard practices [13]. The resulting SMLM estimates are stored for later comparison to the SIMFLUX estimate.

The next step is the estimation of the illumination pattern parameters. First, we make an initial estimate of the spatial frequency vectors $\vec{q}_l = (\cos\beta_l, \sin\beta_l)/p_l$ (with pitch p_l and orientation β_l) of the patterns. The set of molecular on-events with label s contains $L \times K$ single-frame localizations with estimated coordinates (x_s, y_s), signal count N_s^{lk} and background b_s^{lk}. The entire collection of these single-frame localizations is split into subsets corresponding to the $l = 1, \ldots, L$ orientations and $k = 1, \ldots, K$ phases of the illumination patterns. The $L \times K$ subsets of single-frame localizations are used to generate super-resolution reconstructions S_n^{lk} defined on a grid of super-resolution pixels $\vec{r}_n$, with n the index of the super-resolution pixels. We have used Gaussian blob rendering with a width equal to the average localization precision from the single-frame localizations, and a zoom factor of 6 compared to the detector pixel grid to make the super-resolution pixel size comparable to the single-frame localization precision [19]. For the data of Fig. 3.2 we have used a super-resolution pixel size equal to 10.8 nm, comparable to the CRLB in the single-frame localizations of around 12 nm. Each Gaussian blob is multiplied with a weight factor equal to the estimated signal photon count N_s^{lk}. The spatial frequencies $\vec{q}_l$ are then detected by finding the peak in the Fourier domain of the reconstructions S_n^{lk}.

In a next step, sequences of $L \times K$ single-frame localizations where the molecule under consideration is partially in the off-state are rejected by application of a modulation error filter. Sequences are selected where the prediction error is below a user set maximum

relative error:

$$\max_{k,l}\left(\frac{N_s^{lk}}{N_s}-P_l(\phi_{lk}(\vec{r}_s))\right)^2<\gamma_{\max} \tag{3.2}$$

where $P_l(\phi_{lk}(\vec{r}_s))$ expected illumination pattern. The choice for the threshold $\gamma_{\max}$ is based on a simulation study of realistic filamentous objects (see Supplementary Fig. 3.22). It appears that a Jaccard index of approximately 65% is achieved, where the Jaccard-index is defined as the fraction TP/(TP+FP+FN), with true positive localizations (TP), false positive localizations (FP), and false negative localizations (FN). The false positive rate and false negative rate depend smoothly on $\gamma_{\max}$ (Supplementary Fig. 3.22h), but not so much on signal photon count and background level. For the experimental data a value in the range between 0.01 and 0.06 is selected such that about 30% of originally detected events is rejected. For the DNA-origami nano-rulers of Fig. 3.2 a setting $\gamma_{\max}=0.012$ is used, for the tubulin-PAINT dataset of Fig. 3.3 a setting $\gamma_{\max}=0.05$ is used, and for the tubulin-STORM dataset of Fig. 3.3 a setting $\gamma_{\max}=0.04$ is used.

This first estimate of pitch and orientation of the patterns is improved by an iterative refinement procedure. The first step here is to estimate the illumination pattern phases ψ_{lk}, as well as the modulation depths m_l, and relative intensity η_l for illumination patterns with orientation l (normalized as $\sum_l \eta_l = 1$, nominally $\eta_l = 1/L$). These estimates are obtained by a least squares fit of the illumination pattern to the detected photon counts N_s^{lk} with error metric:

$$E_{lk}=\sum_s\left|N_s^{lk}-\eta_l\frac{N_s}{K}(1+m\cos(\phi_{lk}(\vec{r}_s)))\right|^2 \tag{3.3}$$

with $\phi_{lk}(\vec{r}_s)=2\pi\vec{q}_l\cdot\vec{r}_s-\psi_{lk}$ the phase at localization position $\vec{r}_s$. Illumination pattern phase estimation biases originating from the structure of the underlying fluorescently labelled structure are mitigated by taking into account the sum of all detected photon counts $N_s=\sum_{lk}N_s^{lk}$ as weight factor for the illumination pattern in the error metric. The minimization of Equation 3 with respect to the 0th and 1st order Fourier coefficients $(\eta_l,\eta_l m_l\cos\psi_{lk},\eta_l m_l\sin\psi_{lk})$ of the sinusoidal illumination results in:

$$\begin{bmatrix}\sum_s\frac{N_s^2}{K^2} & \sum_s\frac{N_s^2}{K^2}\cos(2\pi\vec{q}_l\cdot\vec{r}_s) & \sum_s\frac{N_s^2}{K^2}\sin(2\pi\vec{q}_l\cdot\vec{r}_s)\\ \sum_s\frac{N_s^2}{K^2}\cos(2\pi\vec{q}_l\cdot\vec{r}_s) & \sum_s\frac{N_s^2}{K^2}\cos(2\pi\vec{q}_l\cdot\vec{r}_s)^2 & \sum_s\frac{N_s^2}{K^2}\sin(2\pi\vec{q}_l\cdot\vec{r}_s)\cos(2\pi\vec{q}_l\cdot\vec{r}_s)\\ \sum_s\frac{N_s^2}{K^2}\sin(2\pi\vec{q}_l\cdot\vec{r}_s) & \sum_s\frac{N_s^2}{K^2}\sin(2\pi\vec{q}_l\cdot\vec{r}_s)\cos(2\pi\vec{q}_l\cdot\vec{r}_s) & \sum_s\frac{N_s^2}{K^2}\sin(2\pi\vec{q}_l\cdot\vec{r}_s)\end{bmatrix}$$
$$\times\begin{bmatrix}\eta_l\\ \eta_l m_l\cos\psi_{lk}\\ \eta_l m_l\sin\psi_{lk}\end{bmatrix}=\begin{bmatrix}\sum_s\frac{N_s^{lk}N_s}{K}\\ \sum_s\frac{N_s^{lk}N_s}{K}\cos(2\pi\vec{q}_l\cdot\vec{r}_s)\\ \sum_s\frac{N_s^{lk}N_s}{K}\sin(2\pi\vec{q}_l\cdot\vec{r}_s)\end{bmatrix} \tag{3.4}$$

which can be solved in a straightforward way. The robustness of the fit is further enhanced by an iterative procedure in which the median of the quadratic error distribution over the localizations in Equation 3 is determined, and the localizations with error less than the median are kept for a second phase estimation. After this second phase estima-

tion the median of the quadratic error of the original set of localizations is determined again, and the localizations with error less than the median are kept for a third phase estimation, etc. This procedure converges within 3 iterations. We apply this procedure on the set of localizations that is obtained before application of the modulation error filter. In this way blocks of frames in which the molecule is partially in the on-state (say in the last 3 but not in the first 3 frames) aid in the fitting. The phase estimation has a standard error of the mean typically between 0.5 and 1.0 deg (Supplementary Fig. 3.11). The modulation depths m_l are typically estimated around 0.95, in agreement with the calibration measurements on beads. The modulation depth is typically underestimated for non-sparse datasets. In that case it is better kept fixed to 0.95, the typical value obtained for sparse datasets. The relative intensity $\eta_1 = 1 - \eta_2$ is found to be around 0.455 in our setup.

Next, an MLE based estimate is made of the molecule's position, using both image centroid information and photon count information. The PSF model, log-likelihood, and relevant derivatives with respect to the fit parameters are defined in the Supplementary Note. Initial values for the parameter estimation are taken from the analyses on single-frame and moving sum frame data, the optimization uses the Levenberg-Marquardt algorithm. The previously estimated illumination pattern parameters are assumed to be constant throughout the experiment.

This SIMFLUX estimate differs $\delta\vec{r}_s$ with the corresponding SMLM localization, where s labels the different localization events. An improved estimate of the spatial frequencies can now be made by minimizing the overall error in the illumination pattern phases $\psi_{lk}(\vec{r}_s) = 2\pi\vec{q}_l \cdot \vec{r}_s - \psi_{lk}$. The average phase error per orientation is:

$$\delta\phi_l(\vec{r}_s) = 2\pi\vec{q}_l \cdot \delta\vec{r}_s + 2\pi\delta\vec{q}_l \cdot \vec{r}_s - \delta\psi_l \tag{3.5}$$

where $\delta\vec{q}_l$ is the error in the spatial frequency vector, and where $\delta\psi_l$ is the average error in the pattern phase. These errors can be estimated by linear regression, i.e. by minimizing:

$$F_l = \sum_s |\delta\phi_l(\vec{r}_s)|^2 \tag{3.6}$$

This results in a linear set of equations for $\delta\vec{q}_l$ and $\delta\psi_l$:

$$\sum_s 2\pi(\delta\vec{q}_l \cdot \vec{r}_s)\vec{r}_s - \sum_s \delta\psi_l\vec{r}_s = -\sum_s 2\pi(\vec{q}_l \cdot \delta\vec{r}_s)\vec{r}_s \tag{3.7a}$$

$$\sum_s 2\pi(\delta\vec{q}_l \cdot \vec{r}_s) - \sum_s \delta\psi_l = -\sum_s 2\pi(\vec{q}_l \cdot \delta\vec{r}_s) \tag{3.7b}$$

which can be solved in a straightforward way. After updating the spatial frequency vectors to $\vec{q}_l' = \vec{q}_l + \delta\vec{q}_l$ the estimation of the pattern phases ψ_{lk} as explained above is repeated, as well as the SIMFLUX MLE fit. This procedure converges in 3 to 4 iterations.

The quality of convergence can be assessed by the rms value of the SMLM-SIMFLUX

localization difference $\delta r_{\mathrm{rms}} = \sqrt{\langle \delta \vec{r}_s^{\,2} \rangle}$. It appears that at convergence this rms value is about 13.0 nm for the nanoruler dataset of Fig. 3.2 (see Supplementary Fig. 3.24). This value is on the order of the localization uncertainty, which seems physically reasonable. It implies an error in the overall pattern phase of about $\delta\phi \approx 2\pi\delta r_{\mathrm{rms}}/p\sqrt{N_s} = 1.0$ deg with $N_s = 431$ the number of imaged binding sites used in the analysis and $p = 220$ nm the nominal pitch. This can be related to the final precision in the pitch estimation δp, which scales with the precision of the overall pattern phase estimation according to $\delta\phi \approx 2\pi|\delta\vec{q}_l| \cdot R_{\mathrm{FOV}}/p^2$, with $R_{\mathrm{FOV}} = 13$ μm the FOV size. This gives a precision in the pitch estimation of about $\delta p \approx 0.1$ nm. The distribution of SMLM-SIMFLUX localization differences in x and y for the other datasets is unbiased as well, with a width that increases with the localization precision. No correlation with the position in the FOV is observed in all cases.

Sample drift is corrected on the localization data following the method of Schnitzbauer et al. [18], implemented using the Picasso software tool, available at `https://github.com/jungmannlab/picasso`. We note that sample drift does not influence the pattern parameter estimation as the projected pattern is static under sample drift. Therefore, we do not need to re-estimate the pattern parameters after drift correction is applied to the localizations.

All images are rendered by histogram binning on a grid with 0.52 nm (Fig. 3.2d,e,p,q,r,s and Supplementary Fig. 3.14) or 0.52 nm (Fig. 3.2b,c) super-resolution pixel size with additional Gaussian blurring with kernel size (sigma) equal to 1 super-resolution pixel. The overview image Fig. 3.2a and Fig. 3.3a,k are rendered with a super-resolution pixel size of 33.85 nm and a Gaussian pixel blur of 19.5 nm. The sub images in Fig. 3.3b-e, l-o, and h are rendered with a super-resolution pixel size of 3.25 nm and a Gaussian pixel blur of 3.25 nm.

Data analysis

The spread of localizations is estimated using the Fourier Ring Correlation (FRC) [19] of the entire super-resolution reconstruction. The two image halves are found by randomly selecting localizations to the two subsets. This gives rise to FRC curves largely determined by the localization precision, eliminating correlations arising from having multiple localizations from the same binding site ("spurious correlations") would result in an FRC-curve determined by the structure of the sparsely distributed binding sites [19]. The split datasets are used to generate reconstructions on a 2 nm super-resolution pixel grid (super-resolution pixel size must be less than about 0.25× the FRC-resolution for a valid FRC estimation) by the histogram binning method. For the DNA-origami nanoruler dataset of Fig. 3.2 with a cluster analysis of the localization point clouds around each binding site. A kernel density estimate of the histograms is used to measure the FWHM of the histograms.

These estimates are based on localizations accumulated over the entire duration of the acquisition, and therefore take into account the impact of residual drift. A more direct estimate of localization uncertainty is based on repeated localizations of the same molecule during long lasting on-events, which are short compared to the time scale

of drift. These extended on-events are detected by linking localizations in subsequent 6 frame blocks that are spatially proximate13. Two localizations are assumed to arise from the same emitting molecule if the distance between the localizations is less than r times the largest localization uncertainty value of the two localizations. A heuristic choice is $r = 3$. Small values of r will lead to an underestimation of the localization uncertainty, as the localizations are restricted to a (too) small region in space, large values of r will lead to an overestimation of the localization uncertainty, as localizations from neighbouring binding sites or false positive localizations are linked into the set. For example, for the nano-ruler dataset of Fig. 3.2 the value for the localization uncertainty varies with about 15% in the range $2.5 \leq r \leq 4$ around the given value 2.70 nm for $r = 3$. Similar variations with r are also found for the other datasets considered. The localization uncertainty is defined as the (unbiased) sample variance over the repeated localizations within the set of linked localizations. This is compared to the average CRLB value over the set of linked localizations. This analysis also provides a way to estimate the fluorophore on-time. A fit of the distribution of the number of linked localization events as a function of the run length with an exponential distribution can then be made, the fitted time constant is the estimate for the on-time. Analysis of the nano-ruler dataset of Fig. 3.2 gives an estimated on-time of 19.1 frames. The tubulin datasets of Fig. 3.3 reveal an average on-time of 7.4 frames (DNA-PAINT) and 11.8 frames (STORM).

We have analysed long lasting on-events for intensity fluctuations above the level expected from shot noise statistics (Supplementary Fig. 3.15). To this end we imaged an 80 nm DNA-PAINT nano-ruler as well as a COS7 Alexa 647 (d)STORM sample with a static illumination pattern in order to image spots with a wide range of intensities. Well isolated spots corresponding to on-events that last at least 10 frames were extracted (see Supplementary Fig. 3.15a and d for examples) and fitted with a standard Gaussian PSF model. For DNA-PAINT, the unbiased variance of the estimated signal photon count during the on-events as a function of the time separation of the photon count estimates T is about 27% above the level expected from the CRLB, where the deviation increases with only about 3% with T (Supplementary Fig. 3.15b). The variance in the fitted intensities follow the CRLB if the emitted number of photons follows the assumed Poisson statistics (Supplementary Fig. 3.15c), and is larger than CRLB in case there are additional sources of intensity fluctuations such as sub-frame blinking events. For (d)STORM, the unbiased variance of the estimated signal photon count during the on-events as a function of the time separation of the photon count estimates T is about 125% above the level expected from the CRLB, where the deviation varies with about 12% with T (Supplementary Fig. 3.15e). The overall higher level of the error could come from model errors in the fitting (non-constant background, simplified Gaussian PSF model, aberrations, error in gain calibration, etc.), and from intensity fluctuations above the shot noise level.

We have analysed the impact of intensity fluctuations on the outcome of the fitting routines by a simulation study. To that end we modified the image formation model of the Supplementary Note by replacing the overall photon count N by $N' = N(1 + E)$, where E is a variable that takes random values from a normal distribution with zero mean and standard deviation σ_E in each camera frame. This variable describes intrinsic

intensity fluctuations of the emitter during the on-time, giving rise to an apparent variance $\Delta N'^2 = \Delta N^2 = (\langle N \rangle^2 + \Delta N^2)\sigma_E^2$, with $\langle N \rangle$ the average photon count, a variance that is higher than the variance ΔN^2 according to the CRLB. The experimental values for PAINT are $\Delta N = 47$ and $\Delta N' = 60$. This results in $\sigma_E = 0.031$, for an average fitted photon count $\langle N \rangle = 1180$. The experimental values for (d)STORM are $\Delta N = 49$ and $\Delta N' = 111$. This results in $\sigma_E = 0.093$, for an average fitted photon count $\langle N \rangle = 1062$. With the simulations we have computed the relative improvement of SIMFLUX over conventional SMLM as a function of σ_E (Supplementary Fig. 3.15f). This implies an improvement factor for PAINT that is practically at the value 2.2 simulated with zero intensity fluctuations, and an improvement factor in the range 1.6 to 2.0 for (d)STORM, depending on signal photon count. These values are somewhat lower than the optimum, in agreement with the relative improvement in apparent image quality and FRC of the (d)STORM data in comparison to the PAINT data. It also turns out that the sensitivity to intrinsic intensity fluctuations is larger for higher average photon counts. This can possibly be attributed to the photon count errors of the Gaussian PSF model, which are more grave for higher signal photon counts [23].

3.3 References

[1] S. W. Hell. "Microscopy and its focal switch". In: *Nature Methods* 6.1 (2009), pp. 24–32. ISSN: 15487091.

[2] B. Huang, H. Babcock, and X. Zhuang. "Breaking the diffraction barrier: Super-resolution imaging of cells". In: *Cell* 143.7 (2010), pp. 1047–1058. ISSN: 00928674.

[3] T. Klein, S. Proppert, and M. Sauer. "Eight years of single-molecule localization microscopy". In: *Histochemistry and Cell Biology* 141.6 (2014), pp. 561–575. ISSN: 1432119X.

[4] J. Ries et al. "A simple, versatile method for GFP-based super-resolution microscopy via nanobodies". In: *Nature Methods* 9.6 (2012), pp. 582–584. ISSN: 15487091.

[5] A. Raulf et al. "Click chemistry facilitates direct labelling and super-resolution imaging of nucleic acids and proteins". In: *RSC Advances* 4.57 (2014), pp. 30462–30466. ISSN: 20462069.

[6] H. Li and J. C. Vaughan. "Switchable Fluorophores for Single-Molecule Localization Microscopy". In: *Chemical Reviews* 118.18 (2018), pp. 9412–9454. ISSN: 15206890.

[7] S. Strauss et al. "Modified aptamers enable quantitative sub-10-nm cellular DNA-PAINT imaging". In: *Nature Methods* 15.9 (2018), pp. 685–688. ISSN: 15487105.

[8] H. Heydarian et al. "Template-free 2D particle fusion in localization microscopy". In: *Nature Methods* 15.10 (2018), pp. 781–784. ISSN: 15487105.

[9] J. B. Grimm et al. "A general method to improve fluorophores for live-cell and single-molecule microscopy". In: *Nature Methods* 12.3 (2015), pp. 244–250. ISSN: 15487105.

[10] R. Kaufmann et al. "Super-resolution microscopy using standard fluorescent proteins in intact cells under cryo-conditions". In: *Nano Letters* 14.7 (2014), pp. 4171–4175. ISSN: 15306992.

[11] S. Weisenburger et al. "Cryogenic optical localization provides 3D protein structure data with Angstrom resolution". In: *Nature Methods* 14.2 (2017), pp. 141–144. ISSN: 15487105.

[12] C. N. Hulleman et al. "Photon Yield Enhancement of Red Fluorophores at Cryogenic Temperatures". In: *ChemPhysChem* 19.14 (2018), pp. 1774–1780. ISSN: 14397641.

[13] B. Rieger and S. Stallinga. "The lateral and axial localization uncertainty in super-resolution light microscopy". In: *ChemPhysChem* 15.4 (2014), pp. 664–670. ISSN: 14397641.

[14] F. Balzarotti et al. “Nanometer resolution imaging and tracking of fluorescent molecules with minimal photon fluxes”. In: *Science* 355.6325 (2017), pp. 606–612. ISSN: 10959203. arXiv: 1611.03401.

[15] R. Heintzmann and T. Huser. “Super-Resolution Structured Illumination Microscopy”. In: *Chemical Reviews* 117.23 (2017), pp. 13890–13908. ISSN: 15206890.

[16] L. Busoni et al. “Fast subnanometer particle localization by traveling-wave tracking”. In: *Journal of Applied Physics* 98.6 (2005). ISSN: 00218979.

[17] K. Wicker. “Non-iterative determination of pattern phase in structured illumination microscopy using auto-correlations in Fourier space”. In: *Optics Express* 21.21 (2013), p. 24692. ISSN: 1094-4087.

[18] J. Schnitzbauer et al. “Super-resolution microscopy with DNA-PAINT”. In: *Nature Protocols* 12.6 (2017), pp. 1198–1228. ISSN: 17502799.

[19] R. P. Nieuwenhuizen et al. “Measuring image resolution in optical nanoscopy”. In: *Nature Methods* 10.6 (2013), pp. 557–562. ISSN: 15487091.

[20] Y. Li et al. “Real-time 3D single-molecule localization using experimental point spread functions”. In: *Nature Methods* 15.5 (2018), pp. 367–369. ISSN: 15487105.

[21] L. Gu et al. “Molecular resolution imaging by repetitive optical selective exposure”. In: *Nature Methods* 16.11 (2019), pp. 1114–1118. ISSN: 15487105.

[22] A. Chmyrov et al. “Nanoscopy with more than 100,000 ’doughnuts’”. In: *Nature Methods* 10.8 (2013), pp. 737–740. ISSN: 15487091.

[23] S. Stallinga and B. Rieger. “Accuracy of the Gaussian Point Spread Function model in 2D localization microscopy”. In: *Optics Express* 18.24 (2010), p. 24461. ISSN: 1094-4087.

[24] R. Thorsen et al. “Impact of optical aberrations on axial position determination by photometry”. In: *Nature Methods* 15.12 (2018), pp. 989–990. ISSN: 15487105.

[25] J. C. Mullikin et al. “<title>Methods for CCD camera characterization</title>”. In: *Image Acquisition and Scientific Imaging Systems*. Ed. by H. C. Titus and A. Waks. Vol. 2173. 5. SPIE, 1994, pp. 73–84.

[26] R. Heintzmann et al. “Calibrating photon counts from a single image”. In: (2016). arXiv: 1611.05654.

[27] F. Huang et al. “Simultaneous multiple-emitter fitting for single molecule super-resolution imaging”. In: *Biomedical Optics Express* 2.5 (2011), p. 1377. ISSN: 2156-7085.

[28] C. S. Smith et al. “Nuclear accessibility of ß-actin mRNA is measured by 3D single-molecule real-time tracking”. In: *Journal of Cell Biology* 209.4 (2015), pp. 609–619. ISSN: 15408140.

[29] C. S. Smith et al. “Fast, single-molecule localization that achieves theoretically minimum uncertainty”. In: *Nature Methods* 7.5 (2010), pp. 373–375. ISSN: 15487091.

[30] F. Huang et al. “Video-rate nanoscopy using sCMOS camera-specific single-molecule localization algorithms”. In: *Nature Methods* 10.7 (2013), pp. 653–658. ISSN: 15487091.

3.A Appendix 1: Supplementary information

3.A.1 Supplementary note

Image formation model

We have a sequence of $k = 1, 2, \ldots, K$ illuminations for orientations $l = 1, 2, \ldots, L$ with a harmonic intensity profile $P(\phi)$ as a function of pattern phase ϕ that is displaced according to phase offsets ψ_{lk} such that:

$$\sum_{l=1}^{L}\sum_{k=1}^{K} P(\phi_{lk}(\vec{r})) = 1 \tag{3.8}$$

with the phase:

$$\phi_{lk}(\vec{r}) = 2\pi\vec{q}_l \cdot \vec{r} - \psi_{lk}. \tag{3.9}$$

Here the spatial frequency vectors are:

$$\vec{q}l = (q_{lx}, q_{qly}) = \frac{1}{p}(\cos\beta_l, \sin\beta_l) \tag{3.10}$$

where p is the pattern pitch, $\beta_l = \pi l/L + \beta_0$, with β_0 a global angular offset. The Point Spread Function (PSF) is $h(\vec{r})$, and is assumed to be a Gaussian:

$$h(\vec{r}) = \frac{1}{2\pi\sigma^2}\exp\left(-\frac{\vec{r}^2}{2\sigma^2}\right) \tag{3.11}$$

with σ the spot width. The expected photon count on pixel j is:

$$\mu_j^{lk} = NP(\phi_{lk}(\vec{r}_0))h(\vec{r}_j - \vec{r}_0) \tag{3.12}$$

with $\vec{r}_0$ the emitter position and N the total photon count. We will consider a sinusoidal illumination pattern:

$$P(\phi) = \frac{1}{LK}(1 + m\cos\phi) \tag{3.13}$$

with m the modulation. For a perfect modulation m=1, we find:

$$P(\phi) = \frac{1}{LK}(1 + \cos\phi) = \frac{2}{LK}\cos(\phi/2)^2 \tag{3.14}$$

The phases of the different illumination patterns are assumed to be equidistant. For a full 2π phase scan this implies:

$$\psi_{lk} = 2\pi(k-1)/K + \chi_l \tag{3.15}$$

where χ_l is the phase offset of the patterns in direction $\vec{q}_l$. We then find that:

$$\phi_{lk}(\vec{r}_0) = \xi_l(\vec{r}_0) - 2\pi(k-1)/K \tag{3.16}$$

with the global phase $\xi_l(\vec{r}_0)$ of the molecule with respect to the phase offset of the illumination patterns in direction $\vec{q}_l$ defined by:

$$\xi_l(\vec{r}_0) = 2\pi\vec{q}_l \cdot \vec{r}_0 - \chi_l \tag{3.17}$$

Note that the use of equidistant phases over the full 2π phase range ensures that the normalization condition Equation 1 is automatically satisfied. This condition requires that the number of phase steps $K \geq 2$. It turns out, however, that for $K = 2$ and global phase $\xi_l(\vec{r}_0) = 0$ or $\xi(\vec{r}_0) = \pi$ (molecule at maximum and minimum of pattern for the $K = 2$ images) there is no improvement over conventional localization. For that reason $K \geq 3$ is used in practice. In the following, we will use this model to derive the Fisher-matrix and Cramér-Rao Lower Bound (CRLB) for the estimation of the position of the molecule.

The image formation model must be amended in case a non-zero background and/or a non-zero pixel size is taken into account. The expected photon count on pixel j then becomes:

$$\mu_j^{lk} = NP(\phi_{lk}(\vec{r}_0))E(\vec{r}_j - \vec{r}_0) + b/LK \tag{3.18}$$

with b the cumulative background over $L \times K$ frames. The background is assumed to be uniform over the Region Of Interest (ROI), and constant from frame-to-frame. The integration of the PSF over the pixel area gives the factor:

$$E(\vec{r}_j - \vec{r}_0) = \int_{\vec{r}\in A_j} d^2r\, h(\vec{r} - \vec{r}_0) \tag{3.19}$$

with A_j the $a \times a$ sized area of pixel j. For the Gaussian PSF this results in:

$$\begin{aligned} E(\vec{r}_j - \vec{r}_0) = \frac{1}{4}&\left[\mathrm{erf}\left(\frac{x_j - x_0 + a/2}{\sqrt{2}\sigma}\right) - \mathrm{erf}\left(\frac{x_j - x_0 - a/2}{\sqrt{2}\sigma}\right)\right] \\ &\left[\mathrm{erf}\left(\frac{y_j - y_0 + a/2}{\sqrt{2}\sigma}\right) - \mathrm{erf}\left(\frac{y_j - y_0 - a/2}{\sqrt{2}\sigma}\right)\right] \end{aligned} \tag{3.20}$$

Simple analytical results for the CRLB cannot be obtained in this more general case, and we must resort to fully numerical simulations.

In the numerical analysis of our experimental results we also need to take into account that the modulation depth and the overall intensity of the illumination patterns can vary with the direction of the illumination pattern. In that case the illumination pattern for orientation $l$changes to:

$$P_l(\phi) = \frac{\eta_l}{K}\left(1 + m_l \cos\phi\right) \tag{3.21}$$

where η_l is the relative intensity factor normalized as $\sum_l \eta_l = 1$, nominally $\eta_l = 1/L$. The overall normalization condition changes to:

$$\sum_{l=1}^{L}\sum_{K}^{k=1} P_l(\phi_{lk}(\vec{r})) = 1 \tag{3.22}$$

and the expected photon count on pixel j changes to:

$$\mu_j^{lk} = NP_l(\vec{r}_0)E(\vec{r}_j - \vec{r}_0) + \eta_l b/K \tag{3.23}$$

where the relative intensity also affects the background (that should scale with illumination intensity too).

Image formation model

The mixed shot-noise and readout noise log-likelihood [1] is:

$$\log L = \sum_{l=1}^{L}\sum_{k=1}^{K}\sum_{j=1}^{M}\Big((n_j^{lk})\log(\mu_j^{lk}) - (\mu_j^{lk} + \sigma_{rn}^2) - \Gamma(n_j^{lk} + \sigma_{rn}^2 + 1)\Big) \tag{3.24}$$

with n_j^{lk} the actual detected photon count on pixel j for image lk, where σ_{rn} is the root mean square (rms) readout noise, where $\Gamma(x) = \int\int_0^\infty dt t^{x-1}\exp(-x)$ is the Gamma-function, and where the sum is over the M pixels of the ROI. In the numerical implementation of the MLE problem the parameters $\theta = [x_0, y_0, N, b]$ are estimated. This is done using the Levenberg-Marquardt routine based on the derivatives of the log-likelihood:

$$\frac{\partial \log L}{\partial \theta_r}\sum_{l=1}^{L}\sum_{k=1}^{K}\sum_{j=1}^{M}\left(\frac{n_j^{lk} - \mu_j^{lk}}{\mu_j^{lk} + \sigma_{rn}^2}\right)\frac{\mu_j^{lk}}{\partial\theta_r} \tag{3.25}$$

The relevant derivatives of the expected photon count on pixel j for image lk are:

$$\frac{\partial \mu_j^{lk}}{\partial x_0} = NP_l(\phi_{lk}(\vec{r}_0))\frac{\partial E(\vec{r}_j - \vec{r}_0)}{\partial x_0} + N\frac{\partial P_l(\phi_{lk}(\vec{r}_0))}{\partial x_0}E(\vec{r}_j - \vec{r}_0) \tag{3.26a}$$

$$\frac{\partial \mu_j^{lk}}{\partial y_0} = NP_l(\phi_{lk}(\vec{r}_0))\frac{\partial E(\vec{r}_j - \vec{r}_0)}{\partial y_0} + N\frac{\partial P_l(\phi_{lk}(\vec{r}_0))}{\partial y_0}E(\vec{r}_j - \vec{r}_0) \tag{3.26b}$$

$$\frac{\partial \mu_j^{lk}}{\partial \sigma} = NP_l(\phi_{lk}(\vec{r}_0))\frac{\partial E(\vec{r}_j - \vec{r}_0)}{\partial \sigma_0} \tag{3.26c}$$

$$\frac{\partial \mu_j^{lk}}{\partial N} = P_l(\phi_{lk}(\vec{r}_0))E(\vec{r}_j - \vec{r}_0) \tag{3.26d}$$

$$\frac{\partial \mu_j^{lk}}{\partial b} = \eta_l \tag{3.26e}$$

$$\tag{3.26f}$$

The derivatives of the Gaussian PSF term $E(\vec{r}_j - \vec{r}_0)$ are as in Smith et al. [2]. The derivatives of the illumination pattern factor $P(\phi_{lk}(\vec{r}_0)$ are:

$$\frac{\partial P_l(\phi_{lk}(\vec{r}_0))}{\partial x_0} = -\frac{2\pi q_{l,x}\eta_l m_l}{K}\sin(\phi_{lk}(\vec{r}_0)) \tag{3.27}$$

and similarly for the derivative with respect to y_0. The Fisher-matrix can be computed according to:

$$F_{rs} = \sum_{l=1}^{L}\sum_{k=1}^{K}\sum_{j=1}^{M}\frac{1}{\mu_j^{lk} + \sigma_{rn}^2}\frac{\partial \mu_j^{lk}}{\partial \theta_r}\frac{\partial \mu_j^{lk}}{\partial \theta_s} \tag{3.28}$$

The CRLB follows from the diagonal of the inverse of the Fisher-matrix. The impact of the very small readout noise of sCMOS cameras (typically $\sigma_{rn} \approx 1e$) is neglected in the further analysis.

Analytical approximation Fisher-matrix and CRLB

In order to make a theoretical assessment of the expected gain in localization precision we will develop an analytical approximation to the Fisher-matrix and CRLB. This can be done for the case of zero background, if we ignore the non-zero pixel size, and if we neglect the finite support of the Region Of Interest (ROI). The relevant Fisher matrix elements can be written as:

$$F_{x_0x_0} = \sum_{l=1}^{L}\sum_{k=1}^{K}\sum_{j=1}^{M}\mu_j^{lk}\left(\frac{\partial \log \mu_j^{lk}}{\partial x_0}\right)^2 \tag{3.29a}$$

$$F_{x_0y_0} = \sum_{l=1}^{L}\sum_{k=1}^{K}\sum_{j=1}^{M}\mu_j^{lk}\left(\frac{\partial \log \mu_j^{lk}}{\partial x_0}\right)\left(\frac{\partial \log \mu_j^{lk}}{\partial y_0}\right) \tag{3.29b}$$

$$F_{y_0y_0} = \sum_{l=1}^{L}\sum_{k=1}^{K}\sum_{j=1}^{M}\mu_j^{lk}\left(\frac{\partial \log \mu_j^{lk}}{\partial y_0}\right)^2 \tag{3.29c}$$

For the case with zero background and ignoring the non-zero pixel size and the direction dependence of the illumination intensity and modulation we have:

$$\frac{\partial \log \mu_j^{lk}}{\partial \vec{r}_0} = \frac{\vec{r}_j - \vec{r}_0}{\sigma} + \frac{1}{P(\phi_{lk}(\vec{r}_0))}\frac{\partial P(\phi_{lk}(\vec{r}_0))}{\partial \vec{r}_0} \tag{3.29d}$$

Approximating the summation over the pixels of the ROI with an integration over the entire 2D image plane results in:

$$F_{x_0x_0} \approx \frac{N}{\sigma^2} + \frac{4\pi^2 N}{L} \sum_{l=1}^{L} q_{lx}^2 Q(\xi_l(\vec{r}_0)) \tag{3.30a}$$

$$F_{x_0y_0} \approx \frac{4\pi^2 N}{L} \sum_{l=1}^{L} q_{lx} q_{ly} Q(\xi_l(\vec{r}_0)) \tag{3.30b}$$

$$F_{y_0x_0} \approx \frac{N}{\sigma^2} + \frac{4\pi^2 N}{L} \sum_{l=1}^{L} q_{ly}^2 Q(\xi_l(\vec{r}_0)) \tag{3.30c}$$

Here the function $Q(\xi_l(\vec{r}_0))$ is defined by:

$$Q(\xi_l(\vec{r}_0)) = \frac{m^2}{K} \sum \frac{\sin(\phi_{lk}(\vec{r}_0))^2}{1 + m\cos(\phi_{lk}(\vec{r}_0))} \tag{3.31}$$

Localization precision with perfect modulation

In case of perfect modulation $m = 1$, the function $Q(\xi_l(\vec{r}_0))$ simplifies to:

$$Q(\xi_l(\vec{r}_0)) = \frac{1}{K} \sum_{k=1}^{K} \sin(\phi_{lk}(\vec{r}_0)/2)^2 = \frac{1}{2} \tag{3.32}$$

and is thus independent of position $\vec{r}_0$ and orientation l. For $L \geq 2$ (at least 2 orientations) we find:

$$\sum_{l=1}^{L} = \frac{1}{p^2} \sum^{L} \cos\beta_l^2 = \frac{L}{2p^2} \tag{3.33a}$$

$$\sum_{l=1}^{L} = \frac{1}{p^2} \sum^{L} \cos\beta_l \sin\beta_l = 0 \tag{3.33b}$$

$$\sum_{l=1}^{L} = \frac{1}{p^2} \sum^{L} \sin\beta_l^2 = \frac{L}{2p^2} \tag{3.33c}$$

independent of the overall angle offset β_0. Substituting Equations 26 and 27 in Equations 24 results in the two diagonal Fisher-matrix elements being non-zero and equal to:

$$F_{x_0x_0} = F_{y_0y_0} = \frac{N}{\sigma^2} + \frac{2\pi^2 N}{p^2} \tag{3.34}$$

This gives an isotropic localization uncertainty:

$$\Delta x_0 = \Delta y_0 = \frac{\sigma}{\sqrt{N}\sqrt{1 + 2\pi^2\sigma^2/p^2}} \tag{3.35}$$

which improves over SMLM with a factor of around 2 depending on the pattern pitch p in relation to the spot width σ.

Localization precision with imperfect modulation

In case $m < 1$ the precision will become worse. Moreover, there will be a (slight) dependence on the global phase $\xi_l(\vec{r}_0)$ defined in Equation 10. This will make the localization precision non-uniform and anisotropic to some degree.

In order to analyse these results we will assume, for the sake of simplicity, that the illumination patterns are oriented along the the x-axis and y-axis. Following the same steps as above we then find that:

$$x_0 = \frac{\sigma}{\sqrt{N}\sqrt{1 + 2\pi^2 Q\left(\frac{2\pi x_0}{p} - \chi_1\right)\sigma^2/p^2}} \tag{3.36a}$$

$$y_0 = \frac{\sigma}{\sqrt{N}\sqrt{1 + 2\pi^2 Q\left(\frac{2\pi y_0}{p} - \chi_1\right)\sigma^2/p^2}} \tag{3.36b}$$

The average behaviour can be deduced by replacing the summation over the K phase steps in Equation 25 by an integral over all phases:

$$Q(\xi_l(\vec{r}_0)) \approx \frac{m^2}{2\pi}\int_0^{2\pi} d\phi \frac{\sin\phi^2}{1 + m\cos\phi} = \frac{m^2}{1 + \sqrt{1 - m^2}} = F(m) \tag{3.37}$$

Supplementary Figure 3.10 shows the effect of the dependence of the localization precision on the global phase. The worst case happens when one of the phases $\phi_{lk}(\vec{r}_0)$ (emitter at minimum of illumination pattern for one of the frames). In case of an ideal modulation contrast $m = 1$ this is a perfectly dark fringe and this helps significantly to decrease the CRLB. In case of a non-ideal modulation contrast $m < 1$ there is no added value. For example, the improvement in CRLB for $m = 0.95$ and $K = 3$ phase steps can vary between 1.6 and 2.3, with an average of 2.1 (taking a pitch to spot width ratio $p/\sigma = 2$). These variations decrease when the number of phase steps is increased, making the method more robust. For example, for $m = 0.95$ and $K = 4$, the improvement factor varies between 1.8 and 2.2, for $m = 0.95$ and $K = 5$, the improvement factor merely varies between 1.9 and 2.2. In practice, these variations are further mitigated by the non-zero background.

Localization precision with reduced scan range

The current results can be generalized by changing the translation range of pattern shifting from the pattern pitch p to a smaller range R, similar as in MINFLUX. So, we take pattern phases:

$$\psi_{lk} = 2\pi(k-1)R/Kp + \chi_l \tag{3.38}$$

In order to enforce the normalisation condition Equation 1 (keeping the parameter N the number of detected photons) we must normalize the patterns with a factor:

$$G(\xi_l(\vec{r}_0)) = \frac{1}{K}\sum_{k=1}^{K}(1 + m\cos(\phi_{lk}(\vec{r}_0))) = 1 + m'\cos\left(\xi_l(\vec{r}_0) - \frac{\pi(K-1)R}{Kp}\right) \tag{3.39}$$

with

$$m' = \frac{m}{K}\frac{\sin(\pi R/p)}{\pi R/Kp} \tag{3.40}$$

This normalization factor reaches a minimum when:

$$\xi(\xi_l(\vec{r}_0)) = \frac{2\pi}{p}\left(\frac{p}{2} + \left(\frac{K-1}{K2}\right)R\right) \tag{3.41}$$

which implies that half way the scan the illumination pattern intensity minimum coincides with the molecule. The expected photon count on pixel j is:

$$\mu_j^{lk} = N\frac{P(\phi_{lk}(\vec{r}_0))}{G(\xi_l(\vec{r}_0))}h(\vec{r}_j - \vec{r}_0) \tag{3.42}$$

Taking the same steps as in the previous derivation results in a function $Q(\xi_l(\vec{r}_0))$ that is rather involved:

$$Q(\xi_l(\vec{r}_0)) = \frac{1}{1 + m'\cos\left(\xi_l(\vec{r}_0) - \frac{\pi(K-1)R}{Kp}\right)}\times \tag{3.43}$$

$$\frac{1}{K}\sum_{k=1}^{K}(1 + m\cos(\phi_{lk}(\vec{r}_0)))\left[\frac{m\sin(\phi_{lk}(\vec{r}_0))}{1 + m\cos(\phi_{lk}(\vec{r}_0))} - \frac{m'\sin(\xi_l(\vec{r}_0) - \frac{\pi(K-1)R}{Kp})}{1 + m'\cos(\xi_l(\vec{r}_0)) - \frac{\pi(K-1)R}{Kp}}\right]^2$$

and a localization precision still given by Equations 23. For the limiting case $R << p$ and perfect modulation $m = 1$ the function $Q(\xi(\vec{r}_0))$ is sharply peaked around the value $\xi_l(\vec{r}_0) = \pi$, indicating that a small scan range, centred around the intensity minimum, results in a small localization precision, as in MINFLUX. At points in the FOV close to the crossing points between the intensity minimum lines of the patterns oriented along the x-axis and y-axis there will be a large improvement in precision, given that a constant photon count N per localization event can be achieved. Supplementary Figure 3.6 shows that for a perfect modulation (and zero background) an in principle unlimited improvement over SMLM can be achieved by reducing R, in agreement with Balzarotti et al. [3]. For an imperfect modulation, however, this is not the case. The improvement factor can reach values up to about 10, and has dips for global phase values corresponding to the molecule being at the minimum of one of the illumination patterns, similar to the case of a full scan range

It is mentioned that this type of precision improvement (for a reduced phase scan range) can only be achieved for STORM type of photo-switching, where the typical

number of photons per on-event is molecule specific and intensity independent, as the lower intensity near the illumination pattern minimum will reduce the number of photons per unit time, but at the same time make the molecular on-time longer. The major drawback in this case is that the longer on-time makes the on-off ratio unfavourable, more molecules per unit area will be in the on-state at any given moment in time. For PAINT type of photo-switching the on-off transition is diffusion driven, implying that the gain in localization precision per detected photon is cancelled by a reduction in the number of detected photons per on-event.

Extension to 3D-localization

The reported experiments were done with a TIRF setup, a low background 2D imaging mode. Imaging deeper into a cellular sample would require a change to a HILO-type of illumination with an increased background. This will deteriorate the performance, but the localization precision relative to the zero background case is the same as for conventional SMLM (see Supplementary Figure 3). In this way 2D slices of a 3D sample with around twofold improved in-plane localization precision can be generated.

Improvement in localization precision in 3D single-molecule localization can be realized in a number of ways. The imaging light path can be modified to incorporate the astigmatic [4], bifocal [5], multi-focal [6], double-helix [7], tetrapod [8], or any other method for 3D-localization that relies on modifying the imaging PSF. It can be expected that SIMFLUX is fully compatible with any of these methods, so that the lateral localization precision can still be improved compared to conventional SMLM, while keeping the axial localization precision at a comparable performance.

More exciting are extensions that offer the potential for improvement in localization precision in all spatial directions. This would require illumination patterns that not only depend on the lateral coordinates but also on the axial coordinate. The most straightforward way to do this is to alternate between periodic illumination patterns in the x, y, and z- directions. This results in a minimum of 9 distinct patterns, as at least three phase steps are needed per pattern orientation. The pitch of the interference pattern arising from counter propagating plane waves along the optical (z) axis is $\lambda/(2n)$, leading to a precision in the absence of background equal to:

$$\Delta z_0 = \frac{\sqrt{3}\lambda}{4\pi n\sqrt{N}} \tag{3.44}$$

where the factor $\sqrt{3}$ occurs due to the division of photons over the three independent pattern directions. The lateral precision in the absence of background changes to:

$$\Delta x_0 = \delta y_0 = \frac{\sigma}{\sqrt{N}\sqrt{1 + 4\pi^2\sigma^2/3p^2}} \tag{3.45}$$

because of the same division of photons over the three independent pattern directions. An interesting choice would be to use only the illumination pattern in the z-direction and rely on standard camera based localization in the lateral directions. This would

reduce the required number of images to just 3, and improve the axial precision to:

$$\Delta z_0 = \frac{\lambda}{4\pi n\sqrt{N}} \tag{3.46}$$

which is on par with interferometric axial localization [9]. In this way the axial localization precision can be improved over 3D techniques that rely on detecting spot shape, without compromising the lateral localization precision of standard 2D-localization. Of course, this comes at the expense of having to build and operate a 4π-setup.

Restricting the attention to more standard epi-illumination setups suggests the use of three-beam interference for creating a woodpile shaped illumination pattern, just as in 3D-SIM. The three beams travel along the optical axis and at angles $\pm\alpha$ with the optical axis, and have a lateral pattern pitch $p = \lambda_{ex}/n \sin\alpha$, and an axial pattern pitch $p_{ax} = \lambda_{ex}/n(1-\cos\alpha)$, with λ_{ex} the excitation wavelength and n the medium refractive index. The illumination pattern as a function of lateral pattern phase ϕ and axial pattern phase θ is now:

$$P(\phi,\theta) = a\left[1 + m_1 \cos\theta \cos\phi + m_2 \cos(2\phi)\right] \tag{3.47}$$

with the first and second order modulations m_1 and m_2, and where a is a normalization constant. The lateral pattern phase takes values $\phi_{lk}(\vec{r})$ as a function of lateral position $\vec{r} + (x, y)$ as defined in Equation 2 for $k = 1, 2, ..., K$ lateral pattern phases and $l = 1, 2, ..., L$ pattern orientations, and where the lateral spatial frequencies have magnitude $|\vec{q}_l| = 1/p$. The axial pattern phase takes values:

$$\delta_s = 2\pi(s-1)/S + \epsilon \tag{3.48}$$

with ϵ a constant phase offset, is sufficient for that purpose. The normalization condition Equation 3.8 now becomes:

$$\sum_{s=1}^{S}\sum_{l=1}^{L}\sum_{k=1}^{K} P(\phi_{lk}(\vec{r}), \theta_s(\vec{r})) = 1 \tag{3.49}$$

and the normalization constant should then be $a = 1/(LKS)$. The number of axial phase steps must be $S \geq 3$, as the axial dependence only contains a single harmonic. The requirements on lateral and axial phase steps implies a total $L \times K \times S$ of at least 18 illumination patterns are needed during the time of a typical molecular on-event, an impractically large number. We speculate that the number of phase steps that is required can be substantially reduced by phase shifting in the lateral and axial direction simultaneously. The displacement of the illumination pattern would then be in a single diagonal direction compared to the lateral and axial directions of the woodpile shaped illumination pattern. This could be feasible with $\tilde{\text{k}}$Hz framerate cameras and illumination pattern generators. High camera frame rates are attainable for current sCMOS cameras if a limited set of lines is read out per frame, ferroelectric LCOS devices could enable fast pattern switching. The multi-focus microscope [6] has been shown to be compatible with

single-molecule imaging, and the extension to 3D-SIM has already been demonstrated [10]. This proven platform is possibly a promising route for exploring 3D SIMFLUX configurations in an epi-illumination setting.

3.A.2 Supplementary figures

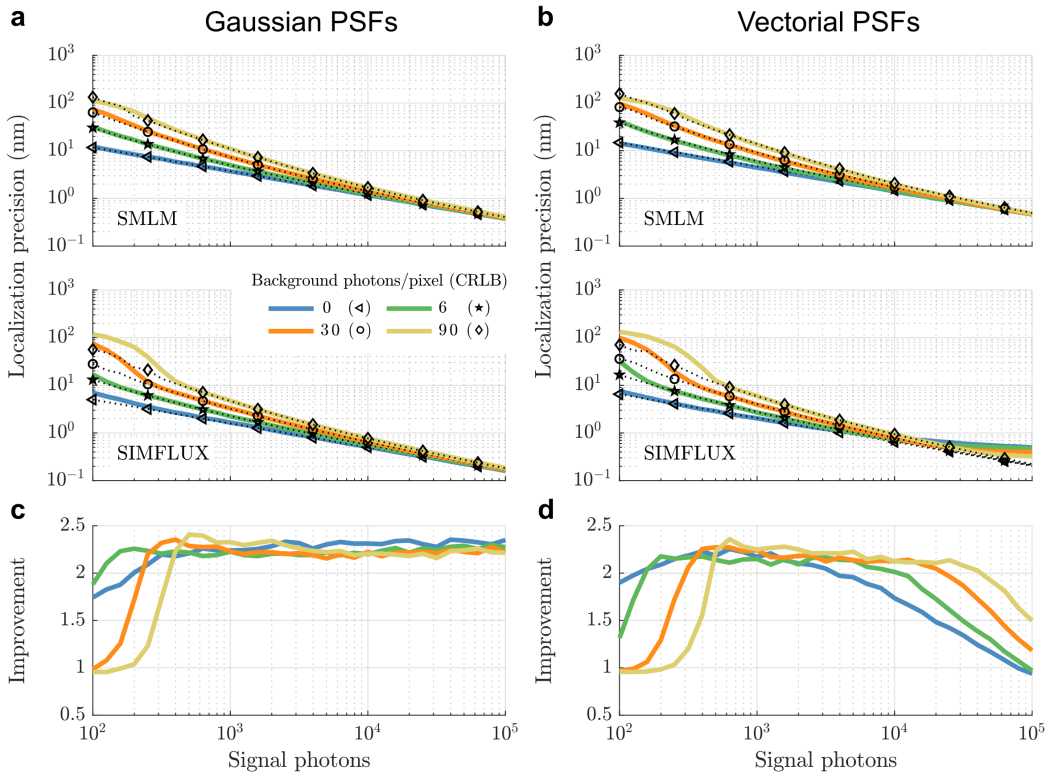

Fig. 3.4: Impact of signal photon count on the localization precision of SIMFLUX in comparison to standard SMLM for different background levels. (a-b) Average lateral localization precision of SMLM and SIMFLUX fits using a Gaussian PSF model on ground truth data simulated with (a) Gaussian PSF (spot width $\sigma_{\mathrm{PSF}} = \lambda/(4\mathrm{NA})$) and (b) vectorial PSF (see Methods), as a function of signal photon count for different background levels. The performance (full, coloured lines) is at the CRLB (black dashed lines and data symbols) except for SIMFLUX Gaussian PSF fitting on vectorial PSF ground truth simulations with very high signal-to-background-ratio (SBR), indicating a sensitivity to PSF model mismatch there. (c-d) Improvement factor of SIMFLUX localization precision over SMLM localization precision ($= \Delta x_{\mathrm{SMLM}}/\Delta x_{\mathrm{SIMFLUX}}$) for fitting with a Gaussian PSF model on ground truth data simulated with (c) Gaussian PSF and (d) vectorial PSF. Gaussian PSF fitting works reliably for realistic signal photon counts (up to about 10^4), with a need for more sophisticated PSF models only arising for extremely bright emitters. Simulation parameters as described in Methods.

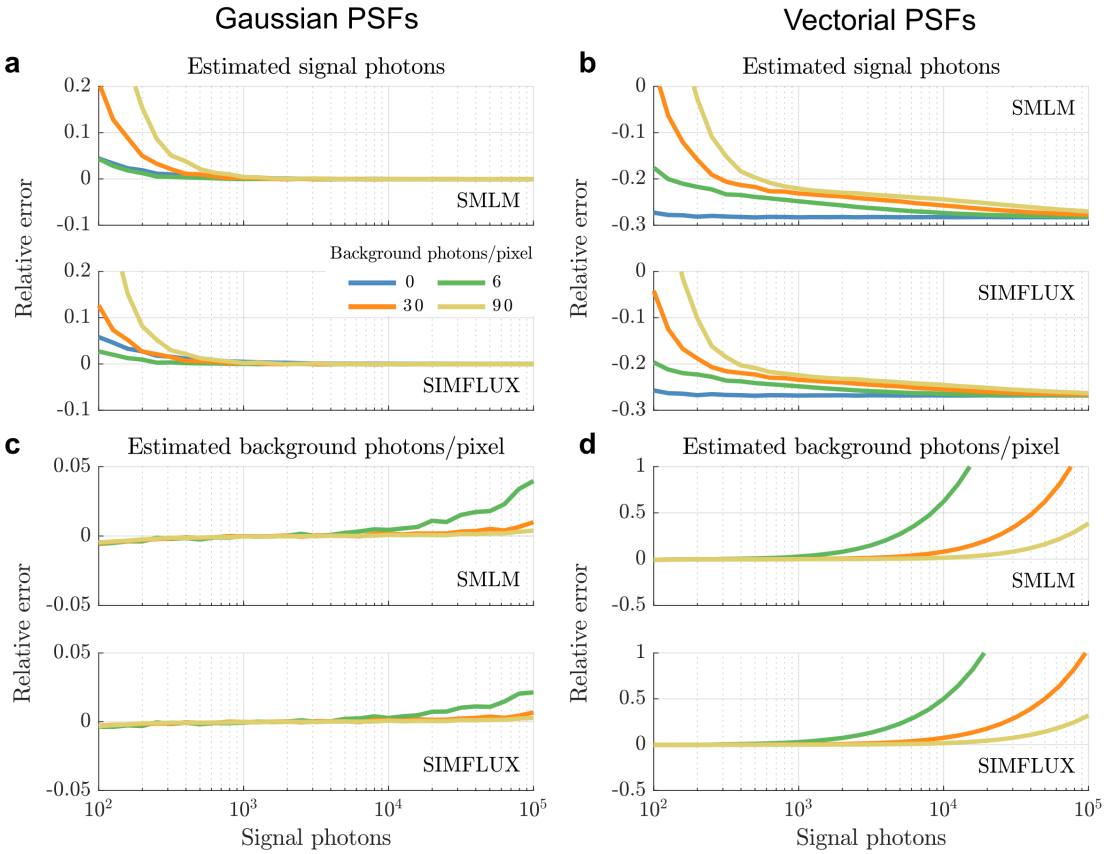

Fig. 3.5: Impact of signal photon count on the photon count estimation of SIMFLUX in comparison to standard SMLM. (a-b) Relative error of the estimated signal photon count of SMLM and SIMFLUX fitting with a Gaussian PSF on ground truth simulated with (a) Gaussian (spot width $\sigma_{\mathrm{PSF}} = \lambda/(4\mathrm{NA})$) and (b) vectorial PSFs (see Methods) as a function of signal photon count for different background levels. showing a perfect fit for Gaussian PSF fitting on Gaussian PSFs and a 30% underestimation for a correct PSF model. (c-d) Similarly; relative error of the estimated background photons per pixel, indicating an overestimation for high signal-to-background ratio. The erroneous signal photon count estimation has an impact of the localization precision of SIMFLUX at high SBR, as shown in Supplementary Figure 1. Simulation parameters as in Methods.

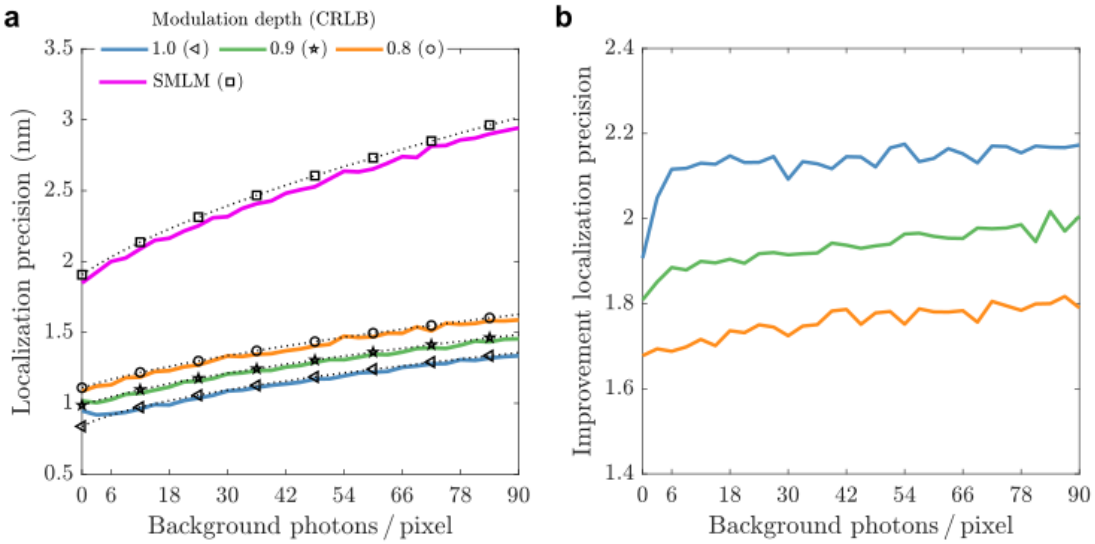

Fig. 3.6: Impact of background photon count on localization precision of SIMFLUX in comparison to standard SMLM. (a) Average lateral localization precision of SMLM and SIMFLUX fitting with a Gaussian PSF model on vectorial PSF generated ground truth data as a function of background photons per pixel for three modulation depths. The performance is at the CRLB in the range of realistic background levels for the considered modulation depths. (b) Improvement of SIMFLUX over SMLM localization precision, showing a small impact of background on the improvement factor. The same relative impact of background on precision as in standard SMLM implies that SIMFLUX can be used under the same experimental conditions as SMLM.

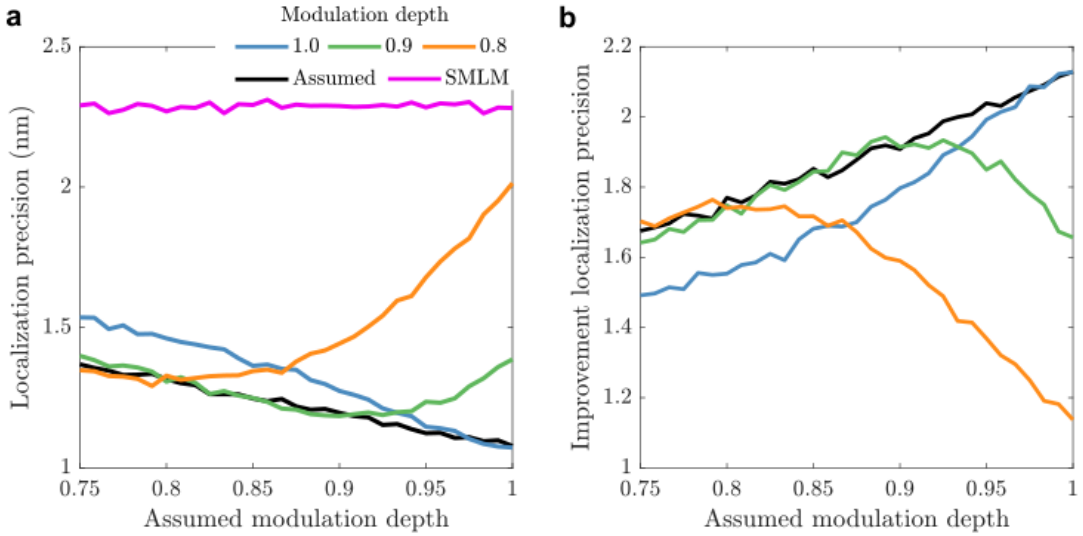

Fig. 3.7: Assessment of illumination pattern modulation estimation on localization precision in SIMFLUX. (a) Average lateral localization precision in SIMFLUX as a function of an (incorrectly) assumed modulation depth in the SIMFLUX fit routine for different actual values of the modulation. For comparison the localization precision for SMLM on the summed simulation frames is plotted. Spots are simulated with 6000 signal photons and 30 background photons per pixel. (b) Improvement in SIMFLUX localization precision over SMLM localization precision as a function of an assumed modulation depth in the SIMFLUX fit routine for different actual values of the modulation, indicating that the modulation depth must be above about 0.9 for a 2× improvement and must be known with a precision of about 0.05 for optimum fit results from comparing the green and black lines around 0.9.

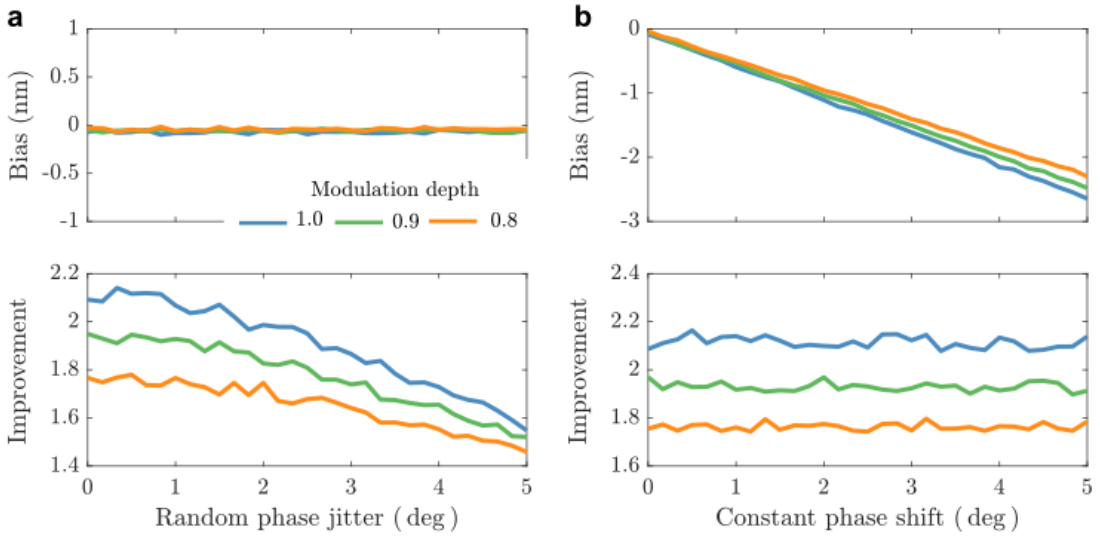

Fig. 3.8: Impact of illumination pattern phase errors on localization precision and bias of SIMFLUX. (a) Average lateral localization bias of SIMFLUX and localization precision of SIMFLUX over standard SMLM for three modulation depths as a function of the standard deviation of random illumination pattern phase jitter, modelled by a Gaussian distribution. (b) Similarly; for a constant phase shift due to a potential bias in the phase estimation. The plots indicate a tolerable phase jitter of about 2 deg.

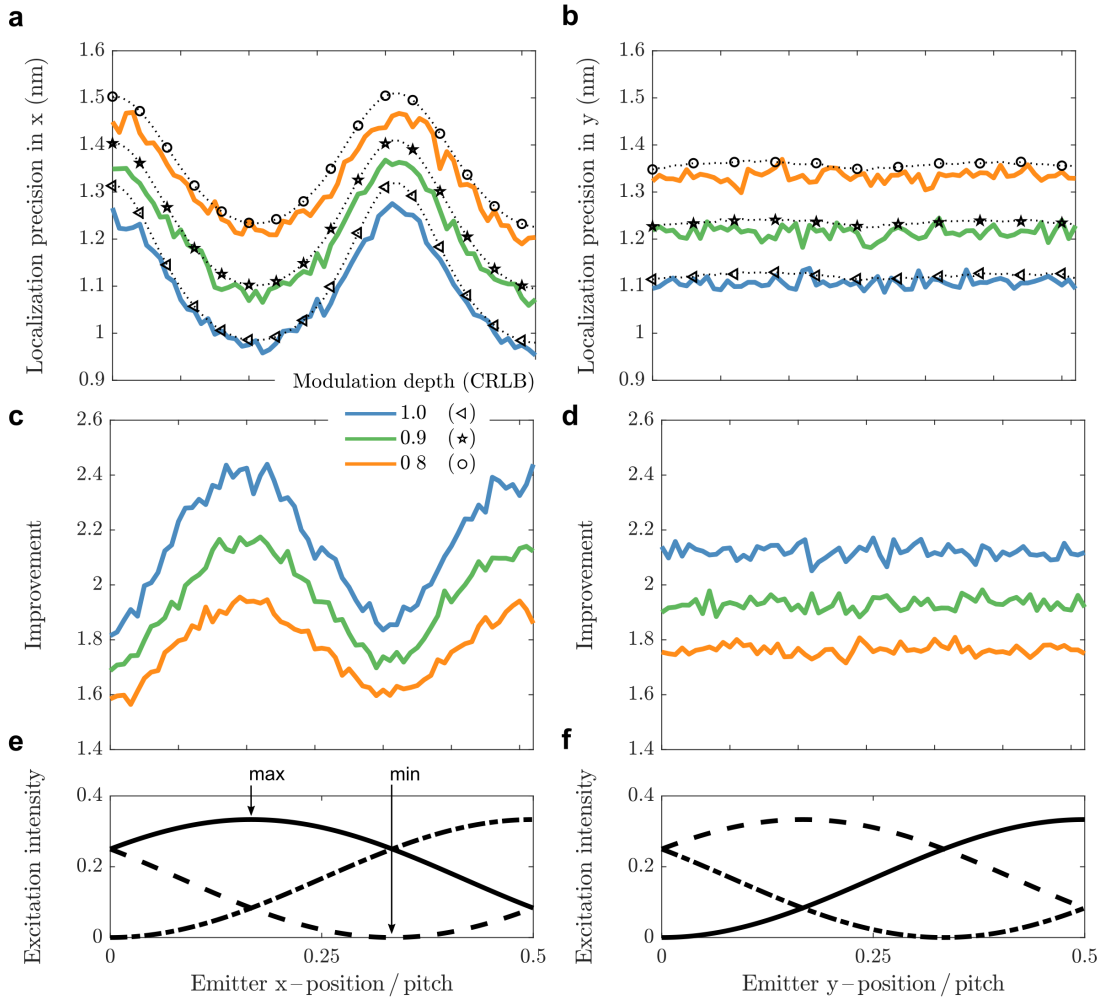

Fig. 3.9: Impact of emitter position in the global phase pattern on localization precision in SIMFLUX. Simulated emitters with ground truth (a) x-positions fixed in the excitation pattern and (b) y-positions randomized in the excitation pattern over half the pitch. (a-b) SIMFLUX localization precision for different modulation depths as a function emitter position in the excitation pattern; the performance is at the CRLB. (c-d) Improvement of SIMFLUX over SMLM localization precision. (e-f) Normalized excitation patterns for perfect modulation in the (e) x-direction in which the x-coordinates are fixed and (f) y-direction where the y-coordinates are randomly distributed. The plots show the position dependent localization precision of SIMFLUX within the global phase pattern and the average localization precision. The best precision is achieved for an emitter position at the center of the illumination pattern maximum and worst for emitters located in a minimum. This is in line with theory (Supplementary Note and Supplementary Fig. 7), and deviates from MINFLUX because of the imperfect modulation depth.

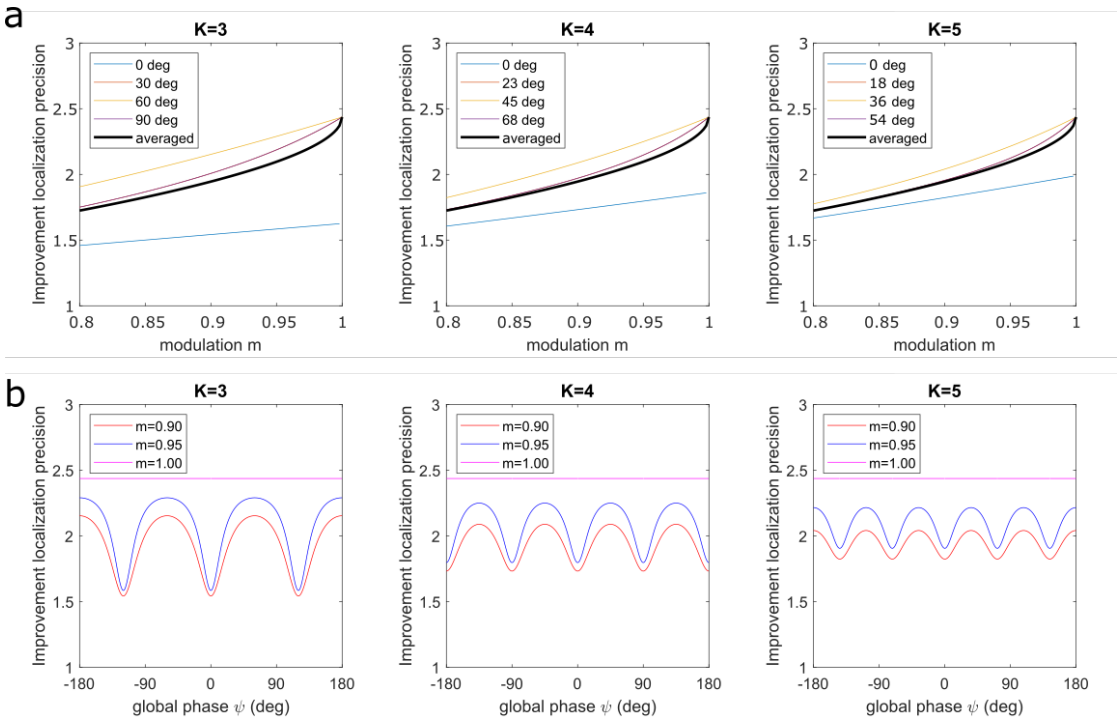

Fig. 3.10: Impact of modulation depth and global phase on zero-background CRLB of the localization precision. (a) The improvement in localization precision of SIMFLUX over standard SMLM for different numbers of phase steps K and global phase of the molecule (measure for the position of the molecule from the intensity minimum of one of the patterns), as a function of modulation depth m, as well as the global phase averaged improvement factor. (b) The improvement in localization precision of SIMFLUX over standard SMLM for different numbers of phase steps K and modulation as a function of global phase. The plots indicate a steep dependence on m close to m=1, in particular for the global phase where one of the images is acquired when the molecule is at the illumination pattern minimum. This agrees with the numerical simulations shown in Supplementary Fig. 6. The performance is worst for these cases in case the modulation is imperfect. For a larger number of phase steps, the variations in CRLB as a function of global phase strongly reduce, making the method more robust. In the computations we take a pitch to spot width ratio $p/\sigma = 2$.

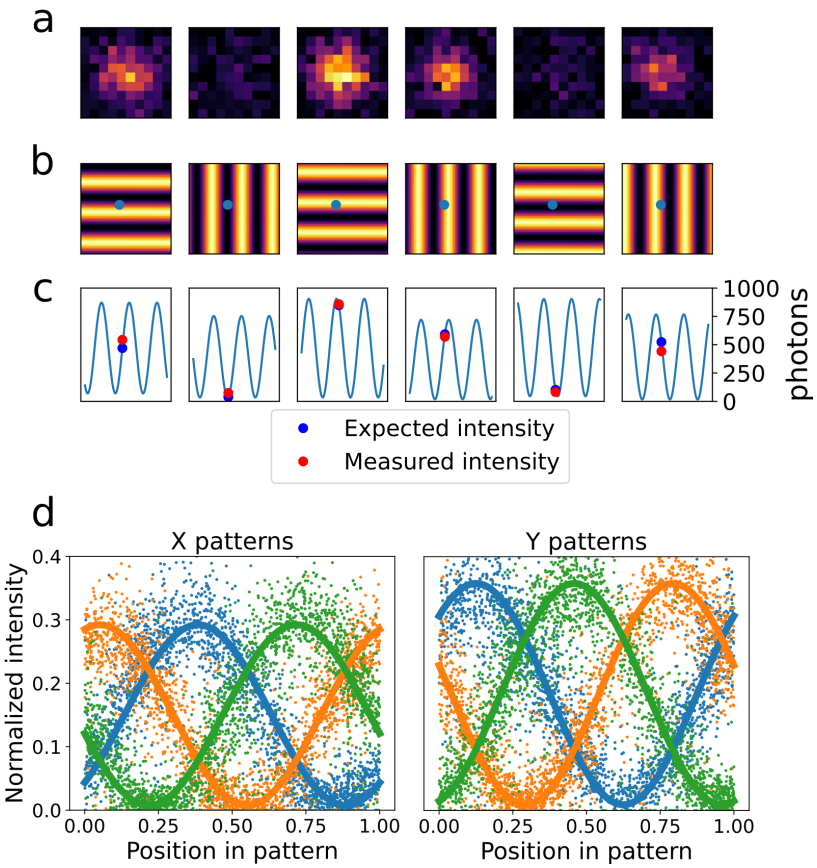

Fig. 3.11: ROI instance and illumination pattern retrieval. (a) Single-molecule image (11×11 pixels of size 65 nm) over 6 subsequent frames, with estimated signal photon counts, showing the frame-to-frame variation in emission intensity caused by the shifting and rotating illumination pattern. (b) Retrieved illumination pattern with position of the molecule with respect to the pattern indicated. (c) Expected and actual signal photon count, showing a good match, within the margins of shot noise induced variations. (d) Fit of the sinusoidal illumination pattern through the entire set of localizations. The point clouds show the estimated ratio of signal photon count to total photon count ("normalized intensity") over the K=3 phase steps per pattern orientation as a function of x and y-position mapped into a single period of the illumination pattern. The pattern phases are estimated with a precision equal to 0.64, 0.59, 0.68, 0.24, 0.55, and 0.41 deg (order pertaining to patterns as shown in second row), which we determine by splitting the entire dataset in 10 bins, repeating the phase estimation for the 10 bins, and computing the standard deviation over the estimated phases (normalized by $\sqrt{10}$).

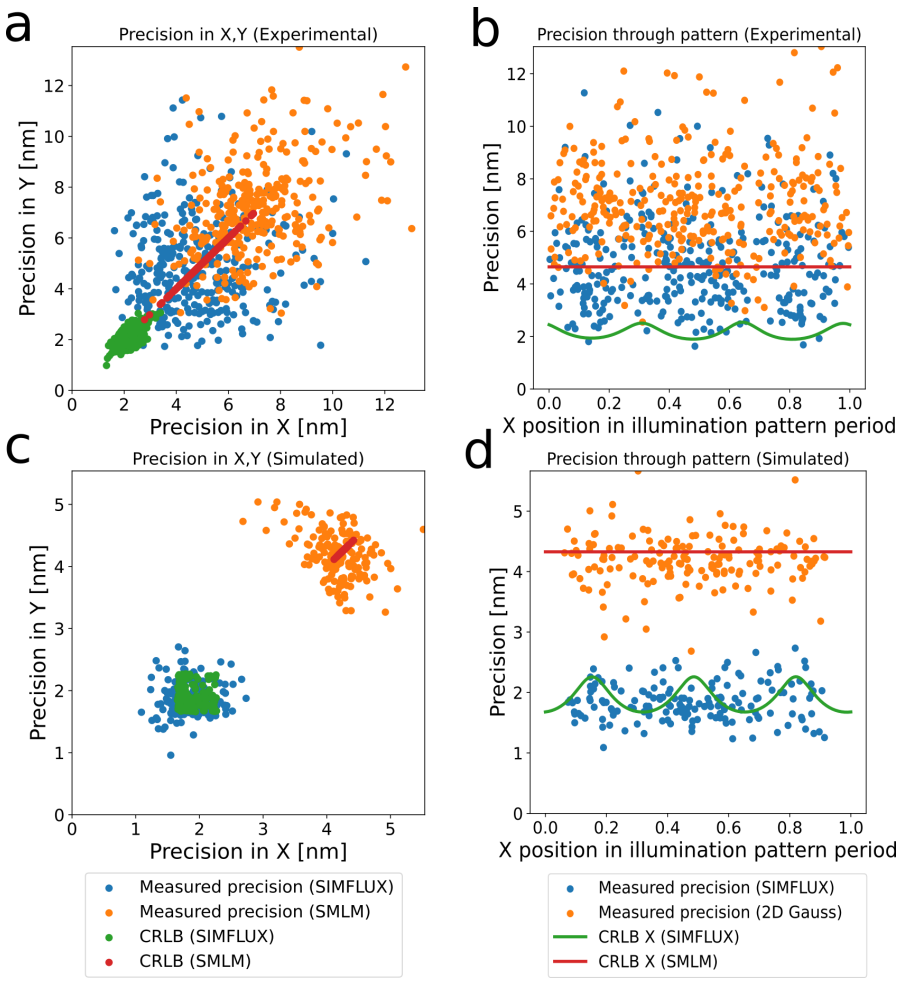

Fig. 3.12: Precision and CRLB as a function of global phase. (a) Measured precision in x and y for 424 analysed clusters of localizations for the 80 nm nanoruler dataset of Fig. 2, in comparison to the average CRLB over the localizations within each cluster. The clusters correspond to the binding sites of the nanorulers, the precision is quantified by the standard deviation of the set of localizations within each cluster. The total set of localizations has a median emitter intensity of 1175 photons, cumulative over the 6 frames, and a background of 10.7 photons/pixel, cumulative over the 6 frames. (b) Measured precision and CRLB as a function of the x-coordinate, where the x-values are mapped into a single period of the illumination pattern (the "global phase"). The median of the distribution of precision values is 4.8 nm for SIMFLUX and 7.3 nm for conventional SMLM, indicating an improvement factor of 1.5. The performance is not on par with the CRLB, probably due to a residual drift of around 4 nm over the full dataset. (c,d) Same as (a,b), for a simulated full-FOV dataset (signal photon count 1291, background/pixel 8.7), indicating a precision improvement factor of 2.2, and a performance on par with the CRLB.

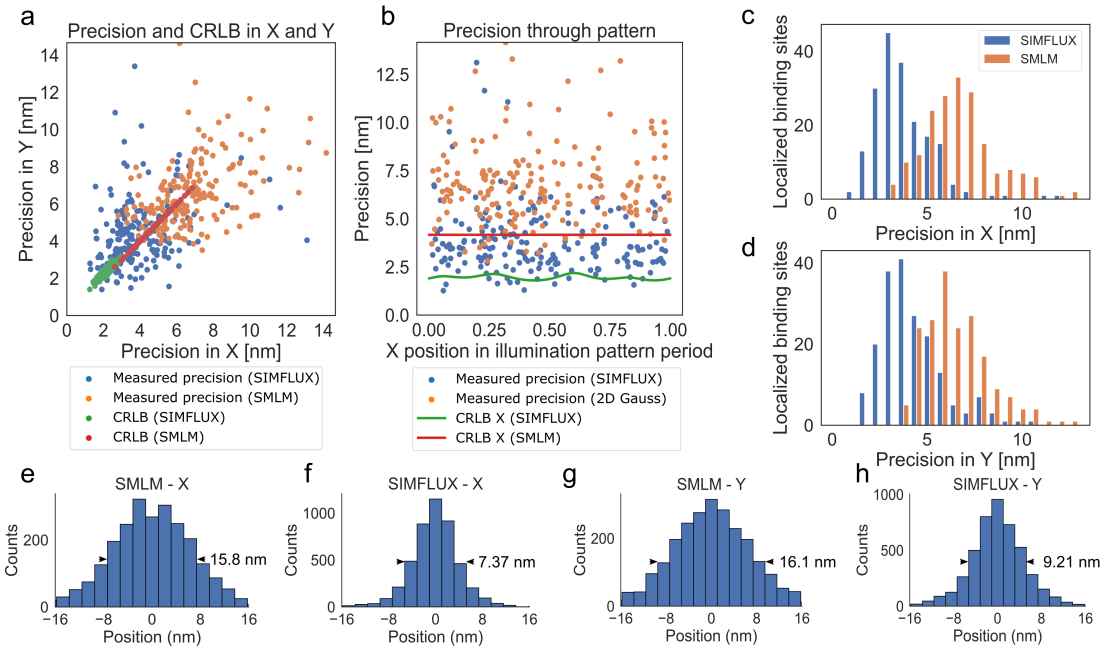

Fig. 3.13: Precision and CRLB for SIMFLUX on 80 nm nanorulers with K=4 phase steps. The data was acquired at 70 fps, the modulation error filter was set to 0.012, and the spot detection threshold at 6. (a) Measured precision in x and y for 279 analysed clusters of localizations, in comparison to the average CRLB over the localizations within each cluster. (b) Measured precision and CRLB as a function of the x-coordinate, where the x-values are mapped into a single period of the illumination pattern (the "global phase"). The total set of localizations has a median emitter intensity of 1551 photons, cumulative over the 8 frames, and a background of 14.5 photons/pixel, cumulative over the 8 frames. (c,d) Distribution of precision values, with median 4.1 nm for SIMFLUX and 6.6 nm for conventional SMLM (average over x and y), indicating an improvement factor of 1.5. (e-h) Histograms of the total set of localizations, with average FWHM equal to 16.0 nm (SMLM) and 9.9 nm (SIMFLUX), indicating an improvement factor of 1.6. Comparison to the similar plots for $K = 3$ phase steps in Supplementary Fig. 9 indicates a comparable precision and a somewhat larger improvement factor.

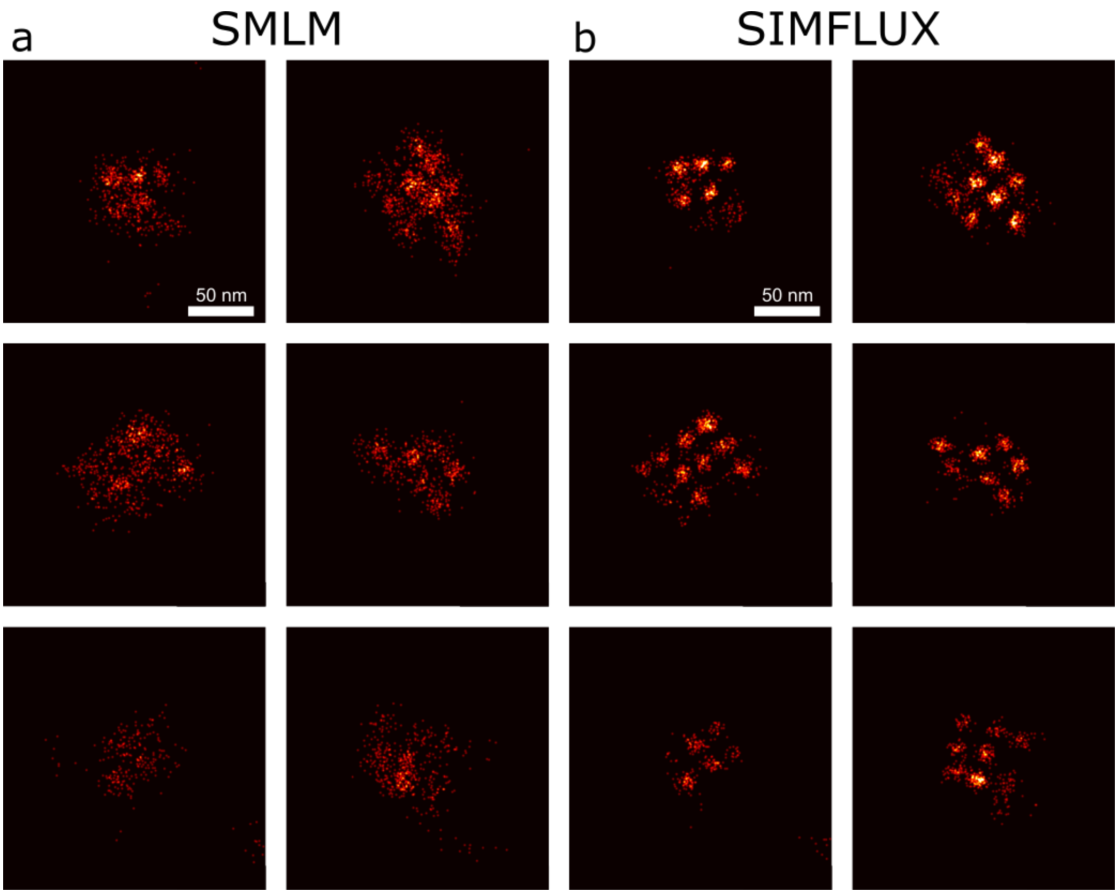

Fig. 3.14: Additional DNA-origami grid results. (a) Conventional SMLM and (b) SIMFLUX images of selected instances of the 20 nm DNA-origami grid structures. The SMLM and SIMFLUX images are based on the same image acquisitions. Imperfect labelling prevents all 4x3 binding sites to be visible. The grid structure is not resolved in SMLM, but clearly distinguishable in SIMFLUX. Two independent imaging experiments were done with similar outcome.

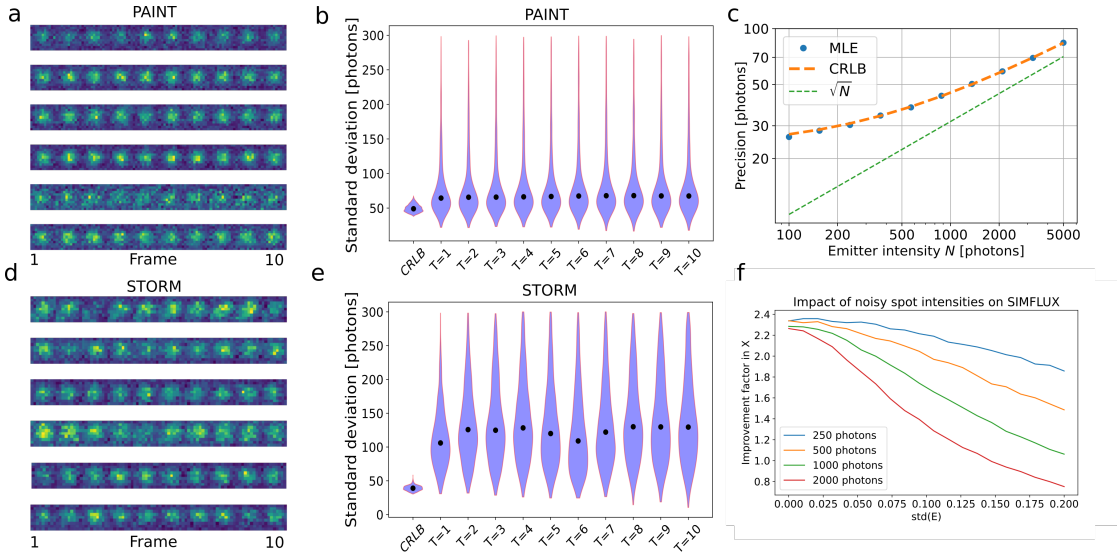

Fig. 3.15: Analysis of intensity variations during the fluorophore on-time for PAINT and STORM imaging. The analysis is based on measurements in which the excitation patterns were not shifted. Spots were selected that are on for at least 10 frames, have a fitted spot intensity of at least 200 photons in each frame, and have an average spot intensity between 500 and 2000 photons (PAINT) or between 300 and 800 photons (STORM), over all on-frames. The PSF sigma was fitted on the sum of all frames of the emitter, and spots with a PSF sigma < 1.7 or > 2 pixels were filtered out, which also filters out any ROIs with overlapping emitters. (a) Examples of the first 10 frames of 6 filtered emitters for PAINT imaging. To quantify variance in spot intensity on different timescales, we compute the 2-point unbiased variances of the spot intensities at frame t and t+T, and plot the means of these $(\frac{1}{L-T}\sum_t^{L-T}((N_t - N_{t+T})^2)/2$, where L is the number of frames for a spot, and N_t the spot intensity at time t) in the histogram ($n = 3586$, dots indicate the mean). The results for PAINT indicate an error level that is 27% above the expected CRLB, and increases slightly with time separation T (by less than 3%). (c) The CRLB of estimating spot intensities for a background noise of 8 photons/pixel (matching that of the DNA paint measurement), showing a CRLB that is not simply $\sqrt{N}$, but substantially higher. This is related to the photon count underestimation of Gaussian PSF fitting (the estimate $N < N_t rue$ while the actual shot noise is $\sqrt{N_{\text{true}}}$. This behaviour is known and explained before23. (d) Examples of the first 10 frames of 6 filtered emitters for STORM imaging. (e) Spot intensity variation as a function of duration T for STORM. The results indicate an error level that is 125% above the expected CRLB, and varies with time separation T by less than 12% ($n = 4534$, dots indicate the mean). (f) Simulation of the impact of intrinsic intensity noise on the improvement factor of SIMFLUX over SMLM. No repeated experiments were done.

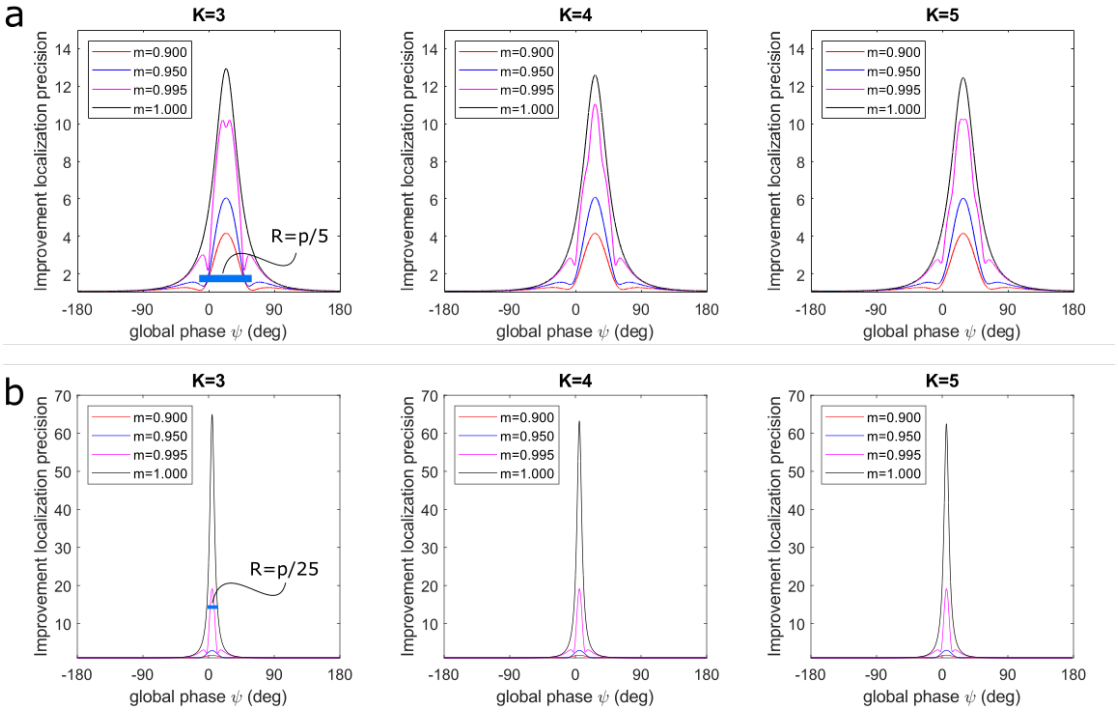

Fig. 3.16: Impact of global phase on zero-background CRLB of the localization precision for a reduced phase scan range. (a) Improvement in localization precision of SIMFLUX over standard SMLM as a function of global phase for four different modulation values for a scan range $R = p/5$, with p the pattern pitch. (b) Same for a scan range $R = p/25$. In the computations we take a pitch to spot width ratio $p/\sigma = 2$. The plots show a huge improvement factor when the molecule is placed within the range of positions where the illumination pattern minimum is scanned. Interestingly, close to the K illumination pattern minima the improvement factor experiences a dip. This is in line with the performance for the full scan range $R = p$, shown in Supplementary Figs. 6 and 7.

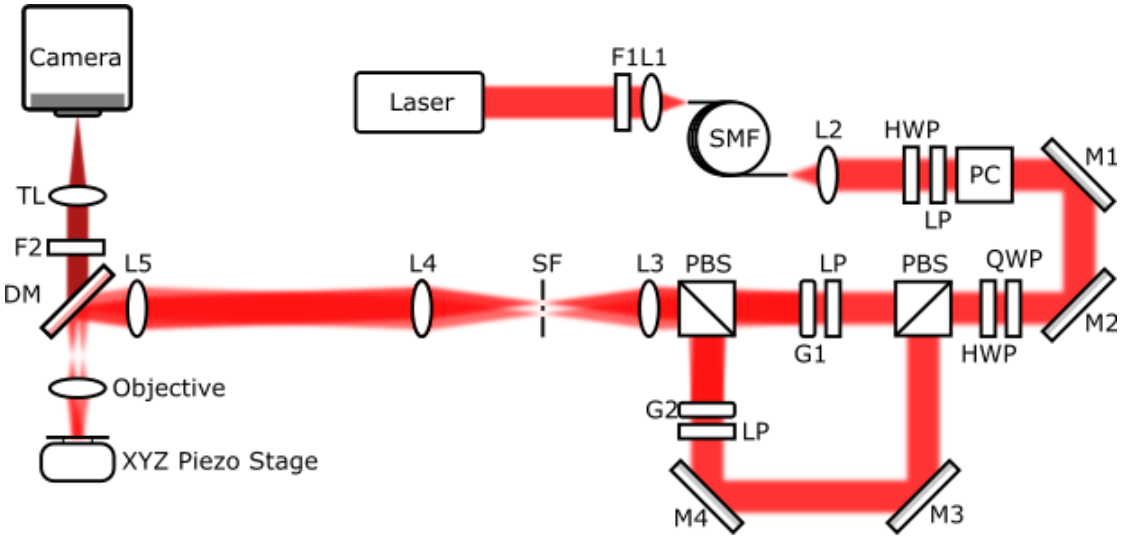

Fig. 3.17: SIMFLUX setup. Laser 640 nm, F1 excitation filter, L1 fiber coupling lens, SMF polarization maintaining single mode fiber, L2 fiber collimation lens, HWP zero order half wave plate 633 nm, QWP zero order quarter waveplate 633 nm, LP glan-laser linear polarizer, PC Pockels cell, M1-4 aluminium steering mirrors, PBS polarizing beam splitter, G1,2 binary phase gratings mounted on piezo stages, L3 75 mm relay lens, SF spatial filter, L4 350 mm relay lens, L5 180 mm relay lens, Objective 1.49 NA TIRF, XYZ Piezo Stage 100x100x100 nm travel range piezo stage, DM dichroic long pass mirror, F2 emission filter, TL tube lens, Camera sCMOS Hamamatsu Orca Flash 4.0 V2.

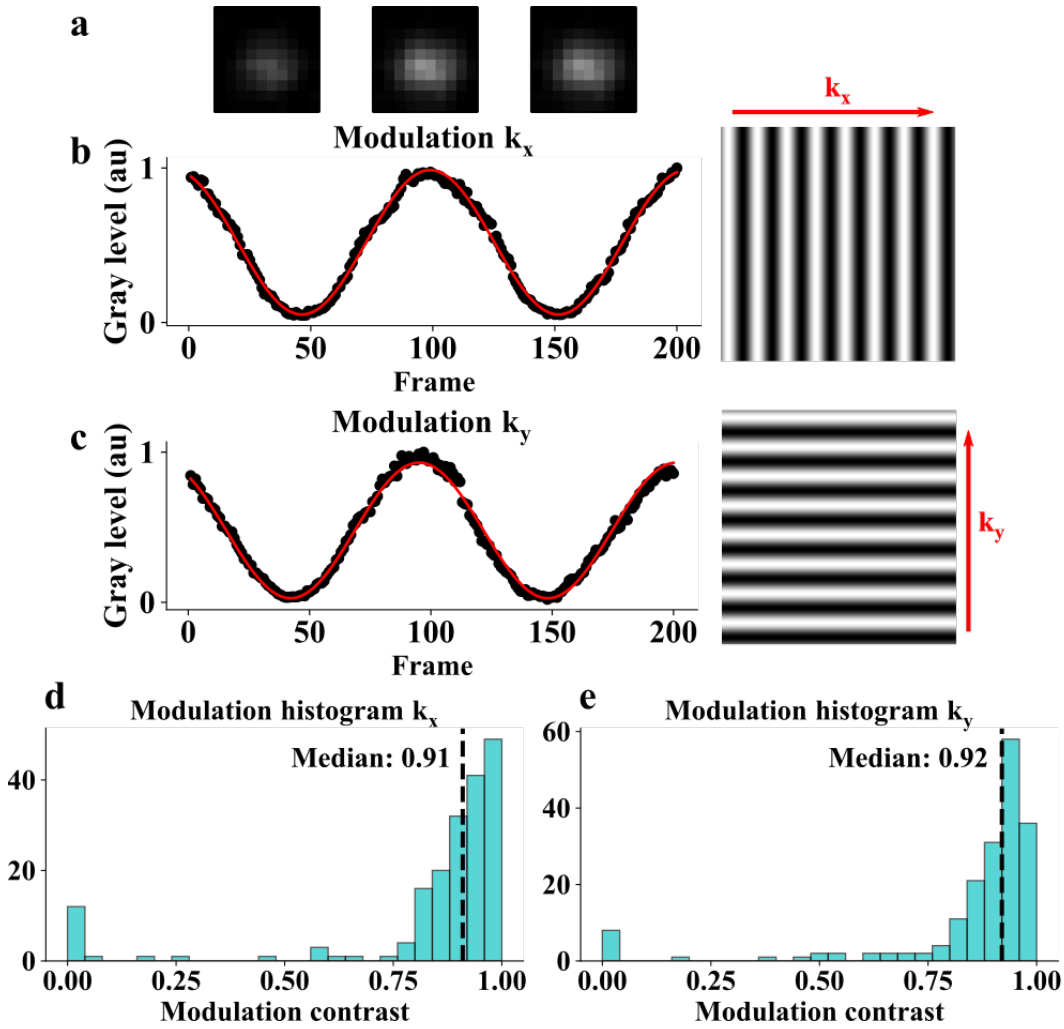

Fig. 3.18: Modulation estimation. (a) Cropped image of a bead in a 10x10 pixel ROI at three phases that roughly correspond to the frame number on the x axis of the x modulation plot (b,c) Measured brightness of a 20 nm bead as a function of camera frame where for each frame the phase grating is shifted by 40 nm, out of a 8.496μm period, in the grating plane with the piezos. ROIs of size 11x11 pixels were automatically segmented from a 26μm field of view, a background that was slowly changing due to photobleaching was fit with a linear decay curve and subtracted, and their summed ADU (minus the background) was fit with a sinusoidal curve with an $R^2 > 0.98$ for both directions. (d,e) Estimated modulation contrast values from 184 ROIs over the 26μm field of view. Outliers at low contrast values ($10 - 20\%$ with $m < 0.75$) are attributed to regions with multiple beads or to false segmentations giving largely noisy regions. No repeated experiments were done.

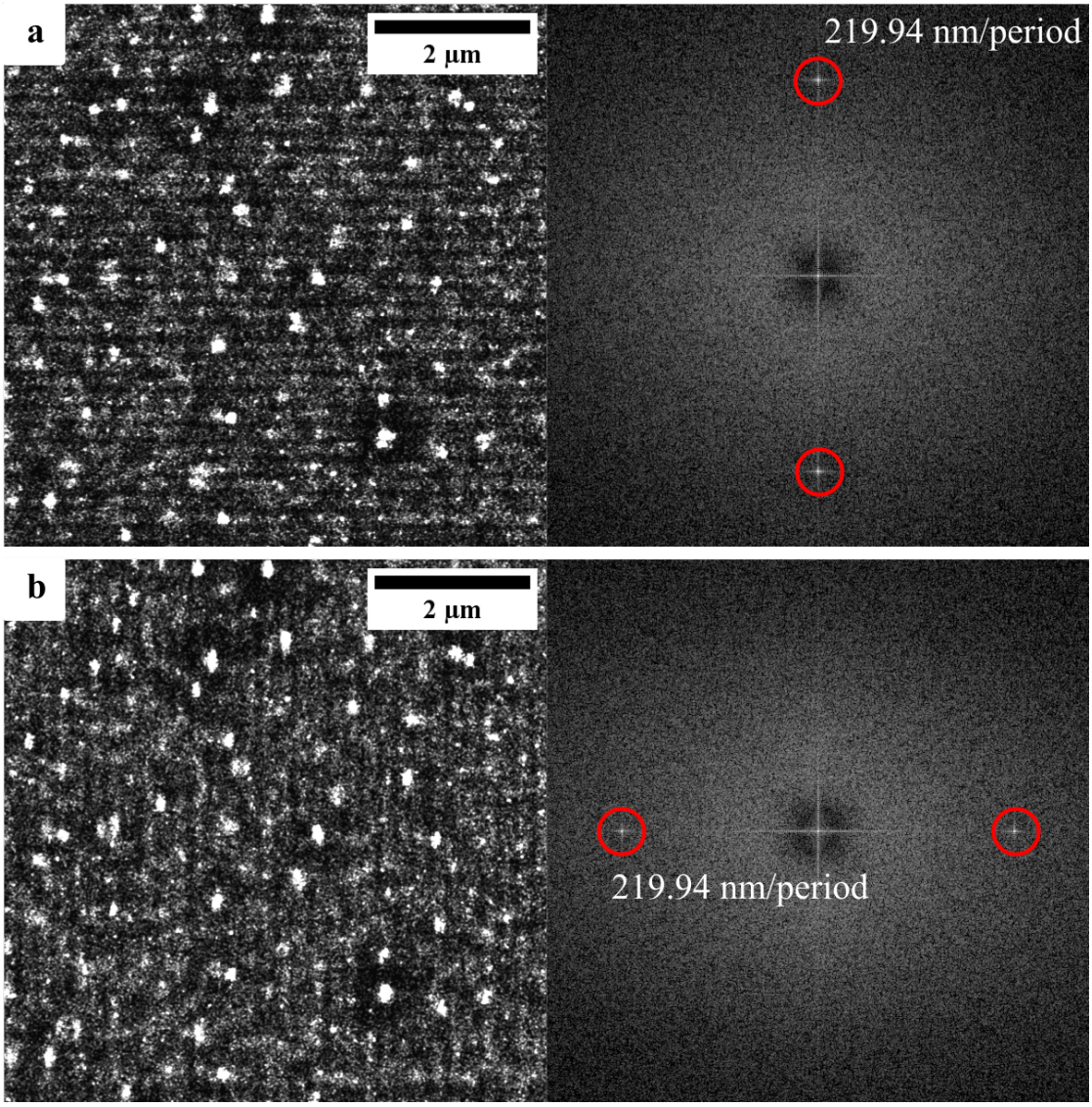

Fig. 3.19: Pattern pitch calibration. (a) 600x600 pixel cropped region of interest from localized high-density fluorophores illuminated with a periodic pattern, and Fourier transform of the image for the x-oriented pattern. (b) Same for the y-oriented pattern. The estimated pitch is displayed in the image, and agrees well with the expected value 219.9 nm (see Methods). No repeated experiments were done.

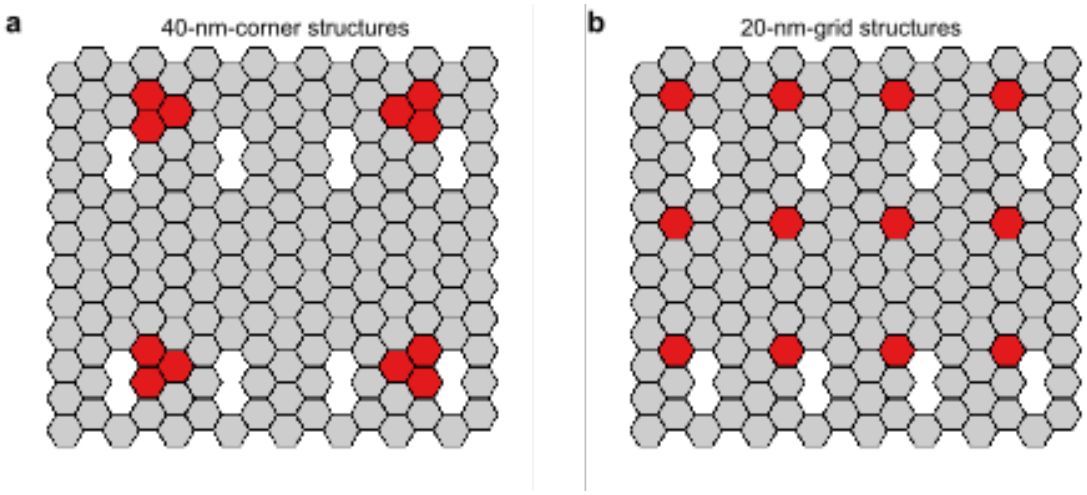

Fig. 3.20: DNA origami structures. (a) 2x2 square with 40 nm spacing between binding sites. (b) 4x3 grid with 20 nm spacing. Not all strands/binding sites are present in the image, however, due to a limited incorporation efficiency.

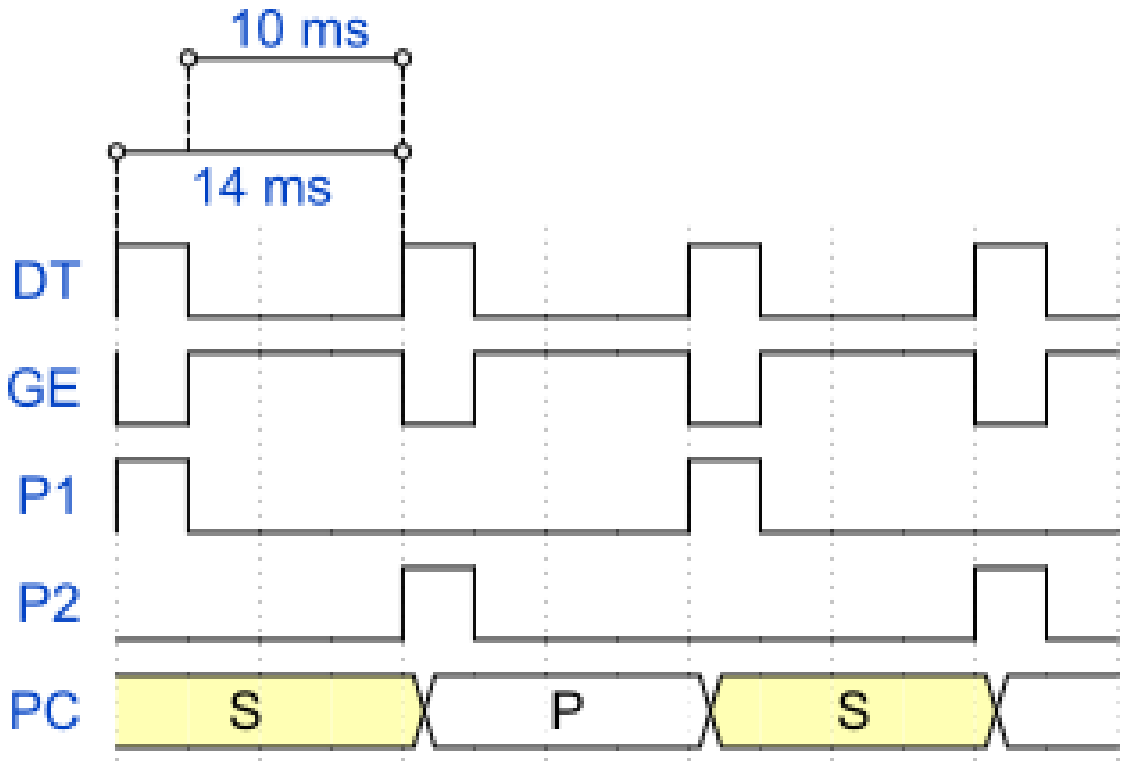

Fig. 3.21: Timing chart. DT digital trigger, GE global exposure, P1, P2 piezos 1,2, PC Pockels cell. The digital trigger for the acquisition (DT) is a digital TTL generator that causes a global exposure (GE) event to occur on the camera. The timings between the DT trigger (10 ms and 14 ms can be adjusted). GE is high when all pixels experience the same amount of exposure. Only acquiring images and illuminating the sample during the global exposure ensures that there is an even flux of photons across the field of view and that there is no cross-talk between our two imaging arms. The falling edge of the GE sequence triggers an Arduino to cycle through a three bit digital output that controls the two translation piezos (P1 and P2) and the Pockels cell (PC). The piezoelectric stages P1 and P2 are set to translate a by a user defined amount every other DT high trigger in between global exposure events, ensuring that the piezo gratings are not moving during their acquisition period. Each piezo mounted grating moves while the opposite grating is illuminated and imaged, thus maximizing imaging speed. The Pockels cell switches between the s and p beam paths by inducing a half wave voltage every DT high trigger event. To ensure that illumination from the s polarized arm does not appear in images from the p polarized arm, and vice versa, the laser was pulsed to only illuminate during the camera global exposure.

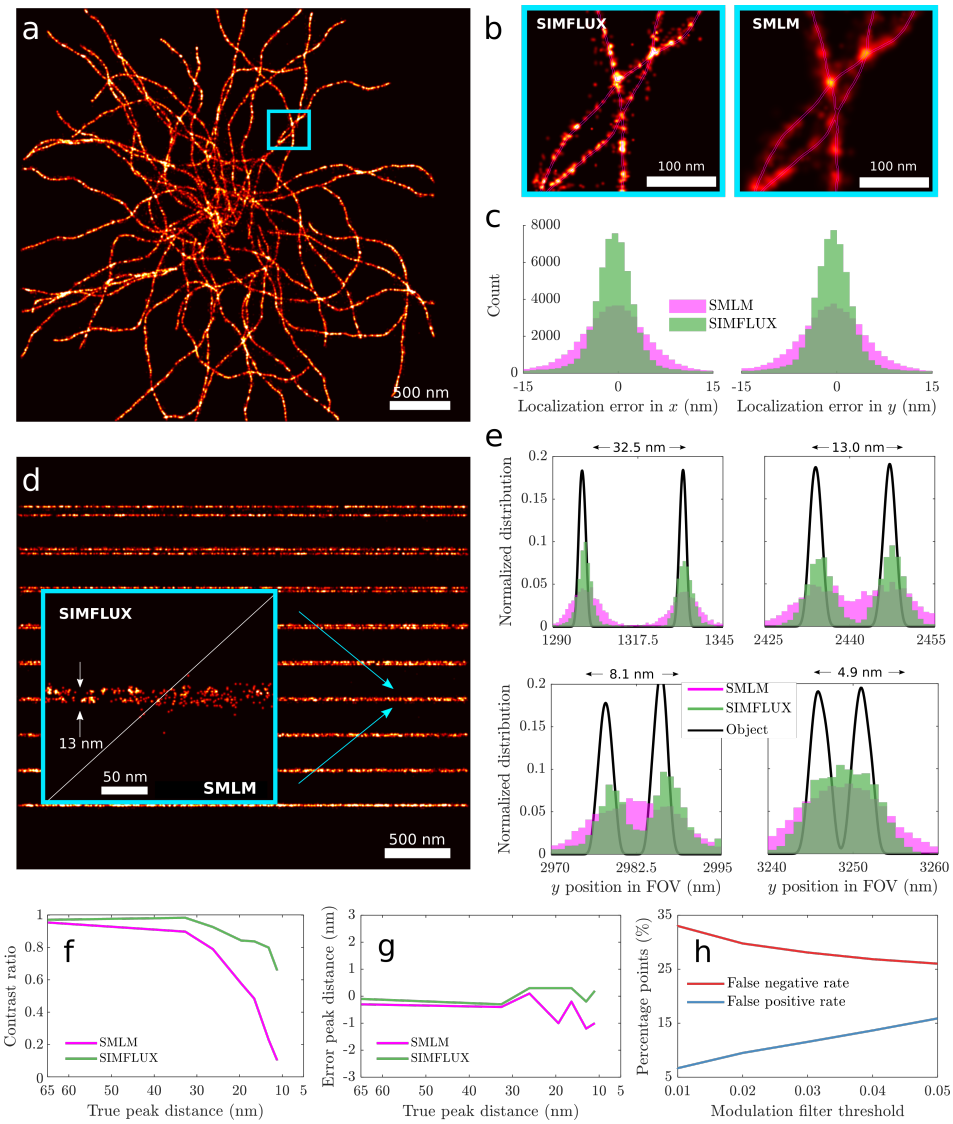

Fig. 3.22: Simulation of SIMFLUX images for a full field of view (FOV). (a) SIMFLUX reconstruction of a simulated filamentous, microtubule-like structure (size FOV 4.2 μm). (b) SMLM and SIMFLUX reconstruction of a zoom-in on a dense area indicated as a turquoise box in (a). (c) Histogram of lateral localization errors in (a) for SIMFLUX and SMLM, resulting in a standard deviation of 8.3 nm and 4.1 nm, respectively. (d) SIMFLUX reconstruction of line-pair objects with decreasing separation distance. (e) Histograms of projected localizations along four different line-pair objects in (d). For well separated objects the estimated line FWHM is 2.6 nm (true), 10.7 nm (SMLM), 5.6 nm (SIMFLUX). (f) Line pair contrast ratio = 1 − valley/ max(peak), showing better resolution of SIMFLUX, and (g) error in the estimated peak distance of SMLM and SIMFLUX as a function of the separation distance of the two line objects, showing a near zero bias. (h) Fraction of false negative and false positives rates for SIMFLUX localizations as a function of the modulation filter threshold. The reconstructions in (a) and (d) are generated with a modulation filter threshold of 0.03.

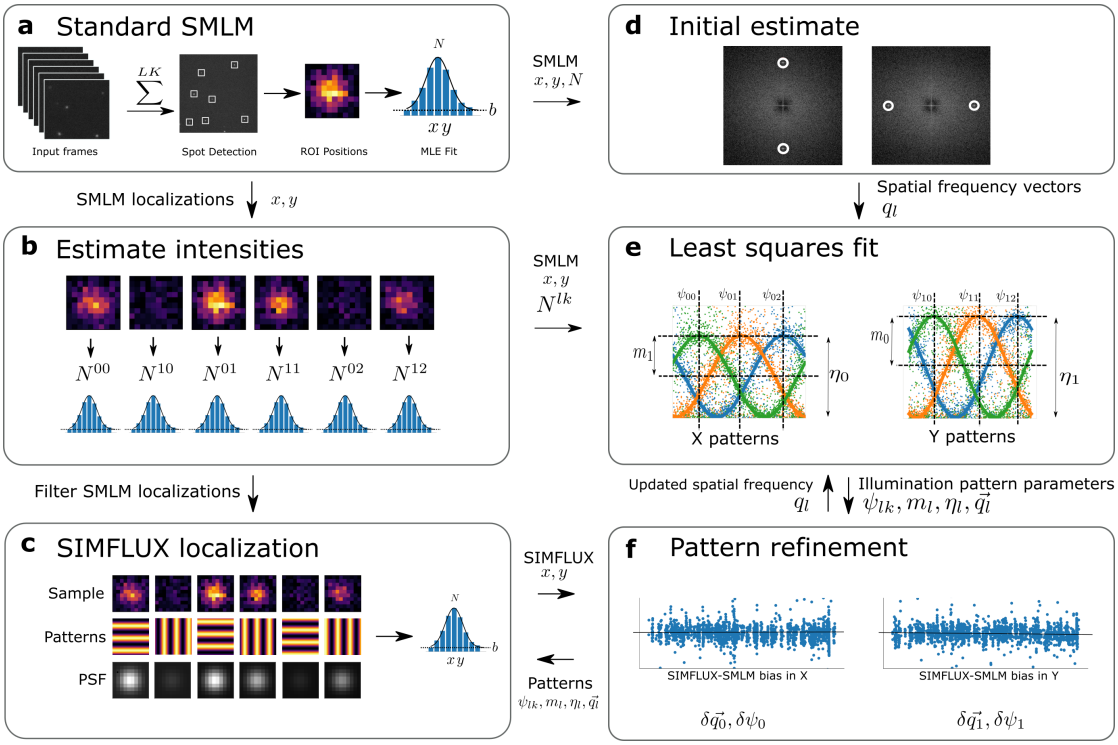

Fig. 3.23: Data processing pipeline for pattern estimation and SIMFLUX localization. (a) The raw frames from the camera are converted to photon counts, and summed in blocks of 6 frames. The conventional localization microscopy pipeline is then used to perform spot detection and 2D Gaussian localization. (b) Filtering of the localizations. The signal intensity (photon count) on the first and the last frame of an on-event is estimated using a 2D Gaussian fit, during which the molecule x, y-position is kept fixed. Molecules for which the signal photon count on the first or last frame is lower than a predetermined threshold N_{min} are rejected. (c) SIMFLUX localization. The 6 ROI frames are fitted to a model that uses both the illumination pattern information and the 2D spot center, resulting in a higher precision. (d). Initial estimates for the illumination pattern pitch and angles are found by locating peaks in the Fourier domain of the rendered standard SMLM image. The SMLM localizations are rendered into a super resolution image with a zoom factor of 6 compared to the camera pixel size. A 2D Fourier transform is then used with zero padding to zoom in on the peak. The peak is then fitted with a 1D quadratic fit in both q_x and q_y-directions to calculate to subpixel peak position. (e) Using the estimated spatial frequency vectors $\vec{q_l}$, intensities N_s^{lk} and SMLM localizations (x_s, y_s), the phases ψ_{lk}, modulation depths m_l and relative intensities η_l of the x and y-pattern are computed using a least square fit as described in the methods section. (f) The pitch and phase offset is refined by doing a least squares line fit on the difference between the SMLM and SIMFLUX localizations in both modulation orientations. A nonzero slope of this line will correspond to an error in the pitch, and a nonzero offset will correspond to a bias shared between all phases of the modulation orientation.

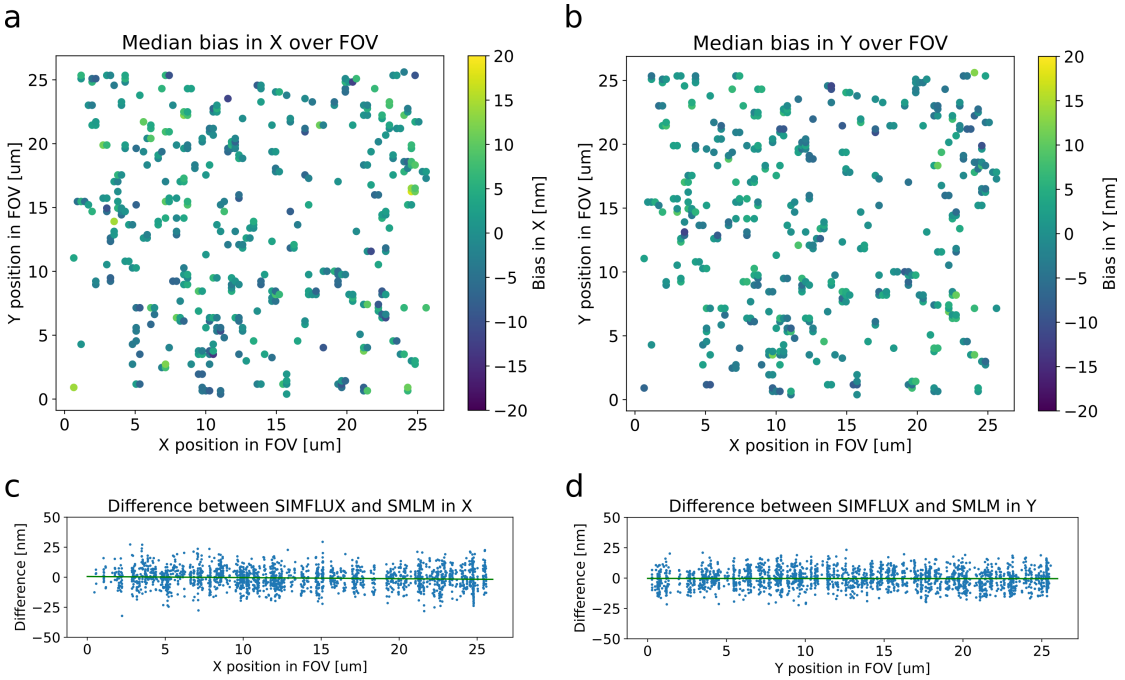

Fig. 3.24: Deviation between SIMFLUX and SMLM localizations over the FOV. (a,b) Difference between the SIMFLUX and conventional SMLM position estimate for 419 analysed clusters of localizations, projected on the x-oriented and y-oriented pattern directions. The data is averaged over all localizations within each cluster. (c,d) show the cross-sections of (a,b). The plots show no systematic error over the FOV, indicating that the iterative procedure of estimating the pitches and orientations of the illumination patterns converges to a uniform description of the sinusoidal illumination pattern. The rms value of the SIMFLUX-SMLM bias over the full dataset is 8.2 nm (x) and 7.5 nm (y), on the order of the localization uncertainty. The rms value over the median values of the clusters is 5.0 nm (x) and 4.2 nm (y).

References

[1] F. Huang et al. "Video-rate nanoscopy using sCMOS camera-specific single-molecule localization algorithms". In: *Nature Methods* 10.7 (2013), pp. 653–658. ISSN: 15487091.

[2] C. S. Smith et al. "Fast, single-molecule localization that achieves theoretically minimum uncertainty". In: *Nature Methods* 7.5 (2010), pp. 373–375. ISSN: 15487091.

[3] F. Balzarotti et al. "Nanometer resolution imaging and tracking of fluorescent molecules with minimal photon fluxes". In: *Science* 355.6325 (2017), pp. 606–612. ISSN: 10959203. arXiv: 1611.03401.

[4] B. Huang et al. "Three-dimensional super-resolution imaging by stochastic optical reconstruction microscopy". In: *Science* 319.5864 (2008), pp. 810–813. ISSN: 00368075.

[5] M. F. Juette et al. "Three-dimensional sub-100 nm resolution fluorescence microscopy of thick samples". In: *Nature Methods* 5.6 (2008), pp. 527–529. ISSN: 15487091.

[6] S. Abrahamsson et al. "Fast multicolor 3D imaging using aberration-corrected multifocus microscopy". In: *Nature Methods* 10.1 (2013), pp. 60–63. ISSN: 15487105.

[7] S. R. P. Pavani et al. "Three-dimensional, single-molecule fluorescence imaging beyond the diffraction limit by using a double-helix point spread function". In: *Proceedings of the National Academy of Sciences of the United States of America* 106.9 (2009), pp. 2995–2999. ISSN: 00278424.

[8] Y. Shechtman et al. "Precise Three-Dimensional Scan-Free Multiple-Particle Tracking over Large Axial Ranges with Tetrapod Point Spread Functions". In: *Nano Letters* 15.6 (2015), pp. 4194–4199. ISSN: 15306992.

[9] G. Shtengel et al. "Interferometric fluorescent super-resolution microscopy resolves 3D cellular ultrastructure". In: *Proceedings of the National Academy of Sciences of the United States of America* 106.9 (2009), pp. 3125–3130. ISSN: 00278424.

[10] S. Abrahamsson et al. "Multifocus structured illumination microscopy for fast volumetric super-resolution imaging". In: *Biomedical Optics Express* 8.9 (2017), p. 4135. ISSN: 2156-7085.

3.B Appendix 2: Additional information

3.B.1 Simulation of a 3D microtubule-like structure

We performed a simulation study to find out how clear the hollow tube structure of tubulin can be seen in an image. The tubulin is modeled as a hollow cylinder of diameter D with labeling molecules attached to the surface of the cylinder at random positions via a flexible linker of length L. Figure 3.25 shows the results of this study. It appears that the hollow tube structure is difficult to observe from an image alone, and that an averages along the tubulin must be taken to clearly see, and make quantitative, the impact of e.g. localization precision. Averaging over a sufficiently large length increases the SNR to the point where the dip in the middle can be seen clearly. This is also in line with Supp. Fig. 3.23 panel d) where the two lines are not observed well in the image but appear clearly in the projection along the tubulin axis.

3.B.2 Impact of non-uniform background

Next to the actual cellular experiments reported in Fig. 3.26, we have analysed the impact of non-uniform background in detail with a simulation study. In short, we have simulated a filamentous sample using the worm-like chain model, populated the filaments with binding sites at a given density, and generated randomized sets of localizations, with on-time according to Poisson statistics (PAINT) or mixed Poisson-geometrical statistics (STORM), and with randomly varying number of emitted photons (shot noise). These simulated frames are fed into the processing pipeline, the resulting sets of localizations can be analysed in comparison to the known ground truth.

Our conclusion is that a gradient in background results in a bias in the SIMFLUX localizations, but this bias appears to be comparable to the bias in conventional SMLM (see panel f). We conclude that SIMFLUX is not particularly sensitive compared to conventional SMLM. This is also consistent with the impact of a constant background, which results in a comparable reduction in precision for SIMFLUX and conventional SMLM (see Supp. Figure 3.3).

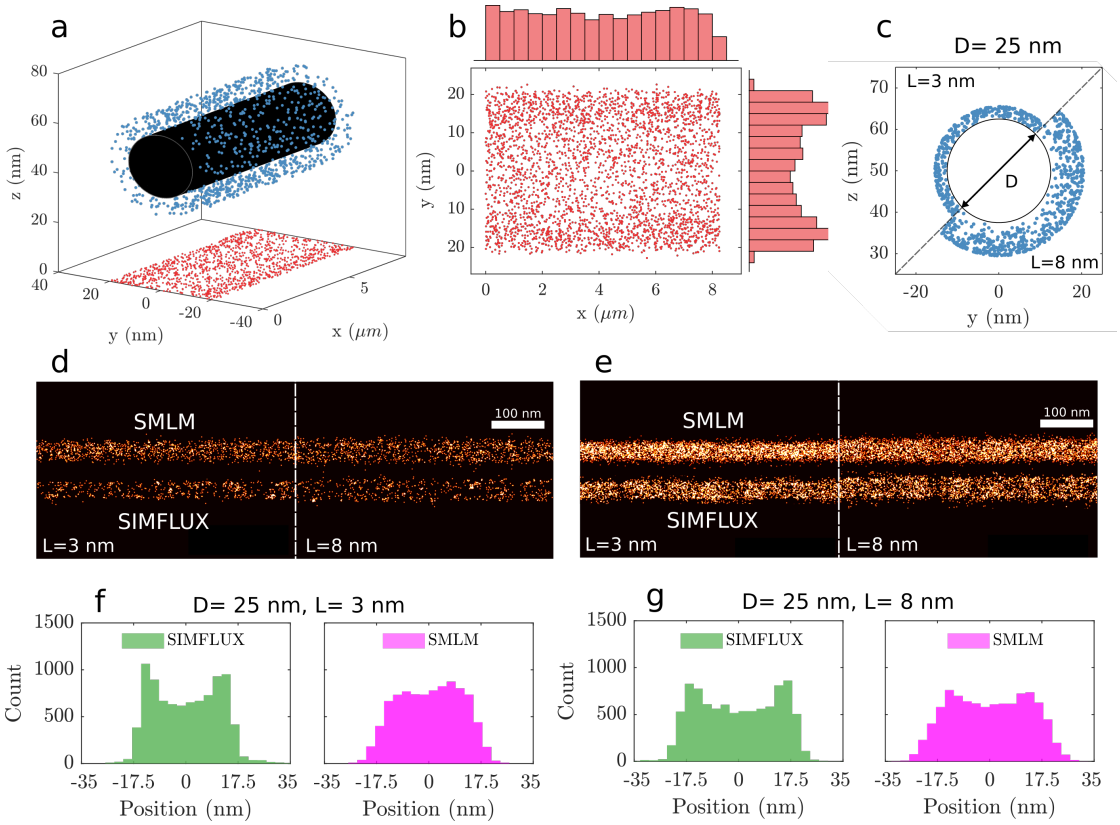

Fig. 3.25: Simulation of a 3D filamentous, microtubule-like structure. (a) 3D representation of the filamentous structure (black) with attached linker sites (blue dots) projected onto the image (xy) plane (red dots). (b) Scatter plot of the image plane projected linker sites with marginal histograms showcasing the non-constant distribution transversal to the filament. (c) Transverse cross-section of the filament with diameter (D) 25 nm and linkers having full rotational mobility outside of the filament but constant length (L) of 3 and 8 nm. (d) Zoom-in regions of simulated FOV (8.25 μm) showing SMLM ($\approx$ 1250) and SIMFLUX ($\approx$ 650) localizations for a 25 nm diameter filament with linker sizes 3 and 8 nm; (e) and more densely labelled SMLM ($\approx$ 4820) and SIMFLUX ($\approx$ 2750) localizations. (f, g) Histograms of projected localization along the filament in the FOV and labelling density as in (d) with a diameter of 25 nm and linker lengths 3 nm (f) and 8 nm (g). Simulated photon count is 2000, 10 background photons per pixel and modulation depth of 0.95.

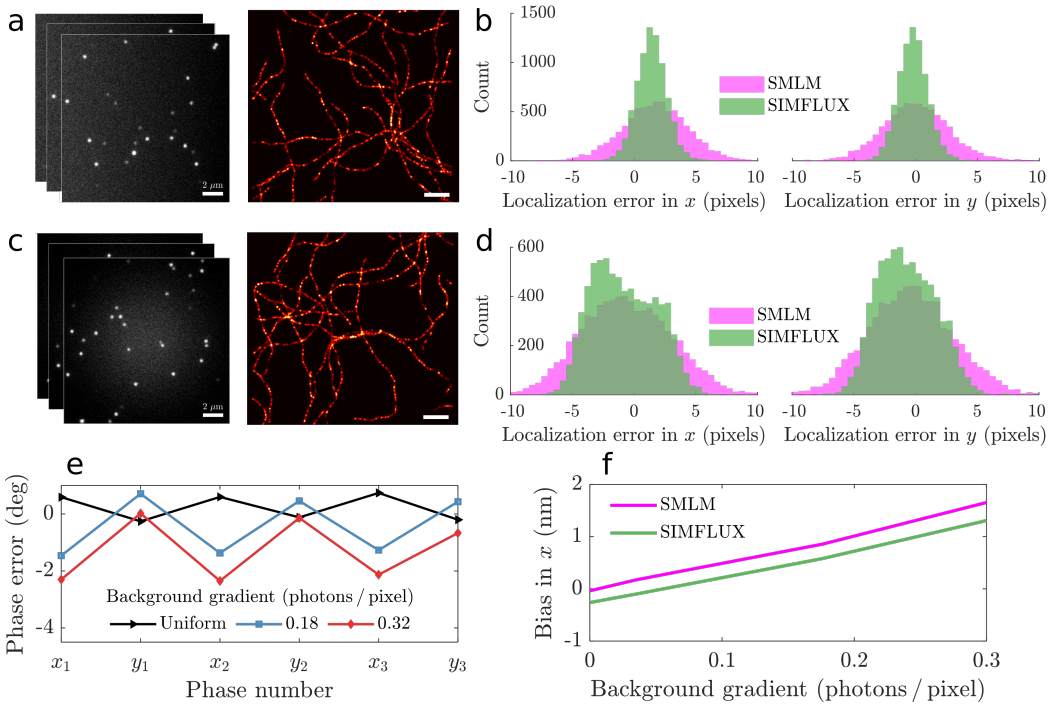

Fig. 3.26: Impact of non-uniform background on SIMFLUX. In panel a) simulations are shown with a linear gradient in background from left to right. In panel b) it appears that this induces a bias in both SMLM and SIMFLUX which appears to be about equal (see also panel f). In panel c) we show simulations with a circularly symmetric background (higher background in the center). The overall effect shown in panel d is that this broadens the total distribution of localizations, both for SMLM and SIMFLUX. The bias in SIMFLUX arises mainly due to a bias in the pattern phase estimate (panel e).

4 Simultaneous orientation and 3D localization microscopy with a Vortex point spread function

4.1 Abstract

We have developed an engineered Point Spread Function (PSF) to enable the simultaneous estimation of dipole orientation, 3D position, and degree of rotational constraint of single-molecule emitters from a single 2D focal plane. Besides giving access to orientation information, the Vortex PSF along with our vectorial fitting routine avoid localization bias common in localization microscopy for fixed dipole emitters. We demonstrate this technique on reorienting single-molecules and using binding-activated localization microscopy on Lambda-DNA with DNA intercalators. Corroborating perpendicular azimuthal angles to the DNA axis for in-plane emitters but find a non-uniform distribution as a function of the polar angle. The Vortex PSF is realized by an affordable glass phase mask and is barely larger than a non-engineered PSF making it easy to combine with localization microscopy techniques on rotationally constrained emitters.

4.2 Introduction

Single-Molecule Localization Microscopy (SMLM), with flavors like (F)PALM [1, 2], (d)STORM [3, 4] and (DNA)-PAINT [5, 6], have made nanoscale structural information beyond the diffraction limit more easily accessible to biologists. These super-resolution techniques commonly focus on localizing single emitters in the two dimensions of the focal plane, and sometimes in the third dimension along the optical axis. The role of molecular orientation in localization can often be ignored as the fluorescent labels are flexibly attached to the biomolecule of interest and can rotate or wobble freely, thereby appearing as isotropic emitters. In case the fluorophores are more rigidly attached, emitter orientation is either a nuisance for estimating the position of the emitters accurately or can give access to the anisotropy of the underlying biological structure. Imaging the orientation of constrained fluorescent labels has been used to visualize changes of fibroblasts under treatment [7], reveal the underlying orientation of amyloid fibrils [8]

Published as *Simultaneous orientation and 3D localization microscopy with a Vortex point spread function*, C.N. Hulleman, **R.Ø. Thorsen**, S. Stallinga, B. Rieger, bioRxiv (2020)

and to track motor proteins [9, 10]. Besides biological applications, the orientational information can also be used to visualize nanoscale deformations in material sciences [11]. In this paper we demonstrate an engineered Point Spread Function (PSF), which allows in a unique manner the simultaneous estimation of the x, y and z position of the emitter, as well as the polar and azimuthal angle θ and ϕ of the molecular orientation, and the degree of orientational constraint g_2, all from a single 2D image. Thereby we can effectively combine orientation estimation and localization microscopy into a single imaging protocol.

Visualization of emission patterns from fixed fluorescent emitters dates back to near-field studies [12] and studies with high-NA fluorescence microscopes, leading to the observation of ring-shaped spots originating from molecules oriented along the optical axis [13]. Localization of these rotationally fixed molecules with a standard 2D Gaussian model leads to inaccuracies due to their dipole emission patterns [14]. The localization accuracy of these fixed dipoles is significantly worse in the presence of aberrations [15], and with a small amount of defocus errors can amount to 100 nm [16]. The impact of rotational diffusion has been studied in ref. [17] in which the authors show that a localization bias on the order of 10 nm already occurs when the fluorophores are constrained to a cone half-angle of 60°. This localization bias could be avoided altogether by removing the radially polarized component [18, 19]. Regrettably doing so reduces the SNR and limits the orientations that can be properly localized.

Instead of only avoiding localization bias the orientation of fixed emitters could be identified. When defocusing fixed emitters, the observed pattern varies more as a function of orientation, opening up a way to estimate the orientation from a single defocused image [20, 21, 22]. A defocus of up to 1 μm spreads the emitted photons over many pixels, which has the drawback of adversely affecting localization precision. By interleaving in-focus localization with defocused spot fitting, a compromise between orientation estimation and localization precision can be made [10]. For a limited set of orientations the angles can even be extracted from in focus single-molecule images in case of sufficiently high Signal-to-Noise Ratio (SNR) [23, 24].

An alternative way to estimate orientation and position comes from engineering the Point Spread Function (PSF). Here techniques modify the emission beam phase profile [25, 26, 27, 28] in the pupil plane and split the polarization [29] to measure different polarization components on the camera separately. The effective size of these engineered PSFs is large, ranging from 4-16 times the Rayleigh criterion in size ($R = 0.61\lambda/\mathrm{NA}$) in each polarization channel. This splitting of photons over a large area and multiple polarization channels reduces the Signal-to-Background Ratio (SBR) [30, 31] and limits the density of emitters per frame for localization microscopy. A recently published method referred to as Coordinate and Height super-resolution Imaging with Dithering and Orientation (CHIDO) [32] overcomes this problem with a more compact PSF that encodes the orientation and position into two different polarization channels. It turns out that this method performs 2-5 times worse on simulations than predicted by theory, despite a good maximal theoretical precision in both 3D location and orientation. Furthermore the experimental precision is even 5-6 times worse than the theoretical precision, which could be explained by the mismatch between their fitting model and experimental data.

This method requires many additional optical components in the emission path such as polarization splitting and a custom produced stress-engineered optic. In addition, the latter component is particularly difficult to align and calibrate.

Here we overcome these drawbacks by introducing the Vortex PSF, a PSF engineering approach to simultaneously determine molecular orientation and position in all three spatial dimensions that does not require different polarization components to be imaged separately. Furthermore the Vortex PSF enables access to the degree of rotational mobility so that the flexibility of binding of the fluorophores can be probed. Both the azimuthal and polar angle precision are good with no ambiguity between $\pm 45°$ azimuthal angles, and the lateral localization precision is close to that of a non-engineered PSF. This is because the single imaged spot has a footprint of only 4-6 times the Rayleigh criterion in size. The small spot footprint on the camera leads to a favorable SBR, high localization precision and a sparsity constraint for localization microscopy on the same order of magnitude as a standard (non-engineered) PSF. The use of a calibrated aberration map over the entire Field-of-View (FOV) with a fully vectorial PSF model in the parameter estimation avoids aberration induced biases and successfully reaches the Cramér–Rao Lower Bound (CRLB). This makes it possible to maintain precision and accuracy across standard FOVs of 10s of μm. Implementation of the Vortex PSF into an existing setup is easy and can be realized via an affordable off-the-shelf component. We showcase the method by tracking orientational jumps of single-molecules on a coverslip and imaging λ-DNA using Binding-activated localization microscopy (BALM) [33, 34].

4.3 Results

4.3.1 Vortex PSF concept

The orientation of a constrained dipole emitter is characterized by three numbers, the in-plane azimuthal angle ϕ, the polar angle with respect to the optical axis θ, and a parameter quantifying the degree of rotational mobility g_2 (Fig. 5.1(a)). The g_2 parameter is a ratio between the fixed and free dipole PSF, which is sufficient to quantify the impact of orientational constraint, irrespective of the form of the constraint, e.g. "wobble-in-cone" or harmonic orientational potential well [35].

A fixed dipole emitter that is oriented perpendicular to the optical axis ($\theta = 90°$) emits fluorescence that is in-phase throughout the Fourier plane of the emission path. When imaged without the vortex, this emitter yields Gaussian-like spots on the camera due to constructive interference in the center. The emission from a dipole oriented along the optical axis ($\theta = 0°$) captured by a high-NA objective has two regions on opposite sides of the Fourier plane of the emission path that are out of phase with respect to each other. Without the vortex this emitter yields a ring-shaped PSF with a zero in the middle due to destructive interference. Simulated images of standard PSFs show these PSF shapes close to in and out-of-plane orientations ($\theta = 80°$ and $\theta = 10°$), yet the slight asymmetry arising from the azimuthal orientation cannot be identified by eye (Fig. 5.1(b)).

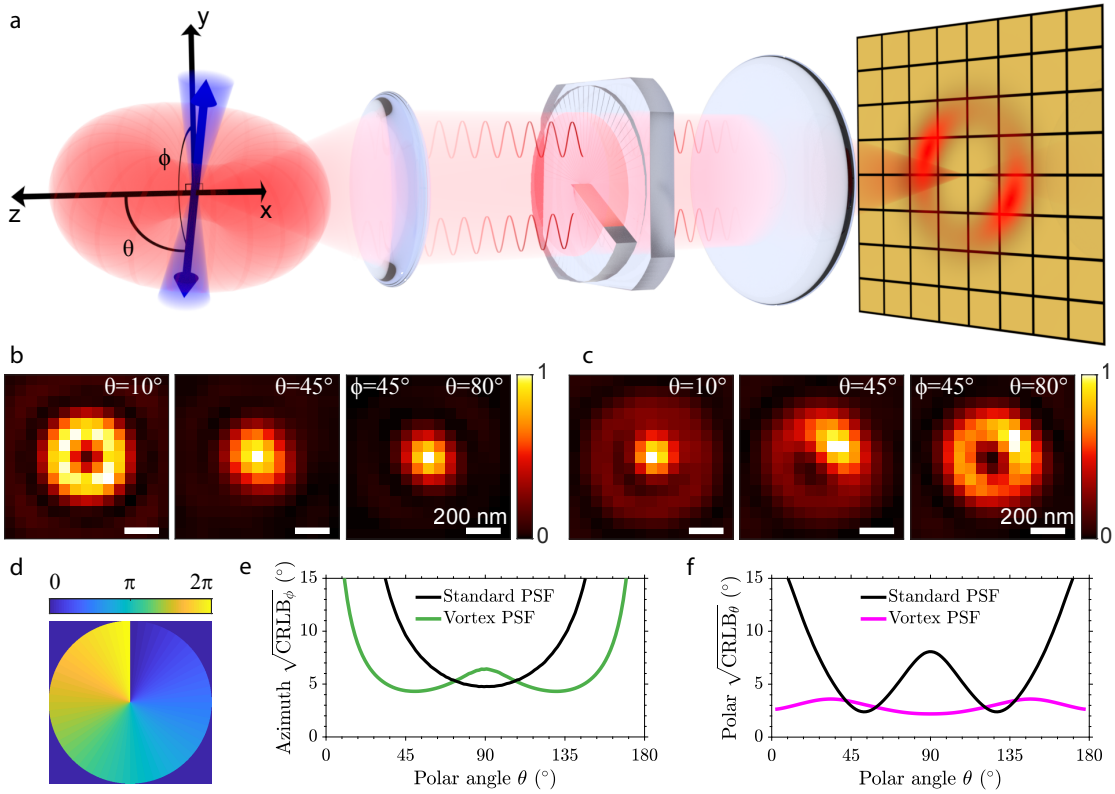

Fig. 4.1: Vortex PSF concept. (a) A constrained dipole emitter is defined by the polar angle θ and azimuthal angle ϕ. The blue cone represents the degree of rotational constraint (g_2) of the dipole emitter and the red torus-like shape represents the dipole emission. The microscope, equipped with a vortex phase plate, induces a radial π phase difference in the Fourier plane of the emission path. This results in an asymmetric donut-like shape for fixed emitters on the camera which we call the Vortex PSF. (b) Simulated standard PSF with polar angles from left to right (10, 45, 80 degrees) and an azimuthal angle of 45 degrees. (c) Simulated Vortex PSF with the same angles. (d) Phase profile of the vortex phase plate. (e) Azimuthal angle CRLB from simulated images as a function of the emitter polar angle (4000 signal photons and 10 background photons per pixel). (f) Polar angle CRLB as a function of the emitter polar angle with the same SBR.

The Vortex PSF can be realized as an addition to any standard fluorescence microscope and only requires a single phase plate in the Fourier plane of the emission path (Fig. 5.1(a)). The phase plate consists of a phase vortex of topological charge 1, thus the phase delay is a single spiral ramp from 0 to 2π, where radially opposing points always have a π phase difference between them (Fig. 5.1(d)). Adding a vortex phase plate in the Fourier plane of the emission path inverts the phase relationship described earlier for a standard PSF and creates what we call the Vortex PSF. Now, out-of-plane ($\theta = 0°$) orientations have a central spot and in-plane ($\theta = 90$) orientations have a ring-shaped PSF. Due to the polarization and directional emission from the fixed dipole emitter, the intensity distribution changes along this ring as a function of the azimuthal angle. Simulated Vortex PSF shapes for polar angles ($\theta = 10°$, $\theta = 45°$, $\theta = 80°$) indicate a substantial change as a function of the polar angle, as well as a clearly recognizable impact of the azimuthal angle ($\phi = 45°$) on spot shape (Fig. 5.1(c)).

Fitting molecular dipole orientations using the standard in-focus PSF is difficult because of its symmetries. The PSF is almost rotationally symmetric for all polar angles except around $\theta = 90°$, where there is a slight asymmetry of the PSF as the spot is wider in one direction than the other. The azimuthal precision, quantified by the CRLB, is indeed worse for all polar angles except near $\theta = 90°$ (Fig. 5.1(e)). Furthermore, the standard PSF is also symmetric around the polar angles $\theta = 0°$ and $\theta = 90°$ yielding an unfavorable precision in estimating the polar angle around these angles (Fig. 5.1(f)). These symmetries are broken by the Vortex PSF, resulting in a good precision over all possible orientations (Fig. 5.1(e,f)). Of course, the precision of the azimuthal angle is still expected to diverge to infinity for polar angles approaching $\theta = 0°$ and $\theta = 180°$ as the azimuthal angle is undefined when the dipole is aligned along the optical axis. Note that due to the symmetry of the dipole it is sufficient to use half the unit sphere to uniquely define the dipole angle.

4.3.2 Simulated precision and accuracy

We have tested the vectorial Vortex PSF model with extensive simulations to predict the experimental conditions under which the Vortex PSF can be used to correctly estimate the parameters $\Theta = (x, y, z, N, b, \phi, \theta, g_2)$ (see Supplementary Note 1 for a detailed description of the model). The parameters are as follows x, y, z is the molecule position, N the signal photons, b background photons per pixel, and orientation parameters ϕ, θ, g_2 as described earlier (Fig. 5.1(a)) . We found that all model parameters can be estimated with precision at the CRLB for all molecular orientations and degrees of orientational constraint (Supplementary Fig. 1), provided the signal-to-background ratio (SBR = N/b) is sufficiently high. A practical lower limit is around SBR $\geq$ 200 (Supplementary Fig. 2).

For dipole emitters orientated uniformly on unit sphere with $g_2 = 0.75$ and SBR = 4000/10 the parameters can be estimated with a localization precision of $\sigma_{xy} = 5.6$ nm, $\sigma_z = 27$ nm and orientation precision of $\sigma_\phi = 5.5°$, $\sigma_\theta = 3.1°$ and $\sigma_{g_2} = 0.08$. The polar precision appears almost constant over the unit sphere, whereas the azimuth precision performs well within polar angles ($20° < \theta < 160°$) after diverging for emitters

along the optical axis. Such polar range is notably broader than the standard PSF, as shown in Fig. 5.1(e). The amount of rotational diffusion of an emitter affects the possible orientational and axial precision while it does not affect the lateral precision. The orientation can be estimated to a precision within $\sigma_\theta < \sigma_\phi < 10^\circ$ given a rotational diffusion $g_2 > 0.4$ ($< 58^\circ$ cone half-angle). Outside this range the PSF becomes too smeared out, and the orientation information is mostly lost. The optimal axial performance is for fixed emitters $\sigma_z = 23$ nm ($g_2 = 1$), whereas it worsens for freely rotating emitters up to $\sigma_z = 49$ nm ($g_2 = 0$). In this case, when the emitters are freely rotating, the Vortex PSF has a slightly worse lateral precision compared to a non-engineered PSF ($\sigma_{xy} = 5.9$ nm versus $\sigma_{xy} = 4.5$ nm). The estimation of all the parameters is uniform over a z-range of ± 300 nm, with a region of interest of 15×15 pixels (Supplementary Fig. 1). A larger region of interest should be used beyond ± 300 nm to capture the whole PSF and attain reliable parameter estimates. However, this is not optimal for dense single-molecule localization microscopy.

Simulations show furthermore that optical aberrations must be taken into account in the fitting model. Unknown or inaccurately calibrated aberrations with values deviating from the actual values by more than 36 mλ affect the imaging model such that the estimator introduces biases and no longer reaches the CRLB (Supplementary Fig. 3). The aberration modes astigmatism and coma notably degrade the azimuthal precision by a factor of ~ 2, and additionally, astigmatism also degrades the localization precision by a factor of ~ 2. However, when the model is well calibrated with these aberrations, the estimator reaches the CRLB with no biases. To avoid such inadequate estimation and variation over a large field of view, we have developed an aberration map based on the Nodal Aberration Theory (NAT) [36] (See Methods and Supplementary Note 2). Using this aberration map we obtain reliable results over a large FOV despite significant changes in aberrations throughout the FOV (Supplementary Fig. 4).

4.3.3 Proof-of-concept

To first verify the Vortex PSF's functionality and performance, we have imaged ATTO 565 embedded in a thin layer of PMMA (Polymethylmethacrylate) (see the methods section for sample preparation and imaging protocol for any samples mentioned). Figure 4.2 shows the results of one of these experiments. Figure 4.2(a) shows through-focus images of a single-molecule in PMMA acquired with the vortex phase plate together with the fitted PSF model and its estimated parameters. Note that a bigger region-of-interest (ROI) 31×31 is used to verify the model over a large z range compared to typical localization, where 15×15 is recommended. The same single-molecule was imaged in quick succession without the vortex phase plate to verify the estimated orientations. As it is challenging to estimate orientations with the standard PSF on a single-frame with high precision, the entire z-stack is used to retrieve a single estimate, which is used as a ground-truth measure. This estimate differentiates slightly from defocus imaging as described in the literature [20, 21, 10], where only a single focal slice is used. For the single-molecule in Fig. 4.2(a), its orientation found for the standard PSF z-stack fit $(\phi, \theta) = (48^\circ, 61^\circ)$ agrees well with the angles found for the Vortex

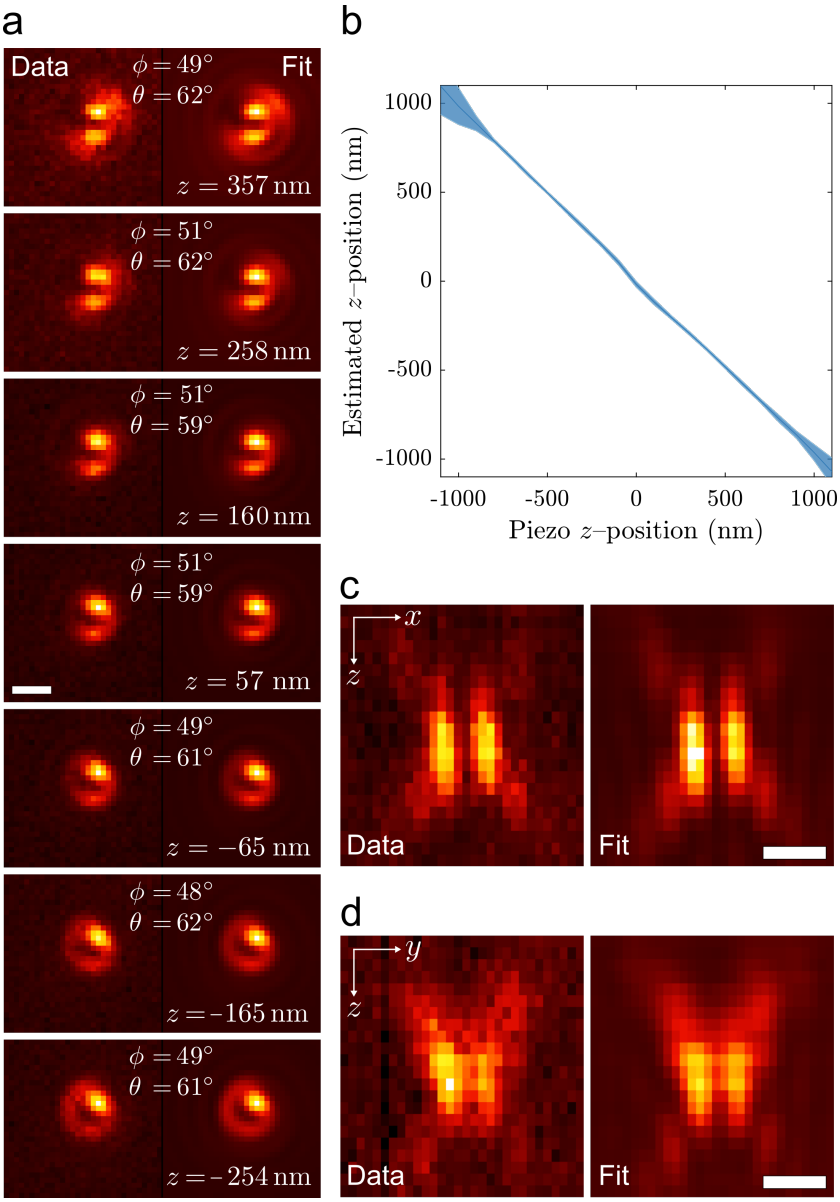

Fig. 4.2: Vortex PSF validation. (a) Vortex PSF model fitted to an experimental z-stack of one single molecule with its estimated parameters listed in each frame. All sub-image pairs are contrast stretched with the same factor for better visibility of the PSF shape. (b) Mean estimated z position as a function of the piezo z position with the shaded region representing $\pm\sigma$. The average is taken from 37 single molecules of varying orientations where the piezo z is realigned in processing to account for the in focus position not corresponding exactly with $z_{\text{piezo}} = 0$. The slope is negative due to the opposing definition of z_{piezo} and the sample z. (c) The cross-section in $x - z$ and (d) $y - z$ of a Vortex PSF, with the measurement left and fit right (pixels are stretched proportionally in z). The estimated signal photon counts were in the range $4 - 50 \times 10^3$, and the estimated background photon counts were in the range $10 - 40$ photons per pixel. All scale bars are 500 nm.

PSF z-slice fits $(\phi, \theta) = (49 \pm 1.5°, 61 \pm 1.7°)$. Here the Vortex PSF uncertainty is the standard deviation estimate of 11 focal slices, corresponding to a dynamic range of 1000 nm. Following the same procedure as for the molecule in Fig. 4.2(a), the estimated orientation of 21 different molecules is depicted in (Supplementary Fig. 5). The mean deviation between the orientation found with the standard PSF and Vortex PSF is $(\Delta\phi, \Delta\theta) = (-0.4 \pm 1.4°, -0.2 \pm 1.2°)$, indicating no bias between the two imaging modes. The Vortex PSF's mean precision is $(\sigma_\phi, \sigma_\theta) = (2.3°, 1.8°)$ which comes close to the estimated lower limit $(\sqrt{\text{CRLB}_\phi}, \sqrt{\text{CRLB}_\theta}) = (1.8°, 1.5°)$.

The estimated z-position shift between frames of the molecule in Fig. 4.2(a) is $\Delta\tilde{z} = 97 \pm 11$ nm, which matches the piezo shifts of 100 nm. The relationship between the estimated z-position and the piezo position averaged over 37 molecules is fitted with a linear function, resulting in a slope of -0.99 ± 0.01 and has a Root Mean Square Error (RMSE) of 16 nm over a 1200 nm range as shown in Fig. 4.2(b). To further show the quality of fit, cross-sections in the $x - z$ and $y - z$ planes are shown in Fig. 4.2(c)-(d). The agreement between the experimental data and fit with the vectorial Vortex PSF model is generally excellent. A striking detail is that even the fringe details away from focus match well. The lateral localization error, measured on individual z-slices between the two estimation modes, is 5 nm and 4 nm (RMSE) in the x and y direction. These validation experiments show that the orientation of fixed dipole emitters and their 3D position can be reliably estimated from individual focal-slice Vortex PSF images.

4.3.4 Re-orientation dynamics

The Vortex PSF can track dynamic changes in the orientation of single-molecules on a coverslip. We have observed that a portion of ATTO 565 single-molecules directly spin-coated on glass (without PMMA) show re-orientation when followed over time, indicating metastable adhesion to the glass surface (see Supplementary Movie 1). The orientation change can be directly seen from the dark region that shifts from the left to the right and back over 7 frames (Fig. 4.3(a)). Time traces of 3 different molecules that show these re-orientation events indicate that the azimuthal angle changes, but the other parameters not that much (Fig. 4.3(b)). These types of azimuthal angle changes would lead to large position biases in standard localization microscopy, which are not present with the Vortex PSF (Fig. 4.3(c)). The orientation constraint g_2 becomes lower at the transition points, which corresponds to a more freely rotating molecule throughout that frame or a superposition of the orientation before and after the transition.

4.3.5 Super-resolved λ-DNA

A wide variety of biological structures can be labeled with rotationally constrained fluorophores [9, 10, 31, 37]. We chose to demonstrate our technique on frequently studied λ-DNA labeled with DNA intercalators [33, 34, 38] that transiently bind between the base pairs. The molecular dipole moment of the DNA intercalators is typically oriented perpendicular to the DNA axis [39, 40, 41], making this an ideal test case. We chose to use Sytox Orange which is believed to be a mono-intercalator [42] and further confirmed

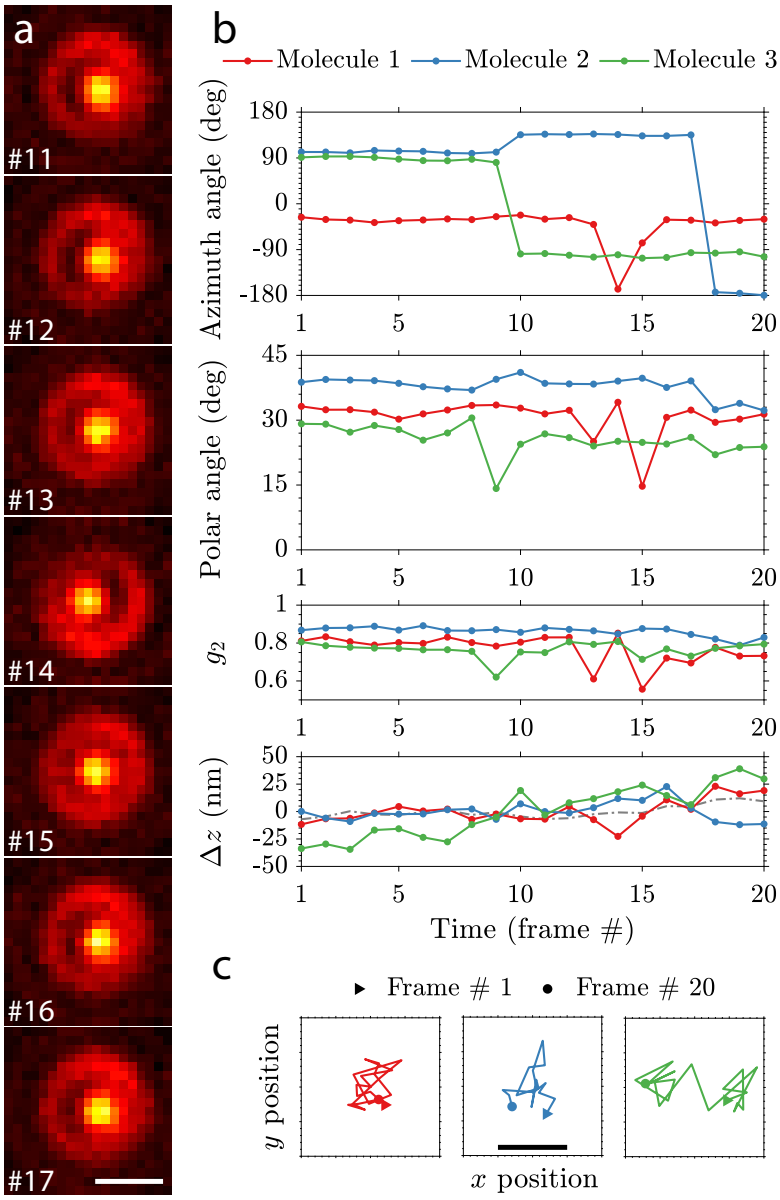

Fig. 4.3: Re-orientation dynamics of single-molecules imaged with the Vortex PSF. (a) Consecutive raw Vortex PSF images of a molecule undergoing an orientational transition (900ms exposure, scale bar 500 nm). (b) Estimated parameters over 20 frames of three different molecules showing orientational transitions (molecule 1 shown in (a)). The gray curve in the Δz plot shows the average upward drift ($\sim$ 20 nm) from 10 stationary molecules. (c) Lateral localization of the emitters undergoing re-orientation with 1 nm ticks and a scale bar of 10 nm.

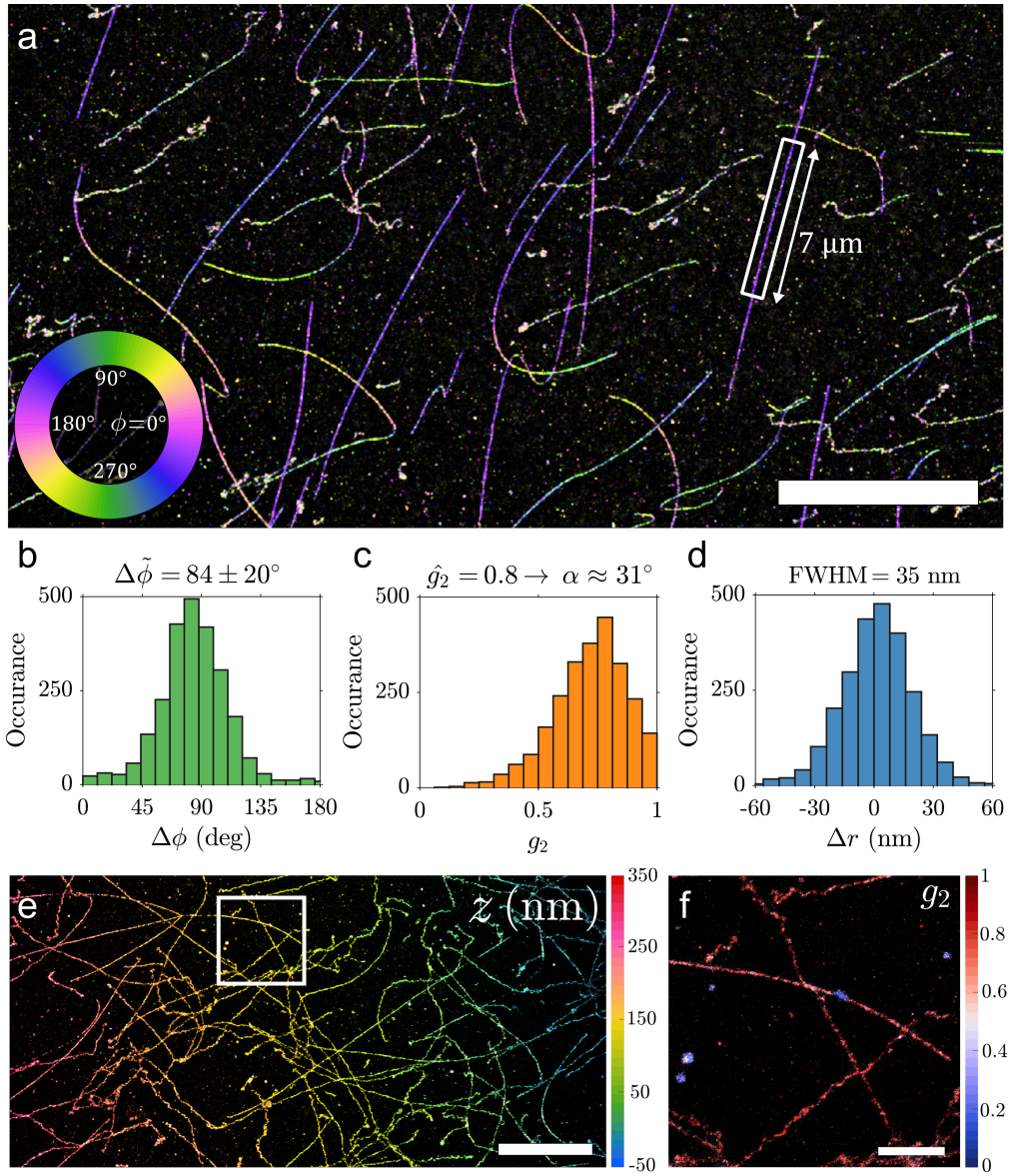

Fig. 4.4: Super-resolution image of λ-DNA. (a) λ-DNA colorized as a function of the azimuthal angle. (b) Azimuthal angle histogram relative to the DNA axis from the DNA strand highlighted in (a) ($\Delta\phi = 84°, \mathrm{MAD}(\Delta\phi) = 20°$). (c) Distribution of g_2 from the same strand, the fitted peak $g_2 = 0.8$ corresponds to a wobble cone semi-angle $\alpha = 31°$. (d) Position deviation from the spline fit to the DNA axis with a FWHM of 35 nm (Filtered to $45° \leq \theta \leq 135°$). (e) Tilted λ-DNA sample colorized as a function of z-position. (f) λ-DNA from highlighted region in (e), colorized as a function of g_2. Scale bars are (a) 10 μm, (e) 5 μm, (f) 1 μm.

by elongation measurements matching that of mono-intercalators [38] (the exact chemical structure is undisclosed by the manufacturer). The sparsity required for localization microscopy is inherent from the transiently binding Sytox Orange that is essentially non-fluorescent when not intercalated [42]. In order to visualize the λ-DNA in a fluorescence microscope, molecular combing is used to align and stretch the DNA on a coverslip by a receding water-air interface [43, 44].

Figure 4.4 shows the potential of combining 3D localization microscopy and orientation estimation by imaging λ-DNA. The super-resolution reconstruction can be color-coded with one of the orientation parameters (azimuthal angle, polar angle or degree of orientational constraint) or the z-position. Figure 4.4(a) shows a subsection of the entire FOV with an azimuthal angle color-coding. The in-plane molecular orientation is clearly perpendicular to the orientation of the DNA-strands. Analyzing a single strand shows an azimuthal angle difference between the fluorophore and the DNA axis of 84° with a median absolute deviation (MAD) of 20° (Fig. 4.4(b)). This is essentially the same as found before ($\Delta\phi = 87°$ and $\mathrm{MAD}(\Delta\phi) = 18°$) [39] and similar to measurements with YOYO [40, 41]. The degree of orientational constraint g_2 along the strand is estimated with a peak at $g_2 = 0.8$, which corresponds to a maximum semi-angle $\alpha \sim 31°$ in the framework of the wobble-in-cone model (Fig. 4.4(c)), slightly larger than $\sim 22°$ found previously [39, 40]. All these parameters are estimated while attaining a lateral resolution (35 nm FWHM λ-DNA line-width) typical for BALM [33, 34] (Fig. 4.4(d)). If the field-dependent aberrations were not taken into account in the fitting model, the localization distribution becomes non-Gaussian with a λ-DNA line-width twice as broad (73 nm FWHM, see Supplementary Fig. 6).

Furthermore, we use an intentionally tilted λ-DNA sample to demonstrate the ability to resolve the lateral structure independent of defocus. This sample is shown in Fig. 4.4(e), where the estimated z position reveals the slope of the tilted λ-DNA sample. Fig. 4.4(f) shows color-coding with the degree of orientational constraint g_2 that can be used to identify patches where binding to partially detached DNA strands and/or non-specific binding occurs. These are visible with a comparably free dipole value $g_2 \sim 0.3$, as opposed to the nearly fixed dipole value $g_2 \sim 0.8$ of the DNA strands. The achieved precision from these experiments, determined from repeated localizations of multiple on-events from the same emitter (Supplementary Fig. 7), is 5.4 nm and 29.7 nm in the lateral and axial dimension, and the azimuth and polar angle precision are 6.0 deg and 3.9 deg, respectively. The localization and orientation precision values determined in this way come close to the predicted CRLB and are within the estimated error bars.

The binding landscape can be investigated by analyzing correlations between the orientational parameters (θ, ϕ, g_2), combined with illuminating with different excitation polarization. To that end we have imaged the same region both with and without a quarter waveplate (QWP) in the illumination laser path (Fig. 4.5(a)). Without the QWP the excitation polarization is vertical and in-plane, most effectively exciting molecules around $\theta = 90°$ (Fig. 4.5(b)). With a QWP the polarization is half in-plane and half out-of-plane resulting in less selective excitation. This results in a polar distribution with more localizations around $\theta = \pm 40°$ (Fig. 4.5(c)). Without the QWP we find the expected relative angle of $\Delta\phi = 87°$ between the fluorophore and DNA axes with almost

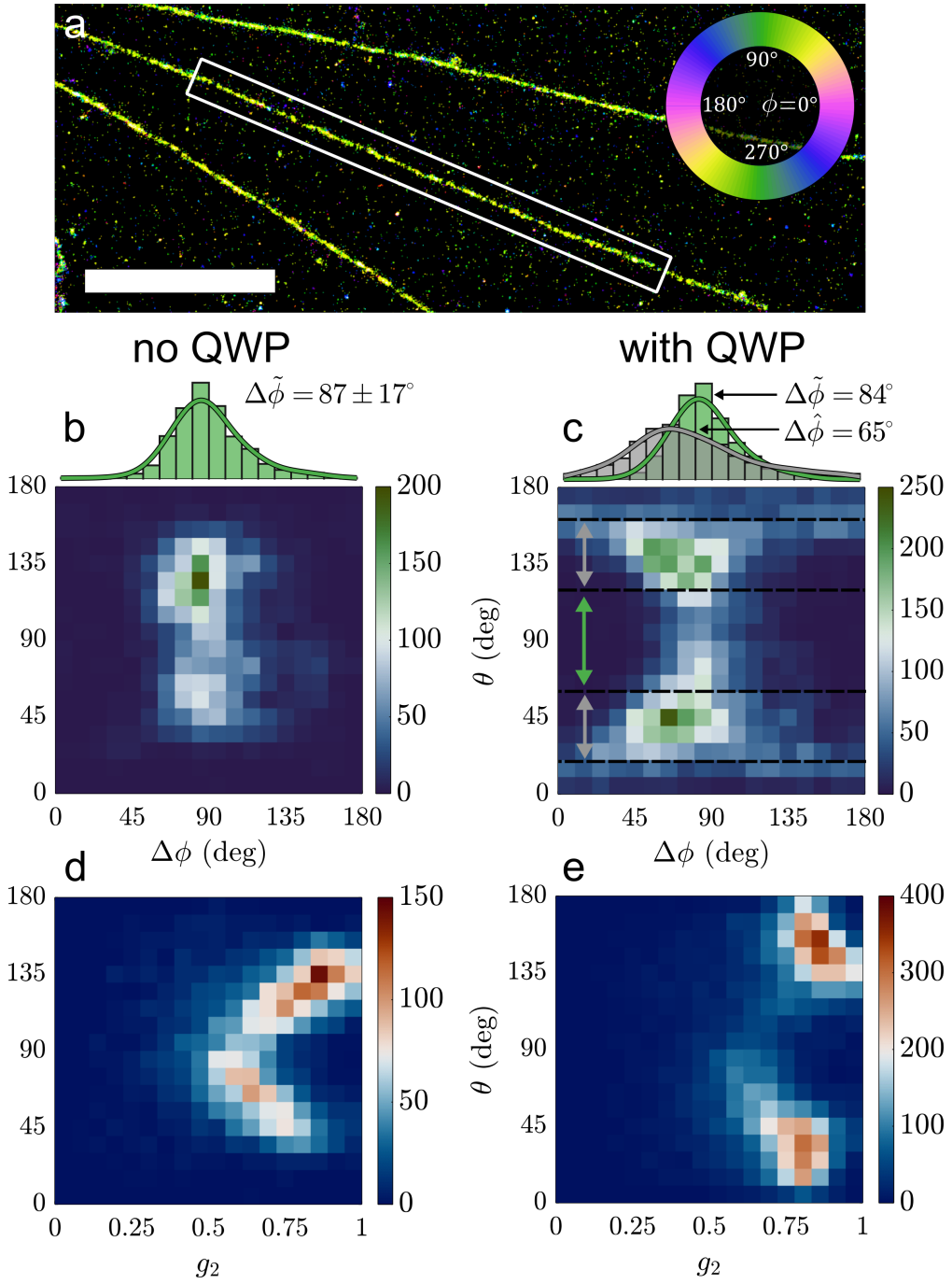

Fig. 4.5: Correlation between orientation parameters of λ-DNA under different excitation polarization. (a) Super-resolution image of λ-DNA strands color coded with the same azimuthal map as Fig. 4.4(a). Scale bar is 3 μm. (b) Histogram of the relative azimuthal angle with respect to the DNA axis from data-set without a QWP in the illumination path. (c) 2D histogram of polar angle vs relative azimuthal angle with the QWP and two highlighted regions of polar angles around $\theta = 90°$ (green) and $\theta = \pm 40°$ (gray). (d) 2D histogram of polar angle vs rotational diffusion coefficient g_2 without a QWP. (e) 2D histogram of polar angle vs rotational diffusion coefficient g_2 with a QWP.

no dependence on the polar angle (Fig. 4.5(b)). With the addition of the QWP a correlation between the polar and azimuthal angle becomes visible. Next to the population of molecules with close to in-plane orientations, that still have the expected relative angle $\Delta\phi = 84°$ (green 1D histogram in Fig. 4.5(c)), a second population of molecules with more out of plane angles $\theta = \pm 40°$ appears, that has a relative angle of $\Delta\phi = 65°$ (gray 1D histogram in Fig. 4.5(c)). Figs. 4.5(d) and (e) show that there is also a correlation between the polar angle and the degree of orientational constraint, where the population of molecules with near in-plane orientation have a smaller g_2 value compared to the population of molecules with clear out-of-plane orientation, showing a looser binding for the in-plane population. These correlations between the orientational parameters are only found in the λ-DNA experiments and are independent of the DNA orientation. Control experiments on fixed single-molecules in air and PMMA show a uniform distribution over the azimuthal angles with no correlation to polar angle or degree of orientational constraint (Supplementary Fig. 8).

One would expect a uniform polar angle distribution for free DNA strands as Sytox Orange should intercalate in any orientation, averaging out any base pair selectivity along the strand. The proximity of the coverslip to the DNA strand could limit the physical space available for intercalators, thereby creating a non-uniform polar angle distribution and possibly shift the equilibrium azimuthal angle away from the orientation perpendicular to the DNA strand. However, this does not explain the preference for $\Delta\phi = 65°$ over $\Delta\phi = 115°$ for both polar angle regions. This may originate from the helical structure of the DNA and the binding potentials between the intercalator and the DNA.

A different hypothesis for the observed correlations between the orientational parameters is a change of the DNA structure to S-DNA due to overstretching. Previously it was found that overstretching results in a change of azimuthal angle to $\Delta\phi \sim 54°$ [40], comparable to the value we find. The typical length of λ-DNA strands in our datasets is 17.4 μm which is 7.4% longer than its crystallographic length [45]. Although this corresponds to a relatively low percentage of overstretching it is possible that the binding affinity is not as low in the proximity of the coverslip as for free DNA strands, resulting in a relatively large population of tilted orientations compared to the DNA strand. We did not observe a correlation between the orientational parameters and the position along the DNA strand, that would correspond to domains along the strand with different orientational binding. This makes this hypothesis less likely.

4.4 Discussion

With the Vortex PSF we achieve a fit that is accurate, avoiding the large position biases commonly seen with fixed dipole emitters in localization microscopy. A key ingredient is that we properly take into account calibrated field-dependent aberrations and supercritical angle fluorescence in the vectorial PSF model to avoid these biases. The relatively compact spot shape enables a more favorable trade-off between the precision of estimating the position and orientational parameters compared to other PSF designs. The

vectorial PSF estimator achieve a precision close to the CRLB, and the CRLB for the Vortex PSF is good for all possible emitter orientations.

We have visualized and measured orientational transitions of single-molecules with metastable attachment to a glass surface. Furthermore we have applied our method to λ-DNA, corroborating previous findings that the azimuthal angle of the intercalator dipoles is almost perpendicular to the DNA axis. Our method uncovered a preferential polar orientation of intercalators attached to λ-DNA on a coverslip, along with a correlation between orientation and orientational constraint. We have applied the Vortex PSF to these two cases to illustrate its functionality, but in principle, the Vortex PSF can be applied to any sparse sample of constrained dipole emitters. Combined with a sparsity inducing single-molecule localization microscopy technique, super-resolution images can be complemented with orientation information to differentiate various sub-sets in the data, such as identifying different binding modes, different orientational configurations or local deformations. Nanoscale interactions could be investigated using chemical models on the single-molecule scale.

An interesting question to address in future studies would be to compare the Vortex PSF to fundamental (quantum) limits of the estimation of orientational parameters [46, 47]. Another step to advance the Vortex PSF concept could be a speed up of the fitting algorithm by developing a GPU implementation, or by using spline interpolated models obtained from PSF calibrations [48] extended to take into account field-dependent aberrations. The feasibility of estimating the emission wavelength in addition to the other parameters could also be investigated. Finally, the analysis could be extended into the regime of slow orientational diffusion. In that regime the illumination polarization has an impact on PSF shape, implying that modulation of the illumination polarization into the method could generate useful information on the orientational constraint and diffusion of the molecule.

4.5 Methods

4.5.1 Fitting model

We use standard Maximum Likelihood Estimation (MLE) using an image formation model that describes the expected photon count across the image as a function of the molecule position $\vec{r}_0 = (x_0, y_0, z_0)$, signal photon count N of the entire PSF on the camera, background photons per pixel b, and dipole orientation $\Omega_0 = (\phi_0, \theta_0)$ with the degree of orientational constraint g_2, giving a total of 8 parameters. The underlying PSF model is the fully vectorial PSF model, as in earlier work [23, 15, 49, 50, 51], but now extended to estimate the dipole orientation along with the degree of orientational constraint. The PSF model is taken to be the weighted sum of the freely rotating dipole PSF and the fixed dipole PSF corresponding to the equilibrium dipole orientation, as appropriate when the rotational diffusion is faster than the fluorescence lifetime [35]:

$$H(\vec{r}, \Omega) = N \left[\frac{(1 - g_2)}{3} H_{\text{free}}(\vec{r}) + \frac{g_2}{3} H_{\text{fixed}}(\vec{r}, \Omega) \right] + \frac{b}{a^2} \tag{4.1}$$

where a is the pixel size and $0 \leq g_2 \leq 1$ represents the degree of orientational constraint, with the limiting cases of a fully free dipole $g_2 = 0$ and a fully fixed dipole $g_2 = 1$. The vectorial model takes supercritical angle fluorescence (SAF) [52, 53] into account. Without accounting for SAF, emitters in the proximity of the coverslip could have an additional position bias up to ~ 10 nm with a medium of water ($n = 1.33$) and ~ 25 nm in air ($n = 1$). Further details on the image formation model are given in Supplementary Note 1.

4.5.2 Microscope calibrated aberrations

An important addition to the fitting model that we make is to take into account calibrated aberrations as done previously [50] and extended further to incorporate the field-dependence of aberrations [54]. We improve upon this treatment by modeling the field dependence of the aberration coefficients using the so-called Nodal Aberration Theory (NAT) instead of 2D polynomials of arbitrary order. This approach is valid for optical imaging systems with small field angles (ratio of FOV to focal length), such as telescopes or microscopes, and has been devised by Shack and Thompson [36], and later extended and used in optical design and characterization studies [55, 56, 57].

The key prediction of NAT is that the dependence of aberration coefficients on the field coordinates is well approximated by Taylor series of a low order, such that there are specific relations between the coefficients of these series for different aberrations. Such relations exist for example between the Taylor series for the two astigmatic and the two coma aberration coefficients, giving rise to zero aberration loci (two, respectively, one for astigmatism and coma), so-called "nodes" in the FOV. The advantage of NAT in the current context is that the Taylor series fit for the different aberrations is more robust due to the predefined number of coefficients. Quantitative details on the aberration field dependence and the calibration procedure are given in Supplementary Note 2. The aberration maps for 12 Zernike modes, determined from calibration measurements on 429 beads, are shown in Supplementary Fig. 4. The NAT predictions are in excellent agreement for astigmatism and coma, and good for the other aberrations modes.

4.5.3 Simulation setup

Simulated point spread functions (PSFs) are generated according to the vectorial PSF model described in Supplementary Note 1. The NA is taken to be 1.45, the wavelength 597.5 nm, the refractive index of the imaging medium 1.33, coverslip 1.523, immersion medium 1.518, and a pixel size of 65 nm in object space in a region of interest (ROI) of 15x15 pixels. Unless stated otherwise, we take 4000 detected signal photons on the camera and 10 background photons per pixel, and we neglect readout noise but add Poisson noise to each image. The number of photons corresponds to the number of photons captured into the NA and thus spread over the entire FOV. The fraction of signal photons captured within the ROI is 0.44 and 0.46 for the standard and Vortex PSF, respectively. The simulations are run for 10,000 randomized instances with coordinates taken from a uniform distribution over ± 1 pixel and molecular dipole ori-

entations uniformly distributed on the unit sphere. That is, if u is a uniform random number from the distribution $U[0,1]$, the simulated angles are taken to be $\phi_0 = \pi u$ and $\theta_0 = \arccos(1-2u)$.

4.5.4 Sample preparation

Cover slips (22x22 mm No. 1.5, Marienfeld-Superior) and microscope slides (Microscope slides, Menzel Gläser Thermo Scientific) are cleaned by sonication in ethanol for 15 minutes and are then blown dry with nitrogen. All further mentions of cleaned cover slips and microscope slides are cleaned the same way except the cover slips for the λ-DNA samples. The microscope slides for the λ-DNA samples have a 5-10 mm hole drilled in them in advance to make it possible for the imaging medium to be added from above. Lambda DNA (λ-DNA) (Lambda DNA, Thermo Scientific) is aliquoted into 10 μL portions in PCR tubes and stored at -20 °C. Ascorbic acid (Ascorbic acid, Merck) is divided into ∼3 mg portions in PCR tubes and the mass written on the tubes and stored at 4 °C. To make a pH 5.5 solution, 1 μL of 400 mM HCl and 600 mM Tris, is diluted in Milli-Q (MQ) water to a pH of 5.5 (approximately 90 mL). Part of a 5 mM stock solution of Sytox orange (SYTOX Orange Nucleic Acid Stain, Invitrogen) is diluted in TE buffer (Tris-EDTA buffer solution pH 7.4, Supelco) by 4 tenfold steps to 500 nM and stored at 4 °C.

Fixed single molecule samples are made by sparsely embedding ATTO 565 in a thin layer of PMMA. 100 mg of PMMA (Poly(methyl methacrylate), Sigma-Aldrich) is dissolved in 10 grams of Toluene (Toluene, Sigma-Aldrich). ATTO 565 (ATTO 565, Sigma-Aldrich) is diluted in MQ water in 100 fold steps to ~ 5 μM. The ATTO 565 dilution is further diluted in PMMA/Toluene in 100 fold steps to a ~ 5 pM concentration. A 20 μL droplet of the mixture is placed on a clean cover slip in the spin-coater and is spun at 3000 RPM for 2 minutes. Two strips of double sided tape (Permanent Double Sided Tape, Scotch) are placed ∼1.5 cm apart on a cleaned microscope slide and the cover slip is placed on top with the PMMA facing the tape side.

For single molecules without PMMA the same procedure is followed except now ATTO 565 is diluted only in MQ water to a final concentration of ~ 500 pM. After spin-coating the coverslip is placed, coated side down, on double sided tape on a microscope slide.

The λ-DNA samples are prepared by dropping a λ-DNA solution onto a rotating silanized cover slip [33, 34]. These cover slips are cleaned more extensively by sonication for 1 hour each in ethanol, acetone and then ethanol again. The cleaned cover slips are stored in ethanol. Before silanizing the surface they are removed from the ethanol and blown dry with nitrogen. An individual dry cover slip is then placed in 15 mL of Poly-L-lysine solution (Poly-L-lysine solution 0.01% sterile-filtered, Sigma-Aldrich) for 5 minutes and slightly shaken 2-3 times. Thereafter the silanized cover slip is rinsed with MQ water and left to dry overnight. A 10 μL $\lambda-$DNA aliquot is thawed and 990 μL of the pH 5.5 solution is added. For a silanized cover slip the optimal combing pH appears to be just below pH 5.5 [45]. 40 μL of this solution is applied in a drop wise fashion to the silanized cover slip on the spin-coater rotating at 2500 RPM for 30 seconds. Thereafter the speed is increased to 7000 RPM and 5 mL of MQ water is applied to rinse away

non attached DNA and left spinning for 2 minutes to dry. A square hole is cut into a piece of double sided tape (64621, Tesa) and placed around the pre-drilled hole in the microscope slide. The cover slip is placed on the tape and pressed down with the λ-DNA side towards the tape. The ascorbic acid is hydrated with TE buffer to a concentration of 200 mM just before the experiment. 25 μL of the ascorbic acid dilution is mixed with 5 μL of 500 nM Sytox Orange and 470 μL of TE buffer. 200 μL of the imaging buffer with a final concentration of 5 nM Sytox Orange and 10mM ascorbic acid in TE buffer is added to the sample through the hole in the microscope slide while on the microscope, focusing and imaging starts as soon as possible.

To determine the aberration maps, 180 nm orange bead samples were used. A 1/100 dilution of 180 nm orange beads (PS-Speck Microscope Point Source Kit, ThermoFisher) is made by mixing 10 μL of beads with 990 μL of MQ water. Using 10 μL of this dilution, 7-10 small droplets are placed around the centre of the cleaned cover slip and allowed to dry for $\sim$3 hours or overnight. Two strips of double sided tape (Permanent Double Sided Tape, Scotch) are placed $\sim$1.5 cm apart on a cleaned microscope slide and the cover slip is placed on top with the beads facing the tape side. When ready to image a 20-30 μL droplet of the mounting medium (in our case immersion oil) is placed on the edge between the cover slip and microscope slide. The capillary action gradually distributes the mounting medium between the cover slip and the microscope slide. The sample is placed on the microscope when the mounting medium has reached the other side.

4.5.5 Imaging protocol

The main component of the optical setup is a standard microscope (Ti-E, Nikon) with a 100x 1.49 NA objective (Supplementary Fig. 9). A 4F relay system consisting of two 100 mm lenses (AC508-100-A-ML, Thorlabs) relays the original image plane of the microscope to the camera (Zyla 4.2 PLUS, Andor) and a vortex phase plate (V-593-10-1, vortex photonics) is placed in the back focal plane between the two lenses. The vortex phase plate is mounted on a small XYZ stage (CXYZ05/M, Thorlabs) for alignment and a kinematic stage (KB75/M, Thorlabs) for quick removal and placement.

The Vortex PSF should be used with a relatively narrow emission bandwidth up to $\sim$ 60 nm. The design wavelength of the phase plate does not need to exactly match the emission peak as long as both parameters are known and set correctly in the estimator. For fixed dipole emission PSF fitting, the fluorophore must have a single molecular dipole moment, this makes bis-intercalators like TOTO [58] and YOYO [59] unsuitable. These dimeric fluorophores have two transition dipole moments between which the excitation energy can hop [60], resulting in emission from either of the two transition dipoles almost perpendicular to one another.

In the proof-of-principle experiments ATTO 565 is embedded in PMMA, where the polymer immobilizes the fluorophores and has a refractive index of $n = 1.49$ close to that of immersion oil ($n = 1.518$). Two z-stack acquisitions with a 100 nm step-size, 600 ms exposure and 300 W/cm^2 epi-illumination are taken in quick succession with and without the vortex phase plate to compare the Vortex PSF to defocused orientation

fitting. Where we use the full z-stack for defocused orientation fitting.

To create a sparse sample of individual dipole emitters that are less constrained and can reorient over time, a low concentration of ATTO 565 without PMMA is spin-coated onto a coverslip. The resulting single-molecules are excited with 3 kW/cm^2 in Total Internal Reflection Fluorescence (TIRF) conditions as the z-component of the TIRF field more effectively excites out-of-plane molecules. A relatively long exposure time of 900 ms is used to yield raw data with a very high SNR.

For the λ-DNA, after applying a fresh batch of imaging buffer and focusing, 20,000 frames are acquired with a single frame exposure time of 100 ms. The sample is illuminated with 3 kW/cm^2 circularly polarized total internal reflection excitation. This results in an excitation profile that is half in-plane and half out-of-plane, and a reduced background due to the limited penetration depth.

4.5.6 Vortex phase plate alignment

The vortex phase plate or spiral phase plate is the same phase profile used to create high-quality donut-shaped depletion and excitation profiles from Gaussian laser beams for STED [61] and MINFLUX [62]. Coincidentally this is also the lowest order component of a Double-helix PSF [63], and a discretized version of a spiral phase plate with only 3-4 phase-steps could be used to generate a rotating PSF [64]. Here we use a vortex phase plate with a single spiral from 0 to 2π in 64 steps (V-593-10-1, vortex photonics).

A 1:1 optical relay is built on the emission path of the microscope to place the vortex phase plate in a plane conjugate to the back focal plane of the objective as illustrated in Supplementary Fig. 9. The phase plate is placed roughly halfway between the two relay lenses. To align the vortex phase plate, defocused images are taken of 1 μm beads (TetraSpeck Fluorescent Microspheres Size Kit, ThermoFisher) and diagonally opposing regions are recorded (Supplementary Fig. 10(a)). If the vortex phase plate is aligned properly, all the PSFs should have the same shape throughout the FOV as shown in Supplementary Fig. 10(b). When the vortex phase plate is not in the correct axial position the PSF will vary over the field of view. This is because light from different areas in the sample do not pass through the vortex phase plate in the same place as it is not conjugate to the back focal plane of the objective. The main parts of the PSF to observe for alignment is the peak in the center that does not move when the phase plate is moved and a ring that moves with the phase plate. The process of aligning the vortex phase plate involves moving the rings to be centered over the peaks over the entire FOV. The vortex phase plate should be translated along the optical axis until all the beads look the same throughout the field of view (same offset between the peak and the ring throughout the FOV) (Supplementary Fig. 10(c)-(d)). Thereafter the vortex phase plate can be shifted horizontally and vertically so the dark spot overlaps with the center of the bead (Supplementary Fig. 10(e)-(f)). Lastly the beads are translated along the optical axis and defocused in the opposite direction to verify that the rings also overlap with the center of the bead there. If the rotation direction of the vortex phase plate is unknown ($K(\vec{\rho}) = \beta/(2\pi)$ or $K(\vec{\rho}) = -\beta/(2\pi)$), then fixed single molecules can be fitted with both orientations and the correct setting will have a visually better fit (should be

especially evident on molecules with $\theta = \pm 45°$).

4.5.7 Data analysis

The acquired images are offset and gain corrected to convert analog-to-digital units (ADUs) into photon numbers [65]. Then, candidate pixels with a single molecule signal are identified using an intensity threshold typically chosen as the background plus a constant of around 10. These candidate pixels are segmented into ROIs of size 15x15 pixels centered at the local centroid. The local centroid gives a better first estimate of the emitter's position than the local maximum due to the Vortex PSF shape. These ROIs are fitted with a vectorial PSF model using Maximum Likelihood estimation (MLE). The vectorial PSF model incorporates emitter parameters described in Supplementary Note 1 and is further tailored to take field-dependent aberrations into account described in Supplementary Note 2. The optical parameters and experimental settings are set to match the experimental setup in Supplementary Fig. 9.

The resulting localizations are corrected for sample drift following the method of Schnitzbauer et al. [66], implemented in the Picasso software (v0.2.8), available at github.com/jungmannlab/picasso. The lateral drift for the λ-DNA experiments was on the order of 1.5 pixels ($\sim$ 100 nm) over 30 minutes. Subsequent localizations of the same emitter during the emitter's on-time are linked under the condition that the position and orientation estimate between subsequent localizations is less than 3 times the largest uncertainty as shown in Supplementary Fig. 7.

All images are rendered with a Gaussian blurring using the scripts from the INSPR toolbox [67]. The images in Fig. 4 are rendered with a super-resolution pixel size of 6.5 nm, and the image in Fig. 5 with a pixel size of 20 nm.

Estimating the axes of single DNA strands is performed by fitting a spline to the localization data. First, a DNA strand is selected from the localization data incorporating all localizations. A spline curve is fitted to the localizations using MATLAB's built-in function *fit()* employing a smoothing spline with a smoothing parameter of 10^{-1}. In order to determine the azimuthal orientations of molecules with respect to the DNA axis, the shortest distance between a given molecule and a point on the spline curve is determined, and the tangent line to the point on the spline is calculated using finite differences, giving the local DNA-strand orientation.

Data availability

Raw image files and processed localization data is available here (10.4121/c.5136125).

Code availability

Matlab code for Vortex PSF simulation, fitting and aberration calibration is available on (github.com/imphys/vecfitcpu_vortex)

Acknowledgments

This work was supported by the European Research Council ERC (648580) and the National Institutes of Health NIH (U01EB021238). We thank Srividya Ganapathy for help preparing the pH 5.5 solution and Marijn Siemons for help with the vectorial PSF estimator applied to SAF conditions.

Author contributions

C.N.H. conceived the project. S.S. and B.R. supervised the research. R.Ø.T., C.N.H. and S.S. developed the PSF estimator. R.Ø.T. developed the NAT aberration estimator and performed all simulations. C.N.H. performed all experiments. R.Ø.T. analyzed the data. C.N.H. and R.Ø.T. wrote the manuscript, S.S. and B.R. edited it.

Competing interests

The authors declare no competing interests.

4.6 References

[1] E. Betzig et al. "Imaging intracellular fluorescent proteins at nanometer resolution". In: *Science* 313.5793 (2006), pp. 1642–1645. ISSN: 00368075.

[2] S. T. Hess, T. P. Girirajan, and M. D. Mason. "Ultra-high resolution imaging by fluorescence photoactivation localization microscopy". In: *Biophysical Journal* 91.11 (2006), pp. 4258–4272. ISSN: 00063495.

[3] M. J. Rust, M. Bates, and X. Zhuang. "Sub-diffraction-limit imaging by stochastic optical reconstruction microscopy (STORM)". In: *Nature Methods* 3.10 (2006), pp. 793–795. ISSN: 15487091.

[4] M. Heilemann et al. "Subdiffraction-resolution fluorescence imaging with conventional fluorescent probes". In: *Angewandte Chemie - International Edition* 47.33 (2008), pp. 6172–6176. ISSN: 14337851.

[5] A. Sharonov and R. M. Hochstrasser. "Wide-field subdiffraction imaging by accumulated binding of diffusing probes". In: *Proceedings of the National Academy of Sciences of the United States of America* 103.50 (2006), pp. 18911–18916. ISSN: 00278424.

[6] R. Jungmann et al. "Single-molecule kinetics and super-resolution microscopy by fluorescence imaging of transient binding on DNA origami". In: *Nano Letters* 10.11 (2010), pp. 4756–4761. ISSN: 15306984.

[7] T. J. Gould et al. "Nanoscale imaging of molecular positions and anisotropies". In: *Nature Methods* 5.12 (2008), pp. 1027–1030. ISSN: 15487091.

[8] H. A. Shaban et al. "Polarized super-resolution structural imaging inside amyloid fibrils using Thioflavine T". In: *Scientific Reports* 7.1 (2017), pp. 1–10. ISSN: 20452322.

[9] E. J. Peterman et al. "Polarized fluorescence microscopy of individual and many kinesin motors bound to axonemal microtubules". In: *Biophysical Journal* 81.5 (2001), pp. 2851–2863. ISSN: 00063495.

[10] E. Toprak et al. "Defocused orientation and position imaging (DOPI) of myosin V". In: *Proceedings of the National Academy of Sciences of the United States of America* 103.17 (2006), pp. 6495–6499. ISSN: 00278424.

[11] M. Wang et al. "Nanoscale deformation in polymers revealed by single-molecule super-resolution localization-orientation microscopy". In: *Materials Horizons* 6.4 (2019), pp. 817–825. ISSN: 20516355.

[12] E. Betzig and R. J. Chichester. "Single molecules observed by near-field scanning optical microscopy". In: *Science* 262.5138 (1993), pp. 1422–1425. ISSN: 00368075.

[13] R. M. Dickson, D. J. Norris, and W. E. Moerner. "Simultaneous imaging of individual molecules aligned both parallel and perpendicular to the optic axis". In: *Physical Review Letters* 81.24 (1998), pp. 5322–5325. ISSN: 10797114.

[14] J. Enderlein, E. Toprak, and P. R. Selvin. "Polarization effect on position accuracy of fluorophore localization". In: *Optics Express* 14.18 (2006), p. 8111. ISSN: 1094-4087.

[15] S. Stallinga and B. Rieger. "Accuracy of the Gaussian point spread function model in 2D localization microscopy". In: *Optics Express* 18.24 (2010), p. 24461. ISSN: 1094-4087.

[16] J. Engelhardt et al. "Molecular orientation affects localization accuracy in superresolution far-field fluorescence microscopy". In: *Nano Letters* 11.1 (2011), pp. 209–213. ISSN: 15306984.

[17] M. D. Lew, M. P. Backlund, and W. E. Moerner. "Rotational mobility of single molecules affects localization accuracy in super-resolution fluorescence microscopy". In: *Nano Letters* 13.9 (2013), pp. 3967–3972. ISSN: 15306984.

[18] M. D. Lew and W. E. Moerner. "Azimuthal polarization filtering for accurate, precise, and robust single-molecule localization microscopy". In: *Nano Letters* 14.11 (2014), pp. 6407–6413. ISSN: 15306992.

[19] M. P. Backlund et al. "Removing orientation-induced localization biases in single-molecule microscopy using a broadband metasurface mask". In: *Nature Photonics* 10.7 (2016), pp. 459–462. ISSN: 17494893.

[20] A. P. Bartko and R. M. Dickson. "Imaging three-dimensional single molecule orientations". In: *Journal of Physical Chemistry B* 103.51 (1999), pp. 11237–11241. ISSN: 15206106.

[21] M. Böhmer and J. Enderlein. "Orientation imaging of single molecules by wide-field epifluorescence microscopy". In: *Journal of the Optical Society of America B* 20.3 (2003), p. 554. ISSN: 0740-3224.

[22] D. Patra, I. Gregor, and J. Enderlein. "Image analysis of defocused single-molecule images for three-dimensional molecule orientation studies". In: *Journal of Physical Chemistry A* 108.33 (2004), pp. 6836–6841. ISSN: 10895639.

[23] K. I. Mortensen et al. "Optimized localization analysis for single-molecule tracking and super-resolution microscopy". In: *Nature Methods* 7.5 (2010), pp. 377–381. ISSN: 15487091.

[24] K. I. Mortensen et al. "Optimized measurements of separations and angles between intra-molecular fluorescent markers". In: *Nature Communications* 6 (2015). ISSN: 20411723.

[25] M. P. Backlund et al. "Simultaneous, accurate measurement of the 3D position and orientation of single molecules". In: *Proceedings of the National Academy of Sciences of the United States of America* 109.47 (2012), pp. 19087–19092. ISSN: 00278424.

[26] A. S. Backer et al. "Single-molecule orientation measurements with a quadrated pupil". In: *Optics Letters* 38.9 (2013), pp. 1521–1523. ISSN: 21622701.

[27] A. S. Backer et al. “A bisected pupil for studying single-molecule orientational dynamics and its application to three-dimensional super-resolution microscopy”. In: *Applied Physics Letters* 104.19 (2014), pp. 1–5. ISSN: 00036951.

[28] O. Zhang et al. “Imaging the three-dimensional orientation and rotational mobility of fluorescent emitters using the Tri-spot point spread function”. In: *Applied Physics Letters* 113.3 (2018). ISSN: 00036951.

[29] S. Stallinga and B. Rieger. “Position and orientation estimation of fixed dipole emitters using an effective Hermite point spread function model”. In: *Optics Express* 20.6 (2012), p. 5896. ISSN: 1094-4087.

[30] B. Rieger and S. Stallinga. “The lateral and axial localization uncertainty in super-resolution light microscopy”. In: *ChemPhysChem* 15.4 (2014), pp. 664–670. ISSN: 14397641.

[31] T. Ding et al. “Single-molecule orientation localization microscopy for resolving structural heterogeneities within amyloid fibrils”. In: *Optica* 7.6 (2020).

[32] V. Curcio et al. “Birefringent Fourier filtering for single molecule coordinate and height super-resolution imaging with dithering and orientation”. In: *Nature Communications* 11.1 (2020), p. 5307. ISSN: 2041-1723.

[33] C. Flors, C. N. Ravarani, and D. T. Dryden. “Super-resolution imaging of DNA labelled with intercalating dyes”. In: *ChemPhysChem* 10.13 (2009), pp. 2201–2204. ISSN: 14397641.

[34] I. Schoen et al. “Binding-activated localization microscopy of DNA structures”. In: *Nano Letters* 11.9 (2011), pp. 4008–4011. ISSN: 15306984.

[35] S. Stallinga. “Effect of rotational diffusion in an orientational potential well on the point spread function of electric dipole emitters”. In: *Journal of the Optical Society of America A* 32.2 (2015), p. 213. ISSN: 1084-7529.

[36] R. V. Shack and K. Thompson. “Influence of alignment errors of a telescope system on its aberration field”. In: *Optical Alignment I*. Vol. 0251. International Society for Optics and Photonics. SPIE, 1980, pp. 146–153.

[37] C. A. V. Cruz et al. “Quantitative nanoscale imaging of orientational order in biological filaments by polarized superresolution microscopy”. In: *Proceedings of the National Academy of Sciences of the United States of America* 113.7 (2016), E820–E828. ISSN: 10916490.

[38] A. S. Biebricher et al. “The impact of DNA intercalators on DNA and DNA-processing enzymes elucidated through force-dependent binding kinetics”. In: *Nature Communications* 6 (2015). ISSN: 20411723.

[39] A. S. Backer, M. Y. Lee, and W. E. Moerner. “Enhanced DNA imaging using super-resolution microscopy and simultaneous single-molecule orientation measurements”. In: *Optica* 3.6 (2016), pp. 659–666. ISSN: 2334-2536.

[40] A. S. Backer et al. "Single-molecule polarization microscopy of DNA intercalators sheds light on the structure of S-DNA". In: *Science Advances* 5.3 (2019). ISSN: 23752548.

[41] H. Mazidi et al. "Dense super-resolution imaging of molecular orientation via joint sparse basis deconvolution and spatial pooling". In: *2019 IEEE 16th International Symposium on Biomedical Imaging (ISBI 2019)*. IEEE, 2019, pp. 325–329. ISBN: 9781538636411.

[42] X. Yan et al. "Development of a mechanism-based, DNA staining protocol using SYTOX orange nucleic acid stain and DNA fragment sizing flow cytometry". In: *Analytical Biochemistry* 286.1 (2000), pp. 138–148. ISSN: 00032697.

[43] A. Bensimon et al. "Alignment and sensitive detection of DNA by a moving interface". In: *Science* 265.5181 (1994), pp. 2096–2098. ISSN: 00368075.

[44] X. Michalet et al. "Dynamic molecular combing: Stretching the whole human genome for high- resolution studies". In: *Science* 277.5331 (1997), pp. 1518–1523. ISSN: 00368075.

[45] J. F. Allemand et al. "pH-dependent specific binding and combing of DNA". In: *Biophysical Journal* 73.4 (1997), pp. 2064–2070. ISSN: 00063495.

[46] O. Zhang and M. D. Lew. "Fundamental limits on measuring the rotational constraint of single molecules using fluorescence microscopy". In: *Physical Review Letters* 122.19 (2019), p. 198301. ISSN: 10797114.

[47] O. Zhang and M. D. Lew. "Quantum limits for precisely estimating the orientation and wobble of dipole emitters". In: *Physical Review Research* 2.3 (2020), p. 33114. ISSN: 0031-899X.

[48] Y. Li et al. "Real-time 3D single-molecule localization using experimental point spread functions". In: *Nature Methods* 15.5 (2018), pp. 367–369. ISSN: 15487105.

[49] C. Smith et al. "Simultaneous measurement of emission color and 3D position of single molecules". In: *Optics Express* 24.5 (2016), p. 4996. ISSN: 1094-4087.

[50] M. Siemons et al. "High precision wavefront control in point spread function engineering for single emitter localization". In: *Optics Express* 26.7 (2018), p. 8397. ISSN: 10944087.

[51] R. Thorsen et al. "Impact of optical aberrations on axial position determination by photometry". In: *Nature Methods* 15.12 (2018), pp. 989–990. ISSN: 15487105.

[52] T. Ruckstuhl and D. Verdes. "Supercritical angle fluorescence (SAF) microscopy". In: *Optics Express* 12.18 (2004), p. 4246. ISSN: 1094-4087.

[53] J. Enderlein, I. Gregor, and T. Ruckstuhl. "Imaging properties of supercritical angle fluorescence optics". In: *Optics Express* 19.9 (2011), p. 8011. ISSN: 1094-4087.

[54] T. Yan et al. "Computational correction of spatially variant optical aberrations in 3D single-molecule localization microscopy". In: *Optics Express* 27.9 (2019), p. 12582. ISSN: 1094-4087.

[55] K. Thompson. "Description of the third-order optical aberrations of near-circular pupil optical systems without symmetry". In: *Journal of the Optical Society of America A* 22.7 (2005), p. 1389. ISSN: 1084-7529.

[56] T. Schmid et al. "Separation of the effects of astigmatic figure error from misalignments using Nodal Aberration Theory (NAT)". In: *Optics Express* 18.16 (2010), p. 17433. ISSN: 1094-4087.

[57] T. Schmid, K. P. Thompson, and J. P. Rolland. "Misalignment-induced nodal aberration fields in two-mirror astronomical telescopes". In: *Applied Optics* 49.16 (2010), p. D131. ISSN: 0003-6935.

[58] H. P. Spielmann, D. E. Wemmer, and J. P. Jacobsen. "Solution structure of a DNA complex with the fluorescent bis-intercalator TOTO determined by NMR spectroscopy". In: *Biochemistry* 34.27 (1995), pp. 8542–8553. ISSN: 0006-2960.

[59] F. Johansen and J. P. Jacobsen. "1H NMR studies of the bis-intercalation of a homodimeric oxazole yellow dye in DNA oligonucleotides". In: *Journal of Biomolecular Structure and Dynamics* 16.2 (1998), pp. 205–222. ISSN: 15380254.

[60] A. Fürstenberg et al. "Ultrafast excited-state dynamics of DNA fluorescent intercalators: New insight into the fluorescence enhancement mechanism". In: *Journal of the American Chemical Society* 128.23 (2006), pp. 7661–7669. ISSN: 00027863.

[61] K. I. Willig et al. "STED microscopy reveals that synaptotagmin remains clustered after synaptic vesicle exocytosis". In: *Nature* 440.7086 (2006), pp. 935–939. ISSN: 14764687.

[62] F. Balzarotti et al. "Nanometer resolution imaging and tracking of fluorescent molecules with minimal photon fluxes". In: *Science* 355.6325 (2017), pp. 606–612. ISSN: 0036-8075.

[63] C. Roider et al. "Axial super-localisation using rotating point spread functions shaped by polarisation-dependent phase modulation". In: *Optics Express* 22.4 (2014), p. 4029. ISSN: 1094-4087.

[64] M. Baránek and Z. Bouchal. "Rotating vortex imaging implemented by a quantized spiral phase modulation". In: *Journal of the European Optical Society* 8 (2013). ISSN: 19902573.

[65] L. V. Vliet, D. Sudar, and I. Young. "Digital fluorescence imaging using cooled charge-coupled device array cameras". In: *Cell Biology* III.Castleman 1996 (1998), pp. 109–120. ISSN: 0263-6484.

[66] J. Schnitzbauer et al. "Super-resolution microscopy with DNA-PAINT". In: *Nature Protocols* 12.6 (2017), pp. 1198–1228. ISSN: 17502799.

[67] F. Xu et al. "Three-dimensional nanoscopy of whole cells and tissues with in situ point spread function retrieval". In: *Nature Methods* 17.5 (2020), pp. 531–540. ISSN: 15487105.

4.A Appendix 1: Supplementary information

4.A.1 Supplementary Note 1: Imaging PSF model

We use a full vectorial PSF model in the Vortex PSF fitting, as initially described in [1], and extend it to incorporate varying degrees of orientational constraint and orientational diffusion [2]. The expected photon count at pixel l depends on the molecule position $\vec{r}_0 = (x_0, y_0, z_0)$, the signal photon count N, background photons per pixel b, and the molecular orientation $\Omega_0 = (\phi_0, \theta_0)$ together with the degree of orientational constraint g_2, giving a total of 8 parameters. The integration of the PSF model H gives the expected photon count:

$$\mu_l = \int_{D_l} \mathrm{d}x\mathrm{d}y\, H(\vec{r} - \vec{r}_0, \Omega) \tag{4.2}$$

where the integration is over the pixel area D_l of size $a \times a$. The PSF model is taken to be the weighted sum of the free dipole PSF and the orientation-dependent fixed dipole PSF, where the relative weights are determined by g_2. This can be written as

$$H(\vec{r}, \Omega) = N\left[\frac{(1-g_2)}{3} H_{\mathrm{free}}(\vec{r}) + \frac{g_2}{3} H_{\mathrm{fixed}}(\vec{r}, \Omega)\right] + \frac{b}{a^2} \tag{4.3}$$

The PSF of a fixed dipole emitter is

$$H_{\mathrm{fixed}}(\vec{r}, \Omega) = \sum_{i,j=x,y,z} A_{ij}(\vec{r}) d_i(\Omega) d_j(\Omega) \tag{4.4}$$

where $d_i(\Omega)$ are the components of the dipole unit vector $\vec{d}(\Omega) = (\sin\theta\cos\phi, \sin\theta\sin\phi, \cos\theta)$. The average PSF of a freely rotating dipole emitter is

$$H_{\mathrm{free}}(\vec{r}) = \frac{1}{3} \sum_{i=x,y,z} A_{ii}(\vec{r}) \tag{4.5}$$

with

$$A_{ij}(\vec{r}) = \sum_{k=x,y} w_{ki}(\vec{r}) w_{kj}^*(\vec{r}) \tag{4.6}$$

where the functions $w(\vec{r})$ represent the electric field component in the image plane proportional to the emission dipole component j. These functions can be expressed as integrals over the pupil plane:

$$w_{kj}(\vec{r}) = \frac{1}{\pi} \int \mathrm{d}^2\rho\, A(\vec{\rho}) \exp\left(\frac{2\pi i W(\vec{\rho})}{\lambda}\right) q_{kj}(\vec{\rho}) \exp(-i\vec{k}\cdot\vec{r}) \tag{4.7}$$

where the integration is over normalized pupil coordinates $\vec{\rho}$, $A(\vec{\rho})$ is the aplanatic amplitude correction factor, and $q_{kj}(\vec{\rho})$ are the polarization vectors given in full detail in

[3]. The wavevector $\vec{k}(\vec{\rho})$ depends on the normalized pupil coordinates by

$$\vec{k}(\rho) = \frac{2\pi}{\lambda}\left(\mathrm{NA}\rho_x, \mathrm{NA}\rho_y, \sqrt{n^2 - \mathrm{NA}^2\vec{\rho}}\right) \tag{4.8}$$

with n the refractive index of the medium. The aberration function $W(\vec{\rho})$ describes the zone function of the vortex phase plate: $K(\vec{\rho}) = \beta/(2\pi)$ where $\beta = \arctan(\rho_x/\rho_y)$ is the azimuth pupil coordinate, and further includes field-dependent aberrations as described in Supplementary Note 2.

The imaging model's partial derivatives with respect to the parameters are needed for the MLE optimization routine. These are easy to evaluate for the signal photon count N, background photons per pixel b, and diffusion weights g_2 as these appear linear in the imaging model μ_k. The derivatives with respect to the fit parameters $\Theta = (x, y, z, \phi, \theta)$ are similar to [4] but now slightly more elaborate:

$$\begin{aligned}\frac{\partial \mu_l}{\partial \Theta} = N \Bigg[& \frac{1-g_2}{3} \sum_{k=x,y} \sum_{j=x,y,z} \int \mathrm{d}^2\rho \, 2\Re\left\{ w_{kj}^* \frac{\partial w_{kj}}{\partial \Theta} \right\} \\ & + \frac{g_2}{3} \sum_{k=x,y} \sum_{j=x,y,z} \int \mathrm{d}^2\rho \, 2\Re\left\{ w_{kj}^* d_j \frac{\partial \left(w_{kj} d_j\right)}{\partial \Theta} \right\} \Bigg]\end{aligned} \tag{4.9}$$

where $w_{kj} = w_{kj}(r - r_0)$ and $d_j = d_j(\Omega)$. The derivatives of w_{kj} with respect to the coordinates of the emitter are needed here:

$$\begin{aligned}\frac{\partial w_{kj}(\vec{r} - \vec{r_0})}{\partial \vec{r_0}} = & \frac{i}{\pi} \int \mathrm{d}^2\rho \, A(\vec{\rho}) \exp\left(\frac{2\pi i W(\vec{\rho})}{\lambda}\right) q_{kj}(\vec{\rho}) \\ & \times \vec{k}(\vec{\rho}) \exp(-i\vec{k}(\vec{\rho}) \cdot (\vec{r} - \vec{r_0}))\end{aligned} \tag{4.10}$$

as are the derivatives of the dipole vector $\vec{d}(\Omega)$ with respect to the polar and azimuthal angles:

$$\frac{\partial \vec{d}(\Omega)}{\partial \phi} = (-\sin\theta \sin\phi, \sin\theta \cos\phi, 0) \tag{4.11}$$

$$\frac{\partial \vec{d}(\Omega)}{\partial \theta} = (\cos\theta \cos\phi, \cos\theta \sin\phi, -\sin\theta). \tag{4.12}$$

4.A.2 Supplementary Note 2: Field dependent aberration coefficients

The aberrations function $W(\vec{\rho})$ is conventionally expressed as a linear sum of the root mean square (RMS) normalized Zernike polynomials $Z_n^m(\vec{\rho})$: $W(\vec{\rho}) = \sum_{n,m} A_n^m \, Z_n^m(\vec{\rho})$. In most studies the Zernike coefficients are constant parameters. In this study we follow the approach of [5] and [6] by taking the dependence on the position in the FOV into account, i.e. we take the Zernike coefficients to be functions of the field coordinates (x, y). These functions $A_n^m(x, y)$ are determined from a calibration procedure. We make

a through-focus image stack of a set of beads randomly spread over the FOV, as opposed to the procedure of [6], where a single bead is positioned on a series of grid positions by the microscope stage. For each bead the Zernike coefficients are retrieved using our previous method [7]. According to Nodal Aberration Theory (NAT), the aberration coefficients $A_n^m(x,y)$ can be suitably described by low order Taylor series in x and y:

$$A_n^m(x,y) = \sum_{jk} \gamma_{nmjk} x^j y^k. \tag{4.13}$$

The set of coefficients γ_{nmjk} of these Taylor series for different positions are related [8], which we use to our advantage as this decreases the number of parameters to be determined from experiments. The NAT-model is fitted to the measured A_n^m at the beads' positions by a straightforward least-squares fit. With this calibration procedure, the estimated Zernike coefficients can effectively be interpolated over the entire imaging field.

We take into account Zernike modes with $n + |m| \leq 6$, which include primary and secondary astigmatism, coma, and spherical aberration, and trefoil, and use the analysis of [9], where polynomials in the field coordinates up to order $6 - n$ are used in the NAT description of the field dependence of the contributing Zernike modes.

In the following, these expressions are summarized as implemented in our fitting using a set of perturbation coefficients $(\chi, \xi, \delta, \mu, \eta, \kappa, \nu)$. Primary astigmatism with perturbation coefficients χ is given by:

$$\begin{aligned} A_2^{-2} &= \chi_1(x^3y + xy^3) + \chi_2(x^2y + y^3) + \chi_3(x^3 + xy^2) \\ &\quad + \chi_4(x^2 + y^2) + \chi_6(xy^2 - x^3) + \chi_7 2xy^2 \\ &\quad + \chi_8 y - \chi_9 x + \chi_{10}(2xy^2) + \chi_{11} x + \chi_{12} y + \chi_{13} \end{aligned} \tag{4.14}$$

$$\begin{aligned} A_2^{2} &= \chi_1(y^4 - x^4) - \chi_2(x^3 + xy^2) + \chi_3(x^2y + y^3) \\ &\quad + \chi_5(x^2 + y^2) - \chi_6 2x^2y + \chi_7(y^3 - x^2y) \\ &\quad + \chi_8 x + \chi_9 y + \chi_{10}(y^2 - x^2) + \chi_{11} y - \chi_{12} x + \chi_{14}, \end{aligned} \tag{4.15}$$

primary coma with coefficients ξ by:

$$\begin{aligned} A_3^{-1} &= \xi_1(x^3 + xy^2) + \xi_2 x^2 + \xi_3 xy + \xi_4 x + \xi_5(x^2 + y^2) \\ &\quad + \xi_7 y + \xi_8 x + \xi_9 \end{aligned} \tag{4.16}$$

$$\begin{aligned} A_3^{1} &= \xi_1(y^3 + x^2y) + \xi_2 xy + \xi_3 y^2 + \xi_4 y + \xi_6(x^2 + y^2) \\ &\quad + \xi_7 x - \xi_8 y + \xi_{10} \end{aligned} \tag{4.17}$$

and primary spherical aberration with coefficients δ by:

$$A_4^0 = \delta_1(x^2 + y^2) + \delta_2 x + \delta_3 y + \delta_4. \tag{4.18}$$

The next aberration order trefoil with coefficients μ is given by:

$$A_3^{-3} = \mu_1(3y^2x - x^3) + \mu_2(y^2 - x^2) + \mu_3 2xy + \mu_4 x + \mu_5 y + \mu_6 \tag{4.19}$$

$$A_3^{3} = \mu_1(y^3 - 3x^2y) - \mu_2 2xy + \mu_3(y^2 - x^2) + \mu_4 y - \mu_5 x + \mu_7 \tag{4.20}$$

secondary astigmatism with coefficients η by:

$$A_4^{-2} = \eta_1 2xy + \eta_2 y + \eta_3 x + \eta_4 \tag{4.21}$$

$$A_4^{2} = \eta_1(y^2 - x^2) - \eta_2 x + \eta_3 y + \eta_5 \tag{4.22}$$

secondary coma with coefficients κ by:

$$A_5^{-1} = \kappa_1 y + \kappa_2 \tag{4.23}$$

$$A_5^{1} = \kappa_1 x + \kappa_3 \tag{4.24}$$

and finally we include secondary spherical aberration, which is expected to be constant in the included polynomial order but here modeled to match equation (4.18), with coefficient ν:

$$A_6^0 = \nu_1(x^2 + y^2) + \nu_2 x + \nu_3 y + \nu_4. \tag{4.25}$$

The independent perturbation coefficients are determined using least-squares over all bead measurements to relate the perturbation coefficient to the Zernike coefficients for the field coordinates. Once the perturbation coefficients are known, the equations (4.14 – 4.25) are used as predictors based on the detected molecule position. The retrieved field-dependent Zernike aberration coefficients for our microscope are shown in Supplementary Fig. 4.9.

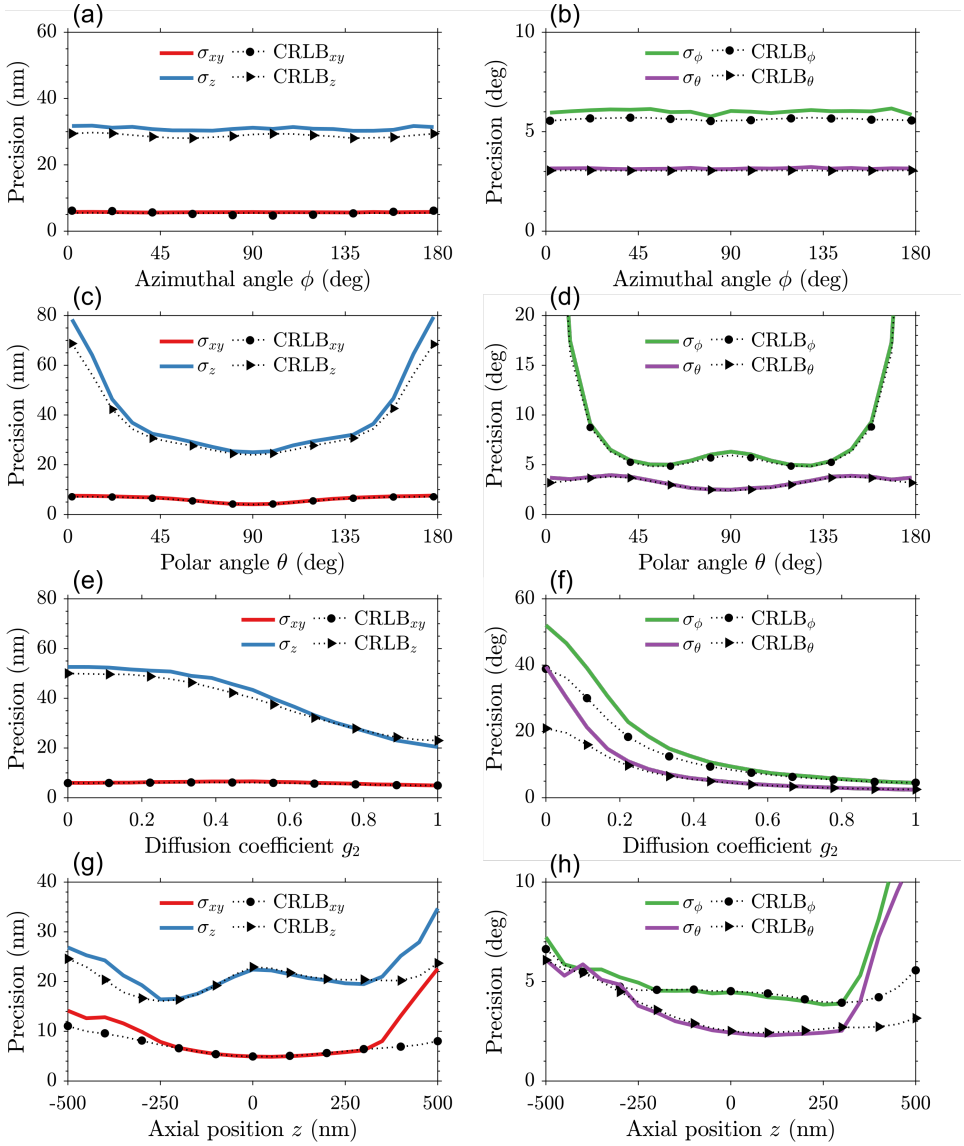

Fig. 4.6: Simulation study of the impact of molecule orientation, rotation diffusion, and axial position on the precision. (a) Average lateral and axial localization precision and (b) orientation precision as a function of the molecule's azimuthal angle with its polar angle uniformly chosen on a sphere, and $g_2 = 0.75$. (c-d) Localization and orientation precision as a function of the polar angle with its azimuthal angle uniformly chosen on a sphere ($g_2 = 0.75$). (e-f) Precision as a function of diffusion coefficient with the molecule's orientation uniformly chosen on a sphere. (g-h) Localization and orientation precision as a function of emitter's axial position, again with the molecule's orientation uniformly chosen on a sphere ($g_2 = 0.75$). The estimator's performance (solid colorized lines) is at the CRLB (black dashed lines with symbols) for all molecule orientations, almost regardless of the rotational diffusion. At extremely low g_2 values (almost a freely rotating dipole) there is however a slight deviation in the angles. The estimator achieves the CRLB for axial positions of $|z| < 300$ and starts to diverge outside this region as the Vortex PSF footprint becomes too large to be contained within the ROI $= 15 \times 15$. Simulation parameters as described in the methods.

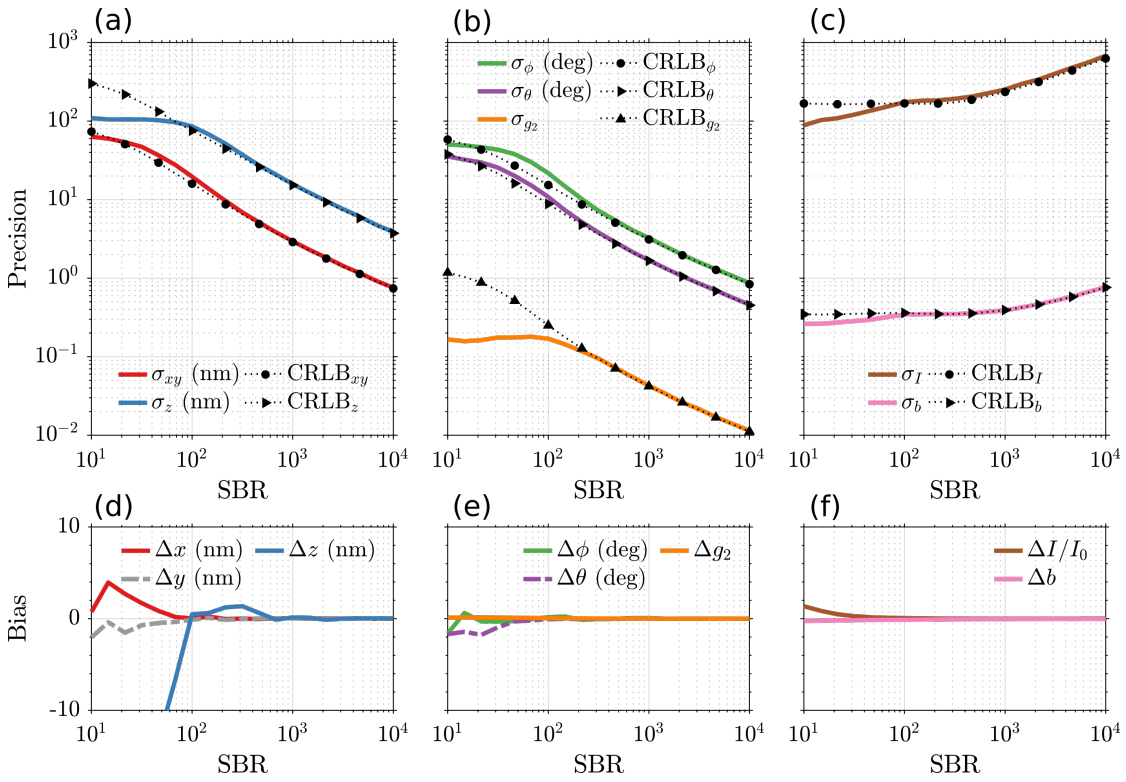

Fig. 4.7: Simulation study of the impact of signal to background ratio (SBR = N/b) on precision and bias of the estimated parameters. (a) Average lateral and axial localization precision using a Vortex PSF model on simulated emitters, simulated with the vectorial PSF (see Methods) as a function of SBR. (b) The orientation precision of the azimuthal and polar angles together with the diffusion coefficient. (c) The photon precision of the signal photons and background photons per pixel. The estimation performance is at the CRLB except at SBR levels below 10^2, indicating that the number of signal photons is too low to assess the Vortex PSF in the image. (d-f) Similarly, the bias of the estimated parameters compared to ground truth for the (d) localization, (e) orientation, and (f) photon errors. Simulation parameters as described in the methods.

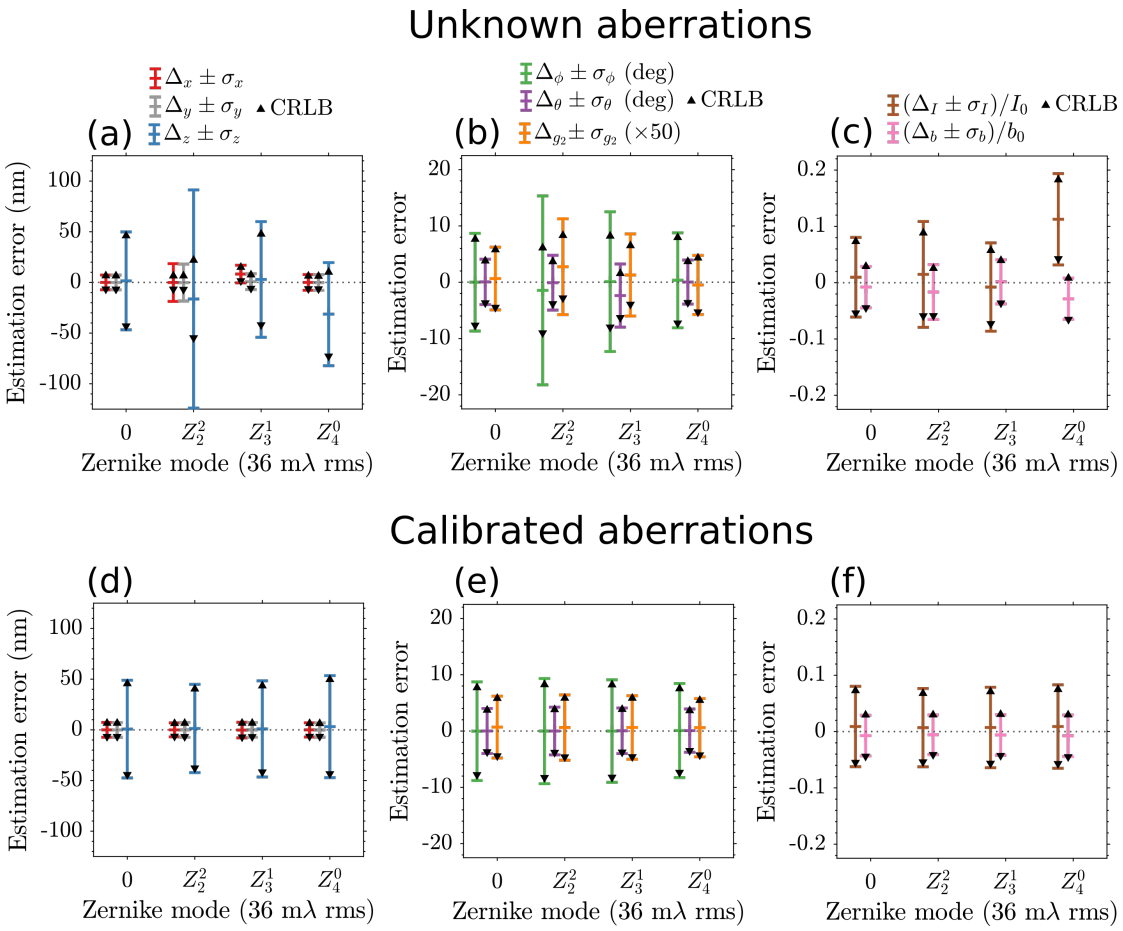

Fig. 4.8: Simulation study of the impact of unknown and known single-mode aberrations while fitting with the Vortex PSF. (a) Lateral and axial localization error using an unaberrated Vortex PSF model on simulated emitters with single-mode aberrations: first-order astigmatism Z_2^2, first-order coma Z_3^1, and first-order spherical Z_4^0 with RMS value of 36 mλ. The error bars indicate the mean and one standard deviation with the black marker indicating the CRLB. (b) In the same way, the orientation error and (c) signal and background photon error. (d-f) Same as (a-c) but including the aberrations in the Vortex PSF model. Fitting with various 36 mλ known aberrations the performance is at the CRLB, and the bias is removed.

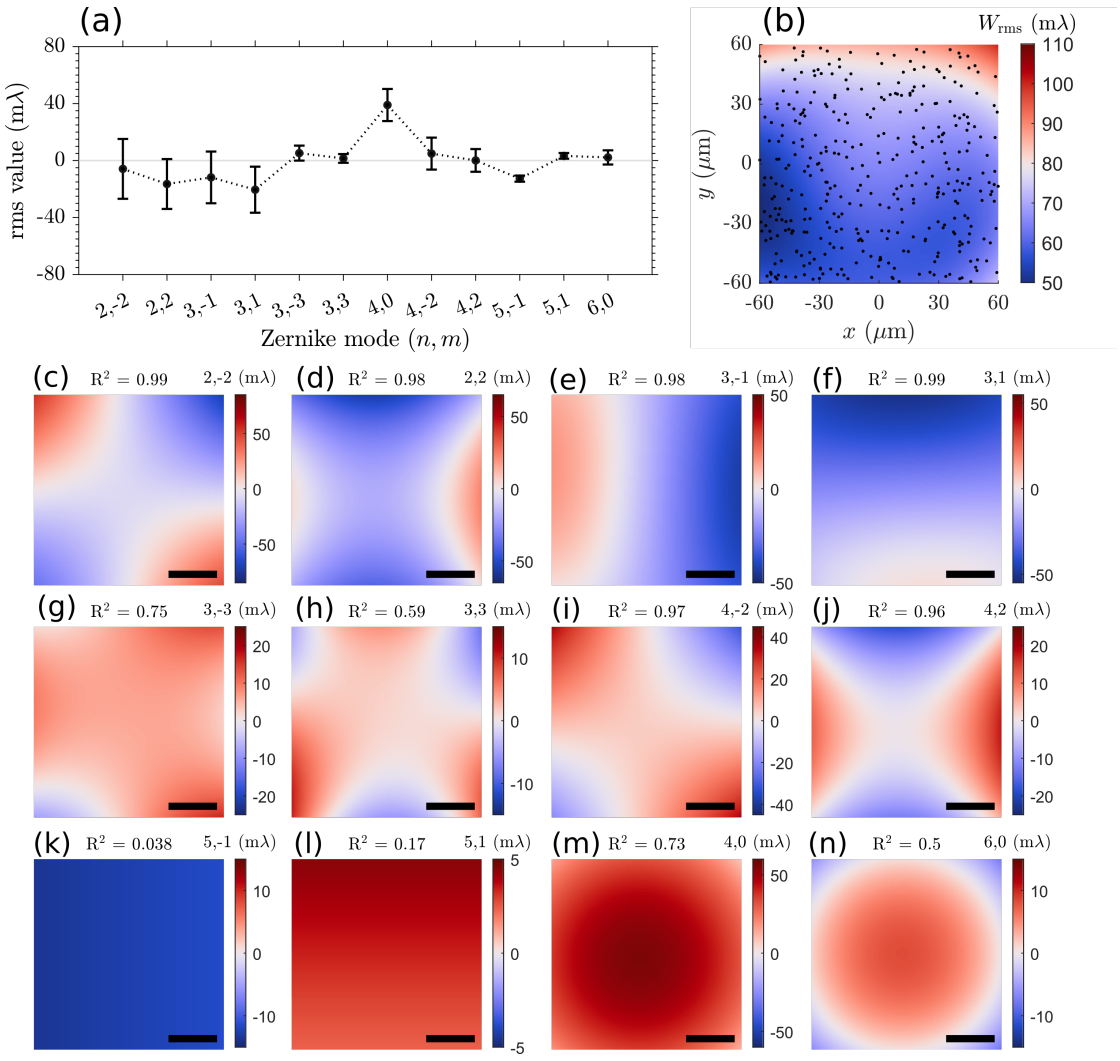

Fig. 4.9: Quantification of aberration retrieval and correction in the field of view (FOV). (a) Fitted Zernike modes and retrieved aberration coefficients over the entire FOV. The coefficients are averaged over 429 bead localizations with error bars indicating the mean and one standard deviation. (b) The total wavefront error from the field aberration surfaces in (c-n). The black dots indicate individual bead locations. (c-n) Fitted field aberrations from the coefficients in (a) and Zernike surfaces as presented in Supplementary Note 2, with R^2 as the quality of fit. Scale bars in (c-n) are 30 μm.

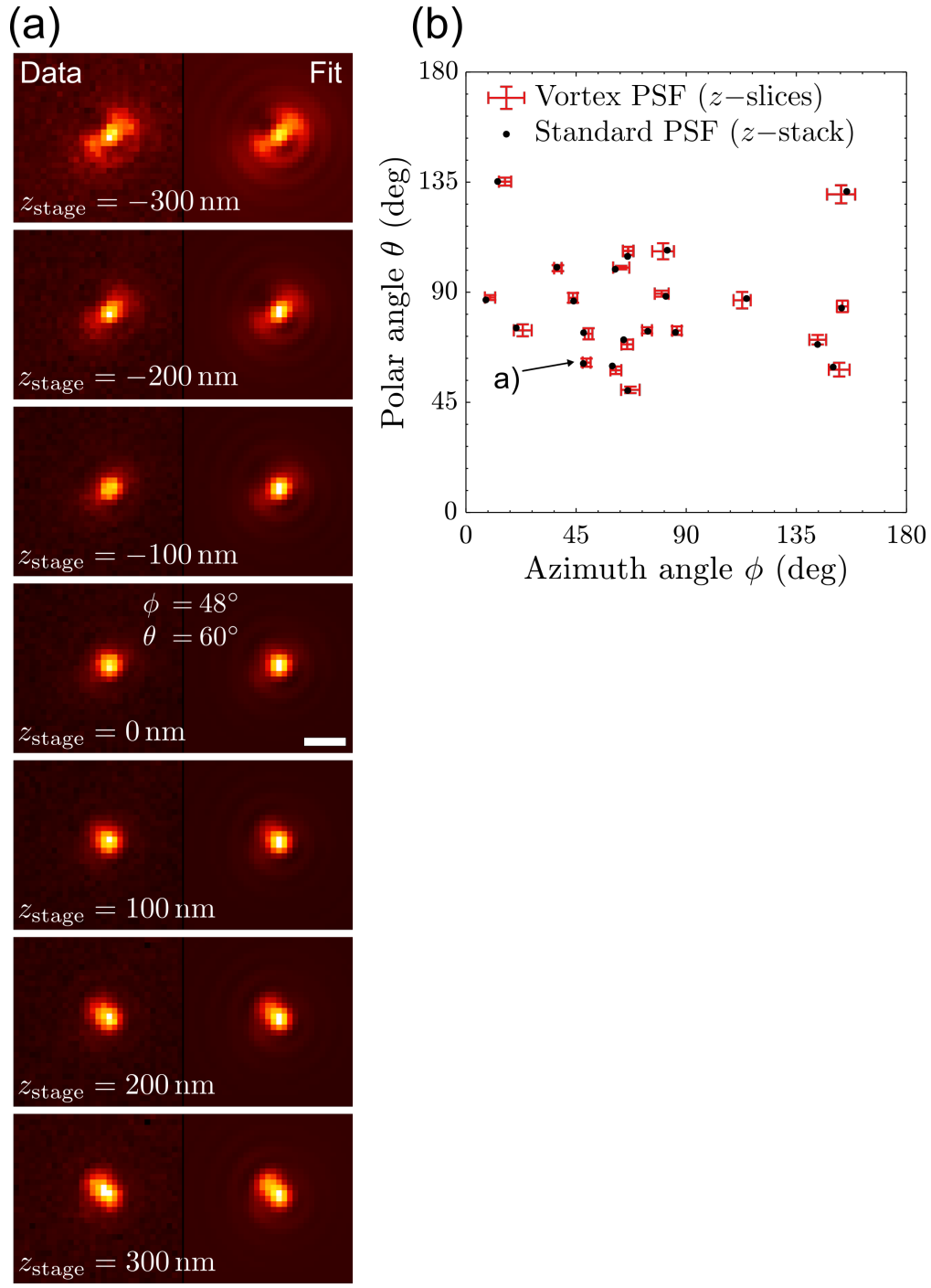

Fig. 4.10: (a) Standard PSF model fitted to an entire z-stack resulting in the estimated orientations of $\phi = 48°$ $\theta = 60°$. This is the same molecule as from Fig. 2 where it was imaged and fitted with a Vortex PSF frame by frame. (b) Estimated orientations of 21 fixed molecules from a standard PSF z-stack and single-frame Vortex PSFs with error bars indicating one standard deviation. Indicating a high precision and no bias between the Vortex PSF and through-focus orientation estimation.

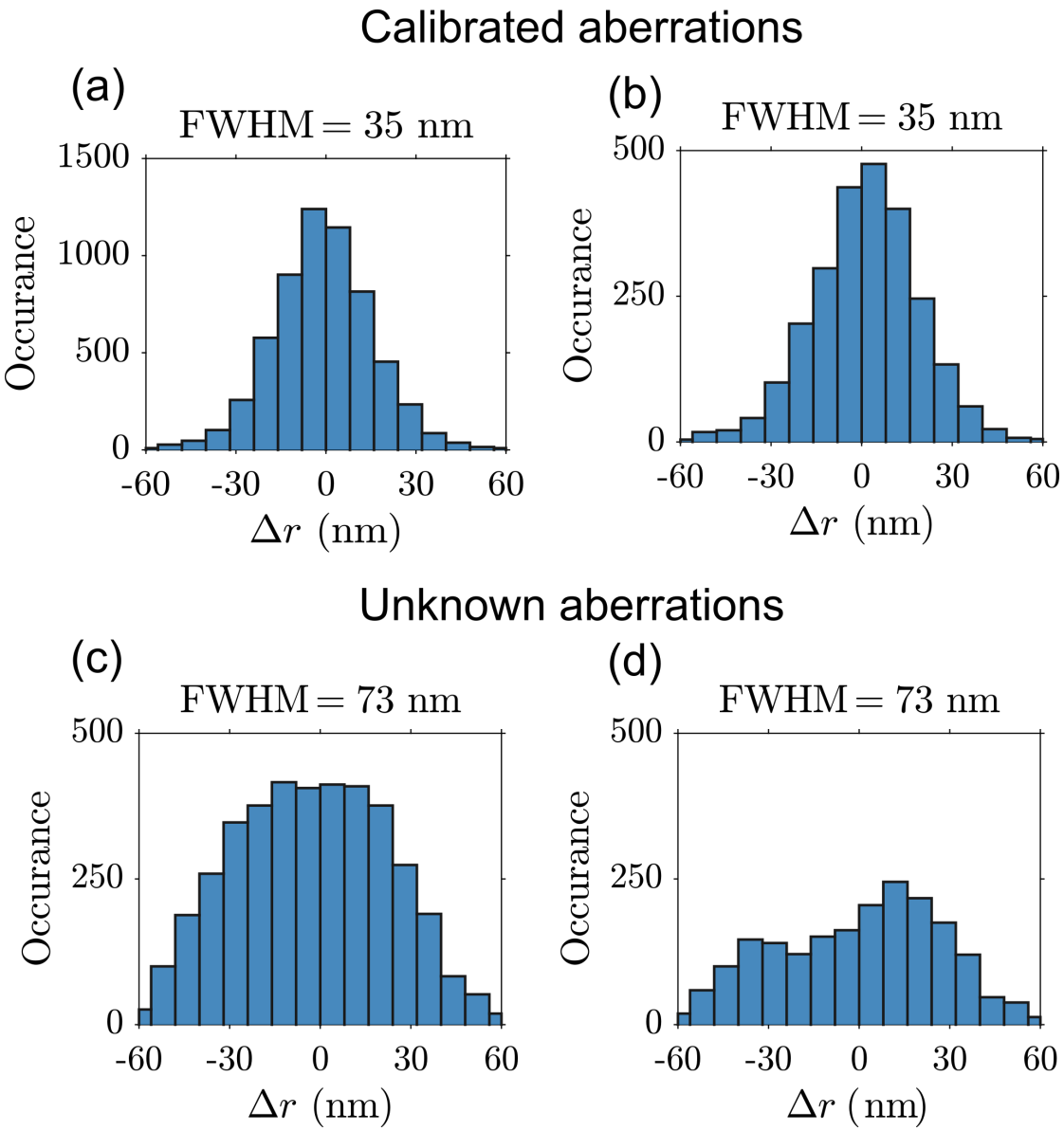

Fig. 4.11: The effect of our calibrated PSF model for the localizations of the $\lambda-$DNA in the main text (Fig. 4(a)). (a) Position deviation from the spline fit to the DNA axis using a calibrated PSF model results in a Gaussian-like distribution with FWHM = 35 nm and (b) for polar angles $45 \leq \theta \leq 135$ results in a similar distribution with FWHM35 nm. (c) Using a PSF model without calibrated aberrations results in a broad distribution with FWHM = 73 nm and (d) for polar angles $45 \leq \theta \leq 135$ results in a non-uniform distribution with FWHM = 73 nm. (a-b) The FWHM is evaluated using a normal distribution fit with support $\Delta r = \pm 40$ nm and (c-d) a non-parametric fit with a normal kernel.

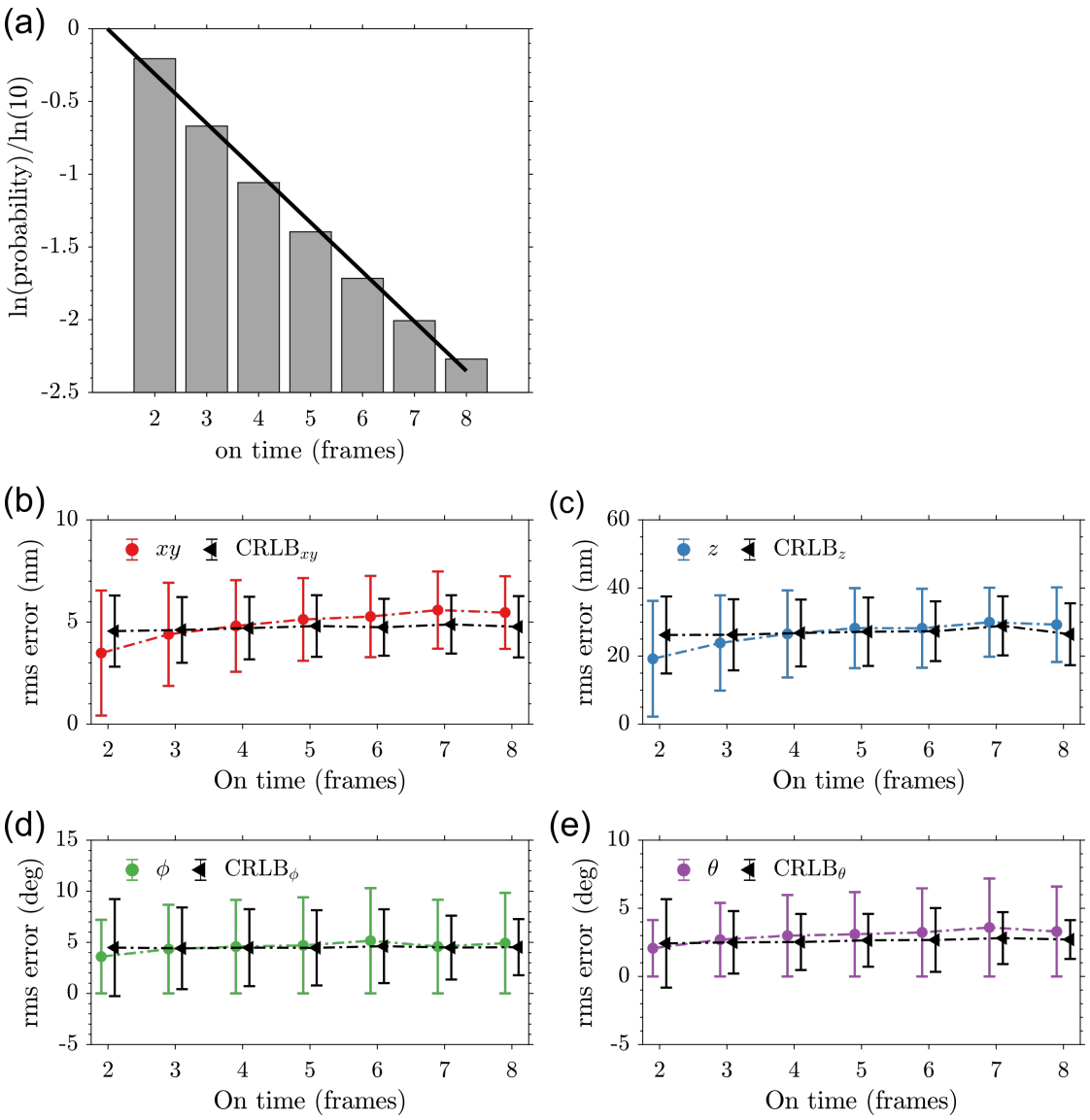

Fig. 4.12: Single-molecule run length analysis in λ-DNA experiment. (a) Natural-logarithm probability-distribution (gray bars) of subsequent on-time events up to 8 frames for the same emitter. The average on-time over all events is 1.5 frames, whereas the fitted exponential distribution gives an on-time of 1.3 frames (black line). (b) Lateral localization error (root-mean-square value) and CRLB (mean and s.d.) determined from repeated localizations. In the same way, (c) axial localization error, (d) azimuth angle error, and (e) polar angle error estimated from repeated localizations. The estimated RMS error matches well with the estimated CRLB for all parameters and the number of on-time events. The total number of linked on-events is 302,541 with experimental conditions and data analysis as further specified in the methods.

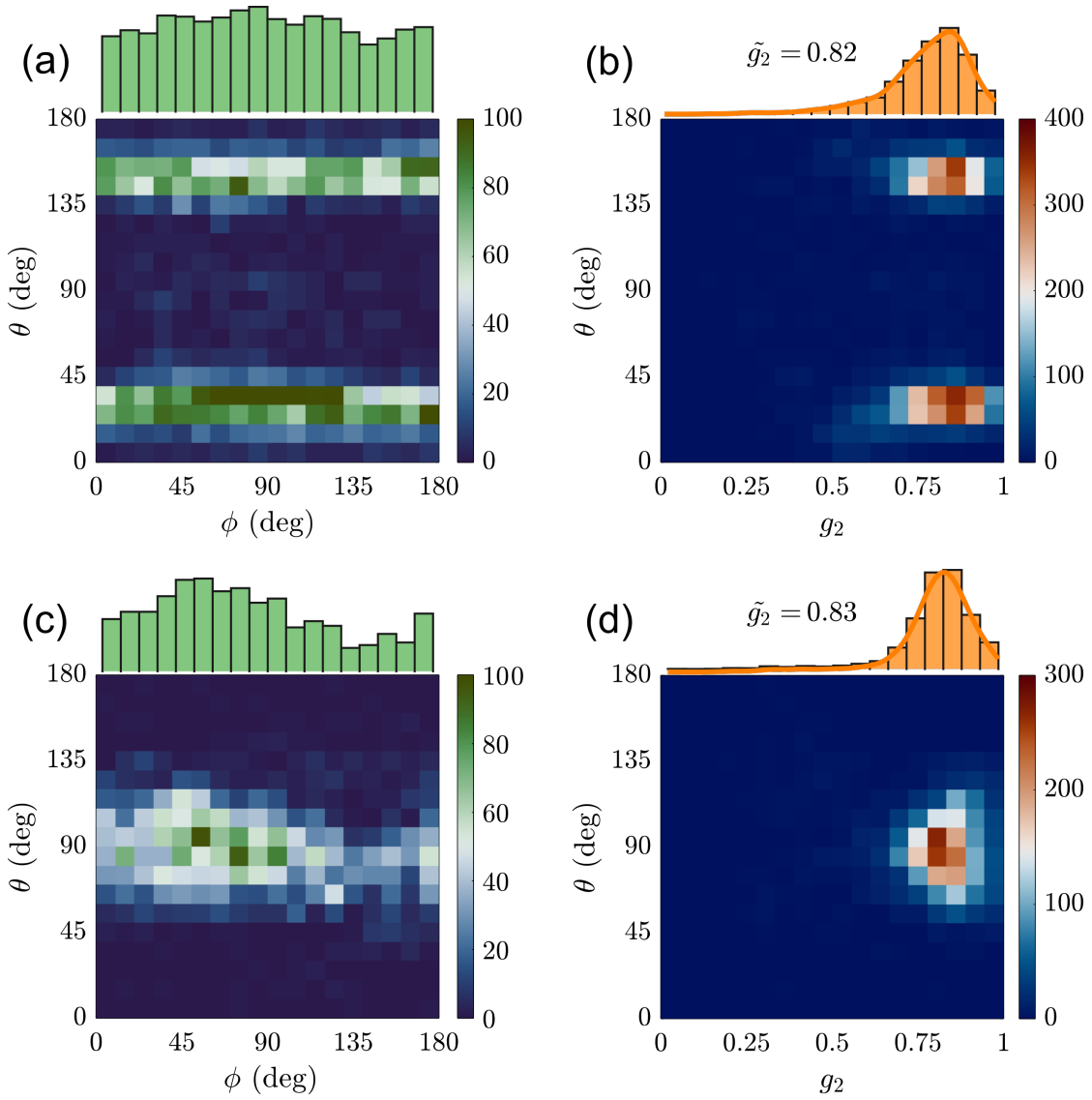

Fig. 4.13: Orientation and diffusion estimation on fixed molecules. (a) Bivariate histogram of the azimuth angle (ϕ) versus polar angle (θ) and (b) diffusion coefficient (g_2) versus polar angle as estimated on single-molecules under TIRF illumination directly spin-coated onto a coverslip. The marginal histograms show the azimuth and diffusion distribution, respectively, with the median diffusion coefficient specified in the plot. (c-d) The same as in (a) and (b), but estimated on single-molecules embedded in a thin layer of PMMA under epi-illumination . In both these experimental cases with different orientation distributions, there is no correlation between the estimated parameters. The number of single-molecules analyzed is 7042 in (a-b) and 4034 in (c-d) with experimental conditions as further specified in the methods.

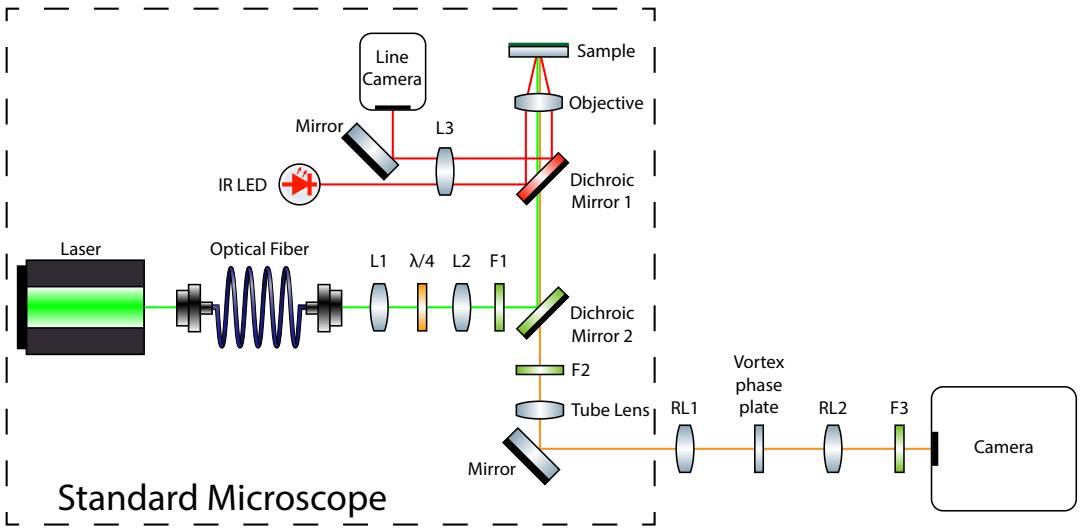

Fig. 4.14: The optical setup, consisting of a simple addition to a standard microscope (Ti-E, Nikon). Lenses RL1 (AC508-100-A-ML, Thorlabs) and RL2 (AC508-100-A-ML, Thorlabs) relay the original image plane to the camera (Zyla 4.2 PLUS, Andor) with no additional magnification resulting in an effective pixel size of 65 nm. The vortex phase plate (V-593-10-1, vortex photonics) is placed in the Fourier plane between these two lenses. The standard TIRF microscope has a focus lock consisting of an infrared light emitting-diode, offset lens L3, Dichroic mirror 1 and a line camera (any unspecified components are part of the Nikon Ti-E or its accessories). The excitation laser (Sapphire 561-150 CW, Coherent) is coupled into a fiber and collimated by lens L1 and thereafter focused onto the back focal plane of the objective (CFI Apochromat TIRF 100XC Oil, Nikon) with lens L2. By translating the fiber face the excitation beam angle coming out of the objective can be adjusted to total internal reflection conditions in the sample. The $\lambda/4$ waveplate converts the linearly polarized laser beam to circular polarization, and the excitation spectrum is filtered by F1 (ZET405/488/561/640x, Chroma). Dichroic mirror 2 (ZT405/488/561/640rpc, Chroma) splits the excitation and emission path and the emission spectrum is further filtered by F2 (ZET405/488/561/640m-TRF, Chroma) and F3 (FF01-609/57-25, Semrock). The tube lens focuses the image from the sample to the front focal plane of lens RL1.

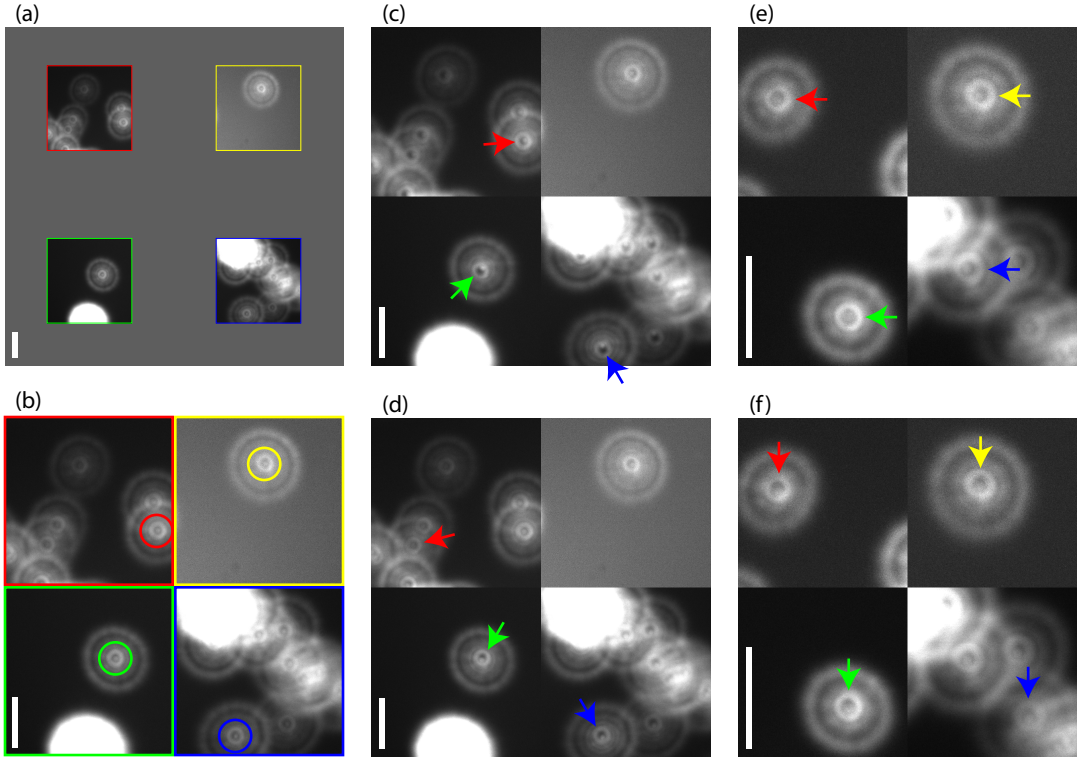

Fig. 4.15: Vortex phase plate alignment. (a) Selected imaged regions of defocused beads on the camera. (b) Zoom in on the four selected regions. The circles highlight the central region where a central peak is surrounded by a bright ring. The bright ring moves as the vortex phase plate is moved, in this image the center of the rings and the peaks coincide and thus the phase plate is properly aligned. (c) Vortex phase plate is too close to the microscope as the rings created by the vortex phase plate are too far radially outward. The arrows indicate the direction in which the rings should be moved. (d) Vortex phase plate is too close to the camera when the rings are too far radially inward. (e) When the vortex phase plate is aligned along the optical axis all spots should look the same throughout the FOV. The position can then be fine-tuned by shifting horizontally. (f) Vortex phase plate slightly misaligned vertically. Scale bars are 10 μm.

References

[1] K. I. Mortensen et al. “Optimized localization analysis for single-molecule tracking and super-resolution microscopy”. In: *Nature Methods* 7.5 (2010), pp. 377–381. ISSN: 15487091.

[2] S. Stallinga. “Effect of rotational diffusion in an orientational potential well on the point spread function of electric dipole emitters”. In: *Journal of the Optical Society of America A* 32.2 (2015), p. 213. ISSN: 1084-7529.

[3] S. Stallinga and B. Rieger. “Accuracy of the Gaussian point spread function model in 2D localization microscopy”. In: *Optics Express* 18.24 (2010), p. 24461. ISSN: 1094-4087.

[4] C. Smith et al. “Simultaneous measurement of emission color and 3D position of single molecules”. In: *Optics Express* 24.5 (2016), p. 4996. ISSN: 1094-4087.

[5] T. Yan et al. “Computational correction of spatially variant optical aberrations in 3D single-molecule localization microscopy”. In: *Optics Express* 27.9 (2019), p. 12582. ISSN: 1094-4087.

[6] M. Siemons et al. “Comparing strategies for deep astigmatism-based single-molecule localization microscopy”. In: *Biomedical Optics Express* 11.2 (2020), p. 735. ISSN: 2156-7085.

[7] M. Siemons et al. “High precision wavefront control in point spread function engineering for single emitter localization”. In: *Optics Express* 26.7 (2018), p. 8397. ISSN: 10944087.

[8] R. V. Shack and K. Thompson. “Influence of alignment errors of a telescope system on its aberration field”. In: *Optical Alignment I*. Vol. 0251. International Society for Optics and Photonics. SPIE, 1980, pp. 146–153.

[9] R. Tessieres. “Analysis for alignment of optical systems”. M.Sc. Thesis. The University of Arizona, 2003.

5 Photon efficient orientation estimation using polarization modulation in single-molecule localization microscopy

5.1 Abstract

The precision of single molecule localization can be improved by shifting a non-uniform illumination pattern. We analyze an extension of this idea to modulation of the polarization of the illumination to enhance the precision of orientation estimation of fixed emitters. Two modes are analyzed: i) normally incident excitation with three polarization steps to retrieve the in-plane angle of the emitters and ii) obliquely incident excitation with p-polarization with five different azimuthal angles of incidence to retrieve the full solid-angle. We present a theoretical study of the Cramér-Rao precision bound for these modes. For the oblique incidence mode we find a favorable isotropic orientation precision for all molecular orientations in case the polar angle of incidence is equal to $\arccos\sqrt{2/3} \approx 35$ deg. A simulation study is performed to assess the performance for low signal-to-background and for inaccurate illumination polarization. We show that a precision, at the Cramér-Rao bound, of just 2.4 deg and 1.6 deg in the azimuthal and polar angles can be achieved with only 1000 detected signal photons and 10 background photons per pixel. These anticipated precision values indicate that modulation of the excitation polarization could enable single molecule orientation imaging at low light levels.

5.2 Introduction

Single-molecule localization microscopy (SMLM) is an established super-resolution microscopy technique, taking image resolution from the 200 nm diffraction limit down to the 20 nm regime with many imaging modalities such as (f)PALM [1, 2], (d)STORM [3], and PAINT [4]. SMLM uses emitters that can switch between off- and on-states such that only a sparse subset of all emitters is active in each image frame of a time series. This temporal modulation allows the active emitters to be localized with a precision an order of magnitude below the diffraction limit. Localizations in different time frames accumulate to a list of emitter positions rather than pixel-based images, which means that

Unpublished work

the image is constituted by a list of single molecule data. New SMLM image modalities can be created by extending this list beyond the x and y coordinates of the molecules [5]. In this paper we focus on the extension with molecular orientation parameters [6]. Typically the emitters are assumed to rotate freely during the emission states. However, cases exist where the emitters have a fixed pose and therefore experience little rotational diffusion, e.g., when rigidly bound to a target [7, 8, 9] or immobilized at a surface [10, 11]. The emitter orientation provides insight into the linker between the biomolecule and fluorophore and must otherwise be taken into account explicitly as it affects the localization precision [12, 13].

The Point Spread Function (PSF) of conventional widefield fluorescence microscopy is poorly suited for orientation estimation because of inherent symmetries such as the symmetry between positions above and below the nominal focus plane. Therefore the imaging system must be altered for extracting this additional information. A first effort was based on defocus imaging for increasing the sensitivity of the PSF shape to changes in molecular orientation [8]. A major drawback is that the defocus spreads the limited number of signal photons across more pixels, which degrades the localization precision. Long exposures are therefore needed to overcome this photon dilution, making these methods less ideal for localization microscopy. An alternative way to increase the orientation information has been proposed with engineered PSFs [14, 15, 16], which can be realized experimentally by adding a phase-shaping element in the optical pathway towards the camera. These PSFs vary in shape and performance, yet commonly increase the PSF size and thereby hinder optimum detection at low signal-to-background ratios (SBRs).

The polarization of the fluorescence excitation and emission is directly coupled to the molecular orientation and therefore offers a direct way to probe orientation. The use of the polarization of the emitted light usually involves placing a polarizing beam splitter in the detection light path to separately collect different polarization components on the camera. The intensity in these sub-images is used as a parametric indicator of molecular orientation [17, 18, 19], which can also be combined with PSF engineering approaches [20, 21, 22, 23]. The polarization of the excitation beam for estimating orientation in SMLM has so far not been explored extensively. Backer, Lee, and Moerner use a sequence of images generated with a normally incident illumination beam with linear polarization that toggles between three different directions [24]. In this technique, three sequential images are used to estimate the in-plane orientation of single molecules. The key advantage of using excitation polarization over emission polarization fitting is that the signal photons are not spread out over a larger area on the camera than the area of a diffraction-limited spot. This implies that extracting orientational information can be expected to be more efficient for excitation polarization schemes at low photon counts, i.e. if the SBR is unfavorable.

In this paper we build on the polarization modulation scheme of ref. [24] by a Cramér-Rao Bound (CRB) analysis of the best possible precision, and by a simulation study of the impact of signal photon count, SBR, and polarization purity on precision. The analysis uses a comprehensive Maximum Likelihood Estimation (MLE) method for simultaneous estimation of position and orientation, improving the routine used by Backer,

Lee, and Moerner that neglects spot shape [25]. In a next step, we overcome a major drawback of the method of ref. [24], namely the inability to estimate the out-of-plane, polar angle of the emission dipole of the molecules. This is achieved by changing the illumination from normal incidence to oblique incidence. Then the illumination polarization can have a sizeable component along the optical axis, which is used to extract the full solid angle (both polar and azimuthal angle). Our re-examination of polarization modulation was inspired by the recent development of modulation-enhanced localization. A series of such estimators have emerged initiated by the work on MINFLUX [26], later followed by SIMFLUX [27] and related proposals [28, 29]. In these concepts a spatially shifted non-uniform illumination pattern is used to improve localization precision, e.g. a standing wave pattern leads to a twofold improvement [27].

The outline of this paper is as follows. We first expand the imaging model by incorporating the excitation efficiency in the signal strength (photon count) by the conventional square of the cosine of the angle between polarization and dipole orientation. We describe a general framework that incorporates both normal and oblique incidence, even for large angles of incidence that may give rise to evanescent wave illumination in Total Internal Reflection Fluorescence (TIRF) imaging. Next, we set up the MLE framework that underlies the CRB analysis. We use this framework for a general theoretical analysis and in our simulation study, in conjunction with a proper vectorial PSF model. The paper is concluded with a discussion of results and an outlook on the next steps.

5.3 Materials and methods

5.3.1 Fluorescence excitation model

Figure 5.1 shows our concept of polarization modulation and spot shape detection. We start by assuming that a single common absorption and emission dipole axis completely describes the emitter's orientation [30]. This orientation is parameterized by the space angle $\Omega = (\phi, \theta)$, a shorthand notation for the combination of azimuthal angle $0 \leq \phi \leq 2\pi$ and polar angle $0 \leq \theta \leq \pi$, or equivalently by its dipole moment along the unit vector $\hat{d} = (\sin\theta\cos\phi, \sin\theta\sin\phi, \cos\theta)$ (Fig. 5.1(a)). This assumption is usually true as most fluorescent label molecules are well-approximated as electric dipoles [31].

The fluorescence excitation efficiency depends on the orientation of this transition moment with respect to the excitation light electric field vector:

$$\mathbf{E} = E\hat{\epsilon}\exp(-i\omega t) \tag{5.1}$$

with E the magnitude, ω the radial frequency, t time, and as always, the physical electric field is given by the real part of this complex expression. The complex vector $\hat{\epsilon}$ fully determines the polarization state and this vector satisfies $|\hat{\epsilon}| = 1$. For a propagating plane wave, the polarization ellipse described by $\hat{\epsilon}$ is perpendicular to the unit vector along the direction of propagation given by the wavevector $\hat{\mathbf{k}} = (\sin\beta\cos\alpha, \sin\beta\sin\alpha, \cos\beta)$, where $\alpha \in [0, 2\pi)$ and $\beta \in [0, \pi/2]$ defines the azimuthal and polar angle of incidence. In the plane perpendicular to this unit vector, the polarization ellipse can be parameterized

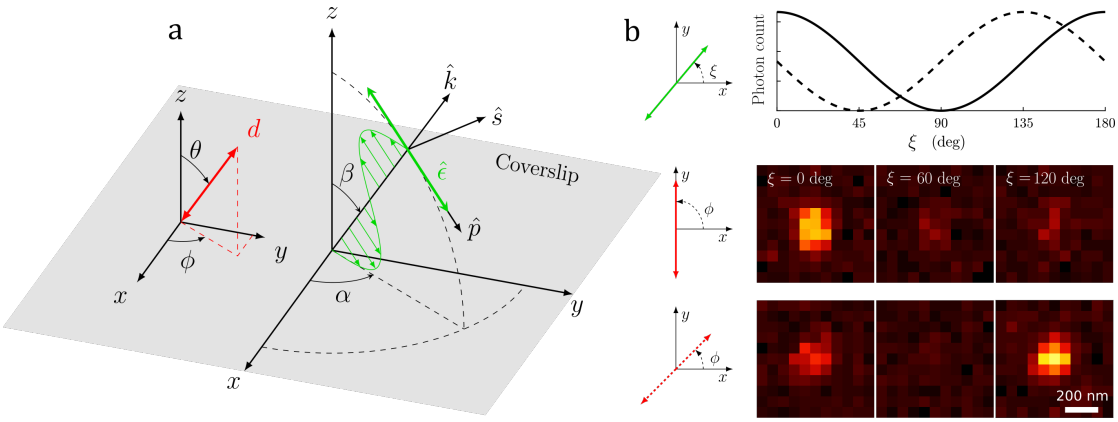

Fig. 5.1: Polarization modulation and spot shape detection. (a) A constrained dipole is characterized by its azimuthal angle ϕ and a polar angle θ, or equivalently its dipole moment $\hat{d}$. The dipole is excited by a plane wave with a direction along the wavevector $\hat{k}$ with incidence angles α and β, and a polarization state $\hat{\epsilon}$ that lies in the plane perpendicular to the wave vector with components $\hat{p}$ and $\hat{s}$. (b) Example of combined estimation for normal ($\alpha = \beta = 0$) excitation with polarization rotation angle ξ. A total of three images are recorded with shifted polarization states at $\xi = [0, 60, 120]$ deg for two dipole emitters with in-plane angles $\phi = 90$ deg and $\phi = 45$ deg. Combining the shape information of the three frames with the photon count in relation to the polarization shift improves the precision.

by an amplitude ratio $\tan\nu$ and a phase delay 2δ leading to:

$$\hat{\epsilon} = \cos\nu\, e^{-i\delta}\hat{\mathbf{p}} + \sin\nu\, e^{i\delta}\hat{\mathbf{s}}, \tag{5.2}$$

with the components $\hat{\mathbf{p}} = (\cos\beta\cos\alpha, \cos\beta\sin\alpha, -\sin\beta)$ and $\hat{\mathbf{s}} = (-\sin\alpha, \cos\alpha, 0)$. In Fig. 5.2(a) the ellipticity angle $\tau \in (-\pi/4, \pi/4]$ and long axis orientation of the polarization ellipse ξ are related to the parameters $\nu \in [0, \pi/2]$ and $\delta \in [0, 2\pi)$ via the Stokes-vector components:

$$S_1 = \cos(2\nu) = \cos(2\tau)\cos(2\xi), \tag{5.3a}$$
$$S_2 = \sin(2\nu)\cos(2\delta) = \cos(2\tau)\sin(2\xi), \tag{5.3b}$$
$$S_3 = \sin(2\nu)\sin(2\delta) = \sin(2\tau), \tag{5.3c}$$

that satisfy $S_1^2 + S_2^2 + S_3^2 = 1$, i.e., Poincaré-sphere coordinates as shown in Fig. 5.2(b) [32]. The ellipticity angle $|\tau| \leq \pi/4$ has limiting cases $\tau = 0$ and $|\tau| = \pi/4$ for linearly and circularly polarized excitation, respectively. For an evanescent plane wave beyond an interface between cover slip and medium at $z = 0$, the relevant unit vectors can be parameterized as $\hat{\mathbf{k}} = (\cosh\sigma\cos\alpha, \cosh\sigma\sin\alpha, i\sinh\sigma)$ and $\hat{\mathbf{p}} = (\sinh\sigma\cos\alpha, \sinh\sigma\sin\alpha, i\cosh\sigma)$, while $\hat{\mathbf{s}} = (-\sin\alpha, \cos\alpha, 0)$ remains unchanged.

If the molecule is effectively stationary during the measurement time, according to the dipole approximation, the measured intensity is proportional to the square of the projection of the transition dipole moment onto the polarization state's direction. Then a fluorophore contributes to the fluorescence signal over a sequence of $m = 1, 2, \ldots, M$

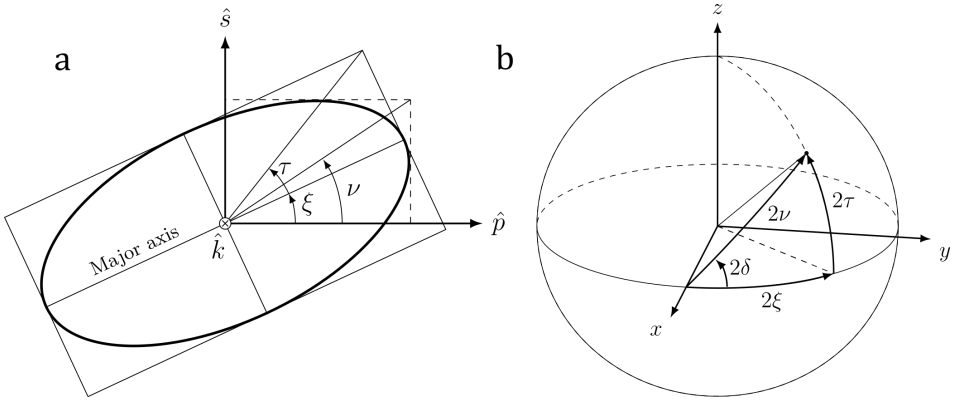

Fig. 5.2: Polarization angles. (a) Polarization ellipse characterized by its major axis angle ξ and ellipticity angle τ or an amplitude angle ν together with the phase delay δ. (b) Poincaré's representation of the state of polarization.

camera frames with changing polarization excitation state $\hat{\epsilon}_m$:

$$
\begin{aligned}
Q_m(\Omega) &= \left|\hat{d}\cdot\hat{\epsilon}_m\right|^2 && (5.4)\\
&= \frac{1}{2}\left[\left|\hat{d}\cdot\hat{p}\right|^2+\left|\hat{d}\cdot\hat{s}\right|^2\right]+\frac{1}{2}\left[\left|\hat{d}\cdot\hat{p}\right|^2-\left|\hat{d}\cdot\hat{s}\right|^2\right]S_1\\
&+ \mathrm{Re}\left\{\left(\hat{d}\cdot\hat{p}\right)\left(\hat{d}\cdot\hat{s}\right)^*\right\}S_2+\mathrm{Im}\left\{\left(\hat{d}\cdot\hat{p}\right)\left(\hat{d}\cdot\hat{s}\right)^*\right\}S_3. && (5.5)
\end{aligned}
$$

From this we define the modulation function :

$$P_m(\Omega)=\frac{Q_m(\Omega)}{Q_{\mathrm{norm}}} \tag{5.6}$$

where Q_{norm} is a normalization condition that depends on the excitation mode such that:

$$\sum_{m=1}^{M} P_m(\Omega)=1. \tag{5.7}$$

This modulation function $P_m(\Omega)$ serves as the expectation function in the estimation process and may often be reduced to a relatively simple expression depending on the excitation mode.

5.3.2 Dipole imaging model

The expected photon count (μ_{nm}) at pixel $n=1,\ldots,N_{\mathrm{pix}}$ is modulated with the function $P_m(\Omega)$ (Eq. 5.6) over a sequence of $m=1,\ldots,M$ frames with different excitation polarization states. This expected count depends on the emitter position $\mathbf{r}_0=(x_0,y_0)$, the total signal photon count N and background photons per pixel b, and the dipole ori-

entation Ω, given a total of 6 parameters to be estimated. The expected photon count is given by:

$$\mu_{nm} = NP_m(\Omega)H_n(\vec{r}_0, \Omega) + \frac{b}{a^2 M} \tag{5.8}$$

where a is the pixel size and $H_n(\vec{r}_0, \Omega)$ is the expected fluorescence intensity distribution of pixel n for a fluorophore at position $\mathbf{r}_0$ and with orientation Ω, normalized such that:

$$\sum_n H_n(\vec{r}_0, \Omega) = 1. \tag{5.9}$$

The normalized fluorescence intensity is computed using the vectorial PSF model described elsewhere [33, 34]. For the sake of completeness, the details are presented in appendix 5.A. We use standard Maximum Likelihood Estimation (MLE) methods based on the Poissonian noise distribution to find the 6 parameters $(x_0, y_0, N, b, \theta, \phi)$ that best fit the observed single molecule spots [35].

5.3.3 Evaluation of Fisher-information and Cramér-Rao bounds

The expected precision for estimating the different parameters can be assessed by developing an approximation to the Fisher-matrix and the Cramér-Rao bound (CRB). Here we focus on the modulated parameters Ω as the unmodulated ones behave as in standard SMLM, which have been investigated extensively previously [33, 36]. The starting point to retrieve the Fisher-information matrix is the log-likelihood function, where its derivatives with respect to the parameters give rise to the Fisher-information elements [35]. These can be expressed in closed-form if we ignore the finite pixel size, neglect the region of interest's (ROI) finite support, and assume zero background. Following the approach in [27] with the imaging model given by Eq. (5.8), the relevant Fisher-matrix elements involving the modulated parameters become:

$$F_{\Omega\Omega} \approx N \sum_{n=1}^{N_{\text{pix}}} \frac{1}{H_n(\mathbf{r}_0, \Omega)} \left(\frac{\partial H_n(\mathbf{r}_0, \Omega)}{\partial \Omega} \right)^2 + N \sum_{m=1}^{M} \frac{1}{P_m(\Omega)} \left(\frac{\partial P_m(\Omega)}{\partial \Omega} \right)^2 \tag{5.10}$$

where the first term arises from orientation-induced information in the shape of the PSF, the same as for conventional SMLM, and where the second term originates from the polarization modulation. This second term implies that modulation makes these diagonal Fisher-matrix elements larger and hence the associated CRB smaller due to the inversion relation $\text{CRB}_\Omega = [F_{\Omega\Omega}]^{-1}$ (the off-diagonal mixing between the orientational parameters Ω and the other parameters is zero).

A simplified approach to assess the impact of modulation is to evaluate Eq. (5.10) under the assumption that the contribution to the Fisher-information from modulation is much larger than the contribution from the PSF shape variations, i.e., the orientation dependency of the PSF is neglected (e.g., for a 2D Gaussian model). This assumption

is, however, not used for the actual numerical parameter estimation in simulation later.

Normal incidence

For normally incident light ($\alpha = \beta = 0$) the polarization vector is restricted to the xy imaging plane ($\epsilon_z = 0$). The non-zero components of the polarization vector are $\epsilon_x = \cos\xi\cos\tau - i\sin\xi\sin\tau$ and $\epsilon_y = \sin\xi\cos\tau + i\cos\xi\sin\tau$, with ξ the in-plane orientation of the polarization ellipse and with τ the ellipticity angle (Fig. 5.2). The polarization modulation is implemented by rotating the long axis of the polarization ellipse with equidistant angles $\xi_m = \pi(m-1)/M + \xi_0,\ s = 1, 2, \ldots, M$. The angles are taken relative to the x axis with offset ξ_0, and the number of polarization steps must be $M \geq 3$ to ensure the uniqueness of the solution. Note that the scan range of the equidistant phases is over the π phase range, which is enough to span the polarization plane due to the head-tail symmetry of the dipole axis. Now Eq. (5.6) gives a modulation function that only depends on the azimuthal dipole angle ϕ:

$$P_m(\phi) = \frac{1}{M}\left[1 + \cos(2\tau)\cos\left(2\phi - 2\xi_m\right)\right]. \tag{5.11}$$

It is seen that the modulation contrast is degraded by the ellipticity factor $\cos(2\tau)$, where $\tau = 0$ results in the often-used cosine squared scaling factor $\cos^2(\phi - \xi_m)$, whereas in the case $|\tau| = \pi/4$ no modulation occurs. This modulation factor results in a CRB with a slight dependence on the dipole azimuthal angle ϕ, making the precision somewhat anisotropic. Figure 5.3(a) shows this dependence indicating a strong response on τ close to $\tau \approx 0$ at dipole orientation when one of the images is acquired when the molecule is perpendicular to a polarization step. These sharp peaks are mitigated in practice due to non-zero background, as indicated with the gray line in Fig. 5.3(a).

The modulation only approximation to the Fisher-information can be deduced by substituting Eq. (5.11) in the second term of Eq. (5.10) and computing the sum over the different excitation polarizations:

$$F_{\phi\phi} = \frac{4N}{M}\sum_{m=1}^{M}\frac{\cos^2(2\tau)\sin^2(2\phi - 2\xi_m)}{1 + \cos(2\tau)\cos(2\phi - 2\xi_m)} \tag{5.12}$$

The average Fisher-information over all the molecule orientations follows as:

$$\tilde{F}_{\phi\phi} = \frac{1}{2\pi}\int_0^{2\pi} \mathrm{d}\phi\, F_{\phi\phi} = 4N(1 - 2\cos\tau\,|\sin\tau|) \tag{5.13}$$

where the integral over ϕ can be evaluated using contour integration in the complex plane (substitute $z = \tan\phi$) or by a computer algebra program. This result in the average precision bound:

$$\tilde{\sigma}_\phi \geq \frac{1}{2\sqrt{N}}\frac{1}{\sqrt{1 - 2\cos\tau|\sin\tau|}} \tag{5.14}$$

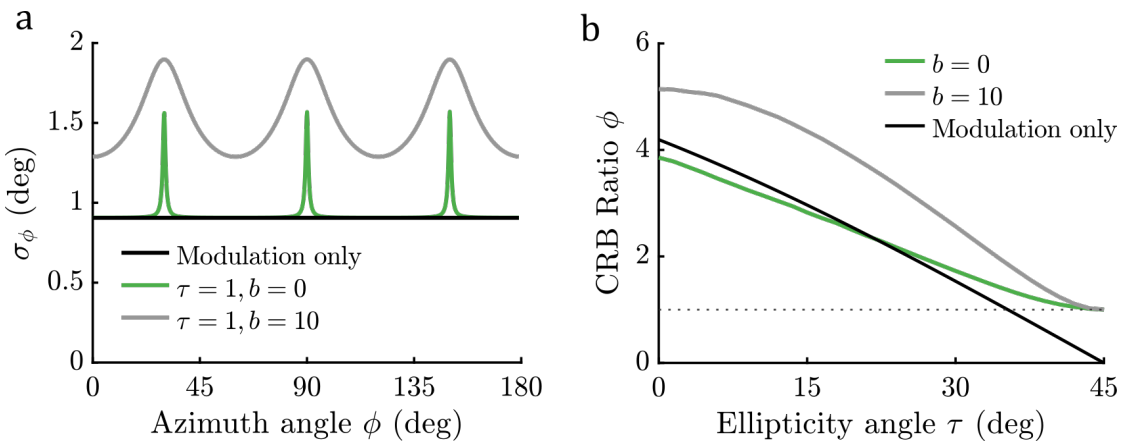

Fig. 5.3: CRB performance for normally incident polarization. (a) The azimuth angle precision σ_ϕ as a function of the dipole azimuth angle ϕ with polar angle $\theta = \pi/2$ using $M = 3$ polarization steps $\xi_m = [0, 60, 120]$ (deg). The precision is computed using Eq. (5.14) with different ellipticity angles τ and numerically with background photons per pixel b. (b) The CRB ratio is computed as the average CRB from the polarization modulation relative to the standard (non-modulated) PSF and is shown as a function of the ellipticity angle. The modulation only is calculated relative to Eq. (5.14). The black dashed line indicates no improvement, i.e., a CRB ratio of 1. All plots are computed with photon count $N = 1000$ and the dipole simulations assumes matched imaging conditions $n = 1.518$.

independent of the angle offset ξ_0 and referred to as the modulation only precision. The scaling with $1/\left(2\sqrt{N}\right)$ for linear polarization is a factor $\sqrt{2}$ better than the scaling found for polarimetric detection schemes [37, 38].

This modulation only CRB is plotted relative to the CRB of the standard (non-modulated, $M = 1$) PSF in Fig. 5.3(b) as a function of the ellipticity angle τ. The CRB of the PSF shape is computed numerically from simulated dipole images. The comparison supports the assumption that the modulation term dominates the Fisher-information, at least for the regime $\tau < 30$ deg. It is likewise seen that effects of the finite support of the fitting Region Of Interest (ROI) and of finite pixel size are negligible. The CRB ratio indicates that the precision improves up to four-fold ($\tau = 0$) by the polarization modulation. The CRB ratio in the presence of background ($b = 10$ counts/pixel) is also numerically computed, where the CRB ratio is found to increase to around five. This indicates that the polarization modulation precision scales better with background than the precision based on PSF shape alone. The average precision for $N = 1000$ with zero background ($b = 0$) is $\sigma_\phi = 0.99$ deg ($\sigma_\phi = 3.8$ deg for $\tau = \pi/4$), whereas for $b = 10$ it is $\sigma_\phi = 1.5$ deg ($\sigma_\phi = 7.7$ deg for $\tau = \pi/4$). These optimum azimuthal precision levels are better than for example the recent Vortex PSF based method [16], and also better than the experimental results of the original polarization modulation method of ref. [24]. There, an experimentally obtained precision of $\sigma_\phi = 233.9/\sqrt{N = 1000} \approx 7.4$ deg for molecules in PMMA (Polymethylmethacrylate) with 50 background counts per pixel per frame is reported. For the same photon counts, we assess the CRB to be around 3.0

deg. This difference could be due to experimental inaccuracies or to the non-MLE based estimation method [25].

Oblique excitation

Favorable precision levels can be achieved for both the azimuthal and polar angle of the molecule if we generalize the previous scheme to obliquely incident light. This approach to polarization modulation uses the polarization component along the optical axis to probe the polar angle. For the sake of simplicity, we ignore ellipticity now and consider only linearly polarized light along with the $\hat{p}$ direction, i.e., $\xi = \tau = 0$. Modulation of polarization is achieved by rotating the direction of incidence around the z-axis, i.e., we take the tilt angle β constant and use azimuthal angles of incidence with equidistant steps $\alpha_m = 2\pi(m-1)/M$. We now find that:

$$Q_m(\phi,\theta) = \left(\sin\theta\cos\beta\cos\left(\phi-\alpha_m\right) - \cos\theta\sin\beta\right)^2 \tag{5.15}$$

giving rise to a normalization factor:

$$Q_{\text{norm}} = \frac{M}{2} f(\theta) \tag{5.16}$$

with angular dependence:

$$f(\theta) = \cos^2\beta - \left(3\cos^2\beta - 2\right)\cos^2\theta \tag{5.17}$$

The relevant angular derivatives of the expectation function $P_m(\theta,\phi)$ are:

$$\frac{\partial P_m(\theta,\phi)}{\partial\phi} = -\frac{4}{Mf(\theta)}\sqrt{Q_m}\sin\theta\cos\beta\sin(\phi-\alpha_m) \tag{5.18a}$$

$$\frac{\partial P_m(\theta,\phi)}{\partial\theta} = \frac{4}{Mf(\theta)}\left[\sqrt{Q_m}\left(\cos\theta\cos\beta\cos(\phi-\alpha_m) + \sin\theta\sin\beta\right) - \frac{Q_m}{f(\theta)}\left(3\cos^2\beta - 2\right)\cos\theta\sin\theta\right] \tag{5.18b}$$

where $Q_m = Q_m(\phi,\theta)$ (Eq. 5.15). These derivatives leads to the modulation-only diagonal Fisher-matrix elements:

$$F_{\phi\phi} = \frac{8N\sin^2\theta\cos^2\beta}{Mf(\theta)}\sum_{m=1}^{M}\sin^2(\phi-\alpha_m) = \frac{4N\sin^2\theta\cos^2\beta}{f(\theta)} \tag{5.19a}$$

$$F_{\theta\theta} = \frac{8N\cos^2\beta\sin^2\beta}{f^3(\theta)}\left[f(\theta) + \frac{c_1}{M}\sum_{m=1}^{M}\cos\left(2\phi-2\alpha_m\right) + \frac{c_2}{M}\sum_{m=1}^{M}\cos\left(\phi-\alpha_m\right)\right] = \frac{8N\cos^2\beta\sin^2\beta}{f^2(\theta)} \tag{5.19b}$$

where $c_1 = 2\cos^2\theta\sin^2\beta$ and $c_2 = \sin(2\theta)\sin(2\beta)$. The off-diagonal Fisher-matrix element $F_{\phi\theta}$ is zero, implying that the precision bounds are:

$$\sigma_\phi \geq \frac{\sqrt{f(\theta)}}{2\sin\theta\cos\beta\sqrt{N}} \tag{5.20a}$$

$$\sigma_\theta \geq \frac{\sqrt{2}f(\theta)}{4\sin\beta\cos\beta\sqrt{N}} \tag{5.20b}$$

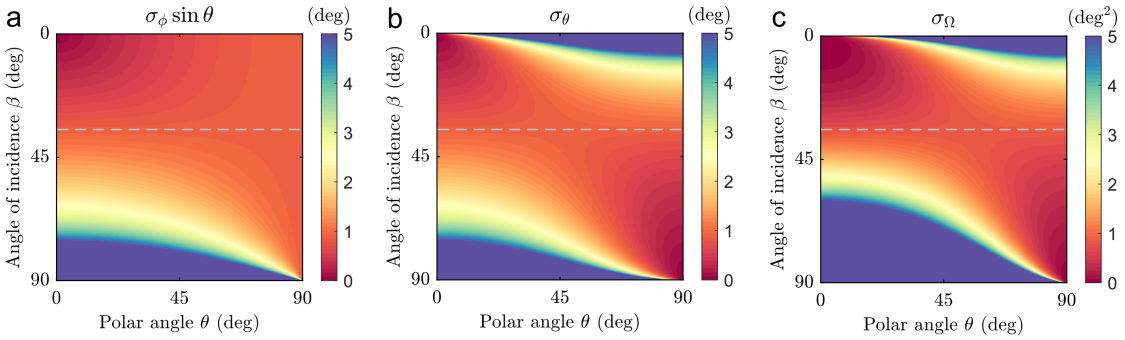

Fig. 5.4: Impact of the angle of incidence on the CRB. (a) The precision of the dipole azimuth angle σ_ϕ scaled by a factor $\sin\theta$, (b) polar angle σ_θ, and (c) solid angle σ_Ω as a function of the dipole polar angle θ and angle of incidence β using Eq. (5.20). The gray dashed line is used to guide the eye for $\beta = \arccos(\sqrt{2/3}) \approx 35\,\text{deg}$. All plots are computed with $N = 1000$.

Figure 5.4 shows these precision bounds as calculated for the azimuthal, polar, and solid angle precision $\sigma_\Omega = \sin\theta\sigma_\theta\sigma_\phi$ as a function of the angle of incidence β and the polar dipole angle θ. It appears that for $\beta < \arccos(\sqrt{2/3}) \approx 35\,\text{deg}$ the precision improves with decreasing polar angle θ, whereas for $\beta > \arccos(\sqrt{2/3})$ the precision improves with increasing polar angle θ. In general, there is no a priori information on the distribution of polar dipole angles, implying that the choice $\beta = \arccos(\sqrt{2/3})$ leading to an isotropic precision is the best choice. This angle of incidence leads to the simplified precision bounds:

$$\sigma_\phi \geq \frac{1}{2\sin\theta\sqrt{N}} \tag{5.21a}$$

$$\sigma_\theta \geq \frac{1}{2\sqrt{N}} \tag{5.21b}$$

where we used $\cos\beta = \sqrt{2/3}$ and $\sin\beta = \sqrt{1/3}$ to simplify the results. The solid angle precision for this angle of incidence is now $\sigma_\Omega = 1/(4N)$, uniform over the unit sphere representing all dipole orientations. These bounds match the quantum bounds derived in [39].

The modulation only precision is shown in Fig. 5.5 and compared to numerical simulations with varying ellipticity angle and background levels. The CRB precision over the entire sphere of dipole orientations is displayed in Fig. 5.5(a,d) with an ellipticity angle

of 1 deg where the peaks are now relative to the five polarization planes. Fig. 5.5(b,e) shows the azimuth and polar angle precision dependency along the molecule polar angle with constant $\phi = 0$ for different polarization ellipticity and background photon counts. The obtained CRB is plotted relative to the CRB of the standard (non-modulated, $M = 1$) PSF in Fig. 5.5(c,f) as a function of the polarization ellipticity angle τ. The CRB ratio indicates that the modulation improves precision by 7.6 and 4.7 for the azimuth and polar angle in the case of zero background and scales to 14.4 and 7.8 in the case of 10 background photons per pixel.

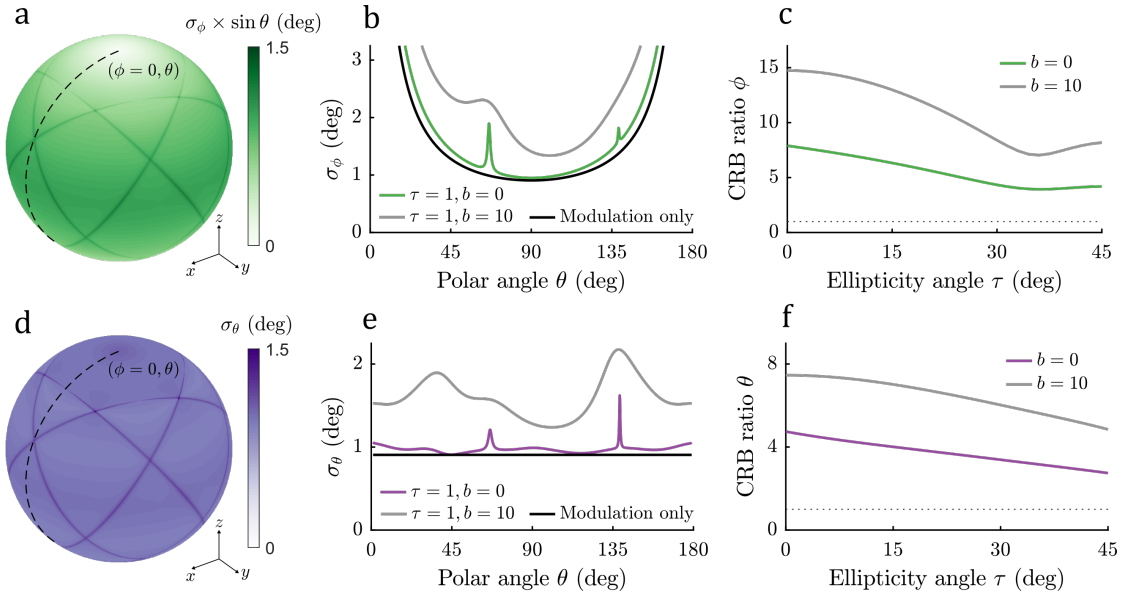

Fig. 5.5: CRB performance for oblique polarization. (a) The azimuth angle precision σ_ϕ scaled by $\sin\theta$ over the sphere of orientations for five oblique polarization steps at $\beta = \arccos(\sqrt{2/3})$ and ellipticity $\tau = 1$ deg. (b) The azimuth angle precision as a function of the dipole angle (θ) along the black dashed line in (a) ($\phi = 0$ deg). The precision is shown for modulation only (Eq. 5.21) and computed numerically with $\tau = 1$ deg and different background counts per pixel b. (c) The azimuth CRB ratio as the CRB from the polarization modulation relative to the CRB of the standard (non-modulated, $S = 1$) PSF as a function of the ellipticity angle. The black dashed line indicates no improvement, i.e., CRB ratio of 1. (d, e, f) Same as above with the polar angle precision. All plots are computed with $N = 1000$ photons and dipole simulations assume matched imaging conditions $n = 1.518$.

5.4 Numerical investigation of estimator performance

We have tested the performance of the combined position and orientation estimator through simulations. We have focused on the impact of SBR and on the tolerances for delivery of the required set of excitation polarization states at the sample. The latter provides a guideline on how well the microscope must be calibrated.

5.4.1 Simulation setup

The numerical studies were performed with ground truth dipole images calculated with the vectorial imaging theory (see appendix 5.A) as input to the developed MLE. We used an image plane grid corresponding to a region of interest (ROI) of 11×11 pixels. The optical settings were taken to match a typical imaging system with a numerical aperture (NA) of 1.49 and a pixel size of 65 nm in object space. We assumed imaging conditions with the refractive indices set to 1.33, 1.523, and 1.518 for the imaging medium, cover slip, and immersion medium. The dipole source is assumed to be at the coverslip and imaging medium interface. Unless stated otherwise, we take 1000 detected photon counts on the camera and 10 background counts per pixel. We neglected readout noise but added Poisson noise to each image with the PSF as the Poisson rate.

The angle of incidence is either $\beta = 0$ (normal incidence) with $M = 3$ or $\beta = \arccos(\sqrt{2/3})$ (oblique incidence) with $M = 5$, where M is the number of different excitation polarizations as outlined in the theory section. Five azimuthal steps were chosen in the case of oblique incidence in order to guarantee the stability of the optimization, even though the theoretical CRB was independent of M. In particular, we found that the sensitivity to the initial values of the parameters in the MLE optimization was too unfavorable for three polarization steps, thereby compromising robustness. This behavior is not unreasonable, as now an additional parameter (the polar angle) must be estimated.

The statistical errors were evaluated from 10,000 random instances with dipole positions taken from a uniform distribution over 1 pixel and dipole orientations uniformly distributed over the unit sphere, i.e., $\phi = \pi u$ and $\theta = \arccos(1-2u)$ where u is a uniform random number from the distribution $U[0,1]$.

5.4.2 Signal-to-background ratio (SBR)

First we quantify the range of photon counts over which the parameters are expected to be estimated reliably. Figure 5.6 shows the performance as a function of the signal-to-background ratio (SBR = N/b) in the dipole images. For an SBR = 1000/10, the normal incidence polarization mode (averaged over in-plane molecular orientations) gives a localization precision $\sigma_{xy} = 3.6$ nm, and an azimuth precision $\sigma_\phi = 1.5$ deg. The signal count and background photon count precision are $\sigma_N = 42$ photons and $\sigma_b = 0.34$ photon per pixel (Fig. 5.6a). For the oblique incidence case (averaged uniformly over the unit sphere) the lateral localization precision is $\sigma_{xy} = 4.6$ nm, azimuth and polar angle precision are $\sigma_\phi = 2.4$ deg, $\sigma_\theta = 1.6$ deg, and signal and background photon count precision are 49 photons and 0.35 photons per pixel (Fig. 5.6b).

Figure 5.6(c-d) show the estimator efficiency given by the ratio CRB/σ^2. Our estimator performs at the precision bound over a broad range of photon counts. At very low SBR values, however, this is no longer the case. We find that the estimator efficiencies drop below 95% for SBR < 30 and SBR < 50 for the normal incidence and oblique incidence modes, respectively.

Figure 5.6(e-f) show the estimator bias Δ relative to the precision σ. A bias arises

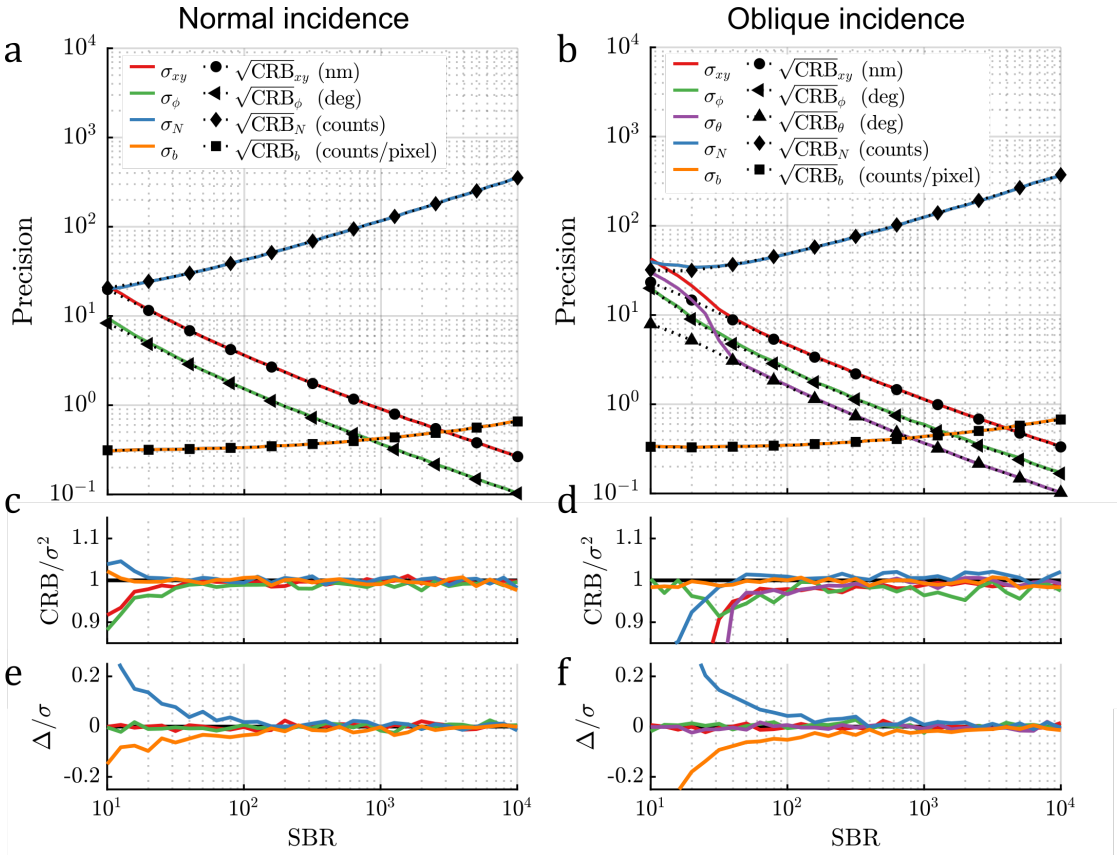

Fig. 5.6: Simulation study of signal-to-background ratio (SBR $= N/b, b = 10$). (a) The precision for the estimated parameters (colored lines) as a function of the SBR compared to the CRB (black lines) for the in-plane and (b) oblique polarization mode. (c-d) The estimator efficiency (CRLB/σ^2) for the in-plane polarization and oblique polarization mode. (e-f) The estimator bias (Δ/σ) for the in-plane polarization and oblique polarization mode.

at low photon counts SBR $< 10^2$ where the estimator tends to overestimate the signal photon count and underestimate the background photon count by a few percentage points of the precision. This mismatch is much smaller than the conventional Gaussian model, where up to 30% photon count underestimation commonly occurs [40, 41]. We also observe that our MLE with a vectorial model achieves the CRB at very high photon counts SBR $> 10^3$, which is not the case for modulation enhanced SMLM when using a Gaussian model due to large photon count errors [27].

5.4.3 Estimation performance dependence on polarization quality

Normal incidence Simulations were performed to obtain insight into the required accuracy for the illumination polarization parameters. Figure 5.7 shows the results of this analysis for the normal incidence case with a relatively low signal count SBR $=$ 1000/10. A significant drawback of this excitation mode is that only the azimuthal angle

is modulated. When the molecules are tilted away from the polarization plane, i.e. if θ is less than 90 deg the performance worsens due to model mismatch (see Fig. 5.7(a,d)). This mismatch is apparent as the photon count bias accumulates up to $\pm 1\sigma$ if θ deviates from the nominal 90 deg by 18 deg. This appears to be the same deviation beyond which the efficiency of the estimator is compromised. Therefore attention must be taken if these tilted molecules are included in the estimation process as their contribution limits the overall localization precision.

The CRB performance as a function of the ellipticity angle τ, or equivalently the (amplitude) extinction ratio $\kappa = \cot \tau$, was plotted in Fig. 5.3. There, the assumption was that the polarization parameters are correctly calibrated, which is not always the case in practice. Figure 5.7(b,e) shows the results of a study where the estimator assumes perfect linearly polarized excitation, whereas the ground-truth extinction ratio is varied. It is seen that the assumption of perfect linear polarization is valid for ground-truth extinction ratios above about 20. When the ground-truth extinction ratio is too low, the estimator no longer reaches the lower bound as the imperfect polarization induces photon count biases. Extinction ratios down to 12-19 have been reported in the literature for similar methods [24], and in these cases, it becomes essential to modify the estimator to take calibrated, non-perfect, excitation polarization states into account. These imperfect extinction ratios, in combination with considering molecules with out-of-plane tilt in the analysis, may be contributing factors why the reported precision in [24] falls short of the CRB derived in this paper.

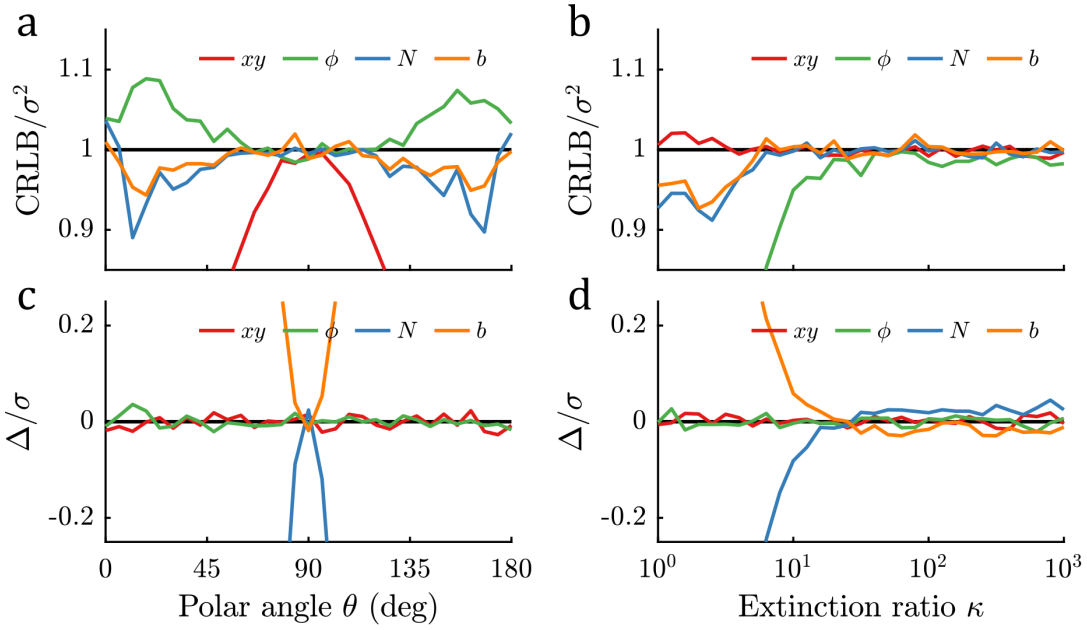

Fig. 5.7: Sensitivity analysis of in-plane polarization parameters (SBR = N/b = 1000/10). (a,d) The estimator efficiency (CRLB/σ^2) and bias (Δ/σ) as a function of dipole polar angle. (b,e) The estimator efficiency and bias as a function of a ground-truth extinction ratio where the estimation assumes perfect linearly polarized excitation.

Oblique incidence In the oblique incidence mode the full solid-angle is estimated, and no deterioration of performance by dipoles tilted from the image plane occurs. On the downside now the angle of incidence β must be calibrated as well. Figure 5.8 shows the results of the sensitivity analysis for the oblique incidence case. The lower limit for the extinction ratio remains about the same, i.e. for values below approximately 20 an experimentally calibrated value must be used in the estimator (see Fig. 5.8(a,d)). It is seen that orientation parameters are the first to drop in estimator efficiency when the extinction ratio is lowered.

The oblique incidence mode requires the calibration of the different directions of incidence of the polarized excitation beams. The estimator maintains an efficiency above 95% for errors in the angle of incidence less than 1 deg. It appears that there is a bias that depends on the ground truth dipole orientation. When averaged over all orientations, however, this bias averages out to zero and instead contributes to the degradation of precision.

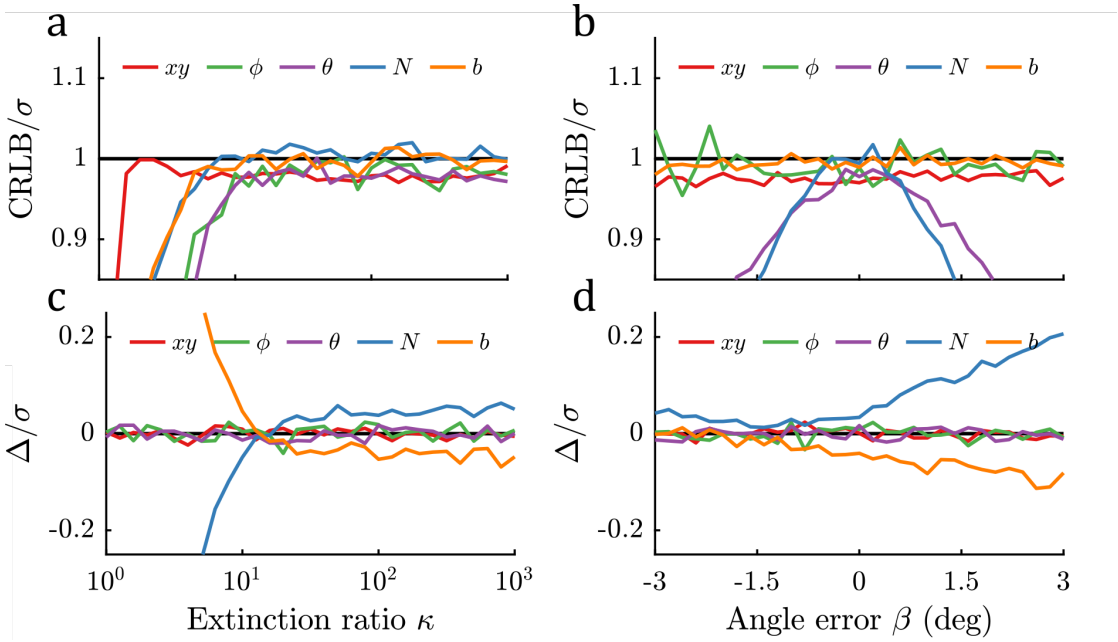

Fig. 5.8: Sensitivity analysis of polarization parameters (SBR $= N/b = 1000/10$). (a,d) The estimator efficiency (CRLB/σ^2) and bias (Δ/σ) as a function of extinction ratio, (c,f) as a function of a constant angle error $\Delta\beta$ between the estimation and the ground-truth polarization steps.

5.5 Discussion

5.5.1 Rotational diffusion

The main limitation of the current image formation model is the assumption that the emitter is stationary (section 5.3), i.e., that it has a completely fixed pose in space with negligible rotational diffusion. This assumption could be correct in applications where the rotational mobility of the molecule can be regarded as completely restricted at typical frame rates of milliseconds [10]. The label molecules in a biological sample, however, undergo rotational diffusion and wobble around an average orientation [42]. For instance, common intercalators (e.g., SYTOX orange) used in λ-DNA experiments report rotational diffusion within a cone with a semi-cone angle on the order of $20-30$ deg [24, 16, 43]. If not taken into account, this would inadvertently affect the estimated photon counts and thereby worsen the quality of the orientation estimation. An interesting extension to the present work is therefore to parametrize the rotational diffusion and jointly estimate these parameters together with the molecule's position and preferential orientation. Here the PSF model appropriate for fast rotational diffusion, where the PSF is a weighted sum of the fully free and fully fixed dipole PSFs, seems the best starting point [44, 16].

5.5.2 Additional parameters

The CRB performance with respect to the orientation estimation or any other parameters could be improved by the use of PSFs engineered to the specific problem in combination with modulation of the excitation polarization. For example, such PSF designs could be designed to estimate axial position information, which would enable the generalization to the case of 3D SMLM. This could, however, come at the cost of reduced lateral localization precision and a limited axial working range because axial localization usually entails a decrease of the signal-to-background ratio. An interesting question to investigate regarding the combination of PSF engineering and polarization modulation would be the quantification of possible differences between the absorption and emission dipole moment [45, 30].

5.5.3 Multiphoton excitation

Multiphoton excitation induces a nonlinear dependence of the fluorescence excitation efficiency on dipole orientation that can be used to enhance the estimation precision. For example, for two-photon excitation, the intensity of fluorescence is proportional to the fourth power of the excitation amplitude $\left|\hat{d}\cdot\hat{\epsilon}\right|^4$ [46]. This fourth power dependence improves the contrast at the intensity minima, and therefore the CRB precision can, in principle, be reduced. For example, in the case of normal incidence described in section 5.3.3, the modulation function now takes the form assuming that $\tau = 0$:

$$P_m(\phi) = \frac{8}{3M}\cos^4(\phi - \xi_m) \tag{5.22}$$

The Fisher-information element can be determined by substituting Eq. 5.22 in the second term of Eq. 5.10:

$$F_{\phi\phi} = \frac{16N}{3M} \sum_{m=1}^{M} [1 - \cos(4\phi - 4\xi_m)] = \frac{16N}{3} \tag{5.23}$$

which yields the precision limit:

$$\sigma_\phi = \frac{\sqrt{3}}{4\sqrt{N}} \tag{5.24}$$

It is seen that the uncertainty is smaller by a factor of $\sqrt{3}/2 \approx 0.87$ as compared to the precision in section 5.3.3.

5.6 Conclusion

In conclusion, we proposed a concept to estimate molecular orientation that is compatible with localization microscopy by using polarized excitation. The theoretical performance limits were quantified using a Cramér-Rao bound analysis in terms of the excitation polarization parameters. To this end, analytic expressions for the CRB for cases of normal and oblique incidence were derived. Numerical simulations were performed to evaluate the performance of the polarization modulation method as a function of SBR and assess the required accuracy of the excitation polarization states in experiments. We showed that a precision below 2.5 deg can be achieved for both the azimuthal and polar angle with only 1000 photons in the presence of 10 background photons per pixel. The method is considered beneficial for orientation measurements where standard SMLM resolution is desired, particularly for cases where only dim fluorophores are available. In future steps a rotational diffusion model can be incorporated, or combinations with PSF engineering approaches can be considered.

Funding

This work was supported by the European Research Council ERC (648580) and the National Institutes of Health NIH (U01EB021238).

Disclosures

The authors declare no conflicts of interest.

5.A Dipole image formation model

The expected photon count for pixel n for a fixed dipole emitter at position $\mathbf{r}_0$ and with orientation Ω is found by integrating the PSF over the pixel area A with size $a \times a$:

$$H_n(\mathbf{r}_0, \Omega) = \int_A \mathrm{d}x\mathrm{d}y\, H(\mathbf{r} - \mathbf{r}_0, \Omega). \tag{5.25}$$

The fixed dipole PSF is proportional to the modulus square of the electric field in the image plane:

$$H(\mathbf{r}, \Omega) = \sum_{j=x,y} |E_j(\mathbf{r}, \Omega)|^2, \tag{5.26}$$

where the electric field in the imaging plane can be written as:

$$E_j(\mathbf{r}, \Omega) = \sum_{k=x,y,z} w_{jk}(\mathbf{r}) d_k(\Omega) \tag{5.27}$$

with components $j = x, y$ taken proportional to the emission dipole component d_k and where the $w_{jk}(\mathbf{r})$ can be computed by integrating over normalized pupil coordinates ρ:

$$w_{jk}(\mathbf{r}) = \frac{1}{\pi} \int \mathrm{d}^2\rho\, A(\rho) \exp\left(\frac{2\pi i W(\rho)}{\lambda}\right) q_{jk}(\rho) \exp(-i\mathbf{k}(\rho) \cdot \mathbf{r}) \tag{5.28}$$

Here the wavevector $\mathbf{k}(\rho)$ is given by:

$$\mathbf{k}(\rho) = \frac{2\pi}{\lambda} \left(\mathrm{NA}\rho_x, \mathrm{NA}\rho_y, \sqrt{n_{\mathrm{med}}^2 - \mathrm{NA}^2\rho^2}\right) \tag{5.29}$$

with n_{med} the refractive index of the imaging medium. The angular representation of the wavevector is:

$$\mathbf{k}(\rho) = \frac{2\pi n_{\mathrm{med}}}{\lambda} (\sin\eta\cos\psi, \sin\eta\sin\psi, \cos\eta) \tag{5.30}$$

Other quantities appearing in the integral expression for the $w_{jk}(\mathbf{r})$ are the aplanatic amplitude correction factor $A(\rho)$ [47, 48], the phase (aberrations) $W(\rho)$, and the polarization vector components $q_{xk}(\rho)$ and $q_{yk}(\rho)$ which depend on the p and s basis vectors and on the Fresnel coefficients for the different interfaces [34]:

$$q_{xk} = \cos\psi T_{\mathrm{p}} p_k - \sin\psi T_{\mathrm{s}} s_k, \tag{5.31}$$

$$q_{yk} = \sin\psi T_{\mathrm{p}} p_k + \cos\psi T_{\mathrm{s}} s_k, \tag{5.32}$$

where the p and s basis polarization vectors are $\vec{p} = (\cos\eta\cos\psi, \cos\eta\sin\psi, -\sin\eta)$ and $\vec{s} = (-\sin\psi, \cos\psi, 0)$ and where the Fresnel coefficients are:

$$T_{\mathrm{a}} = T_{\mathrm{a,med-cov}} T_{\mathrm{a,cov-imm}}, \tag{5.33}$$

for $a = p, s$. Here the Fresnel coefficients for the two contributing interfaces are defined by:

$$T_{\mathrm{a},1-2} = \frac{2c_{a,1}}{c_{a,1} + c_{a,2}}, \tag{5.34}$$

for $a = p, s$ and with $c_{p,l} = n_l / \cos\eta_l$ and $c_{s,l} = n_l \cos\eta_l$ for $l = \mathrm{med}, \mathrm{cov}, \mathrm{imm}$, where the polar angles of incidence are related by Snell's law.

The imaging model's partial derivatives to the parameters are needed for the MLE optimization routine. These are straightforward to evaluate for the signal photon count N and number of background photons per pixel b, as these appear linear in the imaging model. The derivatives with respect to the position parameters $\mathbf{r}_0$ are the same as in refs. [49, 50]:

$$\frac{\partial \mu_{nm}}{\partial \mathbf{r}_0} = N P_m(\Omega) \sum_{j=x,y} \int_A \mathrm{d}x\mathrm{d}y \; 2\mathrm{Re}\left\{ E_j^*(\mathbf{r} - \mathbf{r}_0, \Omega) \frac{\partial E_j(\mathbf{r} - \mathbf{r}_0, \Omega)}{\partial \mathbf{r}_0} \right\}. \tag{5.35}$$

The derivatives with respect to the orientation parameters become:

$$\frac{\partial \mu_{nm}}{\partial \Omega} = N P_m(\Omega) \sum_{j=x,y} \int_A \mathrm{d}x\mathrm{d}y \; 2\mathrm{Re}\left\{ E_j^*(\mathbf{r} - \mathbf{r}_0, \Omega) \frac{\partial E_j(\mathbf{r} - \mathbf{r}_0, \Omega)}{\partial \Omega} \right\} + N \frac{\partial P_m(\Omega)}{\partial \Omega} H_n(\mathbf{r}_0, \Omega) \tag{5.36}$$

where the second term originates purely from the polarization modulation. This involves the electric field derivatives:

$$\frac{\partial E_j(\mathbf{r} - \mathbf{r}_0, \Omega)}{\partial \mathbf{r}_0} = \sum_{k=x,y,z} \frac{\partial w_{jk}(\mathbf{r} - \mathbf{r}_0)}{\partial \mathbf{r}_0} d_k(\Omega), \tag{5.37}$$

with:

$$\frac{\partial w_{jk}(\mathbf{r} - \mathbf{r}_0)}{\partial \mathbf{r}_0} = \frac{i}{\pi} \int \mathrm{d}^2\rho \, A(\rho) \exp\left(\frac{2\pi i W(\rho)}{\lambda} \right) q_{jk}(\rho) \mathbf{k}(\rho) \exp(-i\mathbf{k}(\rho) \cdot (\mathbf{r} - \mathbf{r_0})) \tag{5.38}$$

The orientational derivatives of the modulation function $P_s(\Omega)$ are simple trigonometric functions, the orientational derivatives of the electric field are:

$$\frac{\partial E_j(\mathbf{r} - \mathbf{r}_0, \Omega)}{\partial \Omega} = \sum_{k=x,y,z} w_{jk}(\mathbf{r} - \mathbf{r}_0) \frac{\partial d_k(\Omega)}{\partial \Omega}, \tag{5.39}$$

where the orientational derivatives of the dipole vector $d_k(\Omega)$ are again simple trigonometric functions.

References

[1] S. T. Hess, T. P. Girirajan, and M. D. Mason. "Ultra-high resolution imaging by fluorescence photoactivation localization microscopy". In: *Biophysical Journal* 91.11 (2006), pp. 4258–4272. ISSN: 00063495.

[2] E. Betzig et al. "Imaging intracellular fluorescent proteins at nanometer resolution". In: *Science* 313.5793 (2006), pp. 1642–1645. ISSN: 00368075.

[3] M. J. Rust, M. Bates, and X. Zhuang. "Sub-diffraction-limit imaging by stochastic optical reconstruction microscopy (STORM)". In: *Nature Methods* 3.10 (2006), pp. 793–795. ISSN: 15487091.

[4] A. Sharonov and R. M. Hochstrasser. "Wide-field subdiffraction imaging by accumulated binding of diffusing probes". In: *Proceedings of the National Academy of Sciences* 103.50 (2006), pp. 18911–18916. ISSN: 0027-8424. eprint: `https://www.pnas.org/content/103/50/18911.full.pdf`.

[5] B. Huang et al. "Three-dimensional super-resolution imaging by stochastic optical reconstruction microscopy". In: *Science* 319.5864 (2008), pp. 810–813. ISSN: 00368075.

[6] M. P. Backlund et al. *The role of molecular dipole orientation in single-molecule fluorescence microscopy and implications for super-resolution imaging*. 2014.

[7] E. J. Peterman et al. "Polarized fluorescence microscopy of individual and many kinesin motors bound to axonemal microtubules". In: *Biophysical Journal* 81.5 (2001), pp. 2851–2863. ISSN: 00063495.

[8] E. Toprak et al. "Defocused orientation and position imaging (DOPI) of myosin V". In: *Proceedings of the National Academy of Sciences of the United States of America* 103.17 (2006), pp. 6495–6499. ISSN: 00278424.

[9] H. A. Shaban et al. "Polarized super-resolution structural imaging inside amyloid fibrils using Thioflavine T". In: *Scientific Reports* 7.1 (2017), pp. 1–10. ISSN: 20452322.

[10] M. Wang et al. "Nanoscale deformation in polymers revealed by single-molecule super-resolution localization-orientation microscopy". In: *Materials Horizons* 6.4 (2019), pp. 817–825. ISSN: 20516355.

[11] J. Lu et al. "Single-Molecule 3D Orientation Imaging Reveals Nanoscale Compositional Heterogeneity in Lipid Membranes". In: *Angewandte Chemie* 132.40 (2020), pp. 17725–17732. ISSN: 0044-8249.

[12] J. Engelhardt et al. "Molecular orientation affects localization accuracy in superresolution far-field fluorescence microscopy". In: *Nano Letters* 11.1 (2011), pp. 209–213. ISSN: 15306984.

[13] M. D. Lew, M. P. Backlund, and W. E. Moerner. "Rotational mobility of single molecules affects localization accuracy in super-resolution fluorescence microscopy". In: *Nano Letters* 13.9 (2013), pp. 3967–3972. ISSN: 15306984.

[14] M. P. Backlund et al. "The double-helix point spread function enables precise and accurate measurement of 3D single-molecule localization and orientation". In: *Single Molecule Spectroscopy and Superresolution Imaging VI*. Vol. 8590. SPIE, 2013, p. 85900L. ISBN: 9780819493590.

[15] A. S. Backer et al. "Single-molecule orientation measurements with a quadrated pupil". In: *Optics Letters* 38.9 (2013), p. 1521. ISSN: 0146-9592.

[16] C. N. Hulleman et al. "Simultaneous orientation and 3D localization microscopy with a Vortex point spread function". In: *bioRxiv* (2020). ISSN: 26928205.

[17] T. J. Gould et al. "Nanoscale imaging of molecular positions and anisotropies". In: *Nature Methods* 5.12 (2008), pp. 1027–1030. ISSN: 15487091.

[18] S. R. P. Pavani, J. G. DeLuca, and R. Piestun. "Polarization sensitive, three-dimensional, single-molecule imaging of cells with a double-helix system". In: *Optics Express* 17.22 (2009), p. 19644. ISSN: 1094-4087.

[19] C. A. V. Cruz et al. "Quantitative nanoscale imaging of orientational order in biological filaments by polarized superresolution microscopy". In: *Proceedings of the National Academy of Sciences of the United States of America* 113.7 (2016), E820–E828. ISSN: 10916490.

[20] S. Stallinga and B. Rieger. "Position and orientation estimation of fixed dipole emitters using an effective Hermite point spread function model". In: *Optics Express* 20.6 (2012), p. 5896. ISSN: 1094-4087.

[21] A. S. Backer et al. "A bisected pupil for studying single-molecule orientational dynamics and its application to three-dimensional super-resolution microscopy". In: *Applied Physics Letters* 104.19 (2014), pp. 1–5. ISSN: 00036951.

[22] O. Zhang et al. "Imaging the three-dimensional orientation and rotational mobility of fluorescent emitters using the Tri-spot point spread function". In: *Applied Physics Letters* 113.3 (2018). ISSN: 00036951.

[23] V. Curcio et al. "Birefringent Fourier filtering for single molecule coordinate and height super-resolution imaging with dithering and orientation". In: *Nature Communications* 11.1 (2020). ISSN: 20411723.

[24] A. S. Backer, M. Y. Lee, and W. E. Moerner. "Enhanced DNA imaging using super-resolution microscopy and simultaneous single-molecule orientation measurements". In: *Optica* 3.6 (2016), p. 659. ISSN: 2334-2536.

[25] R. Henriques et al. *QuickPALM: 3D real-time photoactivation nanoscopy image processing in ImageJ*. 2010.

[26] F. Balzarotti et al. "Nanometer resolution imaging and tracking of fluorescent molecules with minimal photon fluxes". In: *Science* 355.6325 (2017), pp. 606–612. ISSN: 10959203. arXiv: 1611.03401.

[27] J. Cnossen et al. "Localization microscopy at doubled precision with patterned illumination". In: *Nature Methods* 17.1 (2020), pp. 59–63. ISSN: 15487105.

[28] L. Gu et al. "Molecular resolution imaging by repetitive optical selective exposure". In: *Nature Methods* 16.11 (2019), pp. 1114–1118. ISSN: 15487105.

[29] P. Jouchet et al. "Nanometric axial localization of single fluorescent molecules with modulated excitation". In: *Nature Photonics* (2021), pp. 1–8. ISSN: 17494893.

[30] N. Karedla et al. "Simultaneous Measurement of the Three-Dimensional Orientation of Excitation and Emission Dipoles". In: *Phys. Rev. Lett.* 115 (17 2015), p. 173002.

[31] B. R. Lentz. "Use of fluorescent probes to monitor molecular order and motions within liposome bilayers". In: *Chemistry and Physics of Lipids* 64.1-3 (1993), pp. 99–116. ISSN: 00093084.

[32] M. Born et al. *Principles of Optics*. Cambridge University Press, 1999.

[33] K. I. Mortensen et al. "Optimized localization analysis for single-molecule tracking and super-resolution microscopy". In: *Nature Methods* 7.5 (2010), pp. 377–381. ISSN: 15487091.

[34] S. Stallinga and B. Rieger. "Accuracy of the Gaussian Point Spread Function model in 2D localization microscopy". In: *Optics Express* 18.24 (2010), p. 24461. ISSN: 1094-4087.

[35] J. Chao, E. Sally Ward, and R. J. Ober. "Fisher information theory for parameter estimation in single molecule microscopy: tutorial". In: *Journal of the Optical Society of America A* 33.7 (2016), B36. ISSN: 1084-7529.

[36] B. Rieger and S. Stallinga. "The lateral and axial localization uncertainty in super-resolution light microscopy". In: *ChemPhysChem* 15.4 (2014), pp. 664–670. ISSN: 14397641.

[37] M. R. Foreman and P. Török. "Fundamental limits in single-molecule orientation measurements". In: *New Journal of Physics* 13.9 (2011), p. 093013. ISSN: 13672630.

[38] S. Stallinga and B. Rieger. "Position and orientation estimation of fixed dipole emitters using an effective Hermite point spread function model". In: *Optics Express* 20.6 (2012), p. 5896. ISSN: 1094-4087.

[39] O. Zhang and M. D. Lew. "Quantum limits for precisely estimating the orientation and wobble of dipole emitters". In: *Phys. Rev. Research* 2 (3 2020), p. 033114.

[40] C. Franke, M. Sauer, and S. V. De Linde. "Photometry unlocks 3D information from 2D localization microscopy data". In: *Nature Methods* 14.1 (2016), pp. 41–44. ISSN: 15487105.

[41] R. Thorsen et al. *Impact of optical aberrations on axial position determination by photometry*. 2018.

[42] I. Munro, I. Pecht, and L. Stryer. "Subnanosecond motions of tryptophan residues in proteins." In: *Proceedings of the National Academy of Sciences of the United States of America* 76.1 (1979), pp. 56–60. ISSN: 00278424.

[43] A. S. Backer et al. "Single-molecule polarization microscopy of DNA intercalators sheds light on the structure of S-DNA". In: *Science Advances* 5.3 (2019), eaav1083. ISSN: 23752548.

[44] S. Stallinga. "Single emitter localization analysis in the presence of background". In: *Optical Systems Design 2015: Computational Optics*. Ed. by D. G. Smith, F. Wyrowski, and A. Erdmann. Vol. 9630. SPIE, 2015, p. 96300V. ISBN: 9781628418194.

[45] T. Ha et al. "Polarization spectroscopy of single fluorescent molecules". In: *Journal of Physical Chemistry B* 103.33 (1999), pp. 6839–6850. ISSN: 15206106.

[46] W. L. Peticolas, J. P. Goldsborough, and K. E. Rieckhoff. "Double photon excitation in organic crystals". In: *Physical Review Letters* 10.2 (1963), pp. 43–45. ISSN: 00319007.

[47] P. Török, P. D. Higdon, and T. Wilson. "Theory for confocal and conventional microscopes imaging small dielectric scatterers". In: *Journal of Modern Optics* 45.8 (1998), pp. 1681–1698. ISSN: 13623044.

[48] T. Wilson, R. Juškaitis, and P. Higdon. "The imaging of dielectric point scatterers in conventional and confocal polarisation microscopes". In: *Optics Communications* 141.5-6 (1997), pp. 298–313. ISSN: 00304018.

[49] C. Smith et al. "Simultaneous measurement of emission color and 3D position of single molecules". In: *Optics Express* 24.5 (2016), p. 4996. ISSN: 1094-4087.

[50] M. Siemons et al. *High precision wavefront control in point spread function engineering for single emitter localization*. 2018. arXiv: 1802.06584.

6 Conclusion and outlook

6.1 Conclusion

6.1.1 Photon count estimation in localization microscopy

In Chapter 2, we quantified how pixel photon counts are often wrongly estimated in standard localization microscopy. This was shown in the context of a debated photometric approach to retrieve 3D information, namely TRABI [1]. TRABI uses the detected number of photons for a single molecule localization event as a parametric indicator of a molecule's axial position. The ratio between the photon count derived from a standard Gaussian fit to the number of photons detected within a region close to the emission peak on the camera, the so-called TRABI value, was proposed for this purpose.

A proper quantitative explanation of the underlying mechanism of TRABI was lacking, as well as an analysis of the sensitivity of the method to system imperfections such as aberrations. We demonstrated that a Gaussian function cannot fit the long tail of a realistic PSF at all. This long tail entails a systematic overcounting of background photons to compensate for the Gaussian mismatch, resulting in undercounting of signal photons up to 30 percentage points of the true count reported in ref. [1]. Next, we analyzed the impact of optical aberrations on the photon count estimations based on both the Gaussian model and on the aperture based method. The response to aberrations turns out to be different for both methods. Hence measurements of the photometric ratio on realistic spots quickly result in deviations when the level of aberrations is increased.

The photometric ratio performance was experimentally assessed on seven different microscopes with optical aberrations ranging from 13 mλ to 61 mλ, which produced systematic errors on the order of 50 to 100 nm in axial position. We revealed that to convert the photometric ratio to an accurate depth map with axial uncertainty less than 20 nm an aberration calibration better than 10 mλ is needed.

6.1.2 Modulation enhanced localization microscopy

Chapter 3 contains a proposal for a new modulation-enhanced localization approach dedicated to SMLM data referred to as SIMFLUX. SIMFLUX was proposed to solve the challenge of extending the MINFLUX triangulation procedure to sinusoidal illumination patterns. In this way, the field-of-view could be improved, as well as the imaging throughput, approaching standard SMLM experimental settings. SIMFLUX combines centroid estimation and illumination pattern induced photon count variation to extract position information. The photon count variation was induced over six images recorded with three shifted patterns per orthogonal orientation of a sinusoidal line pattern, which

in theory improves the localization precision twofold over standard SMLM with the same photon count. With an extensive simulation study, we quantified the experimental conditions under which the method reaches a two-fold precision improvement. Based on these conditions, the method was evaluated in experiments to achieve an impressive FRC-resolution of 8.6 nm, whereas standard SMLM resulted in 16.4 nm.

6.1.3 Imaging molecular orientation with PSF engineering

In Chapter 4 we proposed an estimation strategy to estimate dipole orientation and the degree of rotational diffusion using an engineered PSF named the Vortex PSF. The Vortex PSF was introduced because of its relatively compact spot, which enables a more favorable trade-off between the estimation of 3D position and orientation than existing PSF designs. We evaluated the Vortex PSF on the reorientation dynamics of single molecules adhered to a coverslip and on binding-activated localization microscopy on lambda-DNA using DNA intercalator dyes.

Most PSF engineering methods suffer from an enhanced sensitivity to optical aberrations as the molecular parameters (axial position, orientation) are deliberately incorporated into the PSF shape. We showed that field-dependent microscope aberrations could efficiently be calibrated by analyzing through-focus stacks of a series of beads spread over the field-of-view using the vectorial PSF model and fitting the field-dependence of the aberrations using Nodal Aberration Theory (NAT). We concluded that the spatially variant PSF model is the optimal solution for single molecule imaging in a large field-of-view, where optical aberrations can vary substantially between various locations.

6.1.4 Localization microscopy with modulated enhanced orientation

Chapter 5 contains a proposal for a new modulation-enhanced approach to estimate molecular orientation by using the latest insights obtained with SIMFLUX (Chapter 3). The polarization state of the illumination was modulated instead of the spatially varying illumination pattern. This allowed us to extract the molecule's position and orientation in a combined estimation from the detected camera spot shapes and positions together with photon count variations induced by the modulated polarization. Two modes were demonstrated: i) polarized epi-illumination with three polarization steps to extract the in-plane angle and ii) oblique incident polarized light with five polarization steps to extract the full solid-angle.

The performance limits were quantified using the Cramér–Rao lower bound. We showed that with only 1000 detected photons and 10 background photons per pixel, the expected precision is 2.4 deg and 1.6 deg in the azimuth and polar angles. With an extensive simulation study, we explored different experimental conditions that influence the method, i.e., the requirements of the experimental parameters under which the estimation works and the ultimate precision that can be achieved given a particular set of experimental parameters.

6.2 Recommendations and outlook

6.2.1 Accurate single molecule estimation

A significant source of inaccuracy is model mismatch. In particular, the default Gaussian PSF model fails in several respects, such as photon count estimation and molecular orientation induced position biases. The drive to image with higher photon counts from a single fluorophore, i.e., under cryogenic conditions, for improving the localization precision, makes the model mismatch become even more decisive. Further advances in the performance of localization algorithms will come from more accurate modeling of image formation. A necessary step is to adjust the model to each fluorophore depending on how rigid it links to a binding site, its overall field position, and nearby background environment. Below we will discuss a few inroads to address these problems.

Point-spread-function model There are several possible advancements of the vectorial PSF model that could include performing more extensive calibration measurements. Typically we use sub-diffraction sized beads to retrieve the Zernike coefficients as these only increase the full-width half maximum of the PSF while giving access to more light compared to single molecules. The in-focus spot width increase is incorporated in the model by convolution with a 3D sphere of equal diameter as the bead. A limitation of this approach is the unknown refractive index contrast between bead and imaging medium and how that affects the fluorescence emission from within the bead to the outside world. A further limitation on the accuracy of the estimation of the Zernike coefficients and the absolute z-position is imposed if the refractive index mismatch between medium and immersion oil becomes too prominent as a depth-varying relationship exists between the actual and nominal focus positions in an index-mismatched high-NA imaging system. We suggest developing a more physically accurate bead imaging model to avoid these estimation inaccuracies.

Additional inaccuracies could originate from several non-uniformities not taken into account. This could include refractive index variations in the specimen and thickness variations of the glass cover slip that may not be polished to optical flatness. Incorporation of the finite bandwidth of the fluorescence emission spectrum into the vectorial model may further enhance the agreement between the model and experimentally retrieved PSFs. Such improvements, however, add to the already substantial computational cost of the vectorial imaging model.

Field dependence of the imaging model This thesis showed that Nodal Aberration Theory (NAT) provides an effective spatially variant PSF model. NAT was adopted from application in large astronomical telescopes to microscopy since both optical imaging systems operate at small field angles. The key advantage is that optical-based expectation functions with set coefficients are used to describe the field dependency of aberrations instead of 2D polynomials of arbitrary order [2], which make it more robust to potential outliers. NAT has the potential to be used as a standard calibration tool in localization microscopy to ensure accurate estimation in the context of ultra-wide field-of-view

(FOV) SMLM [3].

A straightforward extension to Chapter 4 is to include even higher-order Zernike modes in the calibration. So far, we have showcased the developed least-squares routine to include primary and secondary astigmatism, coma, and spherical aberration, and trefoil. Once higher-order modes are expanded in the field-coordinates, these are readily incorporated into the least-squares routine.

Another interesting follow-up investigation using NAT is to investigate image distortion across the FOV, which could be particularly relevant when multiple FOVs are stitched together [4]. We further propose to set up a calibration procedure to determine the NAT coefficients for a full-field aberration map, not based on beads, as shown in Chapter 4, but instead on the SMLM data directly [5]. Additional developments could include a step that includes specimen-induced aberrations in addition to the optical aberrations of the microscope [6].

Orientation and rotational diffusion We demonstrated a significant advancement in the imaging model in Chapters 4 and 5 to incorporate molecular orientation and, importantly, the rotational mobility of the molecule. This advancement makes it possible to quantify how rigidly the fluorescent label attaches to a target molecule directly from the imaged emission pattern. We demonstrated this using the symmetric rotational potential well model derived in [7] with a single parameter indicating the well depth. This may, however, not be the most appropriate rotational diffusion model, depending on how the label attaches to the target molecule. For instance, the rotational diffusion is not necessarily symmetric, for example when the label molecule intercalates.

We reflected in Chapter 4 that the intercalated molecule could be expected to rotate more about the lambda-DNA axis while remaining roughly parallel to the neighboring base pairs. Therefore we recommend investigating asymmetrical rotational diffusion when imaging intercalator fluorescent labels [8, 7]. This would require more parameters in the image formation model but is potentially feasible given the current analysis in Chapter 4. Yet care must be taken not to overfit the emission pattern, and prior knowledge could be needed for a robust estimation without depending on extremely bright fluorophores.

Another step in the rotational mobility analysis could be to extend it into the regime of slow orientational diffusion. In Chapter 4 we assumed that the rotational diffusion was much faster than the fluorescent lifetime. When this is not the case, the illumination polarization impacts the PSF shape, implying that the illumination polarization could generate valuable information on the orientational constraints and diffusion of the molecule in the orientational potential well. This is entirely similar to classical fluorescence anisotropy imaging [9].

A final interesting question to address in future studies would be to compare the orientation modalities to fundamental (i.e., quantum) limits of the estimation of orientational parameters [10, 11].

Background model The standard imaging model in SMLM, used in this thesis, assumes a locally constant background. However, this approximation fails when SMLM is performed in thick or dense samples, as then fluorescence emission of nearby fluorophores can introduce significant background variations. Further work could assess the merits of more advanced background models. Particular care must be taken to improve accuracy in case of non-uniform background and the precision affected by the increased Poisson noise from a high background. This work should not only focus on localization but also to ensure accurate photon count estimates as these are increasingly used as parametric indicators.

A first inroad to study these effects is to add a degree of freedom to the background of the imaging model, i.e., a local gradient or even higher-order variances. A second, and potentially more robust, inroad is to infer a global model for background non-uniformity from the image data, and to use this as a prior on the local imaging model for a single molecule emission event. Here one can turn to spline surfaces, which are already used to model experimental PSFs [12, 13]. Such a global background map map could be obtained by fitting a surface spline to the temporal variations in the SMLM camera frames [14]. This would also help the detection of single molecule emission events since the odds that signal is mistaken for background decrease when the background model is more realistic.

A fully data driven way to address background non-uniformity is the use of deep learning [15], potentially joined with new model-independent deep learning image denoising algorithms to extract the non-uniform background more accurately [16, 17].

6.2.2 Precise single molecule estimation

Besides improving accuracy, advances in precision of single molecule estimations could provide further benefits. These could be twofold: it makes observation of structures at even smaller length scales possible, and it enables imaging with less light coming from less photo-efficient fluorophores. The previous chapters suggested two new estimation schemes to enhance the localization and orientation estimates based on modulation enhanced parameter estimation and PSF engineering. Below we discuss a number of ways to improve the precision of these estimation schemes.

PSF optimization An exciting way to optimize precision is to use deep learning to tailor the PSF shape to enhance the estimation of a parameter of interest. An implementation of such an approach has been demonstrated in dense 3D localization microscopy data [18]. This can directly be used to extend the approach of Chapter 4, where we introduced an engineered PSF to retrieve position and orientation. The proposed shape, the vortex PSF, proved useful in many ways. It removes the precision divergence near focus and breaks orientational symmetries, and is easily implemented with an off-the-shelf optical element. Its shape, however, was not optimized to retrieve any of the estimated parameters with optimal precision, whether in molecule 3D position, orientation, or degree of orientational constraint.

We recommend developing a deep neural network to optimize the PSF shape for high precision in orientation imaging while keeping standard localization precision. Such an optimization can be achieved with a carefully designed cost-function incorporating the Cramer-Rao bound with attention to experimental conditions to keep the PSF footprint small. Another term that must be taken into account is to avoid any dipole orientation related degeneracies in the PSF shape. This advancement can take orientation imaging with PSF engineering to the next level without relying on a more advanced imaging system such as the polarized excitation discussed in Chapter 5.

A more comprehensive approach could be taken to develop a more general cost-function from a detailed image formation model. This cost-function would consist of several tuning parameters as a trade-off between what parameters to optimize. Based on prior knowledge of imaging conditions and the biological system, an optimized PSF could be designed to resolve the structure at hand. This could be with optimal lateral/axial resolution to visualize the structure, or optimal orientation precision to resolve the pitch inside the structure, or optimal rotational diffusion estimation, to investigate how the molecule links to the structure, or any other parameter of interest, or merely via a trade-off between these as defined by the user.

Modulation enhanced localization The power of the recently developed modulation enhanced localization methods comes from the extra information one can extract from a structured illumination pattern. An improvement in localization precision is achieved by adding more information into the system in the form of a spatial illumination shape and translations thereof. This well-characterized pattern and its precise displacement relative to the molecules lead to a predictably modulated response of the number of captured photons from which extra information can be gained. Even though any structured illumination with high-contrast could work in theory, so far, only a doughnut-shaped pattern from STED [19] and sinusoidal patterns from SIM [20] have been demonstrated.

As described in Chapter 1, MINFLUX was the first in this series of techniques, using a doughnut-shaped pattern with nanometer shifts. An area of about 100×100 $(\mathrm{nm})^2$ limited the first MINFLUX implementation [21], but meanwhile, it has been extended to FOVs of approximately 10×10 $(\mu\mathrm{m})^2$ [22]. Other extensions to the MINFLUX idea have been proposed with 3D, multicolor, and iterative fluorophore targeting [22], interleaved laser pulses to give access to the fluorescence lifetime (p–MINFLUX) [23], and two-photon MINFLUX to double the localization precision [24].

SIMFLUX as presented in Chapter 3, extended the MINFLUX idea to typical micron-sized FOVs using sinusoidal patterns. Other techniques have been developed alongside the introduction of SIMFLUX, such as ROSE [25] and SIMPLE [26] based on the same illumination pattern but with different optical hardware. These all demonstrate an improvement factor of around two over standard 2D SMLM over large FOVs, making these approaches very compelling and pushing SMLM to sub 10 nm resolution. Instead of improving the lateral (x, y) localization, the same principle has been demonstrated along the optical axis to enhance the axial (z) localization precision (ModLoc) [27], which provides almost a uniform 3D localization precision.

While all these methods improve localization precision, it comes at a cost that a molecule needs to be in the on-state for multiple successive frames to estimate the molecule position successfully. In SIMFLUX, the requirement is to have blocks of at least six on-state frames and molecules that are in the on-state for a shorter time need to be rejected in the estimation to avoid outliers. We analyzed this in Chapter 4 and implemented a modulation error filter with a predicted error threshold based on expected values from the retrieved illumination patterns. The Jaccard index of the detection rates was quantified to be approximately 65 percentage points, which leaves room for improvement compared to 2D SMLM methods [28].

A more advanced detection and rejection step is advised for a more robust estimation process. For instance, this can be implemented as a post-processing step by quantifying the resulting fit and data, with e.g. the Wasserstein-induced flux (WIF) [29] or the log-likelihood ratio. The event rejection method, however, is particularly challenging for molecules that are in the on-state when the zero of the sinusoidal pattern is very near to the molecule's position. In such an instance only a few signal photons are captured, which makes intensity-based rejection less robust. Therefore a pre-detection step could be explored on denoised data to identify these very dim spots using deep learning. A few of such methods have been shown recently to have excellent promise for such a purpose [16, 17]. This could be combined with a probabilistic segmentation algorithm to only pass molecules that are likely to be in the on-state for at least six frames.

Another challenge of modulation enhanced localization microscopy is to use all the information present in the SMLM data. As discussed with SIMFLUX, molecules that are not in the on-state for six successive frames are rejected in the estimation and are, so far, considered as noise. This results in general in a loss of image resolution. Therefore the future of modulation enhanced localization microscopy should build on both a calibrated illumination pattern that optimizes the localization precision as well as an estimation scheme that fully utilizes all the single molecule spots to optimize the overall image resolution.

6.2.3 Software

There are two ways to promote the usefulness to the SMLM community of the vectorial PSF fitting pipeline, as used in Chapters 4 and 5, namely by ease-of-use to non-experts and by faster processing times.

Software distribution The developed algorithm is open source and publicly available for users to download and run. However, the primary tools are implemented in MATLAB, a commercial software package. Potential users need to install the MATLAB runtime library, which may be impractical for specific users. Therefore, a first extension to this work is to convert to a completely open-source platform like Python or C. This would allow much more users in the field to make use of vector PSF fitting algorithms.

A subsequent extension is to enable non-experts to use the software with an open-source plugin in, e.g., ImageJ, providing effortless distribution in the biological community. Here, widgets serve as the interface between the user and the functionalities with

a top-level graphical user interface (GUI) that instantiates the parameters of interest to make it easy to use.

GPU acceleration The vectorial PSF fitting is currently parallelized in MATLAB to use different CPU cores, which speeds up the computation time. However, on a typical hardware setup, the number of cores is limited, which stands in the way of an orders of magnitude speed-up. Implementing the algorithm using graphics processing unit (GPU) computation will significantly reduce the computation time, as computation of each instance of the vectorial PSF is not that costly. The computation is mostly spent evaluating 2D Fourier transforms implemented using the chirp z-transform technique [30, 31], which limits the current CPU implementation. However, given the recent efforts of numerous SMLM algorithms using GPUs [32, 33, 34, 35], we envision the vectorial PSF to be performed with GPU computation as well. Along with a GPU implementation, another way to optimize computation speed is to develop a deep learning library [36], e.g., based on TensorFlow or PyTorch, where the vectorial PSF is used as training data.

References

[1] C. Franke, M. Sauer, and S. V. De Linde. "Photometry unlocks 3D information from 2D localization microscopy data". In: *Nature Methods* 14.1 (2016), pp. 41–44. ISSN: 15487105.

[2] "Computational correction of spatially variant optical aberrations in 3D single-molecule localization microscopy". In: *Optics Express* 27.9 (2019), p. 12582. ISSN: 1094-4087.

[3] K. M. Douglass et al. "Super-resolution imaging of multiple cells by optimized flat-field epi-illumination". In: *Nature Photonics* 10.11 (2016), pp. 705–708. ISSN: 17494893.

[4] D. Mahecic et al. "Homogeneous multifocal excitation for high-throughput super-resolution imaging". In: *Nature Methods* 17.7 (2020), pp. 726–733. ISSN: 15487105.

[5] F. Xu et al. "Three-dimensional nanoscopy of whole cells and tissues with in situ point spread function retrieval". In: *Nature Methods* 17.5 (2020), pp. 531–540. ISSN: 15487105.

[6] D. Burke et al. "Adaptive optics correction of specimen-induced aberrations in single-molecule switching microscopy". In: *Optica* 2.2 (2015), p. 177. ISSN: 2334-2536.

[7] S. Stallinga. "Effect of rotational diffusion in an orientational potential well on the point spread function of electric dipole emitters". In: *Journal of the Optical Society of America A* 32.2 (2015), p. 213. ISSN: 1084-7529.

[8] A. S. Backer and W. E. Moerner. "Determining the rotational mobility of a single molecule from a single image: a numerical study". In: *Optics Express* 23.4 (2015), p. 4255. ISSN: 1094-4087.

[9] J. Schaffer et al. *Identification of Single Molecules in Aqueous Solution by Time-Resolved Fluorescence Anisotropy.* 1999.

[10] M. P. Backlund, Y. Shechtman, and R. L. Walsworth. "Fundamental Precision Bounds for Three-Dimensional Optical Localization Microscopy with Poisson Statistics". In: *Physical Review Letters* 121.2 (2018), p. 023904. ISSN: 10797114. arXiv: 1803.01776.

[11] O. Zhang and M. D. Lew. *Quantum limits for precisely estimating the orientation and wobble of dipole emitters.* 2020. arXiv: 2003.07846.

[12] H. P. Babcock and X. Zhuang. "Analyzing Single Molecule Localization Microscopy Data Using Cubic Splines". In: *Scientific Reports* 7.1 (2017), pp. 1–9. ISSN: 20452322.

[13] Y. Li et al. "Real-time 3D single-molecule localization using experimental point spread functions". In: *Nature Methods* 15.5 (2018), pp. 367–369. ISSN: 15487105.

[14] E. Hoogendoorn et al. "The fidelity of stochastic single-molecule super-resolution reconstructions critically depends upon robust background estimation". In: *Scientific Reports* 4.1 (2014), pp. 1–10. ISSN: 20452322.

[15] L. Möckl et al. "Accurate and rapid background estimation in single-molecule localization microscopy using the deep neural network BGnet". In: *Proceedings of the National Academy of Sciences of the United States of America* 117.1 (2020), pp. 60–67. ISSN: 10916490.

[16] A. Krull, T. O. Buchholz, and F. Jug. "Noise2void-Learning denoising from single noisy images". In: *Proceedings of the IEEE Computer Society Conference on Computer Vision and Pattern Recognition* 2019-June (2019), pp. 2124–2132. ISSN: 10636919. arXiv: 1811.10980.

[17] J. Lehtinen et al. "Noise2Noise: Learning image restoration without clean data". In: *35th International Conference on Machine Learning, ICML 2018* 7 (2018), pp. 4620–4631. arXiv: 1803.04189.

[18] E. Nehme et al. "DeepSTORM3D: dense 3D localization microscopy and PSF design by deep learning". In: *Nature Methods* 17.7 (2020), pp. 734–740. ISSN: 15487105.

[19] T. A. Klar et al. "Fluorescence microscopy with diffraction resolution barrier broken by stimulated emission". In: *Proceedings of the National Academy of Sciences of the United States of America* 97.15 (2000), pp. 8206–8210. ISSN: 00278424.

[20] M. G. Gustafsson. "Surpassing the lateral resolution limit by a factor of two using structured illumination microscopy". In: *Journal of Microscopy* 198.2 (2000), pp. 82–87. ISSN: 00222720.

[21] F. Balzarotti et al. "Nanometer resolution imaging and tracking of fluorescent molecules with minimal photon fluxes". In: *Science* 355.6325 (2017), pp. 606–612. ISSN: 10959203. arXiv: 1611.03401.

[22] K. C. Gwosch et al. "MINFLUX nanoscopy delivers 3D multicolor nanometer resolution in cells". In: *Nature Methods* 17.2 (2020), pp. 217–224. ISSN: 15487105.

[23] L. A. Masullo et al. "Pulsed Interleaved MINFLUX". In: *Nano Letters* (2021). ISSN: 15306992.

[24] K. Zhao et al. "Two-photon MINFLUX with doubled localization precision". In: *arXiv* (2020). ISSN: 23318422. arXiv: 2012.02499.

[25] L. Gu et al. "Molecular resolution imaging by repetitive optical selective exposure". In: *Nature Methods* 16.11 (2019), pp. 1114–1118. ISSN: 15487105.

[26] L. Reymond et al. "SIMPLE: Structured illumination based point localization estimator with enhanced precision". In: *Optics Express* 27.17 (2019), p. 24578. ISSN: 1094-4087.

[27] P. Jouchet et al. "Nanometric axial localization of single fluorescent molecules with modulated excitation". In: *Nature Photonics* (2021), pp. 1–8. ISSN: 17494893.

[28] D. Sage et al. "Super-resolution fight club: assessment of 2D and 3D single-molecule localization microscopy software". In: *Nature Methods* 16.5 (2019), pp. 387–395. ISSN: 15487105.

[29] H. Mazidi et al. "Quantifying accuracy and heterogeneity in single-molecule super-resolution microscopy". In: *Nature Communications* 11.1 (2020), pp. 1–11. ISSN: 20411723.

[30] J. L. Bakx. "Efficient computation of optical disk readout by use of the chirp z transform". In: *Applied Optics* 41.23 (2002), p. 4897. ISSN: 0003-6935.

[31] M. Leutenegger et al. "Fast focus field calculations". In: *Optics Express* 14.23 (2006), p. 11277. ISSN: 1094-4087.

[32] A. Przybylski et al. "Gpufit: An open-source toolkit for GPU-accelerated curve fitting". In: *Scientific Reports* 7.1 (2017), pp. 1–9. ISSN: 20452322.

[33] I. Munro et al. "Accelerating single molecule localization microscopy through parallel processing on a high-performance computing cluster". In: *Journal of Microscopy* 273.2 (2019), pp. 148–160. ISSN: 13652818.

[34] L. Li et al. "Divide and conquer: real-time maximum likelihood fitting of multiple emitters for super-resolution localization microscopy". In: *Optics Express* 27.15 (2019), p. 21029. ISSN: 1094-4087.

[35] K. Bernhem and H. Brismar. "SMLocalizer, a GPU accelerated ImageJ plugin for single molecule localization microscopy". In: *Bioinformatics* 34.1 (2018). Ed. by R. Murphy, pp. 137–138. ISSN: 14602059.

[36] P. Zhang et al. "Analyzing complex single-molecule emission patterns with deep learning". In: *Nature Methods* 15.11 (2018), pp. 913–916. ISSN: 15487105.

7 Acknowledgements

Since beginning this thesis four years ago, I have met many people whose assistance, support, or presence have helped me work toward the finish line.

Bernd and Sjoerd, thank you for providing me with this opportunity and giving me so much freedom in this work, for all our discussions, for fun we had at conferences close to home and far away, and for making an excellent supervisor pair. I think we found the perfect balance between science and football discussions.

In the group, I want to especially thank Ronald and Annelies. For all the help you provided over the years with computer problems and with the administrative side that made my work so much easier and for setting the scene for a great atmosphere in the group.

I want to thank all the Quantitative Imaging group members for the best coffee breaks, interesting office discussions, fun summer outings, Friday afternoon drinks, and much more.

I want to thank my family and friends for their fun and support in the difficult final stages of writing my thesis during a pandemic, and especially Yu Wah, who had a front-row seat to the whole thing. Thank you for your patience over these years and for accepting the peculiarities of living with a PhD student. I look forward to our future together.

8 List of Publications

Below is a list of publications that have been compiled during the period of work on this thesis:

Journal Publications

1. *High precision wavefront control in point spread function engineering for single emitter localization*, M. Siemons, C. N. Hulleman, **R.Ø. Thorsen**, C. S. Smith, S. Stallinga, Optics Express, **26** (7), 8397-8416 (2018)

2. **(Chapter 2)** *Impact of optical aberrations on axial position determination by photometry*, **R.Ø. Thorsen**, C.N. Hulleman, M. Hammer, David Grünwald, S. Stallinga, B. Rieger, Nature Methods, **15**, 989-990 (2018)

3. **(Chapter 3)** *Localization microscopy at doubled precision with patterned illumination*, J. Cnossen, T. Hinsdale, **R.Ø. Thorsen**, M. Siemons, F. Schueder, R. Jungmann, C.S. Smith, B. Rieger, S. Stallinga, Nature Methods, **17**, 59-63 (2020)

4. **(Chapter 4)** *Simultaneous orientation and 3D localization microscopy with a Vortex point spread function*, C.N. Hulleman, **R.Ø. Thorsen**, S. Stallinga, B. Rieger, bioRxiv (2020)

Unpublished work

1. **(Chapter 5)** *Photon efficient orientation estimation using polarization modulation in single-molecule localization microscopy*, **R.Ø. Thorsen**, C.N. Hulleman, S. Stallinga, B. Rieger, in preparation (2021)

9 Curriculum vitae

Rasmus Thorsen was born on Bornholm, Denmark on August 18, 1989. He obtained his electrician diploma in 2010 from the company Knudsker-el in Rønne. He received his Bachelor of Science and Master of Science degrees with honors in Electrical Engineering from the Technical University of Denmark in 2014 and 2016. During his Master's program, he spent seven months at the University of Arizona as a visiting scholar to collaborate research in the computational electromagnetic lab. He concluded this work with a research thesis on metamaterial-inspired nanoantennas.

In 2017 he started as a PhD student in the Computational Imaging group of the Imaging Physics department at the Delft University of Technology. His research focused on parameter estimation in single-molecule localization microscopy, of which the most important findings are presented in this thesis.

Since July 2021, he is a Design Engineer working on lens models in the extreme ultraviolet lithography machines at ASML.